Damage tolerance of refill Friction Stir Spot Weld application for the aircraft industry

Vom Promotionsausschuss der

Technischen Universität Hamburg

zur Erlangung des akademischen Grades

Doktor-Ingenieur (Dr.-Ing.)

genehmigte Dissertation

von

Robson Cristiano Brzostek

aus

Erechim

2019

Gutachter:
Prof. Dr.-Ing. Norbert Huber
Prof. Dr. Xiang Zhang

Vorsitzender des Prüfungsausschusses
Prof. Dr.-Ing. Christian J. Cyron

Tag der mündlichen Prüfung:
26.04.2019

Acknowledgments

This work is a result of four years of research on refill Friction Stir Spot Weld at Helmholtz-Zentrum Geesthacht (former GKSS). The results presented here could not have been achieved without the help and support of many colleagues and friends. I would like to express my sincere gratitude to those who have supported and contributed to this Ph.D. work, which would not have been without any of them.

- Head of Institute Prof. Dr.-Ing. Norbert Huber for support within the institute, recommendation and supervision of the work.
- Prof. Dr. Jorge dos Santos for the opportunity to perform this research within his department, constant support, recommendation, encouragement throughout all stages of my Ph.D., and all the opportunities to develop my academic career at HZG. His enthusiasm and motivation have significantly inspired this work.
- Prof. Dr. Xiang Zhang for accepting to review this Ph.D. work and for her contribution during the Ph.D. and to the examination process.
- Several colleagues from HZG, particularly Jürgen Knaack, and Kay Erdmann for their assistance with mechanical testing. All colleagues of the solid-state joining department (WMP), for their friendship, teamwork, and helpful discussion. I would like to mention the help and technical support of Luciano Bergmann, Jan Carstensen and Menno Peters. The members of the refill Friction Stir Spot Weld team. With a special mention to Dr. Uceu Suhuddin. Thanks for having contributed immensely to my professional career, for great teamwork, cheerful company and friendship.
- Coordenação de Aperfeiçoamento de Pessoal de Nível Superior – Capes (Brazil) for supporting the project and sponsoring my Ph.D.
- My beloved mother Lucia who always encouraged and supported me along the way, and brothers Jeferson, Juliano and Fernanda.
- My lovely wife Maiara for her uninterrupted support, understanding, exceptional inspiration and patience, especially during the most difficult times. My beloved son Ian and four-legged-daughter Zara. I am grateful for having you always by my side, and I would not have made it this far without your continuous support to all my pursuits and love throughout my life.

Zusammenfassung

Reibpunktschweißen ist ein Festphasen-Schweißverfahren, das zum Schweißen von Leichtbauwerkstoffen in ähnlicher oder unähnlicher Überlappverbindungen für die Konfiguration geeignet ist. Es erweist sich als eine vielversprechende neue Fügetechnologie, insbesondere für hochfeste Aluminiumlegierungen, die im Vergleich zu herkömmlichen Schweißverfahren große Vorteile aufweisen. Gegenwärtig wird Reibpunktschweißen als eine mögliche Alternative für eine genietete Struktur anerkannt. Es ermöglicht eine Erhöhung der Herstellungskosteneffektivität aufgrund einer vernünftigen Kostenreduzierung und strukturellen Effizienz. Das Hauptziel dieser Arbeit ist es, das mechanische Verhalten und die Rissausbreitung in Verbindungen zu untersuchen, die von Reibpunktschweißen verursacht werden. Die Studie konzentriert sich auf die Anwendung der Schadenstoleranz in integralen Strukturen von Reibpunktschweißen in Aluminiumlegierung AA2024-T3 hergestellt.

Bisher waren die Prozessentwicklung und die mechanische Leistungsstudie überwiegend empirisch. Daher ist ein Übergang zu einem wissenschaftsbasierten Ansatz dringend erforderlich. Die hier vorgestellte Arbeit wurde durchgeführt, um eine Beziehung zwischen der experimentellen Erforschung und numerischen Modellen zu etablieren, die für die Entwurfsoptimierung und Ermüdungsrisswachstumsanalyse verwendet werden können. Davor wurden die Schweißverbindungen mechanisch und metallurgisch beurteilt, um die Optimierung der Prozessparameter (Drehzahl, Schweißdauer und Eindringtiefe) für Festigkeit und Ermüdungsbelastung zu untersuchen. Diese Untersuchung zeigt die Entwicklung der strukturellen numerischen Modelle, wo zwei strukturelle Modelle entwickelt wurden, um die Entwurfsoptimierung zu analysieren. Das erste Modell umfasst die Spannungsanalyse, die Last, die durch Reibung übertragen wird, die Spannungskonzentration und die Position der Höchstspannung. Es wurde unter Berücksichtigung des strukturellen und kohäsiven Ansatzes gebaut. Das zweite numerische Modell berücksichtigt den eingebetteten Ansatz; es kann für parametrische Studien mit guter Genauigkeit verwendet werden. Dann wurde die Entwurfsoptimierung unter Berücksichtigung der Abstände entwickelt: Anzahl der Schweißpunktreihen, Punktschweißreihenabstand, Punktschweißabstand in der Reihe und Abstand der Punktschweißung von der Blechkante. Die Entwicklungen der Entfernungen wurden unter Berücksichtigung ihrer Leistung in quasi-statischen und Ermüdungsbelastung durchgeführt.

Eine fraktographische Analyse bei verschiedenen Brucharten wurde durchgeführt. Dies ist notwendig, um die Rissausbreitung nach der Bruchmechanik zu verstehen und zu beschreiben. Dann wurde ein numerisches Modell entwickelt und kalibriert, um Spannungsintensitätsfaktoren für die zuvor beschriebenen Risse zu erhalten. Das numerische Modell wurde mit der eXtended Finite Element Methode erstellt.

Abschließend behandelt die Arbeit die Rissausbreitung und Restfestigkeit von Reibpunktschweißen in dünnen Platten für Flugzeugrumpfanwendungen. In dem Vollmaßstab wurde eine detaillierte experimentelle Untersuchung durchgeführt, um die Rissausbreitung unter verschiedenen Versagensszenarien zu verstehen. Darüber hinaus wurden die experimentellen Ergebnisse verwendet, um das entwickelte Modell des Ermüdungsrisswachstums zu verifizieren und zu kalibrieren. Das Modell wurde verwendet, um die Rissausbreitung in verschiedenen Verbindungskonfigurationen und anfänglichen Rissen zu simulieren. Das numerische Modell wurde mit der eXtended Finite Element Methode erstellt. Die Ergebnisse zeigen eine gute Übereinstimmung der Vorhersage-Ermüdungslebensdauer mit den experimentellen Ergebnissen. Dann wurden beide Modelle der Finite-Elemente-Methode für die Restfestigkeitsvorhersage von

gecrackten unversteiften Platten hinsichtlich des Spannungsintensitätsfaktors verwendet. Die Ergebnisse zeigen, dass Reibpunktschweißen sowohl hochfeste Verbindungen herstellen kann als auch die Bedeutung des Gelenkdesigns, bei dem durch Verwendung der richtigen Abstände, eine signifikante Verbesserung erzielt werden kann. Das aus den numerischen Modellen gewonnene Wissen über das strukturelle Verhalten und das Ausmaß der Rissausbreitung ist bedeutsam, um den Einfluss der sekundären Biegung auf gerissene Platten und die Entwicklung von Residual-Strength-Diagrammen zu verstehen.

Abstract

Refill Friction Stir Spot Welding (refill FSSW) is a solid-state process technology that is suitable for welding lightweight materials in similar or dissimilar overlapped configurations. Refill FSSW has been demonstrated to be a promising new joining technique, especially for high-strength aluminium alloys, which has presented significant advantages compared with conventional welding processes. Currently, refill FSSW is recognised as a potential alternative for riveted structures; it enables an increase in the manufacturing cost effectiveness due to sensible cost reduction and structural efficiency. The main objective of this study is to investigate the mechanical behaviour and crack propagation in joints produced by refill FSSW. The study focuses on the application of the damage tolerance design philosophy in integral structures produced by refill FSSW in aluminium alloy AA2024-T3.

Currently, the majority of studies of the process development and mechanical performance have been empirical. Thus, a transition to a science-based approach is necessary. This study was conducted to establish a relationship between experimental investigation and a set of numerical models that can be employed for design optimisation and fatigue crack growth analysis. Previously, welded joints were mechanically and metallurgically assessed to investigate the mechanism and optimisation of process parameters (rotation speed, welding time and plunge depth) in terms of quasi-static loading and fatigue loading. This investigation has assisted the development of structural numerical models, in which two structural models have been developed to explore the design optimisation. The first model addresses the stress analysis, load transferred, load transferred by friction, stress concentration and peak stress location; it was built considering the structural and cohesive approach. The second numerical model considers the embedded approach; it can be applied for parametric studies with acceptable accuracy. Next, the design optimisation was developed considering the distances: number of spot weld rows, spot weld row spacing, spot weld pitch in a row and distance between a spot weld and sheet edge. The development of the distances were performed considering their performance in quasi-static and fatigue loading.

A fractography analysis at various fracture modes has been performed to understand and describe the crack propagation according to the fracture mechanics. Next, a numerical model has been developed and calibrated to obtain stress intensity factors for the previously described cracks. The numerical model has been built with the eXtended Finite Element Method.

This thesis addresses the crack propagation and residual strength of refill FSSW in thin panels for aircraft fuselage applications. A detailed experimental investigation of the refill FSSW of panels has been conducted to understand crack propagation in different failure scenarios. The experimental results have been employed to verify and calibrate the developed fatigue crack growth numerical model. The model has been applied to simulate crack propagation in different joint configurations and initial cracks. The numerical model has been built with the eXtended Finite Element Method. The experimental results are consistent with the predicted fatigue life. Next, both eXtended Finite Element Method numerical models have been employed for the residual strength prediction of cracked unstiffened panels in terms of the stress intensity factor. The results of this study have demonstrated the feasibility of refill FSSW to produce high-strength joints and the importance of the joint design, which can be significantly improved using correct distances. The knowledge concerning the structural behaviour and extent of crack propagation gained from the numerical models is valuable for elucidating the influence of secondary bending on cracked panels and the development of residual strength diagrams.

Symbols and Abbreviations

3D	Three Dimensions
ANOVA	Analysis of Variance
BB	Box-Behnken
BW	Bonded Width
CCT	Centre Crack Tension
CV	Coefficient of Variation
CDF	Cumulative Density Function
DIC	Digital Image Correlation
DoE	Design of Experimental
FAA	Federal Aviation Administration
FAR	Federal Aviation Requirement
FCG	Fatigue Crack Growth
FE	Finite Element
HAZ	Heat Affected Zone
HLT	High Load Transfer
Hh	Hook Height
K-factors	Stress Intensity Factors
LEFM	Linear Elastic Fracture Mechanics
LSS	Lap Shear Strength
MR	Bernard's Median Rank
MSD	Multiple Sites Damage
MTTF	Weibull Mean Time to Failure
PD	Plunge Depth
PDF	Probability Density Function
PPO	Plug Pull-Out
refill FSSW	Refill Friction Stir Spot Welding
RSM	Response Surface Methodology
RS	Rotational Speed
SEM	Scanning Electron Microscope
SD	Standard Deviation
SZ	Stir Zone
t	Welding Time
TMAZ	Thermo-Mechanical Affected Zone
TW	Through the Weld, also known as Interfacial Fracture Mode
TS-UP	Through the Sheet – Upper Plate
TS-LP	Through the Sheet – Lower Plate
USAF	United States Air Force
VCCT	Virtual Crack Closure Technique
XFEM	eXtend finite element method
a	Half of the crack length
a_c, a_{cri}	Critical crack length
a_f	Final crack length
$\mathbf{a}_I$	Nodal displacement vector

a_i	Initial crack length
a_m, a_n, a_0	Constant for the mixed model
b	Elliptical crack shape length
$\mathbf{b}_I^{\alpha}$	Nodal displacement vector
B	Thickness
$\boldsymbol{B}$	Pre-logarithmic energy factor matrix
c_1, c_2, c_3, c_4	Material constants for fatigue crack growth model
$C0$	Number of central points for DoE - BB
C	Material constant for fatigue crack propagation – Paris law
C_{excl}	Excluded number of contours (XFEM model)
C_{SN}	Coefficient of the SN curves
C_{tot}	Total number of contours in the contour domain evaluation (XFEM model)
d_{hole}	Diameter of the hole
d_{rivet}	Diameter of the rivet
d_{SW}	Diameter of the spot weld nugget
e	Edge distance
E	Young's modulus
E_{fhole}	Efficiency of a plate with a hole
E_{fSpot}	Structural efficiency of the lap joint produced by refill FSSW
f	Fracture criterion
f_r	Frequency
f_{tol}	Fracture criterion tolerance
$f(x)$	Distribution of the two-parameter Weibull distribution
$F_f(x)$	Integration of the Weibull distribution
F_{max}	Maximum load force of the lap shear test
F_x	Nodal reaction forces in x direction
F_y	Nodal reaction forces in y direction
$F_\alpha(x)$	Crack-tip enrichment functions (XFEM model)
G_I, G_{II} G_{III}	Energy release for fracture mode I, mode II and mode III
G_{IC}, G_{IIC}, G_{IIIC}	Critical equivalent energy release for fracture mode I, mode II and mode III
G	Griffith energy
G_C	Griffith energy criterion
G_{equiC}	Equivalent fracture energy release rate
G_{max}	Maximum energy release rate
G_{pl}	Energy release rate - upper limit
G_{thresh}	Threshold energy release rate
h	Elliptical crack shape height
$H(x)$	Heaviside jump function
i_{MR}	Failure serial number of the Weibull distribution
I_n	Integration constant as function of n
k_b	Bending factor
k_f	Number of factors for DoE - BB
K_0	Stress intensity factors for a body without boundaries
K_I, K_{II}, K_{III}	Stress intensity factor for mode I, mode II and mode III, respectively
K_{Ic}	Plane stress fracture toughness for mode I

K_I^{FE}	K_I-*factor* obtained from the numerical model
$K^{´}{}_I$ and $K^{´}{}_{II}$	*K-factors* as function of distance x_c
$\boldsymbol{K}$	$= [K_I\ K_{II}\ K_{III}]$ (matrix)
K_c	Fracture toughness
K_{c0}	Apparent fracture toughness
K_{eff}	Effective stress intensity factor
K_i	Stress intensity factor at crack initiation
K_n	*K-factors* for body with boundary
K_{nn}	Contact penalty constrains in normal (cohesive model)
K_{op}	Stress intensity factor when the crack opens
K_{ss}	Contact penalty constrains in shear (cohesive model)
K_t	Stress concentration
K_{th}	Fracture threshold
K_{tt}	Contact penalty constrains in tangential (cohesive model)
l_c	Clamping length lap shear samples
l_f	Free length between clamps for lap shear samples
L_e	Finite element length
m	Material constants for fatigue crack propagation – Paris law
m_{SN}	Exponent of the SN curves
n	Material hardening exponent
$\mathbf{n}$	Unit outwards normal to the crack at $\mathbf{x}^*$ (XFEM model)
n_j	Component of the unit vector normal to Γ (J-Integral)
n_{MR}	Total number of samples for Weibull distribution
n_{SW}	Number of spot welds rows
$N_I(x)$	Nodal shape functions of XFEM
N	Number of cycles
N_f	Number of cycles to failure
NE	Number of experiments – Doe - BB
N_{boun}	Boundaries into auxiliary configurations
N_{R_x}	Fatigue life indicating $X\%$ of reliability for Weibull distribution
Ov	Overlap Length of the lap shear sample
p	Spot weld row spacing,
P	Load perpendicular to the crack
r	Radius of the plastic zone at the crack tip
r_p	Second-order of the plastic zone at the crack tip
r_y	First-order of the plastic zone at the crack tip
R	Stress ratio
R_e	Reliability for Weibull distribution
S_{11}	Local stresses in the load direction
S_{22}	Local stresses perpendicular to the top surface
S_{33}	Local stresses perpendicular to the load direction
S	Spot weld pitch in row
S_a	Nominal stress amplitude
S_e	Spot weld from the sheet edge
S_{faying}	Peak stress at the root of spot weld

S_{max}^{local}	Local maximum stress
S_{min}	Local stress relate to minimum remote stress
S_{max}	Local stress relate to maximum remote stress
t_I, t_{II}	Load in direction of mode I and mode II
${t_n}^0$, ${t_s}^0$,${t_t}^0$	Maximum contact stress for the surface separation normal, shear and tangential (cohesive model)
t_n , t_s, t_t	Internal variable of contact stress for surface separation normal, shear and tangential (cohesive model)
T_{bp}	Bypass load
T_{ij}	Force transferred by each spot weld (i-rows and j-plates)
T_i	Components of the traction vector
T_{tr}	Transferred load by the spot weld
T_{fr}	Friction load
u, u_x, u_1	Displacement in direction x
u_i	Displacement vector components
$\mathbf{u}_I$	Nodal displacement vector
u_l	Node displacements
U	Strain energy
U_{Elber}	Elber's effective stress intensity ratio
U_{Schi}	Schijve's effective stress intensity ratio
v, u_y, u_2	Displacement in direction y
w, u_z, u_3	Displacement in direction z
w_l	Node displacements
W	Specimen width
W_e	Strain energy density
$\mathbf{x}$	Sample Gauss (XFEM model)
$\mathbf{x}^*$	Point on the crack closest to $\mathbf{x}$ (XFEM model)
x_c	Distance of the crack in the x direction
X_i	Nodal forces
Z_i	nodal forces at point
α	Dimensionless constant of the HRR field (XFEM model)
α_{WS}	Characteristic life Weibull distribution
β	Geometry correction function
β_{WS}	Weibull slope (shape parameter)
Γ	Arbitrary path around the tip of a crack – *J-Integral*
$\Gamma()$	Gamma function
ε_0	Reference strain
ε_{ij}	Strain tensor
$\tilde{\varepsilon}_{ij}$	Dimensionless Strain tensor
θ_c	Crack growth direction
μ	Shear modulus
μ_{fric}	Friction coefficient
v	Poisson's ratio
σ	Remote stress to the crack plane

σ_0	Reference stress
σ_b	Local bending stress
σ_e	Yield stress
σ_f	Fracture strength
σ_{fay}	Stress at faying surface
σ_{free}	Stress at free surface
σ_h	Hydrostatic stress
σ_{ij}	Stress tensor
$\tilde{\sigma}_{ij}$	Dimensionless Stress tensor
σ_{max}	Maximum stress
$\sigma_{nominal}$	Stress relate to gross area of the sample
σ_{op}	Crack opening stress
σ_{uts}	Ultimate strength of the base material
σ_{xx}	Stress in direction xx
σ_{YS}	Yield strength
σ_{yy}	Stress in direction yy
σ_{zz}	Stress in direction zz
τ_{xy}	Stress in direction xy

Contents

Chapter 1.
Introduction

1.1. Motivation

Aeronautical and aerospace structures are characterised by severe load service conditions, extreme reliability and high safety requirements. In addition, an increase in the number of requirements to decrease the Direct Operating Costs causes a conflict between economy and safety. Designers must provide efficient joints by reducing the structural weight and minimising the maintenance costs and structures must demonstrate high strength and durability. The need to reduce the energy consumption in the civil aircraft industry has indicated a need for lighter and cost-effective airplanes. This need has prompted a revolution in the design of metallic structures during recent decades; a reduction of the manufacturing costs is a key requirement for enhancing the competitiveness [1-6].

Friction-based processes can generate benefits compared with traditional riveted structures. These processes produce welded joints without flaws or defects and superior metallurgical properties. The heat input and residual stress are comparatively low. The adoption of these welding processes provides weight and costs savings of approximately 15%. The assembly time and cost are also decreased due to reduced assembly operations [7, 8].

Riveting has been the standard joining method of fuselage parts for decades, and friction-based processes have been considered to be a strong candidate to replace riveted structures as they enable sensible cost reductions and structural efficiency [7, 8]. Friction-based joining processes have demonstrated remarkable developments in the transportation industry as they can avoid defects associated with material solidification [9]. Refill Friction Stir Spot Weld (refill FSSW), which is also known as friction spot welding, is considered to be one of the most attractive friction-based solid-state spot processes and produces high-quality spot welds [10-13]. Developed and patented by Helmholtz-Zentrum Geesthacht (formerly GKSS) [US Patent 6,722,556 B2], refill FSSW can join two or more sheet materials in an overlapped configuration. Currently, refill FSSW is recognised as a potential alternative for riveted structures.

Despite these advantages, the change from a differential (riveted) design to an integral (welded) design introduces new challenges that potentially need to be considered in the analysis route for cracked welded components that consist of thin sheets [14]. Typically, the design of airplanes must satisfy the damage tolerance requirements of fatigue and residual strength. The damage tolerance structural design philosophy in aeronautics requires a comprehensive knowledge of fatigue and potential failure modes [1-6, 14].

The residual strength concept permits the determination of the maximum crack length that can be safely sustained. With this information and the characterisation of the crack growth behaviour of a component, the number of loading cycles that is necessary for crack growth to its critical length can be estimated to ensure safe operation. The development of numerical methodologies using small laboratory coupons should be employed to predict the residual strength of complex built-up aircraft fuselage structures [1-6, 14].

1.2. Objectives

The main objective of this study is to improve the knowledge of the mechanical behaviour of refill FSSW under quasi-static and cyclic loading in thin monolithic aluminium AA2024-T3 sheets. Addressing all aspects of the damage tolerance requirements is beyond the scope of this study, which primarily concentrates on fatigue of refill FSSW welded joints and the fatigue crack growth and crack propagation behaviour of integrally welded panels. A successful design optimisation depends on a comprehensive understanding of the mechanical strength of a joint; therefore, numerical models are essential for predicting and optimising structures.

To achieve a science-based design optimisation, the development strategy incorporates the following objectives:

- demonstrate the capabilities of the refill FSSW;
- analyse the structural behaviour of refill FSSW in single- and multiple-spot welds to develop design data (guideline) for design optimisation;
- perform experiments in panels that contain design details and measure crack growth and residual strength considering the damage tolerance approach.

The milestones of the study are described as follows:

- derive the design curves in terms of load vs. displacement under static and dynamic loads;
- application of the Design of Experiment methodology to streamline the experimental data and determine the optimum process parameters in terms of quasi-static lap shear test and fatigue test;
- determine the effect of process parameters on macrostructural features;
- perform fatigue tests and develop SN curves using a statistical analysis in single-, double- and triple-spot weld rows;
- track and describe the crack propagation in quasi-static and dynamic loading;
- develop a structural numerical model to represent single- and multiple-spot welds (quasi-static);
- perform quasi-static tests in panels with multiple-spot welds;
- determine the minimum/optimum distances between spot welds considering the numerical and experimental tests;
- understand the transfer loads, percentage transferred by each spot weld and percentage of the load transferred by friction;
- develop a numerical model to determine the stress intensity factors for different cracks, crack sizes and different hook profiles;
- determine the effective stress intensity factor considering the crack closure phenomenon;
- calibrate and validate the numerical models;
- develop and calibrate a numerical model for fatigue crack growth;
- generate data of fracture process for integral panels and assess the residual strength of welded airframe panels that contain cracks and different crack lengths;
- apply numerical models to the design study and design optimisation and improve the mechanical strength.

1.3. Structure

The thesis starts with a literature review in Chapter 2, and a brief introduction to the actual state-of-the-art of refill FSSW that focuses on the mechanical strength of the joint is presented. Afterwards, the theoretical background to the fracture mechanism in elastic and elastic-plastic material structures was reviewed. The current approach to residual strength predictions of the aerospace damage tolerance philosophy, which highlights the drawbacks when applied to welded structural components, is also presented. Concluding, the different modelling approaches for stress intensity factors and fatigue crack propagation growth have been revised.

Chapter 3 describes the experimental approach in this study, which highlights the laboratory tests of materials and components that were established in the literature to ensure that an aircraft will pass qualifications and certifications programmes.

The results of the experimental programme, including the mechanical behaviour study, is presented in Chapter 4. In this chapter the key design curves in terms of load vs. displacement are derived under quasi-static and dynamic loads. The design optimisation is performed by combining the results and insights of the numerical models and the experimental tests.

In Chapter 5, the stress intensity factors (*K-factors)* for the typical crack propagation in fatigue are obtained. For this purpose, a numerical model using the eXtended finite element method is developed and calibrated. Beforehand, the crack propagation is tracked and described considering the fracture mechanism.

Chapter 6 extends previous studies to the panels. In support of the residual strength calculation, both fatigue crack growth and residual strength will be addressed in the same chapter. An assessment of the crack propagation in terms of fatigue life is performed; as this experimental test is performed in refill FSSW joints for the first time, the failure scenarios for the welded joints had to be defined. Afterwards, a fatigue crack growth model is developed and calibrated; this model can assist the design optimisation in terms of fatigue crack growth. A comparison with experimental data is presented in terms of crack length vs. load cycles for the stiffened panels. The numerical results and experimental data are employed to assess the residual strength of welded airframe panels that contain cracks and different crack lengths.

In Chapter 7, a summary of all findings are provided and conclusions are drawn.

Chapter 2.

Literature Review

In the following section, an overview of the refill FSSW joint is provided with a focus on its mechanical integrity. The background theory and the relevant literature of the fracture mechanics are presented. The fundamental equations of linear elastic fracture mechanics (LEFM) and fatigue crack propagation are given; in addition, the phenomenon of crack closure due to plasticity at the crack tip is described. In the following section, an overview of the design philosophy of damage tolerance is given; this study has a background of riveted structures with an attempt to understand the design factors of these structures. The residual strength approach is also described in terms of riveted unstiffened panels. The available numerical models for stationary crack and fatigue crack growth are presented to select the most efficient numerical technique for fracture mechanics analysis considering damage tolerance approach.

2.1. Refill Friction Stir Spot Weld (refill FSSW)

Reviews of friction-based solid-state processes have been constantly published by many authors with different emphases [15-20]. Therefore, only a brief description of the process is included in this study. The development of friction-based processes satisfied the need of a suitable process that is capable of joining high-strength aluminium alloys. Promptly, it became an important alternative to conventional fusion welding as it provides substantial mechanical properties and repeatability. The advantages of a friction-based process are divided into three main groups: (i) the solid-state nature of the process has numerous metallurgical benefits; (ii) the occurrence of solidification cracking is not common, and (iii) dissolution or no loss of alloying element [15, 21-23]. In addition, the lower temperature during the process causes lower distortion, which is generated by thermal expansion and lower residual stress [4].

Refill FFSW is a friction-based solid-state spot process that is capable of joining two or more sheet materials in an overlapped configuration and combines several material classes, such as aluminium, magnesium, steel and thermoplastic materials in similar or dissimilar configurations [10-12, 24]. Refill FSSW has produced high-quality spot-welds and provided a high potential for industrial application.

A non-consumable tool consists of three independent moving parts, as shown in Fig. 2.1: a stationary clamping ring, a rotating sleeve and a probe. The stationary clamping ring enables the plates to be tightly joined while the probe and sleeve rotate and plunge into the plates; the sleeve and probe are moved in opposite vertical directions to create a reservoir to accommodate the displaced material. Refill FSSW can be divided into four stages, as shown in Fig. 2.2. In the first stage, the stationary clamping ring presses the overlapped plates and holds the material against a backing bar while the probe and the sleeve start to rotate, which produces frictional heat on the upper plate surface. In the second stage, the sleeve plunges into the sheets while the probe moves upwards and creates space. The rotating sleeve generates frictional heating and introduces plastic deformation. Then, the sleeve squeezes the softened material to fill the cavity created by the probe with a constant volume flow rate. In the third stage, when the plunge depth is attained, the sleeve remains rotating in this position

(dwell time). Afterwards, the process is reversed—the probe and sleeve retract to the upper plate surface with the same volume flow rate in the second stage. This process forces the plasticised material to be entrapped in the formed cavity to refill the keyhole created by the sleeve. In the fourth stage, the clamping load is released, and the welding tool is withdrawn; leaving the weld without a keyhole [25, 26].

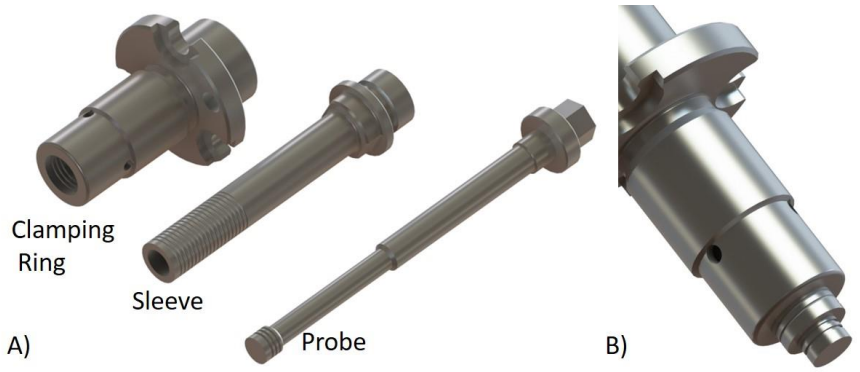

Figure 2.1. A) Schematic of the refill FSSW tool. B) Assembly of the refill FSSW tool.

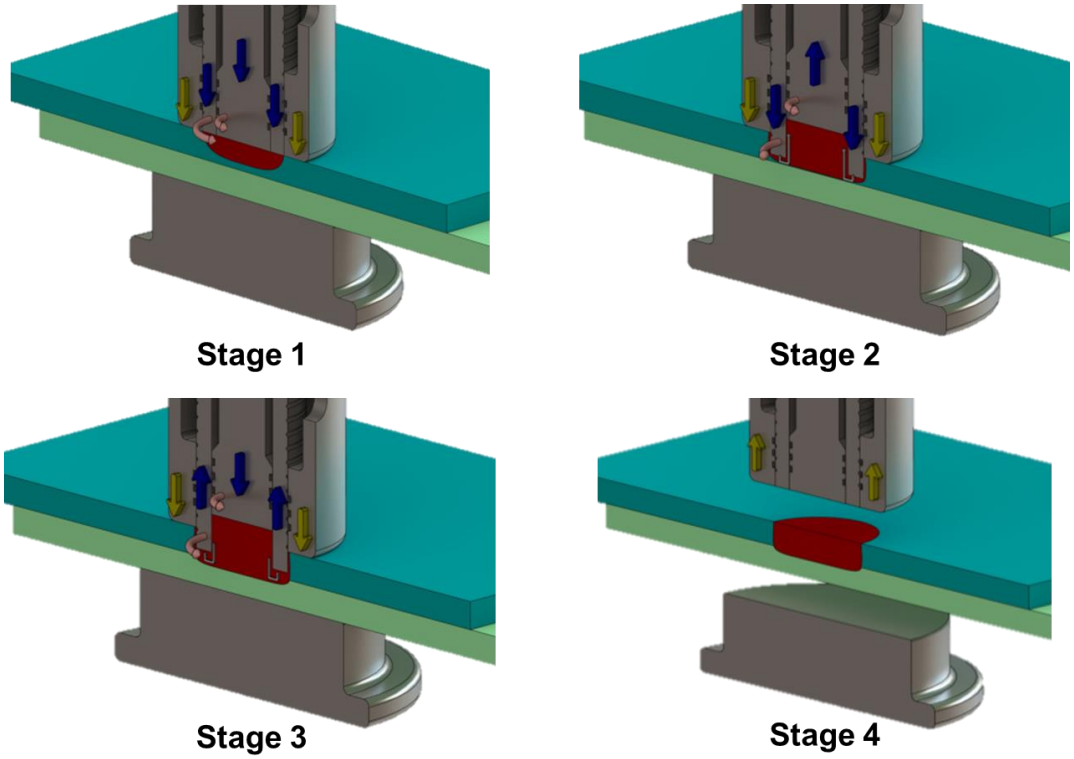

Figure 2.2. Refill friction stir spot welding process.

As previously mentioned, refill FSSW is a solid-state process and produces changes in a microstructure due to its thermal cycle. Fig. 2.3 presents a typical macrograph cross-section of the spot-weld produced by refill FSSW and highlights the different weld zones based on the microstructural characteristics: Stir Zone (SZ), Thermo-Mechanical Affected-Zone (TMAZ) and Heat-Affected Zone (HAZ). In the centre of the cross-section, the SZ is characterised by a refined-equiaxial grain structure, which is a consequence of the dynamic recrystallisation that is promoted by intensive plastic deformation and high temperatures. During the welding process, the SZ experiences frictional heating and stirring deformation induced by the tool rotation [13, 24, 25]. Friction-welded AA2024-T3 alloy can experience dynamic recrystallisation

at process temperatures starting from approximately 50% of the alloy melting temperature ($502 - 638$℃) and high shear rates associated with rotational speeds [27]. According to Amancio-Filho et al. [25] the maximum temperature involved in the refill FSSW for AA2024-T351 varied from $345 - 398$℃. Therefore, the average temperature and shear deformation rates in the SZ were probably sufficiently high to support dynamic recrystallisation, which causes grain refinement compared with the base material.

The surrounding SZ composes the TMAZ. As a result of the stirring action promoted by the tool where the base material is drawn around the sleeve surface, which promotes a large volume of plastic deformation, the TMAZ contains deformed and elongated grain structures. In addition, the transition between the TMAZ and the SZ can present 90-degree bent grains towards the top surface due to the axial retraction movement of the sleeve. Dynamic recrystallisation does not occur in the TMAZ due to the low peak temperatures and limited shear deformation [15, 26, 28-30]. The HAZ is located outside the TMAZ. In the HAZ, plastic deformation does not occur; however, this region undergoes a thermal cycle that affects the mechanical properties [11, 13, 24, 25]. Additional details of the fundamental transformation of the microstructure during the process, which are not described in this review, are discussed elsewhere [15, 31-33].

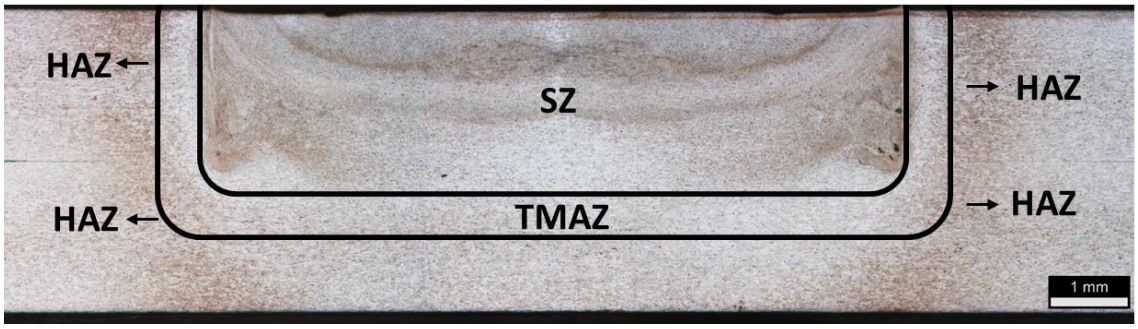

Figure 2.3. Typical cross-section of the refill FSSW process.

2.1.1. Mechanical strength of refill FSSW

Few studies of refill FSSW have been conducted to provide a better understanding of the fundamentals and structural behaviour. Shen et al. [34] reinforced the relationship between voids and flaws within mechanical behaviours, where the defects severely reduce the ultimate lap shear strength (LSS). Tier et al. [13] discovered that the bonding ligament length significantly affected the shear strength and an increase in the bonding ligament length produced high shear strength. In addition, fracture analyses revealed that cracks initiated in the boundary between the TMAZ and the SZ.

At the weld extremities, Rosendo et al. [35] determined that the transition between the unbonded interface of the upper and lower plate and the bonded spot nugget area includes an unbonded curved region, which is referred to as a hook, and a partially bonded region. The partially bonded region is composed of the remaining material from the interface of the sheets, which contain oxide particles and the metallurgically bonded area. In low-strength welds, cracks propagate through the partially bonded line, whereas cracks initiate at the hook tip in high-strength welds [25]. The curved hook intensifies the stated stress and reduces the joint integrity. The crack nucleates at the hook tip under shear loading, and the ultimate lap shear strength is influenced by the hook profile defined by curvature and dimensions [10, 35].

Many authors have identified the importance of the hook profile in the mechanical structure in defect-free spot-weld joints [32, 34, 36]. However, few studies have investigated the influence of the hook profile on the mechanical strength. A curved hook is formed at the spot-weld periphery and exhibits a downward or upward profile that contours the nugget circumference. The profile of a curved hook is defined by the material flow induced during a sleeve axial movement. In the second stage, the sleeve plunges into the lower plate and breaks the oxide at the interface. The broken oxide particles are moved and withheld in an intermittent layer at the weld extremity. Although a hook is inherent to the process, its profile is controlled by the material flow and heat input [10, 37].

A large amount of research effort has been undertaken worldwide regarding the experimental and numerical aspects of the strength mismatch in welded joints. In general, these joints exhibit substantial mechanical heterogeneity with respect to the deformation and fracture properties. The heterogeneity in deformation may affect the crack driving force. The total structural condition determines the triaxiality local stress, which is commonly defined as the ratio of the hydrostatic stress to the yield stress σ_h/σ_e (which is a function of the equivalent plastic strain in a hardening material). The stress triaxility may be interpreted as the local constraints effect. The difference is related to the fundamental mechanism of ductile, which is governed by the void growth and coalescence and is sensitive to the triaxial stress state. High-stress triaxility promotes this ductile fracture process, which causes low fracture toughness [3].

2.2. Theoretical background to fracture mechanics

2.2.1. Stress Intensity Factor (K-factors)

Linear elastic fracture mechanics assumes that at crack tip the localised plastic deformation is small considering the surrounding elastic stress field. In general, LEFM is described in terms of the stress singularity at the crack tip and/or energy balance. The LEFM theory is presented in many different books, such as Broek [38], Schijve [1] and Anderson [39]; its use and limitations are discussed in the following section.

The different crack opening modes are described in Fig. 2.4. According to Irwin [40], the mode I is described as a symmetric opening, where the displacements of the fractures surface are normal to the crack opening. Mode II and mode III are anti-symmetric displacements through the tangential to the crack opening and anti-symmetric displacements parallel to the crack opening, respectively [1, 5].

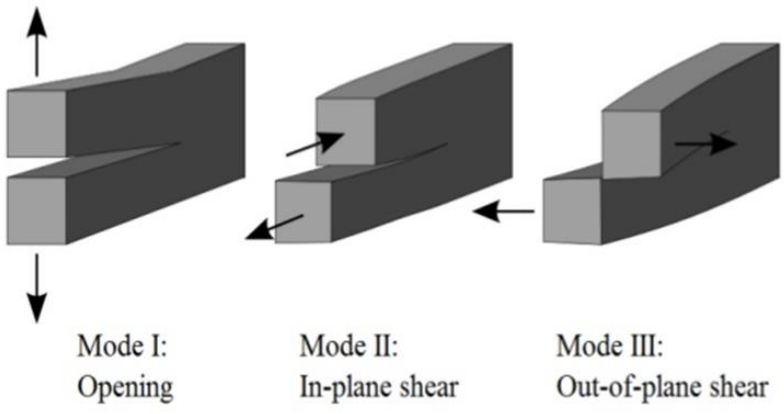

Figure 2.4. Three fracture modes [3].

Irwin [40] developed the stresses singularity field solutions at the crack tip. Generally, the crack growth in aircraft design takes place in mode I. Considering the polar coordinate system described in Fig. 2.5, the asymptotic crack-tip stress fields are

$$\sigma_{xx} = \frac{K_I}{\sqrt{2\pi r}}\cos\frac{\theta}{2}\left[1 - \sin\frac{\theta}{2}\sin\frac{3\theta}{2}\right]$$

$$\sigma_{yy} = \frac{K_I}{\sqrt{2\pi r}}\cos\frac{\theta}{2}\left[1 + \sin\frac{\theta}{2}\sin\frac{3\theta}{2}\right] \qquad \text{Equation (2.1)}$$

$$\tau_{xy} = \frac{K_I}{\sqrt{2\pi r}}\sin\frac{\theta}{2}\cos\frac{\theta}{2}\cos\frac{3\theta}{2}$$

$\sigma_{zz} = v(\sigma_{xx} + \sigma_{yy})$ (for plane strain)

$\sigma_{zz} = 0$ (for plane stress)

where v is Poisson's ratio. The displacement fields are [38]

$$u = \frac{K_I}{8\mu}\sqrt{\frac{2r}{\pi}}\left[(2k-1)\cos\frac{\theta}{2} - \cos\frac{3\theta}{2}\right] \qquad \text{Equation (2.2)}$$

$$\mathrm{v} = \frac{K_I}{8\mu}\sqrt{\frac{2r}{\pi}}\left[(2k+1)\sin\frac{\theta}{2} - \sin\frac{3\theta}{2}\right]$$

and

$w = 0$ (for plane strain)

$w = \frac{-v}{E}\int(\sigma_{xx} + \sigma_{yy})\,dz$ (for plane stress) Equation (2.3)

μ is the shear modulus, $k = 3 - 4v$ for plane strain and $k = (3-v)/(1+v)$ for plane stress [38]. The stress field and displacement at the crack tip for mode II and mode III are defined in a similar method [5].

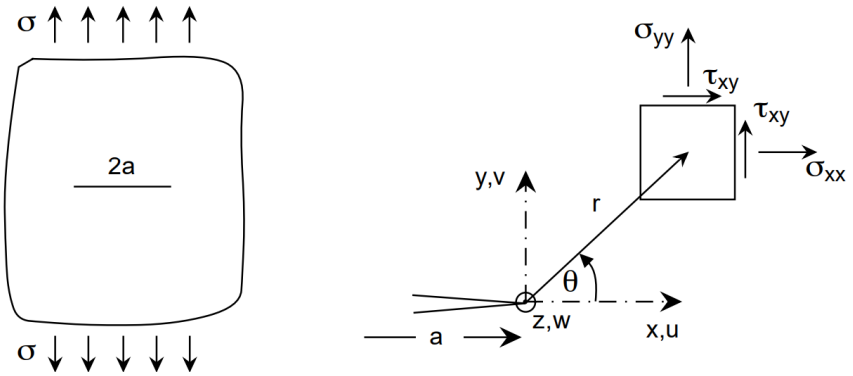

Figure 2.5. Coordinates, stress and displacement components in the crack tip stress field [3].

The parameter K_I describes the intensity of stress singularity at the crack tip and is referred to as the *"stress intensity factor"* for mode I

$$K_I = \beta\sigma\sqrt{2\pi a} \qquad \text{Equation (2.4)}$$

where σ is the remote stress to the crack plane at infinity, a is half of the through-thickness crack and β is the geometry correction function [1]. Using the elastic crack-tip solution and the

energy theory of Griffith [41], Irwin [42] established a simple relationship between the factor K_I and the elastic energy release rate G_I as

$$G_I = \frac{{K_I}^2}{E'} \qquad \text{Equation (2.5)}$$

where $E' = E$ for the plane stress condition, $E' = E/(1 - v^2)$ for the plane strain condition, and E is the Young's modulus. Eq. 2.4 is valid for the through-thickness crack in an infinite plate under tension loads. Consequently, the Griffith energy criterion $G = G_c$ is equivalent to the *K-factors* criterion for an elastic material.

Eq. 2.1 indicates that the stress singularity at the elastic crack-tip tends to infinite when r tends to 0 ($r \to 0$). Infinite stresses do not exist and a plastic deformation at the crack tip is generated, which maintains finite stresses. For the plane stress mode I, Irwin and co-workers have estimated a first-order plastic zone size r_y ahead of the crack tip [1]. To estimate the extent of this plastic deformation, they equated the yield strength σ_{YS} to the σ_{yy} along the *x-axis* in terms of the radius r. The radius value was determined to be the distance along the *x-axis* where the stress perpendicular to the crack direction would be equal to σ_{YS}. The estimated size can be obtained by considering the distance from the crack tip r_y at the local stress σ_{yy} is equal to the yield strength σ_{YS}. For plane stress conditions, yielding occurs when the normal stress is equal to the uniaxial yield strength of the material $\sigma_{yy} = \sigma_{YS}$. Substituting σ_{YS} for σ_{yy} in Eq. 2.1 yields $\theta = 0$, which is the Irwin's plastic zone correction

$$r_y = \frac{1}{2\pi}\left(\frac{K_I}{\sigma_{YS}}\right)^2 \qquad \text{Equation (2.6)}$$

where σ_{YS} is the 0.2% offset yield stress. Eq. 2.6 is correct only for perfectly elastic materials. If plastic yielding at the crack tip is allowed, the plastic zone is large and the second-order plastic zone size r_p can be twice the first-order plastic zone size ($r_p = 2r_y$). A similar conclusion was obtained by Dugdale using a strip-yield model [1, 39].

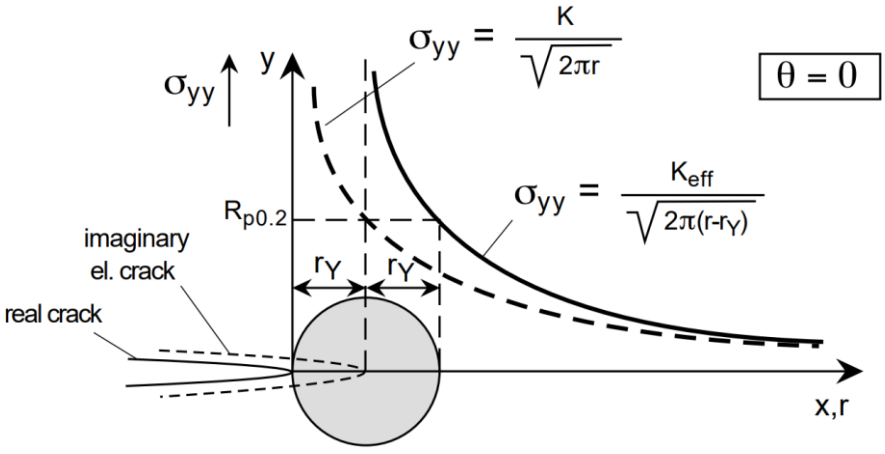

Figure 2.6. Irwin's plastic zone correction and the resulting imaginary elastic crack [3].

The influence of external variables, i.e., magnitude, loading and geometry of the cracked body, is distinguished in the crack tip region via the stress intensity factors. Due to the dependence of the stresses on the coordinate variables, the *K-factors* remain the same for different type of cracks and shaped bodies; thus, it is a single parameter characterisation of the crack tip stress

field. A stress engineer should be able to analytically, numerically or experimentally determine the *K-factors* relationship for almost any conceivable cracked body geometry and loading.

2.2.2. J-Integral concept

When the plastic zone at the crack tip is sufficiently large compared with the crack length or the geometrical dimension of the structure, the stress singularity and the strain field at the crack tip does not comply with the *K-factors*. Cherepanov [43] and Rice [44] introduced the integral *J*-Integral for elastic-plastic fracture mechanics. Rice [44] proposed that the *J*-integral for a nonlinear elasticity material is independent of the path of integration around the crack tip and is defined as

$$J = \oint_{\Gamma} \left(W_e dy - T_i \frac{\partial u_i}{\partial x} ds \right) \qquad \text{Equation (2.7)}$$

where the term Γ represents the counter clockwise arbitrary path around the tip of a crack, as in Fig. 2.7. W_e represents the strain energy density, and T_i represents the components of the traction vector u_i, which are the displacement vector components for the length increment along the contour ds. The rectangular coordinates x and y indicate the origin at the crack tip, the crack length and the normal direction to the crack length, respectively [1, 3]. The strain energy density per unit volume is

$$W_e = \int_0^{\varepsilon_{ij}} \sigma_{ij} d\varepsilon_{ij} \qquad \text{Equation (2.8)}$$

where σ_{ij} and ε_{ij} indicate the stress tensor and strain tensor, respectively. The traction vector is defined as

$$T_i = \sigma_{ij} n_j \qquad \text{Equation (2.9)}$$

where n_j are components of the unit vector normal to Γ.

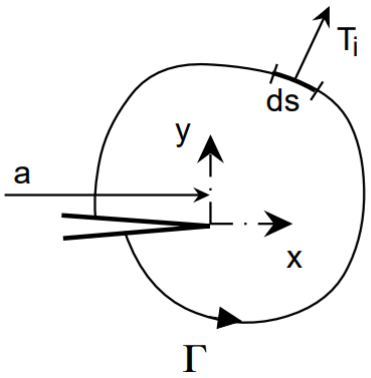

Figure 2.7. Path Γ for the evaluation of the *J*-Integral [3].

In addition, Rice [44] demonstrated that the *J*-Integral is equal to the energy release per unit surface area, which can be expressed for the displacement control conditions as

$$J = -\left(\frac{dU}{Bda}\right)_{\Delta} \qquad \text{Equation (2.10)}$$

where U is the strain energy stored in the body, a is the crack length, B is the thickness and the subscript Δ follows the partial derivative convention, which indicates the displacement variable that is held constant during partial differentiation [1, 44].

Hutchinson [45] and Rice and Rosengren [46] evaluated the characteristics of the crack-tip stress fields for power-law hardening materials given by the Ramberg-Osgood equation. The stress and strain field at the crack tip is also referred to as the HRR field. The HRR field describes the stress intensity singularity at the crack tip for elastic-plastic materials, which is similar to the *K-factors* for linear elastic static stress fields. As noted by McClintock [47], the following asymptotic solutions of crack-tip and strain fields are defined as

$$\sigma_{ij} = \sigma_0 \left(\frac{J}{\alpha\sigma_0\varepsilon_0 I_n r}\right)^{\frac{1}{n+1}} \tilde{\sigma}_{ij}(n,\theta)$$

$$\varepsilon_{ij} = \varepsilon_0 \left(\frac{J}{\alpha\sigma_0\varepsilon_0 I_n r}\right)^{\frac{1}{n+1}} \tilde{\varepsilon}_{ij}(n,\theta) \qquad \text{Equation (2.11)}$$

where σ_0 is the reference stress, $\varepsilon_0 (= \sigma_0/E)$ is the reference strain, α is a dimensionless constant and n is the hardening exponent (note $1 \leq n < \infty$). I_n is an integration constant that depends on n; and $\tilde{\sigma}_{ij}$ and $\tilde{\varepsilon}_{ij}$ are the dimensionless stress and strain, respectively; as functions of n and θ [3]. Huthinson and Paris [48] demonstrated that the J-integral can be employed to characterise the crack growth process when the remaining ligament is sufficiently large and the applied deformation is sufficiently small such that a region of proportional strain field easily encompasses the local crack-tip non-proportional strain field. This concept is referred to as the *J*-controlled crack growth regime [1].

2.2.3. Fundamentals of fatigue crack growth

The fatigue life of a component is usually divided into two periods: (i) crack initiation, and (ii) fatigue crack growth (FCG). The second period represents a large portion of the fatigue life of many materials and structures. A simple example is the fatigue crack growth in sheet materials of an aircraft skin structure. Thus, the accurate prediction of the fatigue life is important to determine how fast the cracks are growing and estimate the remaining life [1, 5, 49].

FCG tests must include the crack growth data that correlates to the stress intensity factor and the similarity principle [1]. This process is considered to be a cycle-by-cycle process with the crack extension Δa in every cycle. FCG data are obtained from pre-cracked specimens that are subjected to cyclic loading [5]. The crack growth is recorded by periodic observations of the locations of the crack tip. The length of a crack (a) is the distance from the centre line of the specimen to the crack tip. In general, the crack symmetrically grows, and the total crack length (from tip to tip) is indicated as $2a$. Since the crack grows perpendicular to the load directions and has only one dimension—crack length [1]. The simplest representation of the FCG data is a graph of crack length vs. number of cycles. The slope of the crack growth is described in the da/dN curve, which describes the crack growth rate [1, 5, 49].

The da/dN diagram describes the crack growth rate in terms of the stress intensity factors, as shown in Fig. 2.8. Then, the experimental results are plotted as $\log da/dN$ vs. $\log \Delta K$, which represents the crack growth rate da/dN for the range of *K-factor* ΔK. To describe the da/dN diagram, two of the four parameters—K_{max}, K_{min}, $\Delta K = K_{max} - K_{min}$ and $R = K_{min}/K_{max}$—are necessary. The da/dN diagram encompasses a range of ΔK and crack growth rates; the curve does not provide any information beyond this range [1, 5, 49].

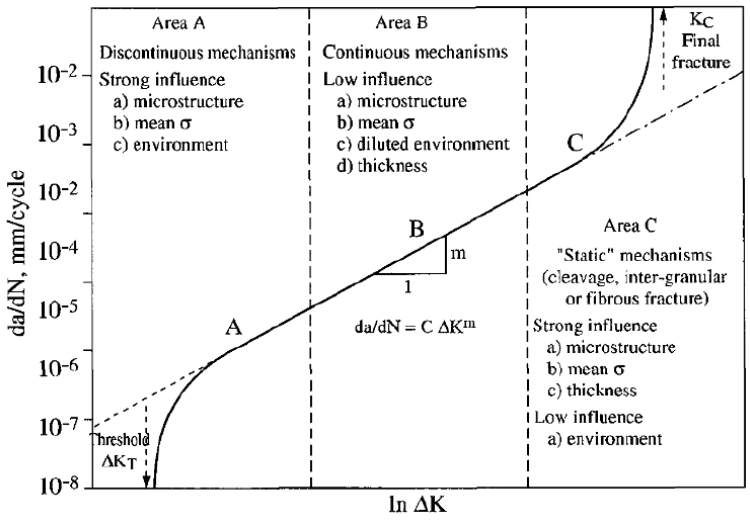

Figure 2.8. da/dN diagram, different region for crack growth rates in metals [50].

As shown in Fig. 2.8, the da/dN curve is divided into three Regions. Region I (the threshold region) shows a vertical asymptote at $\Delta K = \Delta K_{th}$, which indicates that propagation does not occur for the ΔK-values below the threshold level. Note that the K_{th} is a material constant at a given stress ratio R [1]. Region II (the Paris region) corresponds to stable macroscopic crack growth. A significant portion of the fatigue life is occupied in this subcritical crack growth region, particularly materials constructed from sheet or plates that contain stress concentrators (such as rivet holes). If the existence of a pre-crack is assumed to be the number of cycles until the crack reaches the critical size (Region III), it becomes a design criterion and the inspection intervals can be established. Generally, the empirical relationship proposed by Paris and Erdogan [50]—a straight line in $\log da/dN - \log \Delta K$—should represent the FCG resistance for a given material. The Paris potential equation considers the ΔK as the main drive force for fatigue crack growth and becomes the canonical FCG model, which is described in this section. Region III (stable-tearing crack growth region) is associated with the high crack growth rate prior to the final failure. Ductile fractures along the crack front do not occur in this region, and the crack propagation remains stable [1]. However, the fatigue life is very short, which must be avoided by the structural engineer. The asymptote vertical line at $\Delta K = K_c$ implies the occurrence of unstable failure; its prediction is achieved considering $K_{max} = K_c$. By definition, K_c is the stress intensity factor that causes the final failure. Similar to K_{th}, K_c is a material property constant at a given R-ratio [1].

The fracture toughness (K_c) depends on the thickness of the material, the increase in thickness from thin to thick K_c decreases until the lower bound value K_{Ic} is attained. This characteristic is typical of many high-strength structural metals, the change of the fracture behaviour from thin to thick sections are regarded as the change from plane stress to plane strain conditions. Thus, K_{Ic} is referred to as the plane stress fracture toughness for the mode I, which represents the minimum value of the fracture toughness of a material [39, 51]. Fracture toughness can be used as a generic term for the measurement of a material resistance to the extension of a crack; it may also provide a basis for material characterisation, performance evaluation, quality assurance for typical engineering structures and material selection [52].

The fatigue crack growth curve depends on the stress ratio $R = \sigma_{min}/\sigma_{max} = K_{min}/K_{max}$, which implies that the da/dN-diagram is a function of ΔK and R or $da/dN = f(\Delta K, R)$. Thus,

the crack growth rates at the same stress intensity range ΔK generally increase when the stress ratio increases [39].

As previously indicated, Paris and Erdogan [50] suggested that the appropriate ΔK range for fatigue crack growth should be the difference between the maximum *K-factors* and minimum *K-factors* in a cycle of fatigue loading, and the Paris equation is defined as

$$\frac{da}{dN} = C(\Delta K)^m \qquad \text{Equation (2.12)}$$

where $\Delta K = \mathrm{K}_{max} - \mathrm{K}_{min}$; K_{max} and K_{min} are the maximum value and minimum value, respectively, of the stress intensity factor in the load cycle; and *C* and *m* are material constants to be computed with fatigue crack propagation test data of the base material. The constants C and m are empirically obtained from the linear relation in Region II of the da/dN diagram. The equation in a double log plot provides the linear relation $\log(da/dN) = \log C + m \log K$, where m is the slope of the linear function [1], as shown in Fig. 2.8. In general, the experimental fatigue crack growth is well predicted using the Paris equation for specific geometrical configurations and loading conditions [5]. However, the Paris equation has some limitations: (i) the stress ratio is not accounted for in the crack growth; (ii) the asymptotic behaviour in regions I and III is not described with this equation. Several equations and methodologies have been proposed to overcome these problems [2, 53]. However, none of these functions has a physical background; they are proposed to be consistent with trends observed in the test results.

The stress singularity at the crack tip can be described as function of the stress intensity factor K, as described in Eq. 2.4. In a cycle, the applied stress varies from σ_{min} to σ_{max} over the range $\Delta\sigma$. Therefore, the local stresses vary in accordance with

$$\begin{aligned} K_{min} &= \beta(a)\sigma_{min}\sqrt{\pi a} \\ K_{max} &= \beta(a)\sigma_{max}\sqrt{\pi a} \\ \Delta K &= \beta(a)\Delta\sigma\sqrt{\pi a} \end{aligned} \qquad \text{Equation (2.13)}$$

The number of cycles to propagate a crack from its initial length a_i to its final length a_f is computed by the integration of the Paris equation

$$N_p = \frac{1}{C}\int_{a_i}^{a_f} \frac{1}{\Delta K^m}\, da \qquad \text{Equation (2.14)}$$

The definition of the initial crack has a significant influence on the number of cycles to propagate as the ΔK range has smaller values at the beginning of the crack propagation stage. The final crack length is obtained from the material fracture toughness, where $K_{max} = K_{IC} = \beta(a)\sigma_{max}\sqrt{\pi a_{cri}}$ for the critical crack length a_{cri}. The substitution gives the crack growth life

$$N = \frac{1}{C\Delta K^m} = \int_{a_0}^{a_f} \frac{da}{\left(C\beta(a)\sqrt{\pi a}\right)^m} \qquad \text{Equation (2.15)}$$

In general, the integral in this equation must be numerically solved as $\beta(a)$ varies with the crack length and the integration of Eq. 2.15 cannot be directly performed [1].

2.2.4. Crack closure phenomenon in fatigue crack propagation

Elber [54] observed that a crack under remote tension load was already closed during unloading before the tension stress becomes zero. The crack tip was closed with a positive remote stress. The author concluded that a plastic cyclic zone is formed at the crack tip during the fatigue loading and the growth causes a plastic wake. Although the plastic zone at the crack tip consists of small-scale yielding that is embedded within an elastic singularity zone, the local stress increases from S_{min} to S_{max}. A new cycle produces an updated plastic zone at the crack tip that it becomes longer than it was before. Consequently, the new plastic zone is loaded in compression during unloading, and reversed plasticity occurs. The reversed plastic zone is significantly smaller that the plastic zone obtained when S_{max} is attained. The conditions at the crack tip are uniquely defined by the current K*-factors* values, and the crack growth is characterised by K_{min} and K_{max}.

Therefore, Elber [54] proposed that the crack closure decreases the fatigue crack growth rate by the reduced effective stress intensity range. When a specimen is cyclically loaded at K_{min} and K_{max}, the crack surfaces are in contact below K_{op}, which is the stress intensity when the crack opens. The portion of the cycle that is below K_{op} is assumed to not contribute to the fatigue crack growth. The definition of the stress intensity range is

$$\Delta K_{eff} = K_{max} - K_{op} \qquad \text{Equation (2.16)}$$

Elber [54] proposed the effective stress intensity ratio

$$U_{Elber} = \frac{\Delta K_{eff}}{\Delta K} = \frac{K_{max} - K_{op}}{K_{max} - K_{min}} \qquad \text{Equation (2.17)}$$

The crack growth rate can be expressed in terms of ΔK_{eff}

$$\frac{da}{dN} = C\Delta {K_{eff}}^{m} \qquad \text{Equation (2.18)}$$

The crack closure phenomenon explains the effect of the stress ratio R on the da/dN diagram. The effect is a consequence of the crack tip plasticity of the growing fatigue crack, in which an "updated" plastic zone is formed during unloading and the reversed plasticity occurs. [1]. Crack tip plasticity occurs in every cycle, and thus, the crack grows through plastic zones of previous cycles. As a result, plastic deformation occurs in the wake of the crack. In this plastic wake field, the larger part of the material has been subjected to monotonic plasticity during uploading. A substantially smaller circumference of material along the crack edges has been subjected to cyclic plasticity. The material in the plastic wake field is plastically extended in the loading direction, which explains why the crack can be closed during unloading while the specimen remains under a positive tensile stress, i.e., before the specimen is unloaded [2]. The size of this plastic zone at S_{max} is proportional to $(K_{max}/\sigma_{YS})^2$. As described by Rice [44], the reversed plastic zone is ¼ of the plastic zone that is created during loading.

Another important concept defined by Elber [54] is the crack opening stress σ_{op}. This concept pertains to the values of the applied stress when the crack is fully opened. The opening stress can be experimentally obtained from the change in the compliance or by FE analysis. The crack closure causes an increase in stiffness. In addition, the fatigue crack growth occurs when the crack is fully open. Therefore, the ΔK_{eff} can be defined as $\sigma_{max} - \sigma_{op}$. Although the concept

of ΔK_{eff} is generally accepted and applied in prediction, the concept includes the assumption that the fatigue crack extension Δa is fully controlled by $\Delta \sigma_{eff}$.

2.3. Damage tolerance considerations and riveted panel design

2.3.1. Damage Tolerance Philosophy

In aircraft design, the following three approaches are considered to ensure the safety of an aircraft structure [1, 3, 51, 55]:

(a) **Fatigue (safe-life) evaluation,** this approach defines the component safe-life as the period during which the probability of crack initiation has an acceptable low value. During this period, a fatigue crack initiation may occur, but a component may not fail due to fatigue failure. Thus, the safe-live design predicts the replacement for an aircraft element as a function of the number of flight hours or ground-air-ground load service cycle. After the element has attained its safe-life period, it should be replaced. In general, the components that are designed under the safe-life approach are over-designed and the safety factors are conservative;

(b) **Fail-safe evaluation,** considering the fail-safe philosophy, a structure must be capable of sustaining its integrity without catastrophic failure, and an aircraft must remain airworthy even if the structure already contains a certain amount of damage. This design approach must determine the most likely failure locations and modes of failure due to fatigue, corrosion, or accidental damage. Typically, a designer includes redundant structural elements that promote additional load paths to improve the residual strength of the principal structure, keep the remaining structure intact after failure or promote the crack arrest and prevent crack growth. The extent of damage for residual strength evaluation is assured by regular inspection intervals, which are based on the service experience at any time within the operational life;

(c) **Damage tolerance,** this design approach assumes that a structure contains an initial crack or flaw and will grow during operational service. The main objective of the damage tolerance philosophy is to detect a crack and keep the crack growth in the principal structural elements “under control” before they propagate to failure. Therefore, the damage tolerance design approach is substantially based on the fracture mechanics and engineering evaluation of crack growth and residual strength characteristics to establish the inspection intervals. The crack growth investigation indicates the number of cycles before the crack attains the critical size, which is specified via residual strength of the structural element.

To ensure the safety of the aircraft structures and withstand the effect of damage, the Federal Aviation Administration (FAA) and United States Air Force (USAF) have established specific requirements and guidelines. The fail-safe requirements of the Federal Aviation Requirement (FAR 25.571) state that *“it must be shown by analysis, or test, or both that catastrophic failure or excessive structural deformation that could adversely affect the flight characteristics of the airplane are not probable after fatigue failure or obvious partial failure of a single principal structural element”*. To satisfy the damage tolerance requirement, the following three main items must be investigated and defined:

(a) **Life interval,** this is the total interval during which the principal structural element will fail due to an initial crack even if the load is below the ultimate design load. The residual strength provides evidence that the damaged component or structure is capable of maintaining the withstand loads;

(b) **Final life interval,** this is the interval during which the component will fail the residual strength reduction, which is a function of the fracture toughness and stress intensity factor due to a growing crack;

(c) "**Fail-safe" life,** items (a) and (b) the "fail-safe" life. The number of fights is described in terms of the residual strength, crack growth rate and the design limit loads, which is established by a certifying agency. The crack may grow and should not attain the critical length.

Suitable design criteria and appropriate stress analyses of structures eliminate or minimise problems that involve the fatigue life. Thus, an aircraft design must exhibit satisfactory strength by either comparative experience or analysis and testing even if a structure may be designed to be fail-safe. In addition, to satisfy the agency regulation requirements, the fatigue crack grow curves and residual strength diagrams must be investigated. The stress intensity factors for the structural component must be acquired [1, 3, 51, 56].

2.3.2. Design criteria for aircraft panels

To develop an efficient design methodology and improve the structural analysis, the complex loading conditions for a fuselage structure of an aircraft must be understood. The pressure cabin promotes an outward expansion in the skin; consequently, the hoop stress is created in the circumferential direction and acts as an axial stress in the longitudinal direction [57]. This pressurisation has been the source of disaster attributed to fatigue [1, 56]. A typical aircraft structure is manufactured from many parts, components, and substructures, which are designed to resist high concentrated loads [51]. Due to this complexity of a structure, the loading conditions and test samples are simplified. These simplified samples enable isolation of specific parameters that directly affect the fatigue life. The reduction from a complex structure to the level of a component enables a designer to study and understand the behaviours of individual elements in multiple structural configurations.

Although welded structures have exhibited significant applicability in the aerospace industry, the components and panels are traditionally assembled by riveting. The fasteners are designed to resist high loads and transfer them to spars, from which the loads are distributed to the sheet and stringer, as shown in Fig. 2.9. The tension load on the lap-splice introduces secondary bending; it is a consequence of the eccentricity of the load path. Secondary bending is the major aspect for fatigue and directly affects the crack growth and crack growth rate. Depending on the joint design, the bending stress can easily be as large as the applied tensile stress [1].

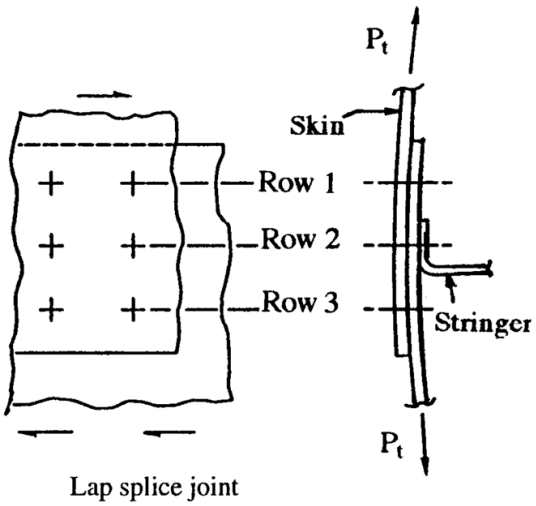

Figure 2.9. Typical panels configuration for civil aircraft [51].

The stress analysis improves the design of the riveted joints. During the design development stage, the design criteria must be established, basic design loads are recorded from laboratory tests, peak stresses are calculated and margins of safety are determined. The designer and stress analyst have the capability of significantly increasing the fatigue performance [51]. The design can be divided into two main testing topics:

(a) **Developmental testing,** this testing is generally focused on locating the critical areas, measuring the fatigue performance and obtaining crack growth data. The fatigue performance of a basic structure is very important since it represents the major part of a structure;

(b) **Fatigue performance analysis,** a panel test is conducted to check and/or develop the design details. Any detail that will affect the fatigue life of a panel should be included in the test specimen. The loads applied to components should produce the desired stresses as closely as possible at all critical points in the structure.

Each joint that is designed for optimum fatigue performance should be checked for the local stresses due to load transfer, notches or stress concentrations and load path eccentricities to ensure the best utilisation joint [51].

2.3.3. Residual strength approach for riveted panels

As previously described, the residual strength capability is defined as the maximum load or stress that a damaged airframe structure can sustain at any time during its service life. A crack in a structure causes a high stress concentration that reduces the residual strength and causes the strength capability to decrease with an increase in the crack length [51]. When the crack extends by a tearing mode of fracture, which typically occurs in thin metal sheets, the crack extension is slow and stable. The current approach to determining the residual strength for an airframe structure is based on LEFM, and the K*-factors* is the crack length parameter. The effective stress intensity factor K_{eff} considers the plastic zone at the crack tip, which indicates that this approach is valid when the plastic zone radius at the crack tip is significantly smaller than other geometrical dimensions, such as the crack length [3].

The schematic in Fig. 2.10 is a typical residual strength diagram for an infinity unstiffened thin plate. At the remote applied stress σ_0, the initial crack length a_i grows in a stable manner. When the remote stress is increased to σ_c, the crack grows to a_{cri} and failure is imminent.

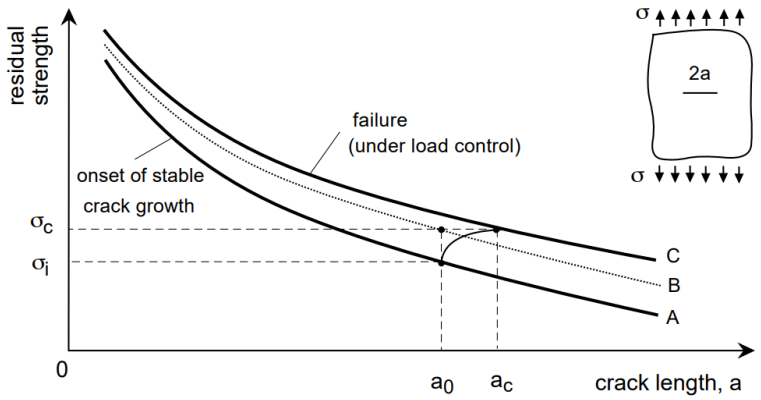

Figure 2.10. Typical residual strength diagram for an infinity unstiffened thin plate [58].

The curve A defines the onset of the stable crack extension

$$\sigma_i = \frac{K_i}{\beta\sqrt{\pi a_i}} \qquad \text{Equation (2.19)}$$

where K_i is the stress intensity at crack initiation.

The curve C is the residual strength as a function of the critical crack length a_c

$$\sigma_c = \frac{K_c}{\beta\sqrt{\pi a_{cri}}} \qquad \text{Equation (2.20)}$$

where K_c is the plane stress fracture toughness. The curve B is based on the initial crack length a_i

$$\sigma_c = \frac{K_{c0}}{\beta\sqrt{\pi a_i}} \qquad \text{Equation (2.21)}$$

where K_{c0} is often referred to as the apparent fracture toughness and is based on the maximum applied stress and initial crack length [3, 59]

The fracture toughness (K_c) varies with the thickness of the sheet and is influenced by the initial crack length and specimen width. The most accurate methodology for obtaining the fracture toughness for a plate is the R-curve approach. The R-curve is the rate of energy that is absorbed when two new surfaces are created and a "new" plastic zone at the crack tip is formed. The R-curve can be directly acquired from an experimental test for a progressive stress increase and measurement of crack growth. Then, the R-curve is defined as a function of the crack tip loading parameter vs. the corresponding stable crack extension. The standard for R-curve determinations is ASTM E561 [60].

2.4. Crack modelling

Closed-forms or analytical solutions of the stress intensity factors can be obtained only for simple crack geometries. More detailed crack geometries or paths are possible only with numerical techniques. Although the developments of new numerical methods for fracture mechanics analysis are constantly enhanced, the accurate modelling of three-dimensional

cracks remains a challenge in computational mechanics. The importance of three-dimensional computation fracture mechanics stems from the need to accurately predict the fatigue life and safety of critical components [61]. Thus, the implementation of finite element (FE) numerical models requires excessive computational effort and precise knowledge of all relevant physical phenomenon. This section succinctly describes available numerical methods for the development of *K-factors* and the fatigue crack growth model. Details of the methods can be obtained elsewhere.

2.4.1. Stationary crack numerical models

Despite the success of finite elements in computational fracture, mesh generation in three dimensions is time-consuming and burdensome for multiple crack configurations and crack growth simulations. The discontinuities, such as a crack, require that the mesh conforms to the geometric discontinuities. Therefore, considerable mesh refinement is needed near the crack tip to adequately capture stress and strain singularities. In addition, the computation of the fracture mechanics via numerical techniques requires calculation of the stress or strain field for each crack length. For complex structures, an analysis that considers all boundary effects near the crack tip. However, the numerical techniques for estimating *K-factors* are more popular than the analytical techniques for estimating *K-factors*. These methods are post-processing techniques as they require the stress field or parameters that measure the energy released by the crack growth in the crack tip vicinity [62-64].

The eXtend finite element method (XFEM) alleviates the shortcomings that are associated with meshing crack surfaces [65]. XFEM is an extension of the conventional finite element method, which is based on the concept of partition of unity, which enables the presence of discontinuities in an element by enriching the degrees of freedom with special displacement functions. The XFEM alleviates the majority of the burden associated with mesh generation as it does not require the finite element mesh to conform to cracks [65-69].

Compounding method

The compounding method proposed by Cartwright and Rooke [70] is used for *K-factors* determination in complex structures, starting with an available solution for simpler problems. This method consists of decomposing a cracked structure with N_{boun} boundaries into n auxiliary configurations, each of which contain one boundary and for which *K-factors* solutions are available. The *K-factors* for a crack tip can be expressed as a function of the N ancillary stress intensity factor values:

$$K_{IN} = K_0 + \sum_{n=1}^{N} (K_n - K_0) \qquad \text{Equation (2.22)}$$

where K_0 is the stress intensity factor for the same body without the boundaries, and K_n is the *K-factors* for the body with the boundary n.

Displacement extrapolation

The stresses singularity at the crack tip and the *K-factors* are obtained by the nodal displacements of the elements around the crack tip. The displacement field may be expressed as function of the stress intensity factors, the distance to the crack tip and the angle with the propagation direction ($\theta = 180°$ along the crack line). The displacements are given by

$$u_x = \frac{K_{II}}{2G}\sqrt{\frac{r}{2\pi}}(1+k)$$

$$u_y = \frac{K_I}{4G}\sqrt{\frac{r}{2\pi}}(1+k) \qquad \text{Equation (2.23)}$$

$$u_z = \frac{2K_{III}}{G}\sqrt{\frac{r}{2\pi}}$$

where $k = 3.4v$ for plane stress, and $k = \frac{3-v}{1+v}$ for plane strain.

Force method

The force method is an alternative to the displacement method. The forces along the crack distance x_c can be acquired using nodal reactions from the finite element model. The forces that are transmitted along the x and y directions are obtained from the following equations:

$$F_y = \int_0^{x_c} \sigma_{yy} dy = K_I \sqrt{\frac{2x_c}{\pi}}$$

$$F_x = \int_0^{x_c} \tau_{xy} dy = K_{II} \sqrt{\frac{2x_c}{\pi}} \qquad \text{Equation (2.24)}$$

The K'_I and K'_{II} values in terms of the function of the distance x_c are given by

$$K'_I = \sqrt{\frac{\pi}{2x_c}} \sum_{i=1}^{n} F_{y,i}$$

$$K'_{II} = \sqrt{\frac{\pi}{2x_c}} \sum_{i=1}^{n} F_{x,i} \qquad \text{Equation (2.25)}$$

To calculating the *K-factors* for several x_c-distances, a linear extrapolation to $x_c = 0$ can be performed, and the stress intensity factor at the crack tip is obtained.

Singularity subtraction technique

The singularity subtraction technique uses the stress field at the crack tip to calculate the *K-factors*. As the stress fields close to the crack tip and the stress intensity equations are known, the *K-factors* may be calculated in any direction. The remote stress σ, which is calculated in terms of the load P, is related to the new t_I and t_{II}

$$K_I = t_I\sqrt{2\pi r}$$

$$K_{II} = t_{II}\sqrt{2\pi r} \qquad \text{Equation (2.26)}$$

***J*-Integral**

The *J*-integral is a contour integral that characterises the strain energy release rate for an elastic-plastic material. The stress field is related to the strain energy density as

$$\sigma_{ij} = \frac{\partial W_e}{\partial \varepsilon_{ij}} \qquad \text{Equation (2.27)}$$

where W_e is the strain energy density per unit volume, σ_{ij} is the traction vector, u is the displacement vector and y is the direction perpendicular to the crack length. From the definition of potential energy along an arbitrary contour, this parameter is related to the stress intensity factor as $G = K^2/E$ for plane stress and $G = K^2/\left(E(1-v^2)\right)$ for plane strain.

Virtual crack closure technique (VCCT)

The VCCT is the numerical method may be the most common method for computations of fracture mechanics; it is based on an energy release rate when a crack grows with an infinitesimal increment:

$$G = \frac{\partial U}{\partial a} \approx \frac{U_{a+\Delta a} - U_a}{\Delta a} \qquad \text{Equation (2.28)}$$

This technique was proposed by Rybicki and Lannin [71]. The energy variation ΔG that is necessary to close the crack along the distance Δa is

$$\Delta G = \frac{1}{2}(X_i \cdot \Delta u_l + Z_i \cdot \Delta w_l) \qquad \text{Equation (2.29)}$$

where X_i and Z_i are the nodal forces at point i and Δu_l and Δw_l are the node l displacements. Therefore, the information required to calculate the energy variation is obtained from a single finite elements analysis, where Δa is the surface area created by a crack propagation of Δa; in the case of plates with thickness B, this area is $\Delta a \cdot B$. The calculation of the strain energy release for each mode is the displacement, and the energy release rate is

$$G_I = -\frac{1}{2\Delta a} Z_i \Delta w_l$$
$$G_{II} = -\frac{1}{2\Delta a} X_i \Delta u_l \qquad \text{Equation (2.30)}$$

eXtended finite element method

The XFEM enriches the original geometrical domain (crack is not included) with local enrichment functions in conjunction with additional degrees of freedom, which is also referred to as phantom nodes, to represent the discontinuity of the cracked element [65, 66, 72]. The crack is typically described by asymptotic enrichment functions to capture the singularities of the crack tip and the discontinuous displacement jump functions across the crack surfaces. The displacement vector function $\boldsymbol{u}$ with the partition of unity enrichment is

$$\mathbf{u} = \sum_{I=1}^{n} N_I(x) \left[\mathbf{u}_I + H(x)\mathbf{a}_I + \sum_{\alpha=1}^{4} F_\alpha(x)\mathbf{b}_I^\alpha \right] \qquad \text{Equation (2.31)}$$

where n is the number of nodes in the mesh; $N_I(x)$ is the nodal shape functions; $\mathbf{u}_I$ is the classical nodal displacement vector; and $\mathbf{a}_I$ and $\mathbf{b}_I^\alpha$ are the nodal displacement vectors that are linked to the Heaviside jump function $H(x)$ across the crack surfaces and the crack-tip functions $F_\alpha(x)$ [65, 66, 72].

2.4.2. Fatigue crack propagation models

Numerous studies have been dedicated to predict the crack growth and crack growth path. In analytical software, such as NASGRO [73], AFGROW [74] and ESACRACK [75], the fatigue crack growth is predicted from libraries of closed-form of *K-factors* solutions, which are developed

for a range of geometries, crack lengths and boundary conditions. These software can analyse the crack growth faster than numerical methods with some limitations regarding their applicability to existing crack libraries; the nonlinear effects may not be included, and the load redistribution may not be considered as the crack grows [76].

Modern numerical techniques have gained importance. However, modelling crack growth is more complicated than modelling a stationary crack as the mesh has to be continuously updated to follow the crack progress. In general, re-meshing techniques have been applied to the finite elements and boundary elements by many researchers [77-79]. The adaptive re-meshing technique can be divided into four steps: (i) development of a representative three-dimensional finite element model; (ii) calculation of the effective stress intensity factors along the crack front, (iii) determination of the crack front advances by applying an adequate fatigue crack growth law, and (iv) definition of a new three-dimensional finite element model that incorporates the new crack front. These steps are repeated to a pre-defined crack length or final fracture.

The crack front is usually defined by two different approaches. The first and simplest approach, which is referred to as the two-degree-of-freedom model, assumes a pre-defined crack shape that is similar to the experimental observation. Although the shape is maintained, the crack aspect ratio is allowed to change. Due to the shape constraints, situations that involve irregular crack shapes, significant crack shape changes during propagation, out-of-plane propagation or complex loading scenarios are not suitable. The second approach, which is referred to as the multiple-degree-of-freedom model, is more versatile and divides the crack front into a set of points and defines the crack shape by connecting the points by cubic splines or polygonal lines. This approach is generally associated with a more precise crack shape and more accurate *K-factors*. Due to its flexibility, this approach has been employed in more complex situations, which range from simple plane propagation to mixed-mode loading.

The XFEM can also simulate fatigue crack growth; the main advantage of this numerical technique is that a re-meshing technique is not necessary to consider the crack growth in an arbitrary crack path. Proposed by Belytschko and Black [65], XFEM curved cracks were treated by mapping a straight enriched field. The method incorporates both the discontinuous function and the near-tip asymptotic functions via a partition of unity method. A crack is grown by redefining the tip location and adding new crack segments. The addition of a discontinuous field enables the entire crack geometry to be modelled independently of the mesh and completely avoids the need to re-mesh as the crack grows [61, 65, 66, 69].

The use of this methodology has certain limitations. A reduced element enrichment formulation is employed in the analysis to consider the asymptotic stress field at the crack tip. Consequently, the crack tip cannot be located inside an element. In addition, few examples of XFEM are applied in safety critical cases due to the relative youth of the technology [80-82].

2.4.3. Summary of cracking modelling

In the literature, force methods provide accurate results; however, they require a stable model and very refined element sizes in front of the crack tip. The modified VCCT has proven to be an efficient tool for the determination of *K-factors* with less computational effort and reasonable accuracy. However, these methods require extensive and time-consuming model preparation when several crack lengths are necessary. The presence of flaws or inhomogeneity, such as

cracks, voids and inclusions, must be considered in mesh generation, as the model must conform to these geometric generations. XFEM is an attractive and effective method for simulating initiation and propagation of a discrete crack along an arbitrary path [65-69].

In the case of crack growth models, the study demonstrates that the accuracy of the extended finite element method in three-dimensional *K-factors* computations. The XFEM provides a robust and versatile numerical tool to solve crack problems in complex structural components without the need to explicitly align a mesh with a crack by eliminating the need to include the crack surfaces in the model. Mesh generation is greatly simplified. The XFEM facilitates the modelling of crack growth for fatigue studies as a single mesh suffices.

Chapter 3.

Experimental Procedure

3.1. Refill Friction Stir Spot Welding

3.1.1. Refill FSSW equipment

The welding experiments were conducted on the RPS200 welding machine (Harms & Wende GmbH, Germany), Fig. 3.1A. This welding machine was custom-designed for high process loads and robustness for comprehensive process development; it is a versatile experimental welding machine. The equipment is capable of delivering a $35\ kN$ welding force, $60\ Nm$ ($90\ Nm$ for $15\ s$) torque, $3300\ rpm$ of bi-rotational speed by the tool elements, $40\ kN$ clamping force and $10\ mm$ strokes by the welding tools. The machine is equipped with sensors for the simultaneous monitoring and recording of axial forces, torques, tool temperature and rotations involved during the welding process. The RPS200 is operated with displacement and position control; the axial displacement of the sleeve and pin can be fully controlled with high precision by an electrical driven ball screw. The work area is equipped with a profiled table that allows simple clamping at the desired position, as shown in Fig. 3.1B. The length and width of the work area are $1000\ mm$ and $500\ mm$, respectively. In addition, high precision of the distances between the spot welds in the x and y directions can be achieved due to the table displacements in both directions and the electrical screw balls in the working area.

The non-consumable tool comprises a clamping ring with a diameter of $17\ mm$, a threaded sleeve with a diameter of $9\ mm$ and a threaded probe with a diameter of $6\ mm$, as shown in Fig. 3.2. The threads in the sleeve and probe enables a better flow of materials and minimises tool wear. As the sleeve plunges into the plates, the nugget diameter is approximately the outer sleeve diameter $d_{SW} = 9\ mm$.

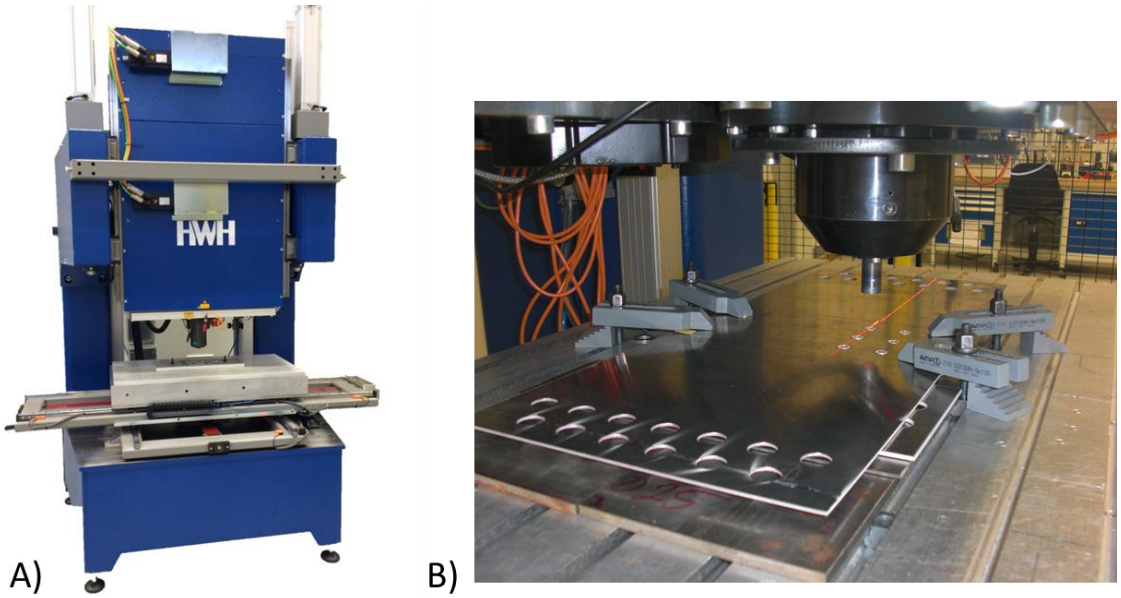

Figure 3.1. Refill FSSW RPS200 experimental welding machine.

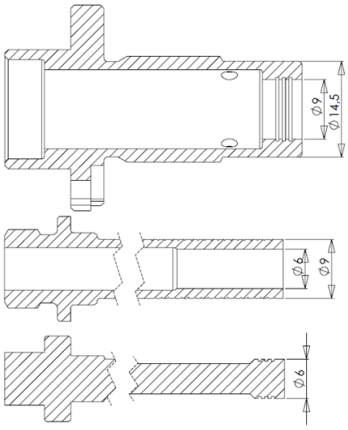

Figure 3.2. Refill FSSW tool.

3.1.2. Process parameter optimisation - Design of Experiment

Although refill FSSW is a very stable and completely automatized process, Zettler [83] stated that *"Spector and newbies are often amazed by the simplicity and seeming effortlessness of the welding procedure. But in truth the factors of good quality joint – or better a joint at all – are depending on complex situation in the welding zone"*.

The selection of the process parameters of any material, in similar or dissimilar configurations, depends on their individual properties, such as material strength, physical properties, and thermal conductivity. The systematic statistical Design of Experimental (DoE) methodology via Box-Behnken (BB) approach, which is applied to weld parameter optimisation, is a powerful method that involves the reduction of experiments, streamlining the impact of the process parameters and optimising the welding process parameters. Additionally, the DoE methodology combined with the Response Surface Methodology (RSM) enables the development of an empirical statistical model and establishment of the relevance of factors and levels [84, 85]. To minimise and systematise the experimental work, a DoE that employs the incomplete rotatory block design of the BB methodology was developed, combined with Analysis of Variance (ANOVA) and the RSM.

Based on previously published studies [13, 25, 35] and a preliminary study by visual inspection, three factors were considered in this study: welding time (t), plunge depth (PD) and rotational speed (RS). The BB number of experiments (NE) is defined by the equation $NE = 2k_f(k_f - 1) + C0$, where k_f is the number of factors, and $C0$ is the central point [84]. A total of 15 experiments was performed, with 13 different weld parameters and three central points. Table 3.1 lists the process parameters and levels that are considered in this study. The plunge depth varies among 1.9 (without penetration in the lower plate), 2.2 and $2.5\,mm$ with rotational speeds of 1400, 1900 and $2400\,rpm$ and welding times of 4.8, 5.2 and $5.8\,s$. The applied welding force was held constant in all cases at $12\,kN$. Prior to the refill FSSW process, no surface treatment was applied and the plates were cleaned with acetone to remove dirt and oil.

Table 3.1. Specimen properties for test programme.

Welding parameter	Low (-1)	Centre (0)	High (+1)
Welding Time, t [s]	4.8	5.2	5.8
Plunge Depth, PD [mm]	1.9	2.2	2.5
Rotational Speed, RS [rpm]	1400	1900	2400

As welding parameter interactions may affect the LSS response, a multivariate optimisation strategy was applied to develop the optimised weld parameters. The multivariate optimisation has two variables: responses and factors. The responses are dependent on factors and can be qualitative and quantitative. A qualitative analysis cannot be measured; it is analysed by evaluations and observations to understand the quantitative responses. In this study, qualitative responses were analysed by microstructural evaluation and fracture mode. The quantitative study was performed by the maximum response on the LSS via the "larger the better" approach. Then, ANOVA of the BB experimental work was performed to understand the quantitative results. An RSM second-order model was developed according to Eq. 3.1 and validated to verify the ability of the analytical model to reproduce and predict the experimental results.

$$y = \beta_0 + \sum_{i=1}^{k} \beta_i x_i + \sum\sum_{i=j} \beta_{ij}\, x_i x_j + \sum_{i=1}^{k} \beta_{ii} x_i^2 + \epsilon \qquad \text{Equation (3.1)}$$

3.2. AA2024-T3

In the aerospace industry, high strength and low density comprise the first priority for the selection of materials in a structural application. The aluminium 2000 and 7000 series are the first options for a structural application. In general, the 2000 series exhibits high fracture toughness and superior crack propagation behaviour [5, 86]. For pressurised fuselage cabins and lower wing skins, the standard material is aluminium 2024-T3 [51]. AA2024 is a commonly employed material for friction stir welding study [23, 25, 30]. The base material in this study was the 2 mm-thick hardened precipitated AA2024-T3. The nominal chemical composition of the base material is listed in Table 3.2 [86, 87]. Aluminium 2024 is a precipitate and hardenable alloy with the atomic formula $AlCu_4Mg$; copper is the major alloying element. The T3 temper designation indicates that the alloy was heat-treated [5, 86]. Fig. 3.3A presents the main microstructural feature—the grains are very flattened and oriented in the drawing direction.

Table 3.2. AA2024-T3 chemical composition [86]**.**

Al	Cu	Cr	Fe	Mg	Mn	Si	Zn
90.7-94.7%	3.80-4.90%	0.10%	0.50%	1.20-1.80%	0.30-0.90%	0.15%	0.25%

Hardness and tensile tests, Fig. 3.3B, were performed in all directions to ensure equivalent material performance; no difference was observed. Hardness testing on the cross-section has indicated an average microhardness of $HV = 141.5$. Table 3.3 presents the tensile properties and fatigue constants that are employed during this study.

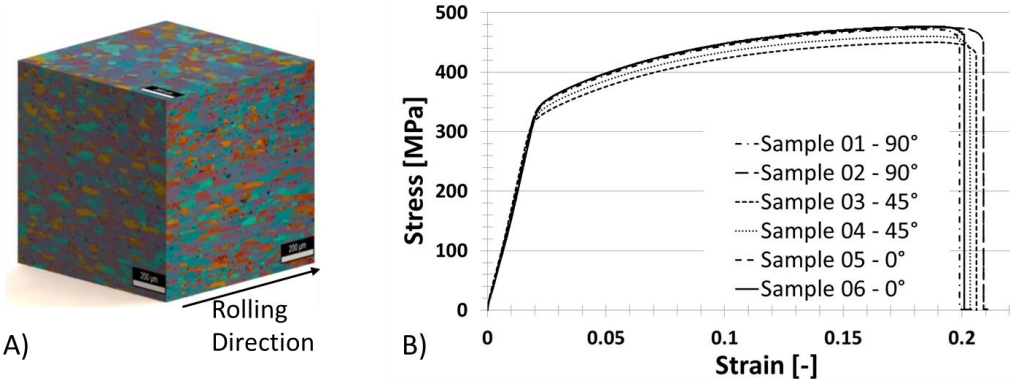

Figure 3.3. A) Microstructural feature; B) Stress vs. Strain curve in all directions.

Table 3.3. Mechanical properties and fatigue constants for AA2024-T3 [59, 88].

Properties	Values
Young's Modulus	73 GPa
Poisson's Ratio	0.33
Yield Strength	345 MPa
Ultimate tensile strength	483 MPa
Elongation	18%
Density	2.7 g/cm^3
Plane stress, K_{Ic}	75 MPavm
Paris constant, C	1.1088E-7
Paris constant, m	2.9436

3.3. Metallurgical characterisation

The optical microstructural investigation were carried out on cross-section in the centre of the spot weld nugget, in which all weld parameters were analysed. The samples were cut by diamond abrasive wheels and embedded in a cold mounting resin (demotec30). For the microstructure analysis, the specimens were polished according to standard procedures. A microstructural analysis was performed using a Leica DM IRm optical microscope (Leica Microsystems GmbH, Germany). The hook profile was analysed in a non-etched specimen because it provides a higher contrast between the hook region and the nugget. Flaws and voids were analysed in a polished specimen etched by the Kroll reagent (96 mL distilled H_2O, 6 mL HNO_3 and 2 mL HF). To evaluate the microstructure of the joints, the polished specimens were etched by Barker reagent (200 mL distilled H_2O, 5 g fluoroboric acid 35%) and analysed under polarised reflective light.

3.4. Mechanical testing

3.4.1. Microhardness

The local mechanical properties were evaluated by Vickers microhardness measurements across the weld section using a Zwick Roell microhardness machine (Zwick Roell, Germany); the applied load was $300\ g$ with an indentation time of $10\ s$. The distance between two indentations—$0.3\ mm$—was carefully chosen to avoid strain influences on the adjacent indentations on the measurements. Horizontal indentation lines were drawn within the base material of the TMAZ and SZ.

3.4.2. Tensile test

The tensile tests of the base material in the rolling direction, 45^o of the rolling direction and perpendicular to the rolling direction were performed using the universal tensile machine Zwick Roell (Zwick Roell, Germany). The testing was accomplished by displacement control with a strain rate of $2\ mm/s$ at room temperature. To obtain the mechanical properties, tensile testing specimens were machined from the plate specimens according to ISO 6892-1 [89].

3.4.3. Lap shear test

The lap shear strength of the spot weld joints were obtained via lap shear tests using a Zwick Roell tensile test machine (Zwick Roell, Germany) at a strain rate of $2\ mm/s$ at room temperature. The elongation measurement was obtained using a Zwick mechanical extensometer as the principal displacement data collection system. The geometry was based

on ISO14324 for Resistance Spot welding [90].The lap shear geometries are presented in Fig. 3.4, and the terms and definitions are described in Table 3.4.

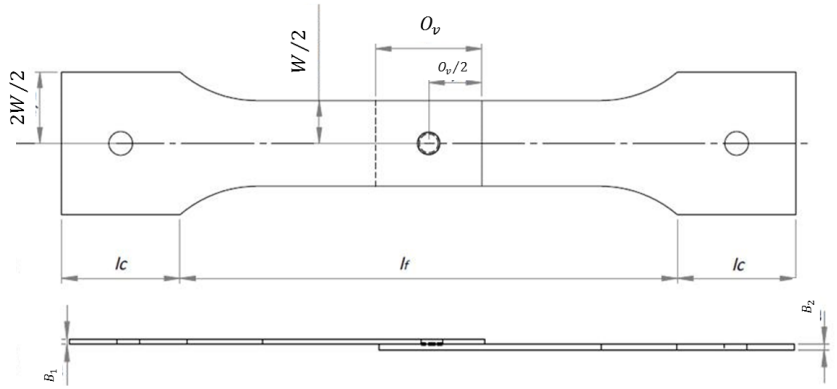

Figure 3.4. Geometry of the lap-shear sample.

Table 3.4. Terms and definitions of the lap shear specimen.

Term	Definition
l_c	Clamping length
l_f	Free length between clamps
W	Specimen width
O_v	Overlap
B	Thickness

3.5. Fatigue & Damage Tolerance evaluation

Coupon-level laboratory tests of materials and components were performed to establish the allowable design to ensure that an aircraft will pass qualifications and certification programmes. The mode of failure of structures associated with design criteria are shown in Table 3.5 [51].

Table 3.5. Design criteria for sizing and damage tolerance evaluations [51].

Mode of Failure	Design Criteria	Allowable Data
Static strength of undamaged structure	Structure must support ultimate loads without failure for three seconds	Static properties
Deformation of undamaged structure	Deformation of a structure at limit loads may not interfere with safe operation	Static properties and creep properties for elevated temperature conditions
Fatigue crack initiation of undamaged structure	1. Fail-safe structure must satisfy customer service life requirements for operational loading conditions. 2. Safe life components must remain crack free in service. Replacement times must be specified for limited life components.	Fatigue properties
Residual static strength of damaged structure	1. Fail-safe structure must support 80-100% limit loads without catastrophic failure. 2. A single member failed in redundant structure or partial failure in monolithic structure	1. Static properties 2. Fracture toughness properties
Crack growth life of damaged structure	1. For fail-safe structure inspection techniques and frequency must be specified to minimise risk of catastrophic failures 2. For safe-life structures must define inspection techniques and frequencies and replacement times to ensure that probability of failure due to cracking is extremely remote	1. Crack growth properties 2. Fracture toughness properties

3.5.1. Quasi-Static testing – multiple-spot weld rows

After the optimised weld parameters were defined, the integrity of the joints was explored. The joint configuration, which is referred to as High Load Transfer (HLT) situation, was considered for this analysis; it means that the load in the lap-joint is transferred only by the spot welds [51]. The quasi-static tests were performed to define the yield strength of the joints and the typical failure modes in an overload situation. Additional details regarding the dimension, joint configuration and distances are provided in Chapter 4.

The tests were performed using a Zwick Roell tensile test machine (Zwick Roell, Germany) at a strain rate of $2\,mm/s$ and room temperature. The elongation measurement was obtained using a Zwick mechanical extensometer as the principal displacement data collection system, an LVDT to measure the elongation in the overlap joints and digital image correlation (DIC) to obtain the deformation; this process is described in Section 3.5.3. All distances and dimensions of the specimen are expressed in terms of the spot weld nugget diameters $d_{SW} = 9\,mm$.

3.5.2. Quasi-Static testing – Panels

A similar approach to the quasi-static tests in multiple-spot welds was employed to perform the quasi-static tests in panels, which are also referred to as the lap splice, where more than one spot weld exists in a row. Fig. 3.5 describes the nomenclature in this study, where the name *Panel row* (number of row) *x Column* (number of columns or number of spot welds in a row) describes the joint configuration, e.g., the panel presented in Fig. 3.5: the *Panel 3 x 5* has three rows and five spot welds in each row. In addition, the following method was applied to highlight a specific spot weld, considering the front view of the panel (where the spot welds can be visualised). The specific spot weld is given by the nomenclature $Spot - Weld_{rowxCol}$, or $SW_{rowxCol}$, e.g., SW_{1x3} is located in the first row and the third column. The tests were performed using a Zwick Roell tensile test machine (Zwick Roell, Germany) at a strain rate of $1\,mm/s$ and room temperature. The elongation measurement was obtained using a Zwick mechanical extensometer as the principal displacement data collection system, an LVDT to measure the elongation in the overlap joints and a DIC to obtain the deformations.

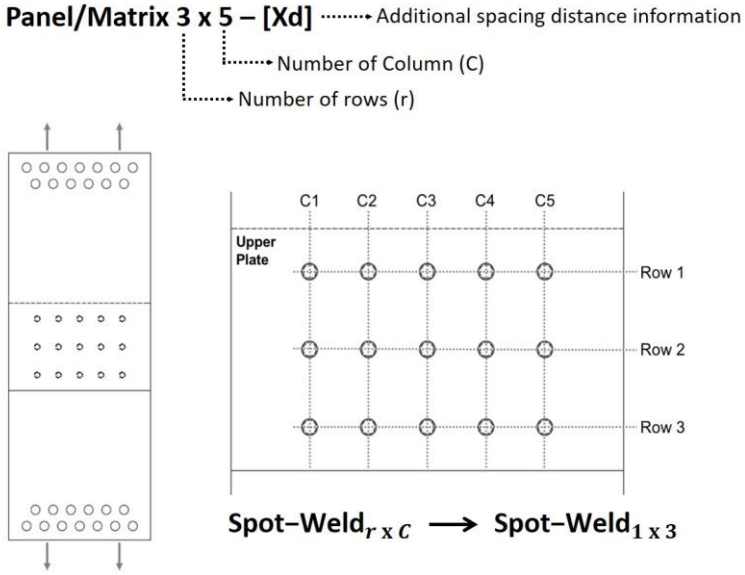

Figure 3.5. Nomenclature of the spot weld panels.

3.5.3. Digital image correlation

A digital image correlation technique was used to measure the local displacement and deformation in the overlap area during the test with an Aramis HS photometric system from GOM GmbH (GOM GmbH, Germany). The Aramis HS system is well suited for deformation measurements of a loaded structure in either a static regime or a dynamic regime. A stochastic pattern was applied to the overlap surface of the lap shear specimens with spray paint to perform the strain measurement. The specimens' surfaces were sprayed with white paint to cover the shiny original surface to avoid any light reflection. Black paint was sprayed onto the white surface to ensure that fine spots were uniformly distributed over the entire range of the desired measurement area. In this study, a random pattern coated on the specimen was initially captured and split in facets by the image processing. Solid movement and local deformation occurred during loading. The processor recognised the pattern displacement and deformation. The spatial coordinates were compiled as a function of time, and thus, the deformation and plane strain tensors over all loading stages could be sketched or exported. Every quasi-static test for the damage tolerance evaluation was performed using the DIC.

3.5.4. Fatigue – SN curves

The fatigue tests were performed using a Schenck servo-hydraulic testing machine (Schenck, Germany). The tests were conducted according to the ISO14324:2003(E) [90] standard for a resistance spot weld, where a minimum of three samples for each load level was tested to ensure repeatability. The stress ratio $R = 0.1$ $(R = S_{min}/S_{max})$ was applied in a sinusoidal axial tensile wave form with a constant amplitude load and a frequency of 10 Hz. The stopping criterion was 10^7 cycles or sample failure.

An optimum fatigue design should exhibit a high reliability for the purpose of aircraft availability, economical operation and a reasonably long safety life, as well as an economical operation by minimising the inspection frequency. SN curves were obtained by measuring the number of cycles to failure. Additionally, Basquin's power function was used to evaluate the fatigue test data, as expressed by Eq. 3.2.

$$S_a = C_{SN} {N_f}^{m_{SN}} \qquad \text{Equation (3.2)}$$

where S_a represents the nominal stress amplitude, N_f is the number of cycles to failure and m_{SN} and C_{SN} are the exponent of the SN curves and the coefficient of the SN curves, respectively. These constants can be derived from the regression given by the SN curves.[91].

The fatigue-life confidence assessment in refill FSSW is introduced by the two-parameter (2P) Weibull distribution, and the probability density function (PDF) is expressed by Eq. 3.3,

$$f(x) = \frac{\beta_{WS}}{\alpha_{WS}} \left(\frac{x}{\alpha_{WS}}\right)^{\beta_{WS}-1} e^{-\left(\frac{x}{\alpha_{WS}}\right)^{\beta_{WS}}} \qquad \alpha_{WS} \gg 0, \beta_{WS} \gg 0 \qquad \text{Equation (3.3)}$$

where α_{WS} and β_{WS} are the characteristic life and Weibull slope (shape parameter), respectively [91-93]. The cumulative density function (CDF), as shown in Eq. 3.4, is obtained by integrating the PDF equation, as expressed in Eq. 3.2,

$$F_f(x) = 1 - e^{-\left(\frac{x}{\alpha_{WS}}\right)^{\beta_{WS}}} \qquad \text{Equation (3.4)}$$

The characteristic life (α_{WS}) and Weibull slope (β_{WS}) are derived from the linear regression of the Weibull plots; they provide a linear graph of $\ln(cycle)$ versus $\ln(\ln(1/1-MR))$ for different load amplitudes [92]. $F_f(x)$ cannot be directly obtained via Eq. 3.4; the Bernard's Median Rank (MR) empirical estimator was employed, as shown in Eq. 3.5,

$$MR = \frac{i_{MR} - 0.3}{n_{MR} + 0.4} \qquad \text{Equation (3.5)}$$

i_{MR} represents the failure serial number, and n_{MR} is the total number of samples. When these grouped material constants are available, the statistical parameters of Weibull at an arbitrary stress amplitude can be determined. In addition, the Weibull mean life or mean time to failure (MTTF), which provides the expected life for a given stress amplitude, can be calculated by Eq. 3.6.

$$MTTF = \alpha_{WS}\Gamma\left(1 + \frac{1}{\beta_{WS}}\right) \qquad \text{Equation (3.6)}$$

where $\Gamma()$ is the gamma function [91-93].

The coefficient of variation (CV), as expressed in Eq. 3.7, highlights the dispersion between the observed values and the MTTF; it is given by the ratio between the standard deviation (SD), as shown in Eq. 3.8, and the MTTF.

$$CV = \frac{SD}{MTTF} = \frac{\alpha_{WS}\sqrt{\Gamma\left(1 + \frac{2}{\beta_{WS}}\right) - \Gamma^2\left(1 + \frac{1}{\beta_{WS}}\right)}}{\alpha_{WS}\Gamma\left(1 + \frac{1}{\beta_{WS}}\right)} \qquad \text{Equation (3.7)}$$

$$SD = \alpha_{WS}\sqrt{\Gamma\left(1 + \frac{2}{\beta_{WS}}\right) - \Gamma^2\left(1 + \frac{1}{\beta_{WS}}\right)} \qquad \text{Equation (3.8)}$$

The reliability describes the probability performance of a component in dynamic conditions and an indefinite time period. The construction of several SN curves on different reliability levels is common; typically, $R_e = 0.99$, $R_e = 0.9$, and $R_e = 0.5$. To obtain the fatigue life N_f for several reliabilities, Eq. 3.9 was applied.

$$N_{R_x} = \alpha(-\ln R_x)^{-\frac{1}{\beta}} \qquad \text{Equation (3.9)}$$

where N_{R_x} is the value of the fatigue life, which indicates $X\%$ of reliability [91-93].

3.5.5. Fatigue crack growth

For the fatigue crack growth (FCG) investigation, Panels 3 x 5 were produced. As FCG tests are performed in lap splices joined by refill FSSW for the first time, the failure scenarios must be investigated; therefore, the initial crack or initial defect are described in section 6.1.2. The loading condition and joint configuration are described in section 6.1.1.

The tests were performed using a Schenck servo-hydraulic testing machine (Schenck, Germany). Fig. 3.6 shows the specimen assembled to the testing machine. The specimens were tightly clamped to the testing machine to ensure a homogeneous load distribution at the specimen ends. The crack growth is recorded by periodic observation of the location of the

two cracks tip by a traveller microscope attached to a ruler. The samples were vertically gridded in the crack propagation area to enable visualisation of the crack tip.

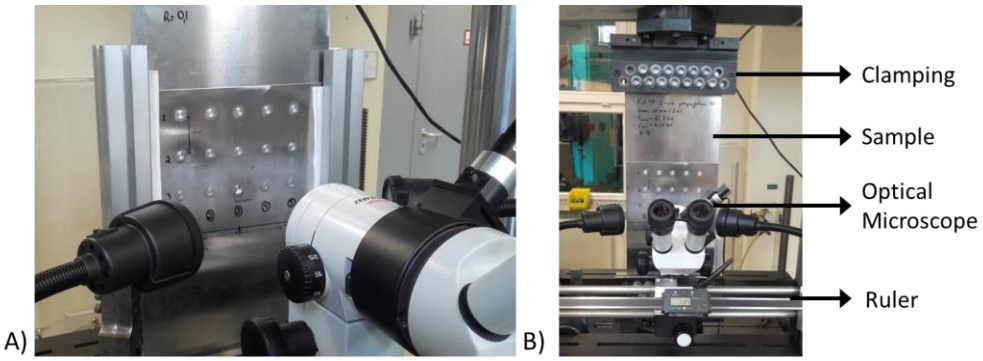

Figure 3.6. Fatigue crack growth testing.

3.5.6. Fractography

The mechanical behaviours of the joints were investigated in terms of failure modes for quasi-static and fatigue loading. The main objectives of fractography are to define the nature of the failure and track the crack propagation for fatigue failure. First, the samples were analysed with the stereomicroscope Wild M8 (Wild Heerbrugg, Switzerland) with a light microscopic (macrofractography). Afterwards, several samples were selected considering the typical failure modes and/or any important peculiarities of the joint configuration or failure mode. The fracture surfaces of these samples were examined using the FEI Quanta 650 scanning electron microscope (SEM) (FEI Company, United States). Of interest is whether the cracks have propagated either through the grain or along the grain or whether the cracks have branched. To investigate the internal structure of the specimen the fractured samples were aligned in a cross-sectional manner to the load direction, gridded, polished and etched with Kroll reagent to prepare for a metallographic analysis, as described in section 3.3. This technique can be employed to determine whether the form of the crack exhibits some correlation with any irregularities in the structure.

Chapter 4.

Mechanical Behaviour of refill FSSW Joint and Design Criteria Limitations

This chapter presents the mechanical behaviours of the joints produced by refill FSSW and the impact of the macrostructure features of the joint on the mechanical integrity, e.g., hook curvature and flaws. In addition, this chapter optimises the structural distances for lap joints in single- and multiple-spot welds joint configurations to develop a design-data/guideline.

A typical aircraft structure is composed of many small components that are fastened by rivets, screws and bolts. As these joints comprise the most common source of failure in an airframe structure, all aspects of the design should be considered. Historically, damage tolerance is the main design criteria for overlap joints under tensile loads [2, 59]. The damage tolerance requires an evaluation of the most likely location of the failure and the failure modes; in aeronautic applications, the cyclic fatigue loading is known to be the critical loading condition. Therefore, an appropriate design must consider the fatigue behaviour using a variety of tests, joint configurations and loading conditions.

The following geometric variables of a riveted lap joint can be applied to refill FSSW joints [51]:

(a) **Eccentricities,** the eccentricity of the joint promotes an internal moment, especially in overlapped joints. It is also known as secondary bending or out-of-plane displacement and induces the joint to an excessive loading, where the stresses are not uniform through the thickness;

(b) **Supported joint,** to reduce the local stress promoted by the eccentricity and increase structural integrity, it is generally applied in fuselage under hoop tension or double- or triple-riveting rows. However, minimum/optimum distances between joints must be carefully established;

(c) **Joint efficiency,** ideally, the joint efficiency of a joint should be equal or greater than the parent structure. Although the maximum efficiency is desired, the fabrication costs and penalty weight have to be considered. A compromise should be made to achieve the most efficient joint and surrounding structure.

In section 4.1, a general design consideration is performed to elucidate the critical geometrical variables for fatigue design in riveting. Afterwards, the load transfer for refill FSSW joints is analysed. Section 4.2 addresses the mechanical performance of spot welds under lap shear loading. In this section, the experimental results of single spot welds under static and cyclic loading and a laboratory analysis are evaluated to determine the effect of the macrostructural features on the mechanical behaviour. The numerical models for structural analysis and design optimisation are described in section 4.3, and the strategy to optimise the distances is quickly described in section 4.4. Afterward, the design optimisation for refill FSSW is thoroughly investigated in section 4.5. Concluding remarks are presented in section 4.6.

4.1. General design consideration

4.1.1. Geometrical variables for fatigue design (lap Joints under shear loading)

For the design of riveted lap joints, several books, such as Skorupa et al. [94], Niu [51] and Schijve [1], describe the influence of the geometrical variables on the strength of the joints. The most common geometrical variables are distance of the rivet from the sheet edge, number and spacing of rivet rows, rivet pitch in a row, sheet thickness, joint size and rivet pattern. These geometrical variables affect the peak stress and stress concentration close to the joints and change the secondary bending. Consequently, they also affect the joint fatigue behaviour.

In this study, as described in Fig. 4.1, the following geometrical variables are analysed for refill FSSW lap joints: number of spot welds in row (n_{SW}); spot weld row spacing (p); spot weld pitch in row (S) and distance of the spot weld from the sheet edge (S_e). The thickness of the sheet and the spot weld diameter are kept constant: $B = 2mm$ and $d_{SW} = 9mm$, respectively. During the initial tests, trials and numerical simulations, the edge distance (e) does not influence the static strength for a minimum distance of $2d_{SW}$. Thus, $e = 3d_{SW} = 27mm$ is maintained constant for all experimental and numerical investigations.

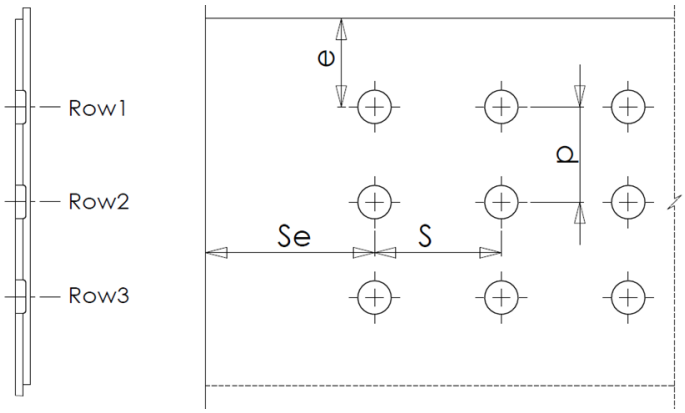

- n_{SW} - Number of spot weld rows;
- p – Spot weld row spacing;
- S – Spot weld pitch in row;
- e - Edge Distance;
- S_e - Distance of the spot weld from the Sheet Edge

Figure 4.1. Nomenclature for dimensions of a longitudinal riveted/refill FSSW lap splice joint.

Schijve [1] have demonstrated that the distance of the rivet from the Sheet Edge (S_e) has a minimal effect on fatigue strength once the minimum distance is obtained. According to Niu [51], the minimum S_e distance should be at least two times the rivet diameter (d_{rivet}).

When the structure must sustain a high load level, the number of joint rows n_{SW} has to be increased. The fatigue strength considerably increases until triple-rivet rows, and the fatigue may not be improved in a meaningful way with more than three rows [1]. The influence of the number of rows on joint fatigue performance observed in the experimental investigations can be explained by a low load transfer through the critical outer rivets. When the row spacing is kept constant, the joint with the larger number of rivet rows implies a reduction of the secondary bending due to the long overlap. An overview of single-, double- and triple-rows for rivets is provided [51]:

- **single-row pattern**, generally, this pattern is employed in stiffened panels that join stringers to skin. A careful design must ensure that the strength of the fasteners is sufficient to transfer the load onto the adjacent part to complete the load path;
- **double-row pattern**, this pattern has the most efficient load transfer. Shear-out failure mode does not occur if the spacing of the fasteners is too close, which is undesirable;

- **triple-row pattern,** this pattern is employed on lap-splice joints on longitudinal fuselage, where the hoop tension load is presented. This pattern reduces the eccentric effect and has superior fatigue life.

In general, increasing the row spacing p improves the fatigue properties. The benefits from applying a large row spacing in a lap joint are associated with a reduction in the secondary bending. A large distance between rivet rows has an unfavourable implication, namely, in joint weight due to the long overlap. The pitch distance in a row S is associated with the stress concentration around the rivet hole. Based on the static strength calculations, the lowest stress concentration factor is obtained with $S = 2.5d_{rivet}$ [51]. According to Schijve [1], the most favourable range of pitch distance in a row for static and fatigue loads is $S = 2.5 - 3.75d_{rivet}$. Additional analyses have demonstrated that large distances decrease the fatigue strength of the panels.

4.1.2. Load transfer in lap joints in refill FSSW spot weld joints

The role of a spot weld is to transfer the shear and tension loads between two plates in an overlap configuration. The knowledge of the stress distribution within a riveted joint is a fundamental step in estimating its fatigue life and damage tolerance characteristics. To approach the problem of the stress conditions at the rivet holes, the distribution of the loads acting in the joint must be known. To analyse the load transfer and secondary bending, the same approach in the riveting analysis was applied in this study, as schematically represented in Fig. 4.2. In a multiple-spot weld, the force P is fragmented into a bypass load (T_{bp}) and a transferred load (T_{tr}). T_{bp} is the load that remains in the plate after the spot weld, and T_{tr} is the load that is transferred between two plates. T_{tr} consists of the spot transfer load (T_{Str}) and the friction load (T_{fr}). T_{Str} is obtained from the load transmitted by the spot weld, and T_{fr} arises from the friction between the welded plates and the friction between the mating sheets [57, 95, 96].

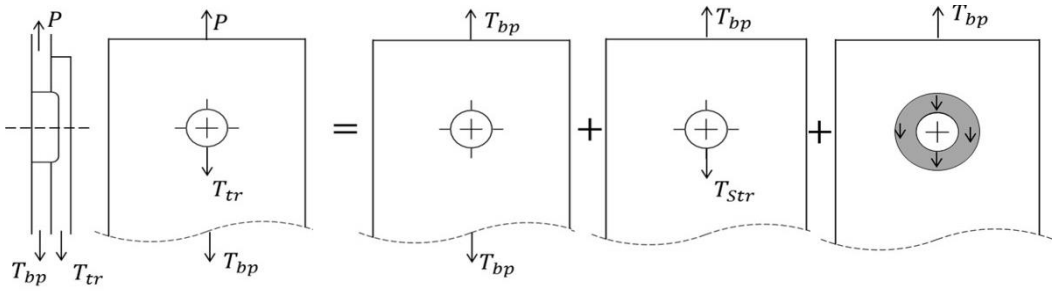

Figure 4.2. Axial forces in sheets of a two-layer lap joint.

When the level of applied load is low, the transferred load (T_{tr}) is dominated by the friction load. The friction is primarily localised in the spot weld vicinity, where maximum clamping forces are applied by the clamping ring during the weld. When the load is increased, at one point when the load overcomes the maximum friction force before sliding, the plates begin to slide relative to each other. Once sliding has initiated, the load that is transferred by the friction between the plates remains essentially constant with additional increases in the applied load. Deviations from this constant value can be explained by local changes in the contact pressure between the plates.

The friction reduces the load carried by the spot weld and increases the fatigue performance of the joint. However, fretting damage may occur as a result of this friction. Fretting damage is a destructive process that is associated with clamped bodies that undergo oscillatory loading. This damaging process is known to generate microcracks in the surface under further loading, which can propagate into the substrate as fatigue cracks [97].

The load transfer is schematically illustrated in Fig. 4.3A, where the load is transferred via the spot between two plates. However, the load path along the upper plate and lower plate is not collinear through the joint—it is offset or eccentric. This eccentricity of the load path causes an internal moment. Consequently, an out-of-plane deformation is formed; the eccentricity of the load path causes secondary bending [96].

In designing multiple-spot weld rows, the correct proportion of the total load that each spot weld transfers to approach the problem of the stress condition must be known. In the case of rivets, tests and theory indicate that the load distribution at the elastic regime is not equally distributed and the outer fasteners carry the majority of the load. Thus, the most important load is the load of the end fasteners, as it takes the highest load in a group of fastener in a joint splice. The proportion or distribution of the transferred load is affected by many variables, such as deformation or elongation - tension or compression, number of spot weld rows, pattern (spacing and rows), diameter, rigidity and material. An accurate analysis of the load distribution is very difficult due to the large number of variables; however, the FEM will provide the best results. As shown in Fig. 4.3B, for the j-plates of a joint with i-rows, the equation that satisfies the equilibrium condition for each transverse section of the overlap is demonstrated in Equation 4.1, where $T_{1,0} = T_{3,2} = P$ and $T_{1,3} = T_{2,0} = 0$.

$$\sum_{j=1}^{i=1} T_{j,i} = P \qquad T_{1,0} = T_{2,3} = P \text{ and } T_{1,3} = T_{2,0} = 0 \qquad \text{Equation 4.1}$$

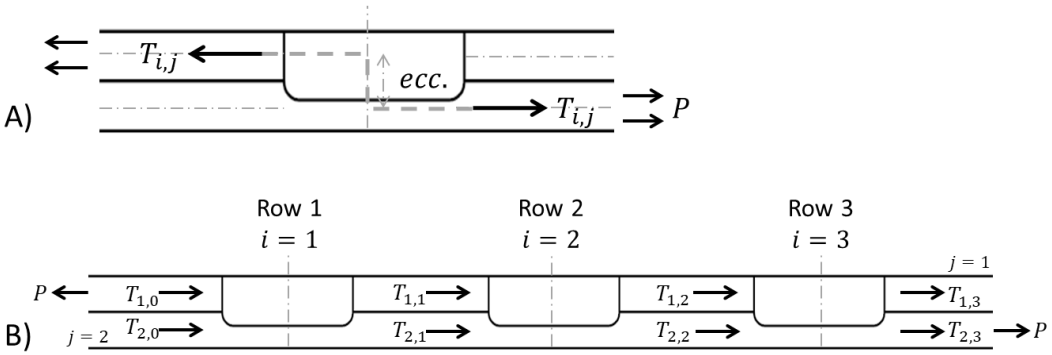

Figure 4.3. A) Load path; B) Axial forces of three spot weld row joints.

According to this approach, the stress in the weld can be divided into the stress that arises from the spot weld loads and the secondary bending stress. Secondary bending is highly dependent on the magnitude of the eccentricity and the tensile stresses that are created along the joint faying surfaces. As this secondary bending stress contributes to the nucleation of fatigue cracks, the effect of secondary bending on a lap joint design must be understood and assessed. Secondary bending is attributed to the geometrical/load path eccentricities present in the joint under tensile loads; it is unfavourable for the fatigue properties of the structure due to the increased stress concentrations by the presence of the bending stress. The use of structural elements usually implies that contact is not treated, or treated in a simplistic

manner, whereas a two-dimensional model cannot be employed to accurately describe a single shear lap joint due to their three-dimensional (3D) stress field.

4.2. Mechanical performance under lap shear loading (static and cyclic loading)

This section presents the experimental results of single spot welds under static and cyclic loading and a laboratory analysis that was performed to evaluate the effects of the joint macrostructural features on the mechanical performance. This information is required to assess the spot weld integrity and damage tolerance. Section 4.2.1 addresses the statistical analysis of the process parameter on mechanical performance using a DoE and the definition of optimum weld parameters. Section 4.2.2 provides an overview of the characterisation of refill FSSW in terms of weld zones, microhardness, flaws and hook formation. The typical fracture modes under static loading are analysed and presented in section 4.2.3. The results of the fatigue tests are investigated in section 4.2.4.

4.2.1. DOE: Box-Behnken design

Table 4.1 summarises the DoE test using the experimental LSS values. The microscopic evaluation, which is also presented, will be subsequently discussed. The BB experiments presented LSS values from 4207 N (C1) to 11181 N (C15). The highest strength was obtained from combination C15 (time = 5.8 s, PD = 2.5 mm and RS = 1900 rpm).

Table 4.1. Summary of the Box-Behnken design conditions: experimental values of LSS, weld description, volume flow rate, hook orientation, fracture mode and failure energy.

Cond.	time [s]	PD [mm]	RS [rpm]	LSS [KN]	Defects	Hook Orientation	Fracture Mode	Failure Energy [kN mm]
C1	4.8	1.9	1900	4.20	Without flaws	Down	Interfacial	3.18
C2	5.2	2.5	1400	5.20	With flaws	Down	Plug pull-out	11.60
C3	5.2	1.9	1400	5.58	Without flaws	Up	Interfacial	4.99
C4	5.8	1.9	1900	5.70	Without flaws	Up	Interfacial	4.98
C5	4.8	2.2	2400	6.22	With flaws	Down	Interfacial	5.28
C6	4.8	2.2	1400	7.72	With flaws	Down	Plug pull-out	13.29
C7	5.2	2.2	1900	8.19	With flaws	Up	Interfacial	11.75
C8	4.8	2.5	1900	8.31	With flaws	Up	Plug pull-out	17.80
C9	5.2	2.2	1900	9.12	Without flaws	Up	Interfacial	13.70
C10	5.2	1.9	2400	9.33	Without flaws	Down	Interfacial	13.80
C11	5.2	2.5	2400	10.30	Without flaws	Up	Interfacial	15.60
C12	5.2	2.2	1900	10.35	Without flaws	Down	Interfacial	14.54
C13	5.8	2.2	1400	10.43	Without flaws	Down	Interfacial	18.23
C14	5.8	2.2	2400	10.73	Without flaws	Down	Interfacial	17.23
C15	5.8	2.5	1900	11.18	Without flaws	Up	Plug Pull-out	26.41

A complete understanding of the influence of the welding parameters on the LSS is important to obtain the optimised combinations. ANOVA is calculated considering the mean squared deviations of the weld parameters. Then, the squared error is obtained by the sum of the squared deviation and divided by the degrees of freedom. The ratio of the mean squared deviations by the mean of the squared error (the F value) is obtained. When the F value exceeds four, the weld parameter is significant for the weld performance [12, 84, 98]. The data for a confidence interval of 95% are listed in Table 4.2. An analysis of the F value indicates that interactions between the plunge depth and welding time, as well as the interactions between the rotational speed and welding time, are significant factors that affect the joint performance. Each weld parameter is equally important for obtaining sound welds. A dominant factor does

not exist. For a better understanding of the welding parameter contributions, the F-value was written as percentage terms. From these results, the second-order term of each considered weld parameter exhibits a similar significance for LSS—17%. Additionally, the interactions between plunge depth and rotational speed (12%) and the interactions between welding time and plunge depth (17%) have a significant influence on LSS. The sum of all contributions is 86%.

Table 4.2. ANOVA performed with the acquired data.

Source	dF	SS	MS	F-value	Contribution (%)
time [s]	1	196907	196907	0.17	0.69
PD [mm]	1	312575	312575	0.27	1.09
RS [rpm]	1	535015	535015	0.46	1.86
Time^2	1	1216661	1216661	4.21	17.09
PD^2	1	364939	3649395	4.23	17.19
RS^2	1	1216446	1216446	4.21	17.09
time *PD	1	42167	42167	0.04	0.16
time *RS	1	778921	778921	0.67	2.72
PD*RS	1	2156742	2156742	3.07	12.46
time * time *PD	1	2800661	2800661	4.21	17.09
time *time*RS	1	820593	820593	0.70	2.84
time*PD*PD	1	4262076	4262076	2.38	9.66
Error	2	233839	1169195		2.55
Total	14	453084			

From the LSS experimental results obtained during the development of BB, the second-order regression model is defined by Eq. 4.2. In this equation, all terms are considered, even the interactions that do not present a significant influence on LSS.

$$\begin{aligned} LSS = {} & 27499 + 121327 \cdot time - 256825 \cdot PD - 123 \cdot RS - 27216 \\ & \cdot time^2 + 157982 \cdot PD^2 + 0.00232 \cdot RS^2 - 25929 \\ & \cdot time \cdot PD + 55.9 \cdot time \cdot RS - 4.9 \cdot PD \cdot RS \\ & + 16599 \cdot time^2 \cdot PD - 5.39 \cdot time^2 \cdot RS - 32440 \\ & \cdot time \cdot PD^2 \end{aligned} \qquad \text{Equation (4.2)}$$

Eq. 4.2 can be represented by a surface response (Fig. 4.4). This diagram outlines the process parameter interactions. It is important to notice a large area, or wide factor levels, that can obtain LSS values greater than $10000\ N$. Additionally, the surface representation suggests that a higher LSS is obtained from longer welding time ($5.8\ s$), medium rotational speed ($1900\ rpm$) and medium-high plunge depth (2.2 to $2.5\ mm$). The surface representation indicates that an appropriate heating balance and material flow must be considered in the optimisation process. Shen et al. [34] and Rosendo et al. [35] suggested that, for refill FSSW, an improper balance between the heat input and the material flow diminishes the joint integrity by promoting voids and flaws.

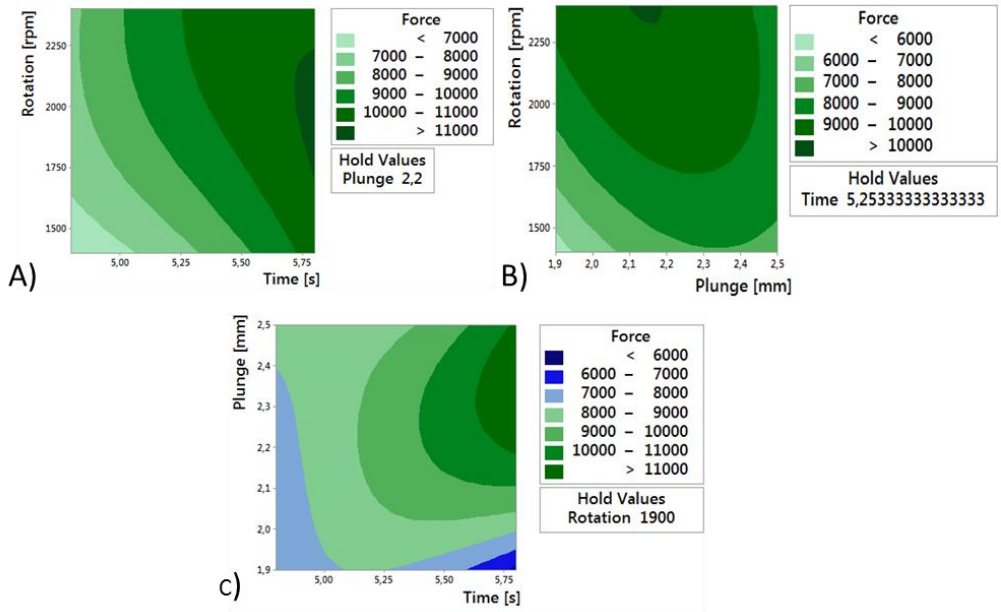

Figure 4.4. Response surface representation plot as a function of A) RS and t; B) RS and PD; C) PD and t.

To verify the developed statistical model and optimise the weld parameters, three evaluation experiments were performed. Condition C16 is indicated as the optimum welding parameter by the statistical model. Condition C17 is predicted as a high-strength weld, and condition C18 is considered to be intermediate strength. In addition to these weld parameters, three weld conditions were selected, considering the high-strength levels during BB development. Additionally, these conditions represent a sound weld, a different hook profile and fracture modes. All weld conditions were tested in triplicate to ensure the reliability of the results. Table 4.3 presents the results for the selected weld parameters. The error between the LSS values predicted by the RSM model and the observed values varies from 3.6% to 9.07%, which indicates an acceptable accuracy of the developed equation for the prediction of LSS in all ranges of the weld parameters selected in the first step of the DoE.

Considering the statistical analyses of the BB approach, ANOVA and RSM, the weld parameter C16 ($t = 5.8\,s$, $PD = 2.35$ mm and $RS = 1800\,rpm$) represents the highest LSS of $10.7\,kN$ and a low scatter of $0.2\,kN$. The low scatter emphasises the reproducibility of the weld conditions and the technological stability of the refill FSSW, which is very attractive for structural applications. Additionally, the condition C15 ($t = 5.8\,s$, $PD = 2.5\,mm$ and $RS = 1900\,rpm$) was considered to be an attractive weld parameter as this condition presented high-strength welds ($9.7\,kN$) and low variability ($0.3\,kN$).

Table 4.3. Summary of experimental test for verification of the statistical model and weld parameter optimisation.

Parameter	time [s]	PD [mm]	RS [rpm]	LSS [kN]	Predict LSS [kN]	Fracture Mode	Hook	Fail. En. [kN mm]
C11	5.2	2.5	2400	7.7±1.1	8.3	Interfacial	Up	11.23±1.5
C14	5.8	2.2	2400	9.0±0.4	9.8	Interfacial	Down	12.22±0.2
C15	5.8	2.5	1900	9.7±0.3	10.4	PPO	Up	21.6±0.5
C16 (Opt.)	5.8	2.35	1800	10.7±0.2	11.1	PPO	Down	26.9±0.4
C17 (Eval.)	5.8	2.5	2400	9.4±0.7	10.4	Interfacial	Down	13.66±1.1
C18 (Eval.)	4.8	2.2	1900	7.0±0.2	6.5	Interfacial	Up	8.20±0.6

4.2.2. Microstructural evaluation and hardness profile

Refill FSSW is a solid-state process that produces changes in the microstructure. Fig. 4.5A presents a typical cross-section of the macrograph of the spot weld produced by refill FSSW—combination C16—and highlights the different weld zones based on the microstructural characteristics. The base material exhibits elongated and pancake-shaped grains deformed by the rolling process (Fig. 4.5B). In the centre of the cross-section (Fig. 4.5C), a refined-equiaxial region—the Stir Zone—is observed [13, 24, 25]. The surrounding SZ comprises the Thermo-Mechanical Affected Zone; the TMAZ contains deformed (Fig. 4.5D) and elongated grain structures (Fig. 4.5E). In addition, the TMAZ presents 90-degree bent grains towards the top surface due to the axial retraction movement of the sleeve (Fig. 4.5E). Fig. 4.5F presents, below the probe, the sharp transition from the refined-equiaxial grain structure of the SZ to the partially recrystallised grains of the TMAZ. Outside the TMAZ, the Heat-Affected Zone is located. In the HAZ, no plastic deformation occurs; however, this region undergoes a thermal cycle that affects the mechanical properties. Fig. 4.5G highlights the presence and location of the downward hook profile [11, 24, 25].

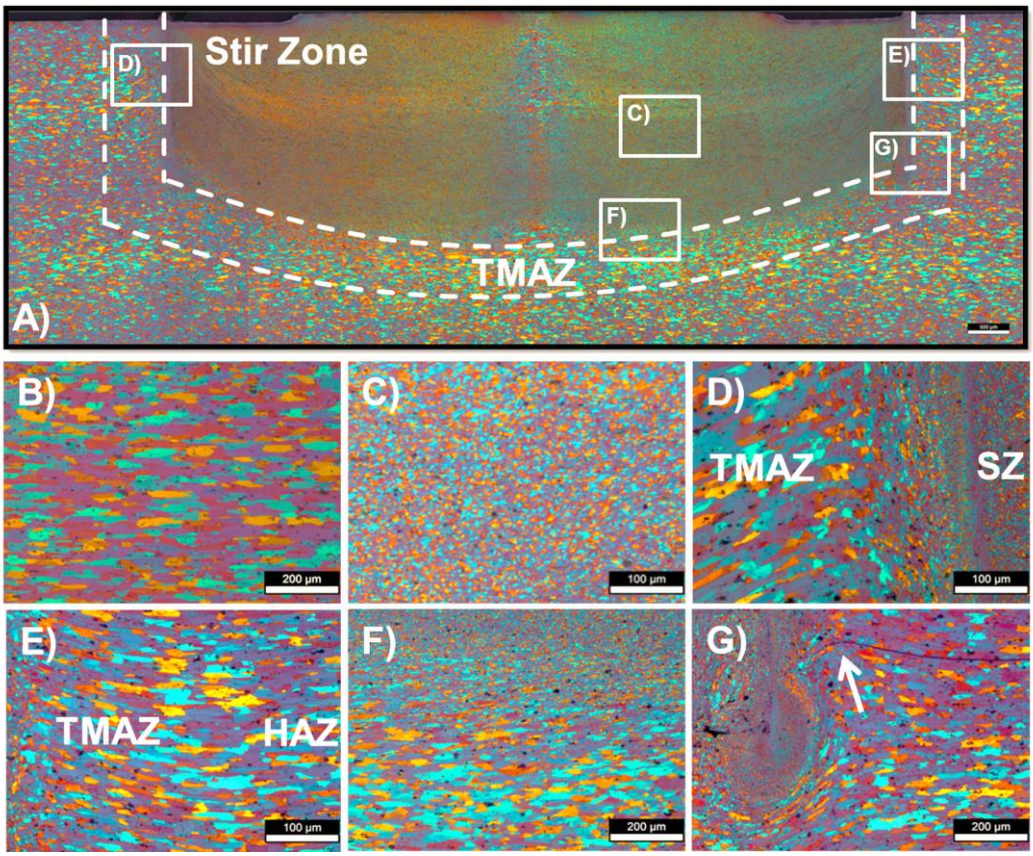

Figure 4.5. Microstructure of the AA2024-T3 alloy friction spot-weld. A) Cross-section macrograph of the spot weld; B) microstructure of the base material; C) Very fine grains in the SZ; D) Transition of the SZ and TMAZ; E) 90-degree bent grains in the transition of the TMAZ and SZ; F) Transition between the SZ and TMAZ below the probe; G) Hook profile location, downward hook profile.

As previously explained, the hook consists of the transition from the metallurgically unbonded region to the partially metallurgically bonded region, as shown in Fig. 4.6A. The hook tip is located at the extremity of the spot weld, in the interface between the upper plate and the

lower plate. The formation of the hook is attributed to the upward and downward material flow generated by the axial sleeve movement. Due to the importance of the hook formation and its influence on shear strength, it is discussed in section 4.2.4.

Similar to hook formation, the partially metallurgically bonded line is inherent to the weld parameters and can be controlled by an appropriate material flow. This microstructural feature consists of intermittent oxide particles that originate from the gap interface of the upper and lower plates, as shown in Fig. 4.6B for C1. The brightness and contrast of the image were adjusted to emphasise the presence of the partially bonded line along the spot weld. The weld conditions C1, C3 and C4 present a very pronounced partially bonded line and lower shear strength. This microstructural feature is correlated to low rotational speed and low plunge depth.

In this current study, voids or grouped voids are the typical flaws observed in refill spot welds, as shown in Fig. 4.7A, which depicts weld condition C5. Usually, the voids are located along the boundary between TMAZ and SZ, at the same location where the outer sleeve surface plunges into the plates (Fig. 4.7B). Considering the microstructural characteristics from Table 4.2, this type of flaw is associated with a low welding time.

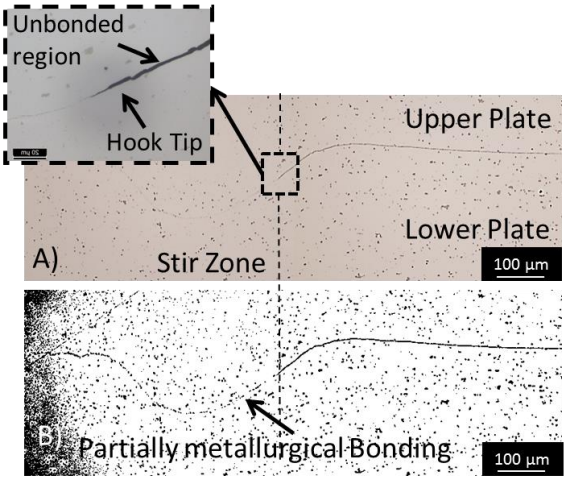

Figure 4.6. Transition of the completely unbonded region to a completely/partially metallurgically bonded region. The partially metallurgically bonded line is very pronounced; A) Hook tip and partially bonded line; B) Treated image of the partially bonded line along the spot weld.

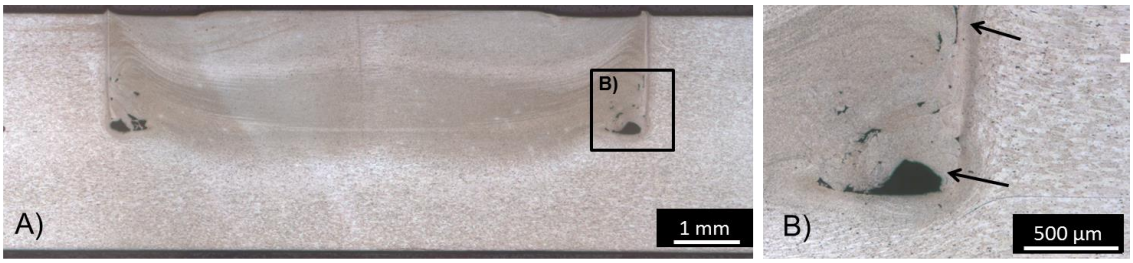

Figure 4.7. Cross-section with typical flaws and voids. A) Macrograph cross-section with flaws; B) Typical location of the flaws.

Fig. 4.8 presents the hardness map of the sample welded by condition C16. From the BM towards the centre of the weld, the hardness level exhibits a slight decline in HAZ, which is

primarily associated with the recovery of the BM microstructure, coarsening precipitates and grains. The decline is accentuated in the TMAZ at a minimum value. With a decrease in the distance from the centre of the weld, the temperature increases, which may cause coarsening and dissolution of the strengthening particles [30]. From this absolute minimum hardness value, closer to the centre of the weld, the hardness levels increase and create a plateau of higher hardness in comparison to BM.

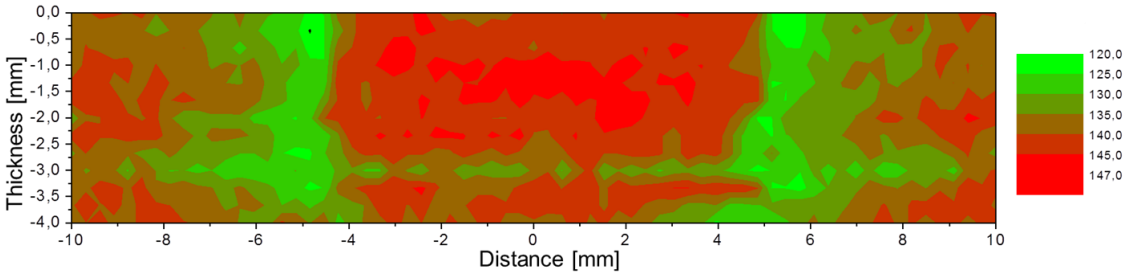

Figure 4.8. Hardness map for condition C16.

4.2.3. Fracture analysis

The fracture analysis revealed two typical fracture modes: Plug Pull-Out (PPO) and Through the Weld (TW), also known as interfacial fracture mode. Fig. 4.9 shows the lap shear test graph (load vs. displacement) of high-strength welds C16 ($10.7\ kN$) and C13 ($10.4\ kN$). From this curve, the ultimate lap shear strength can be obtained. The fracture mode observed from weld C13 is catastrophic. Once the sample attains the maximum load, it abruptly decreases to zero. This behaviour is associated with the through the weld fracture mode, where an annular crack nucleates at the hook tip and propagates through the refined-equiaxial grain zone, parallel to the surface plates. Eventually, the joint unexpectedly fails due to overload associated with tearing. The PPO fracture mode presents a higher deformation after the load reaches its maximum value and is associated with ductile fracture and higher energy absorption. The crack nucleates at the hook tip and propagates through the material thickness towards the free surface and circumferentially propagates to TMAZ. Consequently, the load gradually decreases to zero until complete failure occurs [25, 26]. In the case of the PPO fracture mode, TMAZ is the most likely site for crack nucleation and propagation as this zone presents low hardness, elongated grains, hook and a high stress level. In addition, the eccentricity of the load line between the upper plate and lower plate promotes secondary bending, which generates a triaxial stress state and can cause crack initiation and propagation by either TW or PPO [10, 25, 99].

Considering the area below the lap shear curve as failure energy absorbed by the sample prior to the fracture, this area can be used to correlate the failure mechanisms with optimum weld parameters. The failure energy was calculated using the numerical quadrature approach via the implicit trapezoidal rule, which is a technique for an approximate definite integral, where the region under the curve is divided into several trapezoids, and its area is calculated.

Table 4.1 and Table 4.3 present the energy failure for each specimen. PPO has the highest failure energy, i.e., conditions C15 and C16 have approximately 60% higher energy failure over the samples with similar LSS that experienced the TW fracture mode. The higher values are explained by the crack propagation after the maximum load. The results from Table 4.3 suggest that the LSS scatter is lower in the case of PPO. Thus, the PPO fracture mode is the

preferred fracture mode to select an optimised weld parameter for a single-spot weld row [10, 25, 35].

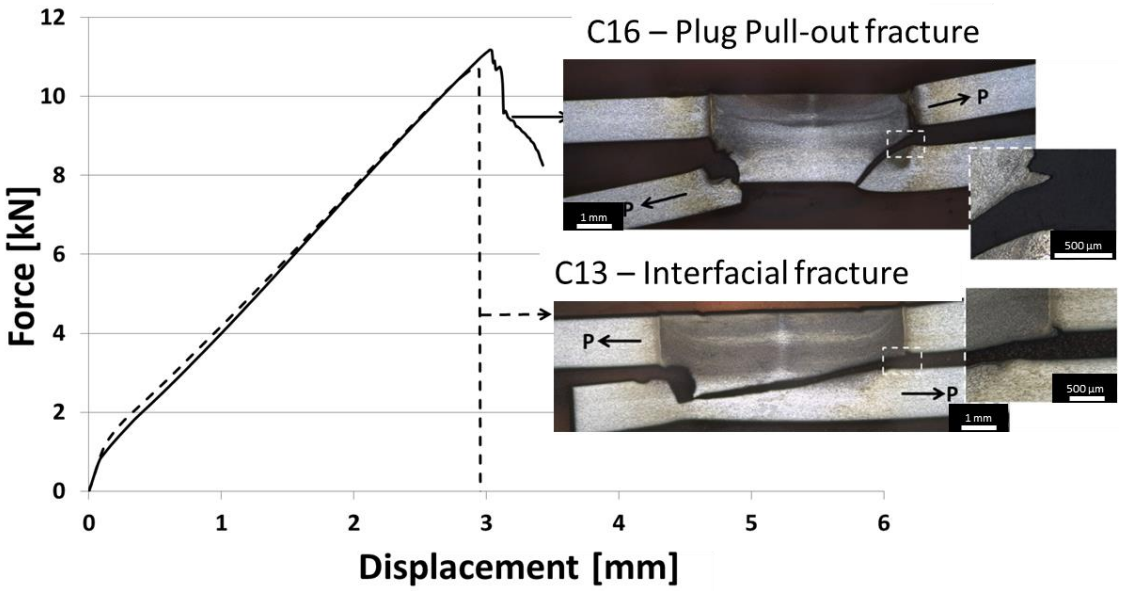

Figure 4.9. Lap shear test curves for C16 (10.7 kN PPO) and C13 (10.4 kN, TW).

As previously mentioned, the crack nucleates at the tip or close to the tip of the unbonded hook region. Fig. 4.9 shows the TW fracture mode for the C3 weld condition and highlights the hook region. This condition presented welds without flaws but a very pronounced partially bonded line. Near the hook tip region (Fig. 4.10B), the fracture surface analysis (Fig. 4.10) reveals a smooth surface indicating non-adhesion between the upper and lower plates [13]. Towards the centre of the weld (Fig. 4.10C), the fracture surface presents a mixture of shallow dimples, shear lip dimples and smooth surface, suggesting that the crack propagates through the path of the partially bonded region. This observation agreed with the Tier et al. [13] results, where the authors suggested that the partial region has poor adhesion. At the centre of the weld (Fig. 4.10D), smooth and uniform dimple dispersion was observed, deformed towards the loading direction, meaning that the ductile fracture occurred under shear loading due to intensive plastic deformation subjected to shear overload, as shown in detail in Fig. 4.10E [100].

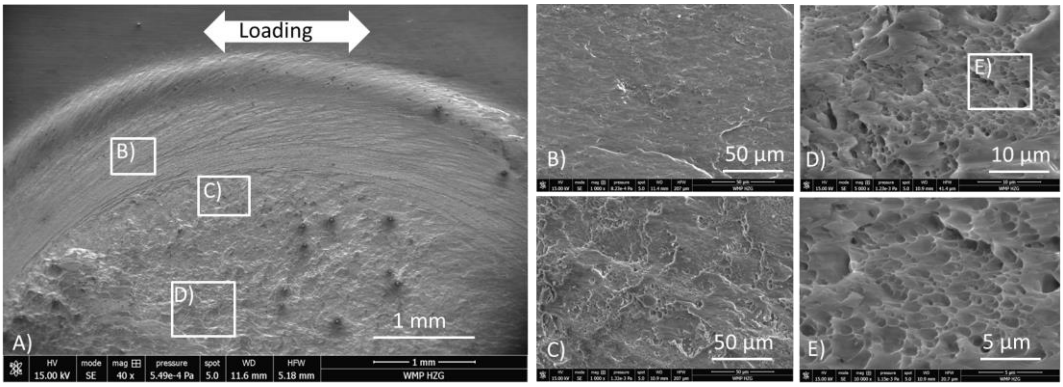

Figure 4.10. TW fracture surface analysis of C3.

In the case of the PPO fracture mode, the spot weld remains attached to one of the plates. The crack nucleates at the hook tip around the spot weld and propagates through the lower plate thickness. Fig. 4.11 shows the SEM fracture surface for the PPO fracture mode. The analysis

was performed in front of the weld, aligned to the load direction. For a better visualisation, the upper plate was removed after the lap shear test. Fig. 4.11B-E magnifies the region close to hook tip. As shown in Fig. 4.11B and C, it is possible to observe deformed downwards dimples, indicating that the crack propagates from the interface of the upper and lower plates towards the lower free surface through the material thickness. In addition, the step-like pattern reveals the circumferential crack propagation. The fracture surface in front of the weld (Fig. 4.11D and E) presents axial deformed dimples with different sizes and planes, suggesting that, in PPO, the crack initated in the region D close to the hook formation is due to a high uniaxial stress level. Then, the crack propagates circumferentially to the SZ and through the lower plates. The uniaxial failure explains the higher mechanical strength and higher failure energy absorption.

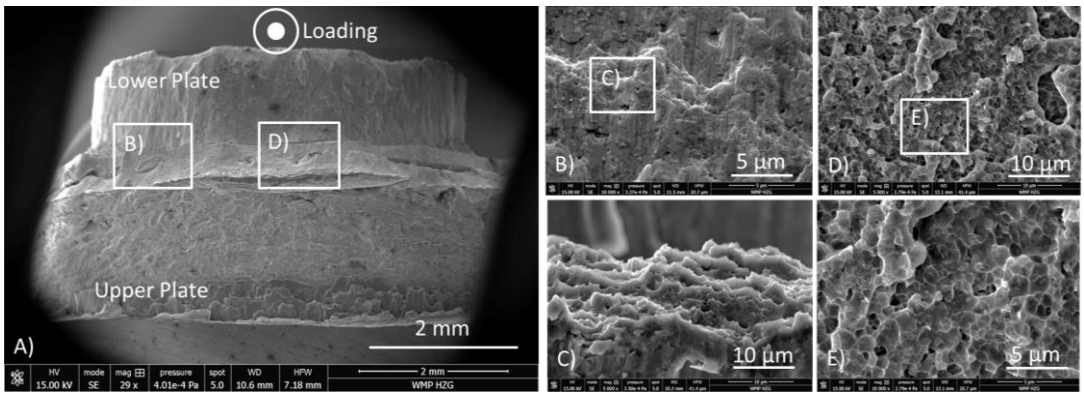

Figure 4.11. PPO fracture mode of C15.

A fracture surface study was also performed in samples that present a large number of flaws and voids—C5. The analysis was focused at the boundary of the SZ and TMAZ (Fig. 4.12A). At higher magnification (Fig. 4.12B and C), it is possible to observe a local ductile plastic deformation fracture characterised by dimples and a free smooth surface due to flaws. The smooth surface suggests non-effective metallurgical bonding was formed. Rosendo et al. [101] indicate that flaws and voids may be considered a circumferential crack and affect the mechanical strength of the spot joint because of the overload tension under low shear loading, which in turn promotes a high local triaxial stress state and local plastic deformation. Shen et al. [34] observed that a crack propagates through the voids, decreasing the critical remaining area, and the welds may fail by shear overload.

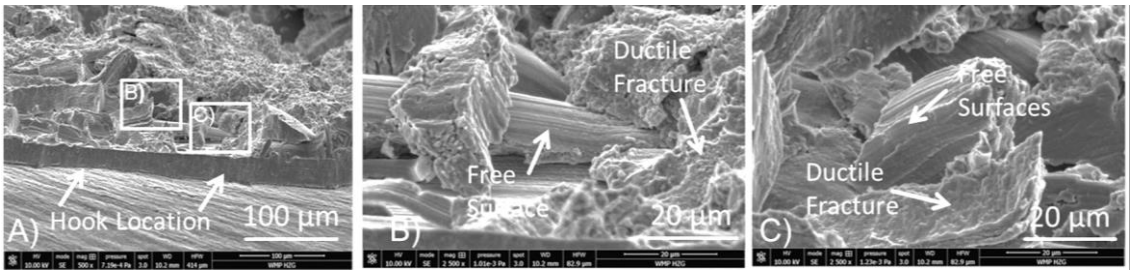

Figure 4.12. Cross-section with typical flaws and voids C5: A) Fracture surface after lap shear test; B) Fracture surface with dimples and free surfaces; C) Fracture surface with dimples and free surfaces.

4.2.4. Hook formation and its influence on the mechanical strength

In the current study, the hook profile is characterised by upward or downward curved sharp edges. As previously mentioned, formation of the hook profile depends on the heat input and

plastic deformation promoted by the tool during the process. The hook is developed when the interface of the overlapped sheets is broken and metallurgical bonding is formed and the gap interface of the overlapped plates is accommodated at the weld extremity [10, 25].

The hook profile schematic measurement is shown in Fig. 4.13. The bonded width (BW) physically represents the metallurgically bonded length or hook tip distance. The hook height ratio is a ratio between the hook height (Hh) and thickness (B). A negative value of the hook height ratio characterises a downward hook profile; the hook tangent angle was measured to better understand the influence of the hook profile, where the inclination of the hook angle θ was measured between the horizontal base material interface and the bent interface up to the hook tip. When $0° < hook\ angle\ \theta < 180°$, the hook is upwards towards the upper surface. Likewise, for $180° < hook\ angle\ \theta > 360°$, the angle is oriented towards the lower surface, which comprises a downward hook profile

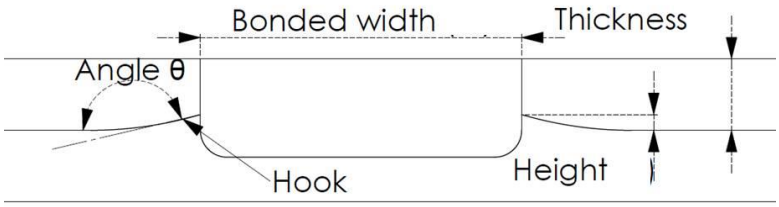

Figure 4.13. Schematic hook profile measurement: bonded width (BW); height (Hh), thickness (B) and hook angle θ.

Table 4.4 correlates the hook profile, weld parameters and mechanical strength. The relationship is demonstrated in Fig. 4.14. A slight difference in mechanical strength was observed with different sizes of bonded width and different hook height ratios (Fig. 4.14A and B). Thus, stating a reliable relationship with mechanical strength is not easy. It is important to emphasize that the current study considers only the high mechanical strength joints. Only the influence of the hook profile on the mechanical strength was investigated. The angle of the hook profile represents a major influence on the LSS value (Fig. 4.14C). When the angle θ is near 90°, the hook tip is perpendicular to the top surface, and the strength of the weld is significantly lower. By increasing the angle θ to almost 180°, the strength of the weld is also increased. As no flat hook profile was observed, a gap in the graph is observed when the angle is near 180°. Angles greater than 180°, with the hook oriented downwards, represents high strength.

Table 4.4. Relationship between hook profile and mechanical strength.

Condition	t [s]	PD [mm]	RS [rpm]	LSS [N]	Hook Orientation	BW	H_h/B	$Angle\ \theta$
C7	5.2	2.20	1900	8195.7	Upwards	9.25	0.1	135º
C8	4.8	2.50	1900	8312	Upwards	9.2	0.25	140º
C9	5.2	2.20	1900	9122	Upwards	9.4	0.1	120º
C10	5.2	1.90	2400	9339	Downwards	9.45	-0.05	190º
C11	5.2	2.50	2400	10305.1	Upwards	9.35	0.05	170º
C12	5.2	2.20	1900	10351.2	Downwards	9.3	-0.1	200º
C13	5.8	2.20	1400	10430	Downwards	9.2	-0.1	210º
C14	5.8	2.20	2400	10730.8	Downwards	9.35	-0.15	215º
C15	5.8	2.50	1900	11181.2	Upwards	9.3	0.12	150º
C16 (Opt.)	5.8	2.35	1800	10700	Downwards	9.54	-0.1	215º
C17 (Eval.)	5.8	2.50	1900	9400	Downwards	9.4	-0.01	155º

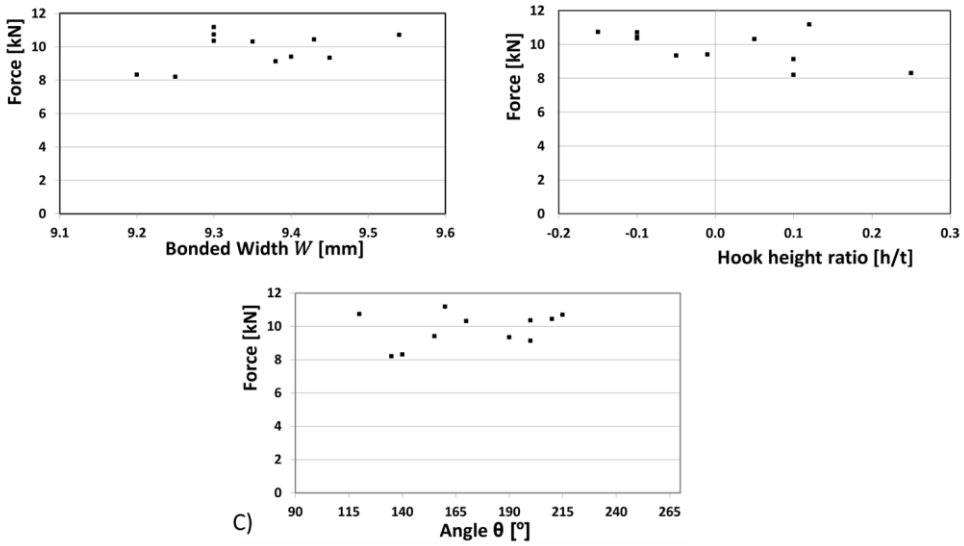

Figure 4.14. Lap shear strength vs. A) Bonded width (BW); B) Ratio between height (Hh) and thickness (B); C) Angle.

The correlation of the welding parameters with the hook profile is shown in Fig. 4.15. Fig. 4.15A and B show the influence of the welding time. In the case of the non-dwell time C8, the hook formation is oriented upwards (Fig. 4.15A). In similar welding conditions but a longer welding time C18, the hook profile is oriented downwards. A distinct influence of the rotational speed on the final hook profile, as shown in Fig. 4.15C and D, C13 and C14, was not observed. The influence of the plunge depth was investigated in Fig. 4.15E and F, C10 and C11, respectively. A distinct influence was not observed as the weld condition presents a similar hook downwards pattern. The welding time definitely has a major influence on the final hook profile; similar welding conditions with a long dwell time present a high bonded width and a downward hook.

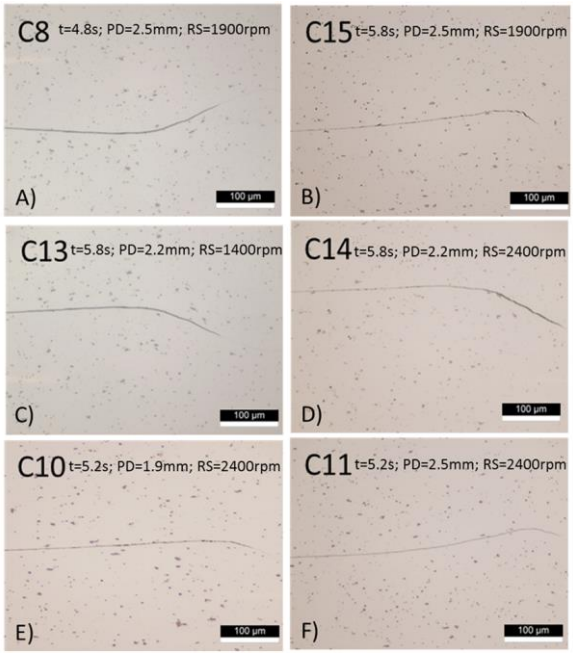

Figure 4.15. Hook profile for several weld conditions.

4.2.5. Fatigue analysis

Based on the previously described study, two weld conditions were selected to conduct the fatigue assessment: C16 and C15. These conditions have been selected due to distinctive geometric features of friction spot welds. Fig. 4.16 presents the cross-section produced by both weld conditions. They present sound joints, similar weld zones and complete refill without flaws. However, a detailed observation of the spot weld periphery reveals different profiles of the tips of the curved hook in Fig. 4.16. C16 (Fig. 4.16A) exhibits a downwards profile, whereas C15 (Fig. 4.16B) presented an upwards profile.

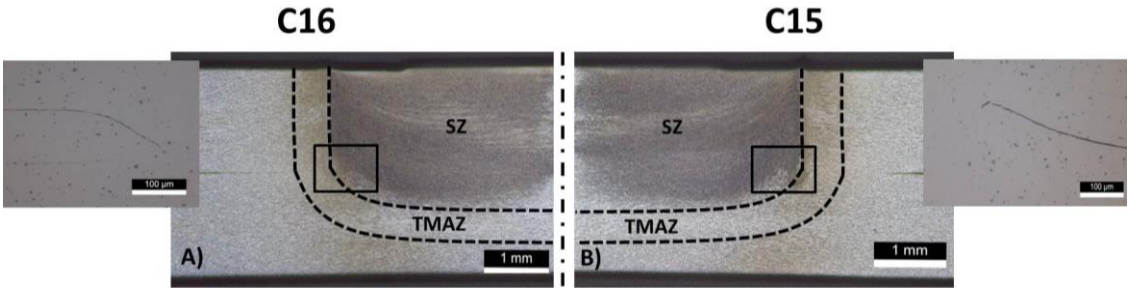

Figure 4.16. A) Cross-section macrograph for C16; B) Cross-section macrograph for C15.

The results of the fatigue tests are shown in Appendix–B, where the load percentages, stresses, cycles to failure and failure mode are presented. The CV (Eq. 3.7) is used to evaluate the relative dispersion of the fatigue data. Fig. 4.17A presents the CV and corresponding MTTF for all conditions tested. According to these results, the scatter in the fatigue for C15 is higher at all load levels than the scatter in the fatigue with the C16. The values of the mean life data for C16 have low variability, which is particularly interesting in terms of data accuracy and repeatability. The scatter demonstrated low values, which indicates the technological stability of the process and suggests that the fatigue behaviour in refill FSSW can be predicted.

The probabilistic fatigue SN curves provide a basis for qualifying the scatter in SN data and solving the problem of variable stress amplitude. Additionally, they provide a method for predicting fatigue life. Fig. 4.17B shows the SN curve obtained for the Weibull mean fatigue life for both weld conditions. The power function (Eq. 3.2) was applied to evaluate the fatigue test data.

In general, the results of the fatigue test indicate that the mean fatigue life of C15 is lower than the mean fatigue life of C16 at the same stress amplitude. Comparing the weld conditions, the main difference in the microstructure is the hook profile—downwards for C16 and upwards for C15. Rao et al. [36] reported that the hook has a strong influence on the fatigue behaviour for FSSW. The fatigue cracks were observed to initiate from this interfacial hook and propagate towards the upper or lower free surface. The authors considered the gap interface to be a stress intensity factor and emphasised that it is probably the nucleation site for a crack under cyclic loading. This observation is consistent with the experimental results of this study, where the upwards hook formation represents a low fatigue life.

In this study, the stress amplitude fatigue limit was $6.625\ MPa$ (15% of the ultimate lap shear strength). This approach to process optimisation can help designers select weld parameters and increase the fatigue limit in terms of accuracy and repeatability. Due to better results in terms of fatigue, additional analysis is concentrated on C16. Fig. 4.18 presents the SN curves

for different values of R_e; the term reliability is used to describe the probability of functional performance in the current service conditions and an indefinite time period, which is characterised by the number of cycles prior to failure. For greater accuracy, four safety levels were considered to predict the fatigue life. As expected, with higher reliability, the number of cycles to failure is low. The reliability $R_e = 0.668$ represents the statistical sample size; additionally, other reliability levels present in this graph are $R_e = 0.99$; $R_e = 0.95$ and $R_e = 0.1$ [92, 93].

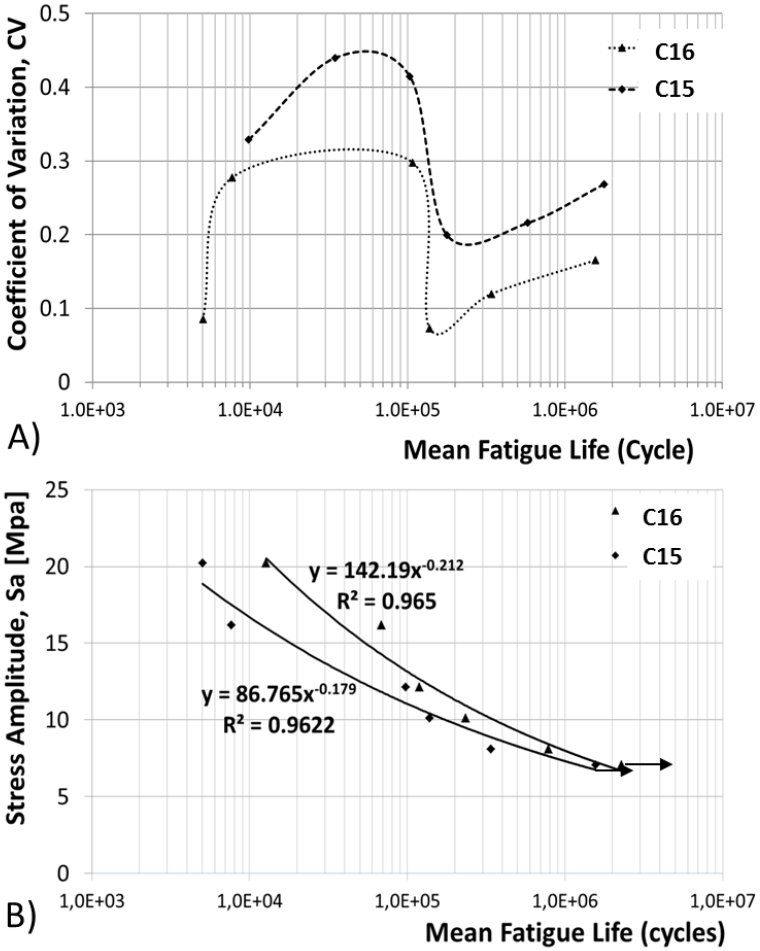

Figure 4.17. Effect of mean fatigue life on the coefficient of variation; B) SN curve of C15 and C16.

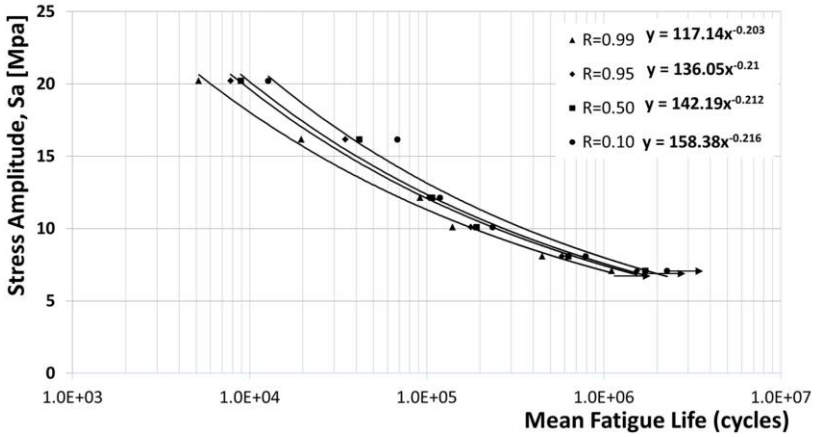

Figure 4.18. SN curves for different reliable levels.

4.3. Generation of three-dimensional numerical models

To analyse the mechanical behaviour and optimise the distances of refill FSSW, two numerical models were developed. The cohesive model is developed in section 4.3.1; it has demonstrated high accuracy for stress analysis, loads transferred by friction, and loads transferred by each spot weld. However, this model is not computationally efficient and its preparation is not simple. In section 4.3.2, a simpler model is developed using the embedded approach; it provides a faster method for obtaining qualitatively results for several joint configurations.

4.3.1. Cohesive model for stress analysis

The modelled weld was composed of three parts: the SZ, upper plate and lower plate. Their dimensions were previously examined considering the microstructural and microhardness changes; their dimensions are presented in Fig. 4.19A and B. A numerical model was built to represent the lap shear test specimen according to the standard DIN EN ISO 14273 [102], as shown in the boundary condition in Fig. 4.19C. The displacements in the u_1, u_2 and u_3 directions were restrained on the extremities. In addition, vertical movement of the external portions of both plates was not allowed. The displacement of the external surface of the upper plate was specified.

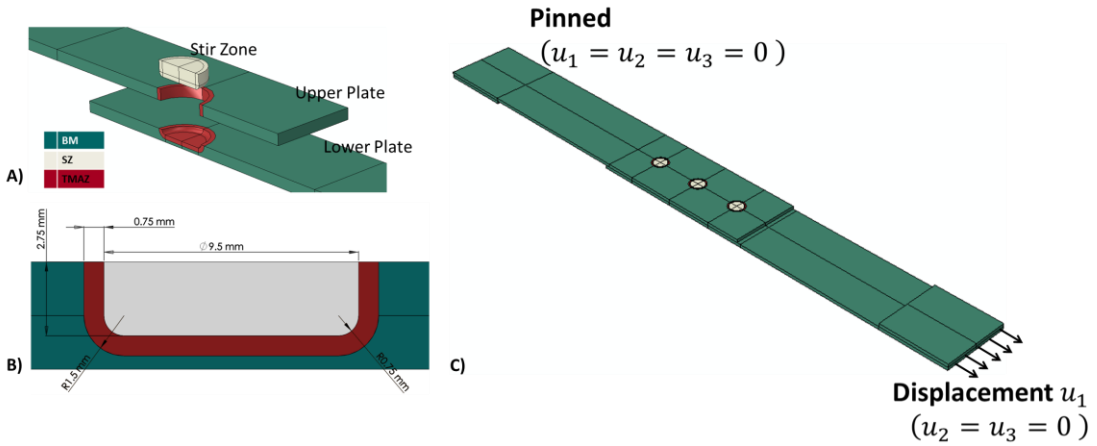

Figure 4.19. A) Three material volumes that represent the different microstructures and three different parts: SZ, upper plate and lower plate. B) Weld geometry; C) Lap shear geometry and boundary condition.

During the evaluation and calibration of the structural model, an interesting phenomena was observed. As shown in the load vs. displacement curve in Fig. 4.20A, the structural model curve and experimental curve are close but not perfectly fitted. Looking closer to the beginning of the simulation and experimental test, as shown in Fig. 4.20B, a change in the global stiffness of the sample is observed. Via a fractured surface investigation using SEM, Fig 4.21, ductile dimples were observed in the TMAZ, as shown in Fig. 4.21A and B. Ductile fracture and a free surface are depicted in Fig. 4.21C and D; this behaviour characterises progressive adhesion on the upper and lower plate in the TMAZ. However, this adhesion is broken at the beginning of the test; to confirm this phenomenon, experimental tests of loading and unloading were performed. With $20\% - 30\%$ of the maximum load, the bond mechanism is broken, and the curves of loading become similar to the structural model.

To simulate the effect of this bonding mechanism, a surface-based cohesive behaviour on the surface near the spot weld nugget was considered, namely, the TMAZ surface of the upper plate is in contact with the TMAZ of the lower plate at the faying surface, see Fig. 4.22. The basic concept of cohesive technology relies that two surfaces are constrained until loads and deformations cause the failure of the bonding mechanism based on energy principle [72].

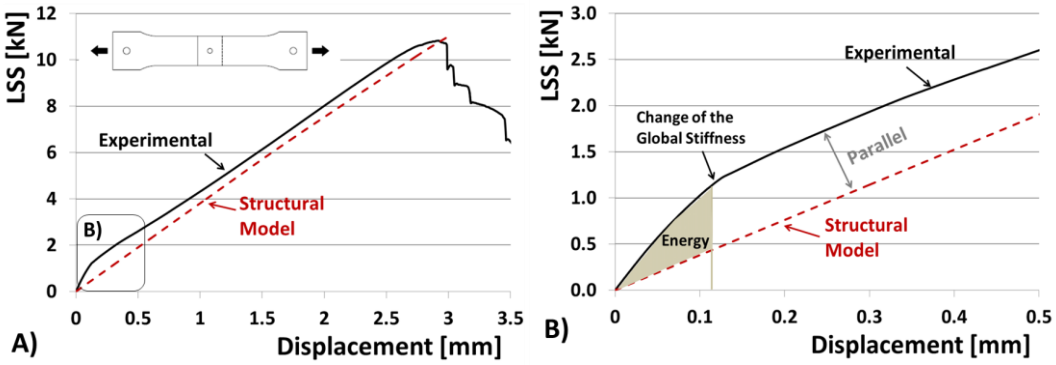

Figure 4.20. A) Lap shear curve of the experimental curve vs. structural numerical B) Change in the global stiffness.

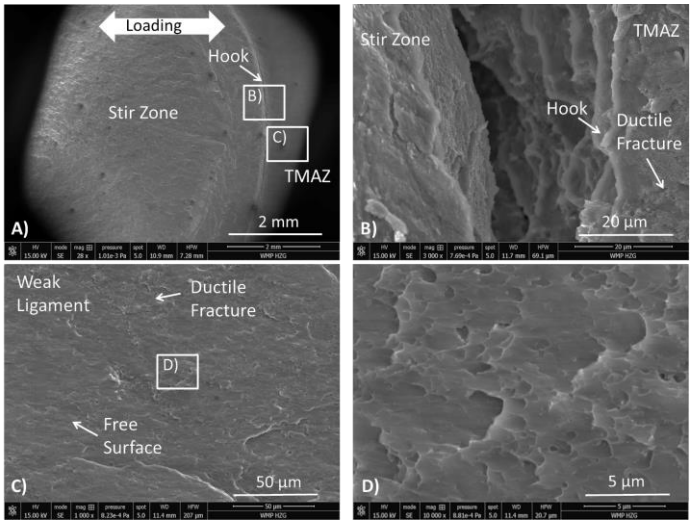

Figure 4.21.Fractured surface investigation A) Boundary of the SZ and TMAZ; B) Ductile dimples present in the TMAZ; C) Weak adhesion of the TMAZ; D) Ductile fractured surfaces inside the TMAZ.

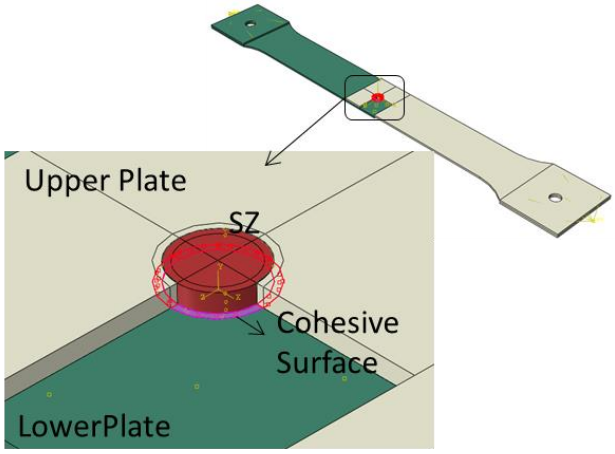

Figure 4.22. Surfaces under surface cohesive behaviour.

The cohesive behaviours of the surfaces generate contact penalty constrains in the normal and tangential directions by the stiffness terms normal (K_{nn}), shear (K_{ss}) and tangential (K_{tt}). It was considered that only the nodes that are in contact with each other at the start of the analysis should experience cohesive forces [72]. The input files are defined as

Input File: *COHESIVE BEHAVIOR, ELIGIBILITY=ORIGINAL CONTACTS, TYPE=UNCOUPLED

The damage initiation criterion for the degradation of the bonding is assumed to initiate when the maximum contact stress ratio attains a value of one,

$$\left\{\frac{\langle t_n \rangle}{{t_n}^0}\right\}^2 + \left\{\frac{t_s}{{t_s}^0}\right\}^2 + \left\{\frac{t_t}{{t_t}^0}\right\}^2 = 1 \qquad \text{Equation (4.3)}$$

where ${t_n}^0$, ${t_s}^0$ and ${t_t}^0$ represent the maximum contact stress for the surface separation [72] and the input file is described as follow:

Input File: *DAMAGE INITIATION, CRITERION=QUADS

The damage evolution of the boding is based on the energy that is dissipated as a result of the damage process. The fracture energy of approximately $42\ N\ mm$, which is represented by the area under the load vs. displacement curve described in Fig. 4.20, and the contact stress were adjusted according to the maximum energy released. Once the bonding mechanism is broken, a normal and tangential contact behaviour is applied.

Input File: *DAMAGE EVOLUTION, TYPE=ENERGY

The output of the analysis are

CSDMG Total value of the scalar variable.

CSMAXSCRT This variable indicates whether the damage initiation criterion at a contact stress has been satisfied at a contact point.

CSQUADSCRT This variable indicates whether the quadratic contact stress damage initiation criterion has been satisfied at a contact point.

The contact point between two different microstructural regions is an important factor that should be considered to obtain trustworthy results. Contact points should be carefully established to avoid mutual penetration and deviation in the prediction. Coherency between adjacent element sizes in different portions of the interacted surfaces should be maintained. The interaction between the SZ surfaces that are in contact with the upper and lower plates was considered to be a surface-based tie constraint. This interaction constrained the translational rotation and rotational motion, as well as all other degrees of freedom for the surface pairs. The surface-to-surface discretisation method minimised noise for the tied interfaces that involve mismatched meshes and was employed to optimise the stress accuracy [72].

The contact between the lower plate and upper plate was defined as tangential, and a friction coefficient that permitted some relative motion of the surfaces was established. When the surfaces were sticking, the magnitude of sliding was limited to the elastic slip or shear stress. In addition, a normal behaviour was considered. The contact properties in this study are listed in Table 4.5.

The coulomb friction model with friction coefficient $= 0.2$ was applied. The penalty method was applied to numerically implement the contact constrains. An iterative penetration checking approach allows changing the contact condition within the Newton-Raphson interaction loop. Using this procedure, the iteration process is simultaneously performed to satisfy both the contact constrains and global equilibrium using the Newton-Raphson methods. This procedure is accurate and stable but may require additional iterations.

Table 4.5. Contact properties of the numerical model.

Type	Discretisation Method	Property	Friction Coefficient	Shear Limit
Tie	surface-to-surface	constrained	-	-
Interaction	surface-to-surface	tangential	0.2-0.4	1-100 MPa
		normal	-	-

Given the extensive variety of element types, selection of the correct element is important. Tetrahedral elements should be avoided in stress analysis problems as they are overly stiff and exhibit slow convergence. If they are required, an extremely fine mesh may be needed to obtain results with sufficient accuracy. Hexahedral second-order elements are highly effective in bending-dominated problems and stress concentration problems. However, the high stress concentrations may not be captured if the mesh is coarse. Quadratic elements can also cause problems in contact calculations as the nodal forces in the vertex nodes that are equivalent to the constant pressure on an element side are zero [72, 103, 104]. In this analysis, the applied meshes were generated from incompatible first-order hexahedral elements (ABAQUS element type C3D8I). The density of the mesh element can be changed according to the relevance deformation mechanism of the region in the model geometry. Thus, the interface between the SZ and the TMAZ, which experienced high strain levels and the highest stress levels, was modelled with finer mesh elements.

Regular first-order elements can exhibit shear locking behaviour; this occurs in elements that are subjected to bending. The numerical formulation of the elements can give rise to shear strains that do not actually exist—they are referred to as a parasitic shear. Therefore, these elements are too stiff for bending, and incompatible mode elements improve their bending behaviours. In addition to the standard displacement degrees of freedom, incompatible deformation modes are internally added to the regular elements. The primary effect of these modes is to eliminate the parasitic shear stress. In addition, this mode eliminates artificial stiffening due to the Poisson's effect on bending. These elements are more expansive than regular first-order displacement elements; however, they are significantly more economical than second-order elements. The incompatible mode elements perform nearly as well as second-order elements in many situations if the elements are well shaped [72].

4.3.2. Embedded models

Although the previously described model has significant accuracy, it is computationally expensive and time-consuming due to its high complexity. Thus, a simpler model is required to analyse and develop several joint configurations; for this purpose, the embedded element technique becomes interesting where a volume remains embedded in a host component or volume. The embedded volume has its translational degree of freedom constrained to the

nodes of the host component [72]. This numerical technique is especially employed for composites [105, 106].

The main advantage of embedded models is the possibility of performing parametric studies of components with complex geometry. The stir zone is embedded in the rectangular upper and lower plates, and a geometric partition is not necessary to generate a proper mesh, as shown in Fig. 4.23. To increase the efficiency of the model, some considerations have been performed: (i) the contact between the upper plate and lower plate is tangential frictionless and normal behaviour, it means that 100% of the load is transferred by the spot welds; (ii) it is considered an elastic-plastic material according to the tensile testing; (iii) the mesh density is kept constant; therefore, when the sample changes the number of elements and nodes also change; and (iv) the boundary condition is similar to the previously described cohesive model.

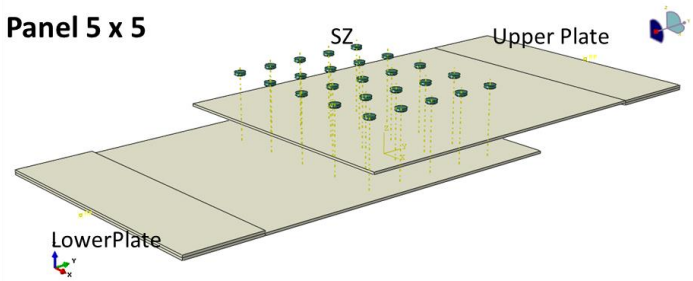

Figure 4.23. Embedded model where the stir zone is embedded in the rectangular upper and lower plates.

4.4. Strategy to obtain the optimum/minimum distances

To optimise the distances and analyse the mechanical behaviour of the single-spot weld and multiple-spot welds, the methodology shown in Fig. 4.24 is proposed. This method is based on typical pyramidal methodology of aircraft design and scientific investigation. Considering the numerical models developed in Sections 4.4 (embedded and cohesive numerical models) and the general considerations for the design described in section 4.1, several joint configurations are simulated using the embedded numerical model for a parametric study of the spacing distances. Then, some geometries were chosen for the cohesive numerical model, lap shear quasi-static test and stress analysis to determine the peak stress location, stress concentration, load transferred by friction and load transferred by each spot weld, load vs. displacement curve, and strains via digital image correlation. Considering these results, a couple of geometries were selected to analyse the fatigue life of spot welds and obtain the SN curves.

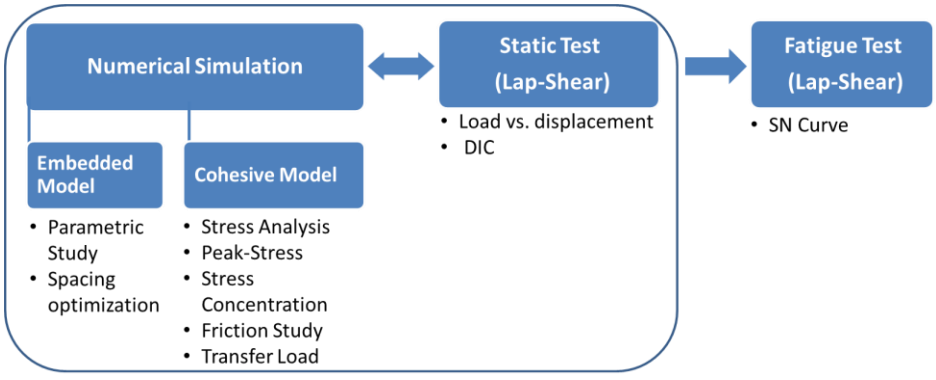

Figure 4.24. Methodology proposed to analyse the mechanical behaviour and spacing geometries.

4.5. Results and discussion

4.5.1. Stress analysis of refill FSSW

As already mentioned, understanding the stress distribution is a fundamental step in estimating the fatigue life and damage tolerance characteristics of refill FSSW and identifying the location of the peak stress. A Mises strain field using DIC was captured every $0.5\ s$ during the test and compared with the numerical analysis to evaluate its accuracy and the strain distribution of the lap shear tests. The strain field analysis of the static test via digital image correlation has demonstrated an increase in the strain near the spot weld nugget precisely at the weld edge in the loading direction in the upper plate and the opposite site of the weld edge in the lower plate, as can be seen in Fig. 4.25. The same behaviour was observed in the strain field that was obtained by the numerical simulations. The coherence of the strain fields between the experimental data and the numerical analysis is evident.

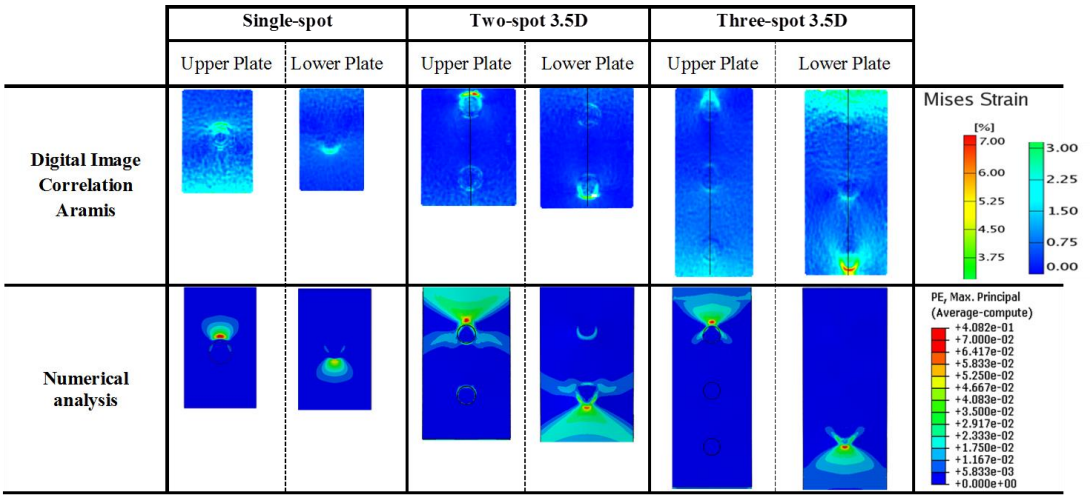

Figure 4.25. Comparison between the experimental digital image correlation and numerical analysis.

The stresses confirm the previously described behaviour, where it has increased predominantly near the SZ region, as demonstrated in Fig. 4.26. In addition, a progressive increase was detected in the stress concentration around the surface contact between the SZ and the upper and lower plates, as shown in Fig. 4.26B. At the boundary of the contact region between the SZ and the TMAZ, the stresses attained their highest levels near the rupture stress. A vertical cut (Fig. 4.26C) reveals that the stress levels decreased at the vicinity of the SZ. The lower plate was removed to provide a better visualisation, as shown in Fig. 4.26D. An annular high stress concentration formed in the upper plate, as previously mentioned, whereas the stress decreased to a minimum in the vicinity of the SZ. A compressive stress field was formed at the opposite side of the region with the highest stress levels. The same behaviour was observed when the upper plate was removed, as shown in Fig. 4.26E. High stress levels were formed on one side, and a compressive stress distribution occurred on the other side.

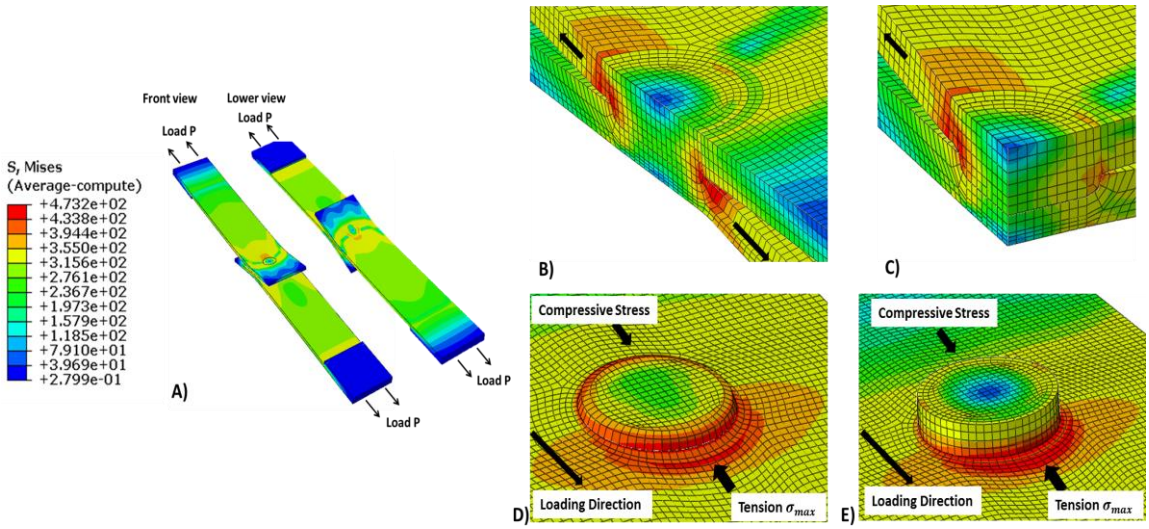

Figure 4.26. A) Stress distribution of a single-spot weld joint. Maximum stress distribution near the ultimate stress: B) In the contact region, C) Horizontal cut, D) The stress levels when the lower plate was removed and E) The stress levels when the upper plate was removed.

The stress distribution along the circumference of the spot weld or in the boundary edge between the SZ and TMAZ of the upper plate are investigated. Fig. 4.27A illustrates the spot weld top view in a cylindrical coordinate system, in which the centre of the weld is the centre point of the cylindrical coordinate system and the angle θ is orientated counterclockwise from the critical point A. Point A is the front of the spot weld that is aligned to the load path, where the stresses show high levels, and point C is the opposite site of point A. The stresses S_{11} correspond to the stresses in the load direction, and the stresses S_{22} and S_{33} correspond to the stresses perpendicular to the top surface and perpendicular to the load direction, respectively. Fig. 4.27B shows the main stress according to its direction as a function of θ based on the numerical model developed for a single-spot weld at two different load levels, as the stresses exhibited symmetry. From the angle $\theta = 0°$ to $180°$, the load corresponds to medium load levels, which comprise *50%* of the maximum load. From the angle $\theta = 180°$ to $360°$, the load corresponds to high load levels, where the ultimate von Misses stresses were attained.

As expected, S_{11} at point A ($\theta = 0°$) exhibited the highest stress which decreased to zero approximately at point B ($\theta = 90°$), and the S_{11} stress continues to decrease until the compressive stress at point C ($\theta = 180°$) is attained. When the load is increased, both the compressive stress and tensile stress are increased. Note that the compressive stresses are not as high as the tensile stresses. The S_{22} stresses at point A decrease to a minimum at point B after increasing at similar levels at point C. When the load is increased, the stresses at point C are lower than the stresses at point A. This behaviour indicates the influence of the secondary bending. S_{33} exhibits low levels even at high load levels. The results presented in Fig. 4.27 indicate that S_{11} is the dominant stress direction for a lap shear test. Note the levels of S_{22} should not be neglected.

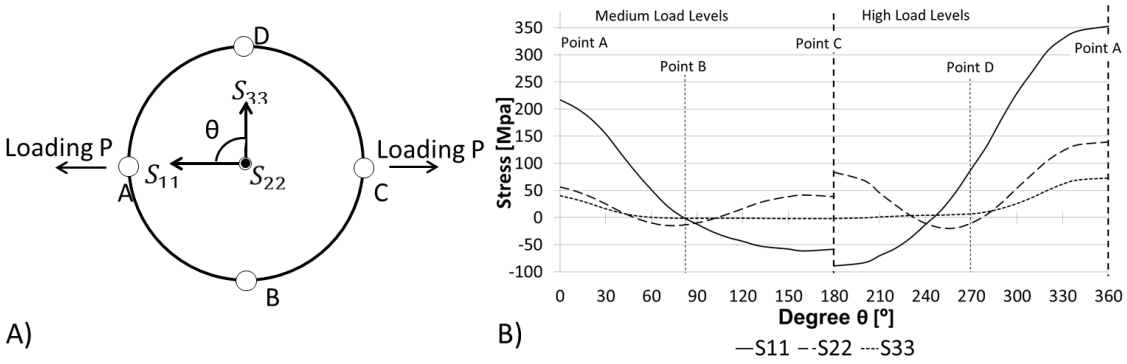

Figure 4.27. Main stress distribution along the circumference of the spot weld: A) Top view of the spot weld with the orientation θ; B) The main stresses for each stress direction as a function of θ.

The peak stress region decreases towards the free surface of the upper or lower plates; the peak stress in front of the spot weld has higher values than the values of the stress at the free surfaces, which is evidence of the secondary bending, as shown in Fig. 4.28A. A schematic cross-section stress distribution of the spot weld is shown in Fig. 4.28B. The zones where the tensile stress is demonstrated consider the bending on the plates.

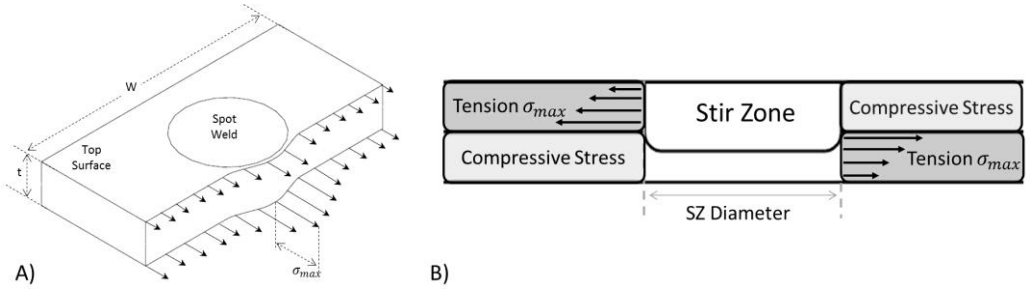

Figure 4.28. Schematic of the stress distribution on the longitudinal cross-section of a spot weld under shear loading. A) Peak stress location; B) Schematic representation of the secondary bending.

According to the literature, the major problem in riveted lap joints is the secondary bending associated with out-of-plane displacements. This bending occurs due to the asymmetric load path promoted by the geometrical eccentricities in the joint under nominal tensile stress. In addition, the consequences of the secondary bending have not received significant attention in the literature; although it significantly influences the fatigue life in a structure. The secondary bending amplifies the stress concentration at the root of the spot weld. To obtain the secondary bending stresses involved in the lap joint, the best approach should be the finite element model, which accounts for the nonlinearities of the joint. The local bending stress σ_b at the faying surface σ_{fay} can be determined from the faying and free surface σ_{free} stress components in the loading direction as

$$\sigma_b = \frac{\sigma_{fay} - \sigma_{free}}{2} \qquad \text{Equation (4.4)}$$

The through the thickness stress analyses from the computational models is a combination of the membrane stress and the applied loading [1]. For the design and structural analysis of lap joints, the bending stresses involved in the joint and how they can be reduced should be understood. As thinner sheets imply smaller eccentricities, and the number of rows and the

pitch distances in the rows directly affect the secondary bending as longer lap joints cause smaller out-of-plane displacement. A comprehensive study of the secondary bending effects are discussed in section 4.5.3, where the number of spot weld rows and the pitch distances are optimised.

For a lap joint with more than one spot weld row, the maximum bending stress occurs at the outer rows, as shown in Fig. 4.29A and B and confirmed by the previously discussed strain distribution. As expected, the stress distribution for multiple-spot weld rows is similar to the stress distribution of a single-spot weld. For three-spot weld rows, the middle spot weld does not experience as much stress and strain as the outer spot weld rows, which indicates that the majority of the load is transmitted by the outer spot welds. The stresses in their counter plates were similar, which signifies that the transmitted loads in the first and last spot welds were similar.

The importance of defining the location of the maximum stress warrants a detailed definition of the joint load distribution. Some plastic deformation in front of the spot weld nugget can occur due to high stress concentration with an inhomogeneous stress distribution through the thickness. The maximum stress σ_{max} due to secondary bending is originated at the faying surface, as shown in Fig. 4.29C, at Point A of the upper plate and Point B of lower plate. As the outer spot welds carries a greater applied load and Points A and B are locations of the maximum tensile stress combined with bending stress; therefore, this location is the most likely location for crack initiation.

Based on the results and the analyses, the global deformation in a single-spot weld during loading can be schematically illustrated, as shown in Fig. 4.30. In the first stage, the load level is low and the load is primarily transferred by friction between the plates. In the second stage, when the bonding ligament around the spot weld nugget is broken, the plastic deformation and secondary bending is initiated, and the overlap area is slightly rotated from its initial position. In the third stage, an increase in secondary bending induces separation of the upper and lower plates. At this point, stretching and necking occurs in the region of the annular spot weld region. A crack is initiated and propagated due to severe plastic deformation around the nugget and high stress levels.

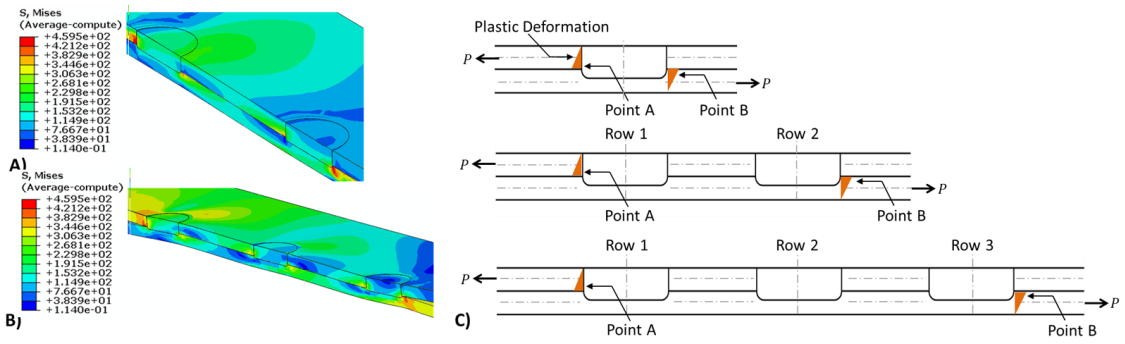

Figure 4.29. A) Stresses for double-spot weld row; B) Stresses for triple-spot weld row; C) Most probable locations for crack initiation.

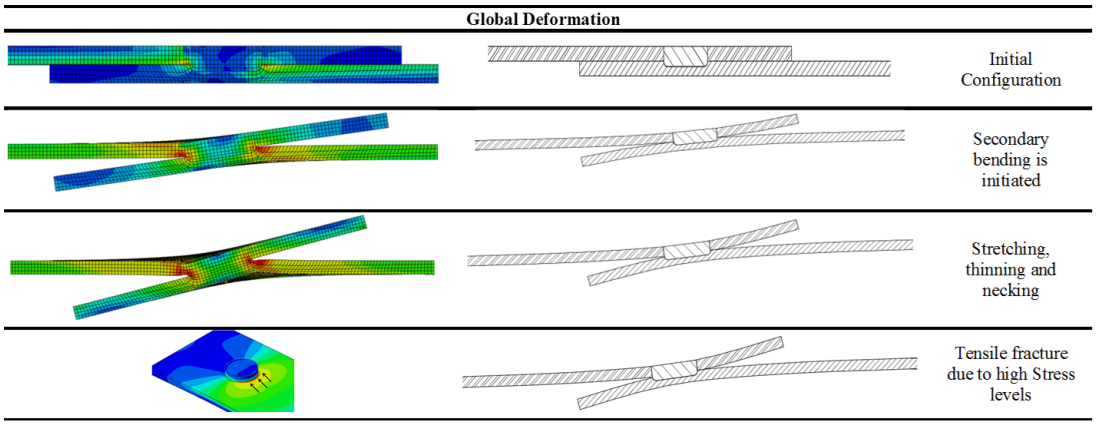

Figure 4.30. Global deformation of single-spot weld during loading.

4.5.2. Distance of the spot weld from the Sheet Edge, Se

As previously mentioned, in the case of riveting, when the minimum distance of the sheet edge is obtained longer *Se* has presented an insignificant influence on fatigue strength. Thus, the minimum distance *Se* must be established; it is investigated in a single-spot weld row with different widths under fatigue loading. In addition, all geometries are analysed at the same load levels. The static tests have revealed minimal influence of the *Se*; according to the standard for resistance spot weld ISO 14273 [102], the samples can be prepared with low width considering a decrease of 10% in the ultimate lap shear strength. The same behaviour was observed in refill FSSW lap joints. Table 4.6 describes the tested geometries: a small width is recommended by Airbus Company for refill FSSW [99], after the width progressively increases until the width recommended for RSW by ISO 14324 standard is attained [90]. Three samples per load level and four load levels were considered in the fatigue test.

Table 4.6. Dimensions considered for determination of the *Se* distance.

Sample	***Se* distances**	**Loading**
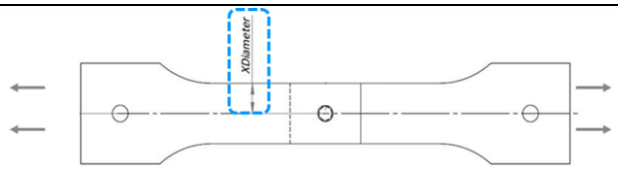	$Se = 1.5d(13.5mm)$Airbus	$O_v = 45mm$ $R = 0.1$ $f_r = 10Hz$
	$Se = 2d\ (18\ mm)$	
	$Se = 2.5d\ (22.5\ mm)$	
	$Se = 3d\ (27\ mm)$	
	$Se = 30\ mm$ – ISO 14324	

The stress analyses revealed that the maximum local stress in front of the spot weld increases with a decrease in width. The initiation of a fatigue crack in a structure generally occurs at geometrical features due to local stress concentration. For this reason, the stress concentration has to be analysed, where it is defined as the ratio of the maximum local stress in points A or B and the nominal applied stress according to the following equation.

$$K_t = \frac{\sigma_{max}}{\sigma_{nominal}} = \frac{S_{max}^{local}}{\sigma_{nominal}} \qquad \text{Equation 4.5}$$

where σ_{max} is the maximum stress, $\sigma_{nominal}$ is obtained by the reference gross area and S_{max}^{local} is the local maximum stress.

Fig. 4.31 presents the stress concentration for the previously described geometries. As this curve indicates, the stress concentration presents a constant value at a ratio of 0.175 and 0.22. The fatigue curve in terms of $\%$ of the lap shear stregth is presented in Fig 4.32; the influence of the sheet edge on the fatigue strength is evident. This influence can be explained

by the combination of stress concentration and maximum stress, where K_t is low but the nominal stress is considerably high at a constant load amplitude and small width. Consequently, the peak stress is high as the stress ratio is constant and the amplitude stress is high. This influence decreases when the width increases until $Se = 3d$, which indicates that an increase in the width does not represent an increase in the fatigue life as the fatigue life is identical for $Se = 3d$ and $30mm$. Thus, the minimum distance of the spot weld from the sheet edge is $Se = 3d$.

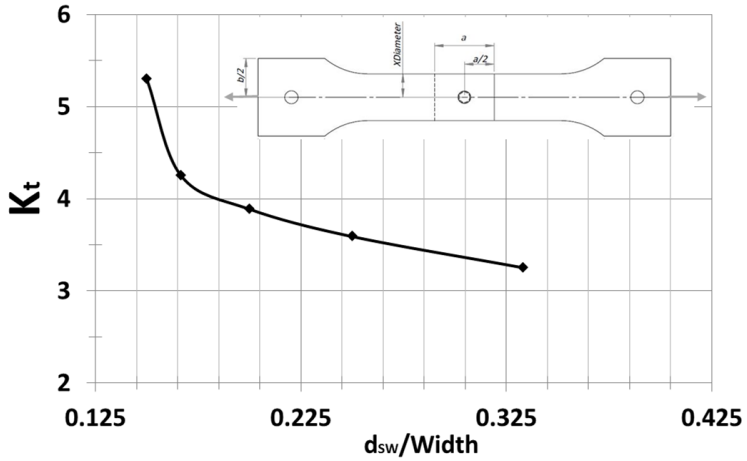

Figure 4.31. Stress concentration of refill FSSW.

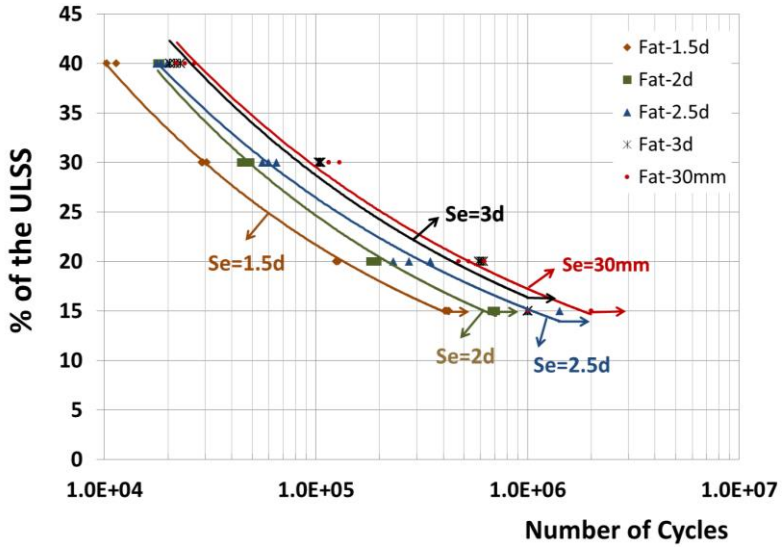

Figure 4.32. Fatigue life in lap joints with different Se.

4.5.3. Number of spot weld rows and pitch row distance optimisation

It is well known that fastener patterns directly affect the quasi-static and fatigue joint strength. The same behaviour is expected in refill FSSW spot weld joints. Consequently, the development of guidelines or minimum distances is essential to the application of the friction process in industrial structures to prevent fatigue problems and improve the joint efficiency. In this section, the influence of the number of spot welds and the spot weld rows distances are investigated. As they are strictly connected, the results are presented to address the quasi-static and fatigue strength. Afterwards, the results are investigated concerning stress concentration and secondary bending. According to Niu [51], the minimum spacing between each fastener row is $4d_{rivet}$, which is critical for tension (stress concentration) and joint

structural efficiency. Schijve et al. [2] emphasise that lap joints that are loaded in tension are subjected to bending due to the eccentricity, which amplifies the stress concentration of the rivet holes and the load transmission.

In aircraft structural design, the fatigue behaviour of a lap joint for practical application must be verified in realistic fatigue conditions, and the structural pattern should be considered. The simplest test for fastener and spot welds joints involves specimens with one spot weld in a row. The outcome of a round-robin exercise is intended to generate input data for static strength and fatigue strength. For lap joints with more than two spot weld rows, the maximum stress is always induced at the outer rows (Points A and B of Fig. 4.29C), and therefore, the most common crack initiation sites. To optimise the analyses and computational time, a parametric study is performed using the embedded models. Considering the embedded numerical model, several geometries were investigated. Table 4.7 presents the joint configuration that is employed for this analysis. All other spacing were kept constant, with the exception of the pitch distance and the overlap area.

Fig. 4.33 shows the results of the spacing optimisation under quasi-static loading. The *y*-axis represents the normalised lap shear force as a function of the maximum force from the geometry in the analysis ($29\ KN$), i.e., for double-spot welds, the strength of each lap joint is normalised with the highest strength obtained for this configuration: $p = 6d$. The *x*-axis represents the spot weld row distance in terms of the spot weld diameter d_{SW}. From the numerical simulation of the double- and triple-spot weld rows, the distance that yields 90% of the maximum load ranges between $3{-}3.5d_{SW}$. From these results, few geometries were selected to perform a quasi-static lap shear test and the simulation that considers the cohesive numerical model; small distance ($p = 2d_{SW}$), optimum/minimum ($p = 3{-}3.5d_{SW}$) and large distance ($p = 5d_{SW}$). The static tests confirmed the results of the numerical simulation, where the pitch distance of $3.5d_{SW}$ represents 90% of the maximum load. These results conclude that the minimum distance where the spot welds rows do not affect each other is $3.5d_{SW}$ for both cases. Although, fatigue tests in fasteners do not reveal benefits from applying more than three rivet rows. An attempt to understand the influence of the number of spot weld rows on the load transfer joints with four and five-spot weld rows were done as well. The results showed identical behavior where the minimum distance is $3.5d_{SW}$.

Table 4.7. Specimen properties for the round-robin exercise for number of spot weld rows and pitch row distance.

<table>
<tr><th colspan="4">Double-Spot weld row</th></tr>
<tr><td rowspan="2"> 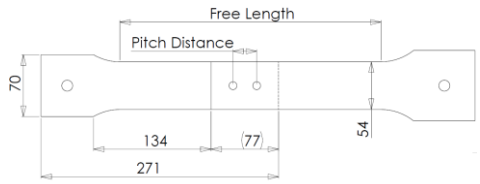
</td><td colspan="2">Sample Geometry</td><td rowspan="2">Fatigue Condition</td></tr>
<tr><td>Spot weld row spacing, p</td><td></td></tr>
<tr><td>$p = 2 - 6d$
increment of $0.5d_{SW}$</td><td>$Se = 3d_{SW}$
$e = 25\ mm$
$W = 54\ mm$
$B = 2\ mm$</td><td>$R = 0.1$
$f = 10Hz$</td></tr>
<tr><th colspan="4">Triple-Spot weld row</th></tr>
<tr><td rowspan="2"> 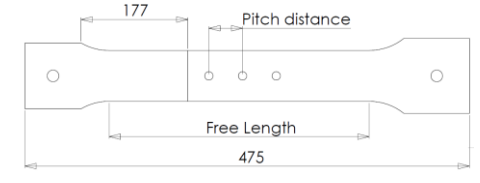
</td><td colspan="2">Sample Geometry</td><td rowspan="2">Fatigue Condition</td></tr>
<tr><td>Spot weld row spacing, p</td><td></td></tr>
<tr><td>$p = 2 - 6d_{SW}$
increment of $0.5d_{SW}$</td><td>$Se = 3d_{SW}$
$e = 25\ mm$
$W = 54\ mm$
$B = 2\ mm$</td><td>$R = 0.1$
$f = 10Hz$</td></tr>
</table>

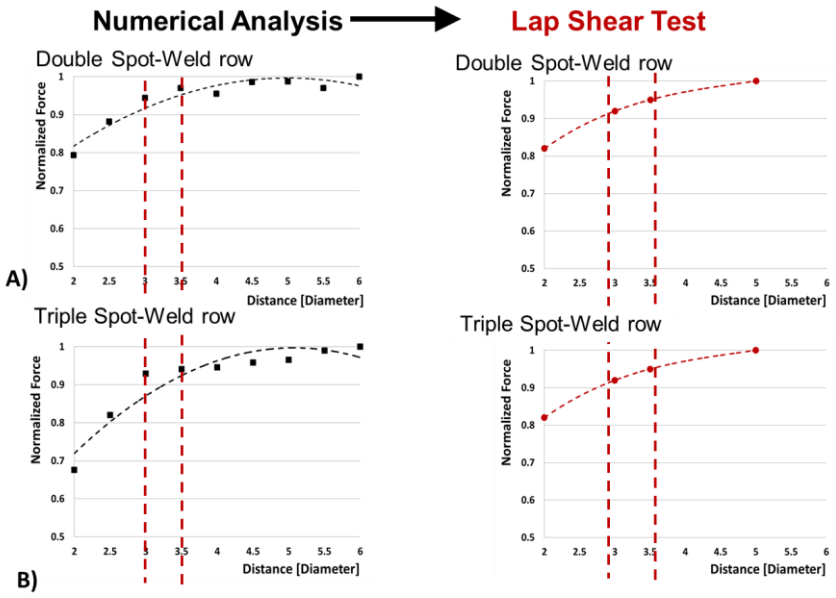

Figure 4.33. Pitch row distance optimisation. A) Double-spot weld; B) Triple-spot weld.

According to the pitch row distance optimisation, few joint configurations were selected to investigate the joint strength optimisation under fatigue loading. For a double-spot weld row, the selected pitch distances were $p = 3d_{SW}$ and $p = 3.5d_{SW}$. For a triple-spot weld row, the selected distances were $p = 3.5d_{SW}$ and $p = 4d_{SW}$. The distances were carefully chosen considering that both joint configurations would represent the same structural behaviour. Then, the optimum pitch distance from the quasi-static test is defined as the central point, and a lower pitch distance was selected in the case of double-spot weld rows and a longer distance was selected in the case of triple-spot weld rows. The fatigue strength results are presented in Fig. 4.34. First, an increase in the number of rows caused a significant increase in the fatigue strength. Second, a decrease in the pitch distance from $p = 3.5d_{SW}$ to $p = 3d_{SW}$ influenced the fatigue strength, namely, when the load levels are high, the difference in the fatigue strength can be significantly high. Last, an increase in the spot weld row distance from $p = 3.5d_{SW}$ to $p = 4d_{SW}$ did not influence the fatigue strength at any level of the test. A spot weld row distance that exceeds $p = 3.5d_{SW}$ has not represented a significant structural improvement, and the minimum distance can be established as $p = 3.5d_{SW}$.

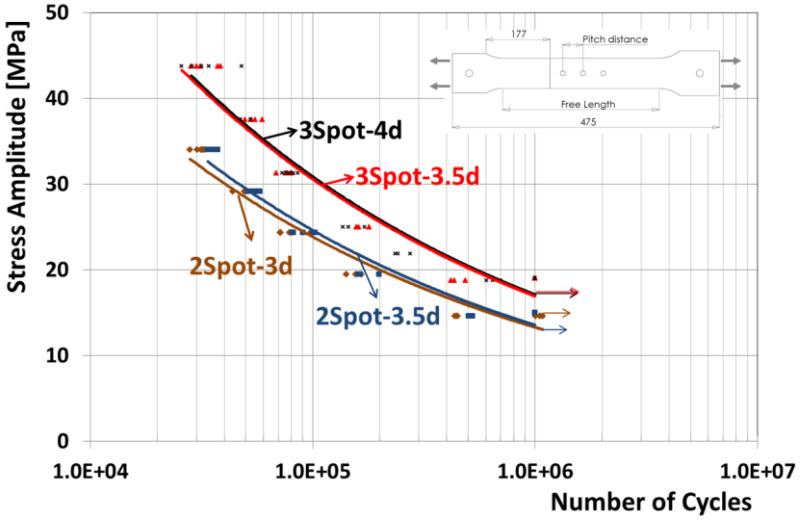

Figure 4.34. SN curves for double-spot weld row and triple-spot weld row.

Fig. 4.35 presents the lap shear test for the optimised samples in the single-, double- and triple spot weld row configurations; the maximum loads were $10.4\ kN$, $20.8\ kN$ and $27.4\ kN$, respectively. The observations from this curve reveals that the joint behaviour is almost linear. If, the number of spot weld rows increases from one row to two rows, the joint strength is twice the strength. However, this proportion is not valid when the number of rows increases from one row to three rows, which is probably related to the low transferred load by the middle row. The fatigue strength of the spot welded lap joint with a single row is poor, and the fatigue strength of two or more spot weld rows is significantly better, as shown in Fig. 4.36. Thus, single-spot weld rows should be avoided in structural applications or should be employed only in situations where additional rows are not possible. The secondary bending decreases with an increase in the overlap area, and when the load is transferred in more than one spot weld row. For riveting, Schijve et al. [2] suggested that a high fatigue strength is a consequence of a long overlap region. The fatigue tests have confirmed that a long distance in the rows of lap joints increases the fatigue life.

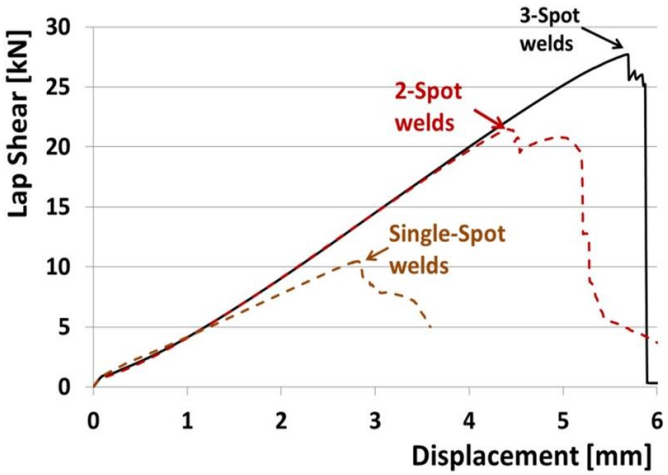

Figure 4.35. Lap shear test (force vs. displacement) for the optimised samples in single-, double- and triple-spot weld row configurations; the maximum loads were $10.4\ kN$, $20.8\ kN$ and $27.4\ kN$, respectively.

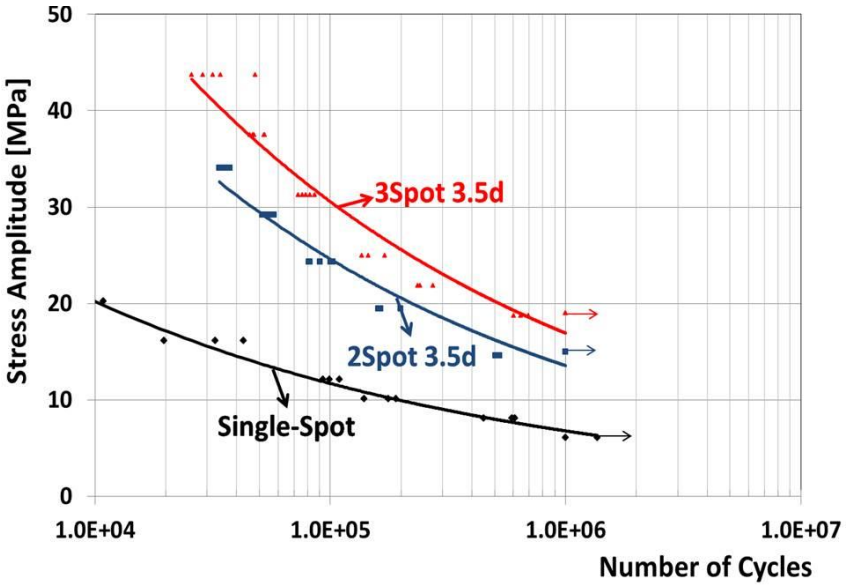

Figure 4.36. SN curve for single-, double-, and triple- spot weld rows.

The conventional design of fasteners and joints considers the stress concentration as the main initial point, which affects the structural integrity under static and fatigue loads. Therefore, an appropriate design methodology is the key to improving the fatigue performance. According to Niu [51], an appropriate detail design is the most important single factor that affects the fatigue life of a structural joint. Consequently, the designer must consider the engineering judgement stress analysis and fatigue experiment.

Fig. 4.37 shows the stress concentration (k_t) in terms of spot weld spacing and number of rows. For a single-spot weld row, the minimum k_t was considered in the results for edge distance. The single-spot weld row is the worst case, where the stresses have a high k_t; thus, single rows must be avoided. In addition, an increase in the number of rows causes a decrease in k_t. For large pitch distances, the stress concentration also decreases. In the design procedures for fasteners, all rivets are assumed to equally carry load; however, this hypothesis is not valid [2, 51, 107]. Similar to rivets, the load is primarily transferred in the outer spot weld rows, whereas the load transferred by the inner rows is rather small. Theoretically, if the transferred load by the outer rows is reduced, the fatigue life would have a significant enhancement. In addition, knowledge of the percentage transferred by each spot weld row can assist in the prediction of the fatigue life. The load distribution was estimated via a cohesive numerical model, and the load was approximately calculated from the measurement of the bypass loads. Fig. 4.38 illustrates the spot weld load distributions, which can be used as a guideline for design. Double-spot weld rows have the most efficient load transfer as half the load is transferred by each spot weld in all cases. For more than two spot weld rows, an increase in the pitch distance causes a decrease in the difference in the load distribution, and a uniform load is transferred. This finding explains the difference of k_t with dissimilar pitch distances. Note that does not matter the distance of spot weld rows, the outer spot weld rows will always carry more load than the inner rows.

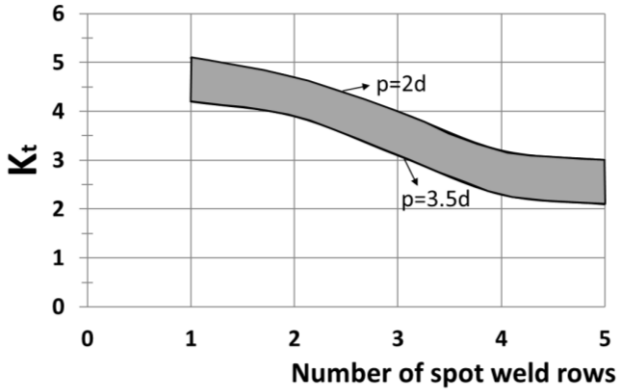

Figure 4.37. Stress concentration for multiple-spot weld rows.

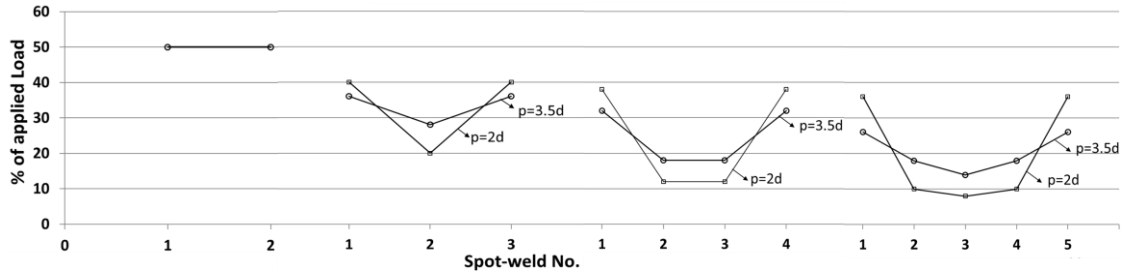

Figure 4.38. Load transferred by each spot weld row.

Many authors have suggested that secondary bending is a major problem in lap joints [53, 95, 107]. Secondary bending is a consequence of the load path asymmetry in a lap joint under tensile load, which is associated with an out-of-plane displacement. Secondary bending significantly amplifies the stress concentration at the root of the spot weld; therefore, it is unfavourable to fatigue strength. In the case of riveting, Ekh et al. [95] demonstrated that the secondary bending is highly dependent on the thickness of the plates and the length of the overlap area.

According to this approach, the stress in the weld can be divided into the stress caused by the spot weld loads and the secondary bending stress. Schijve et al. [107] indicate an interesting approach to compare the bending stress with the nominal/reference tensile stress that considers $\sigma_{tension} = P/(W.B)$, where P is the load applied to the sample, W is the width and B is the thickness. The bending factor is defined as

$$k_b = \frac{S_{faying}}{\sigma} \qquad \text{Equation (4.6)}$$

where the S_{faying} is the peak stress at the root of the spot weld in the faying surface of the joint. Thus, $S_{faying} = \sigma_{bending} + \sigma$. Table 4.8 illustrates the effect of the spot weld row spacing on the bending factor k_b. An increase in the row distance, causes a decrease in k_b, which is beneficial to the fatigue strength; thus, small row distances must be avoided. This might be the reason for the high fatigue strength of the lap joint when a larger overlap is adopted. A low k_b yields a shift to the right of the corresponding SN curve.

Table 4.8. Effect of row spacing on the bending factor.

SW spacing distance	2-SW	3-SW	4-SW	5-SW
$p = 2d_{SW}$	1.56	1.43	1.29	1.21
$p = 3d_{SW}$	1.37	1.29	1.19	1.14
$p = 3.5d_{SW}$	1.29	1.21	1.15	1.09
$p = 5d_{SW}$	1.23	1.1	1.09	1.05

4.5.4. Spot weld row in distance panel, S

An increase in the number of spot welds in a row is presumed to produce a more complex interaction and transfer load. This section explores this issue. In general, the rivet row in distance S is defined based on static strength calculations, and the minimum or optimum S depends on the type of rivet, which varies from $2.5 - 4d_{rivet}$ [94]. The stress distribution analysis of the panels provides more information than the stress concentration magnitude; in addition, the stress state enables the localisation of the crack initiation point and greater insight on fatigue performance. Table 4.9 presents the joint configurations that are used to obtain the optimum spot weld row in distance: Panel 2 x 2, Panel 2 x 3, Panel 3 x 3 and Panel 3 x 5. All other spacings were kept constant; the width of the panel varies with the distance in a row. In this optimisation study, the spot weld row in distance varies from $S = 2 - 6d_{SW}$.

Table 4.9. Specimen properties for the round-robin exercise.

Panel 2 x 2		
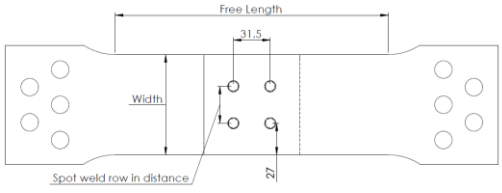	**Sample Geometry**	
	Spot weld row spacing, p	
	$S = 2 - 6d_{SW}$ increment of $0.5d_{SW}$	$Se = 3d_{SW}$ $e = 25\ mm$ $p = 3.5d_{SW}$ $(31.5\ mm)$ $B = 2\ mm$

Panel 2 x 3		
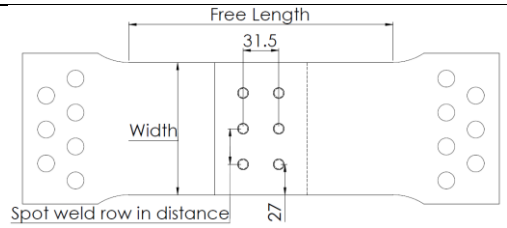	**Sample Geometry**	
	Spot weld row spacing, p	
	$S = 2 - 6d_{SW}$ increment of $0.5d_{SW}$	$Se = 3d_{SW}$ $e = 25\ mm$ $p = 3.5d_{SW}\ (54\ mm)$ $B = 2\ mm$
Panel 3 x 3		
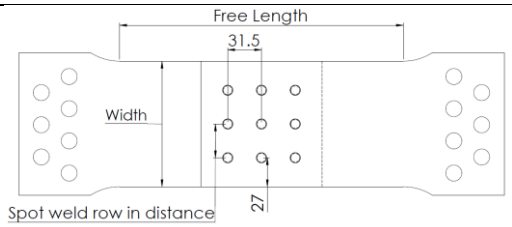	**Sample Geometry**	
	Spot weld row spacing, p	
	$S = 2 - 6d_{SW}$ increment of $0.5d_{SW}$	$Se = 3d_{SW}$ $e = 25\ mm$ $p = 3.5d_{SW}\ (54\ mm)$ $B = 2\ mm$
Panel 3 x 5		
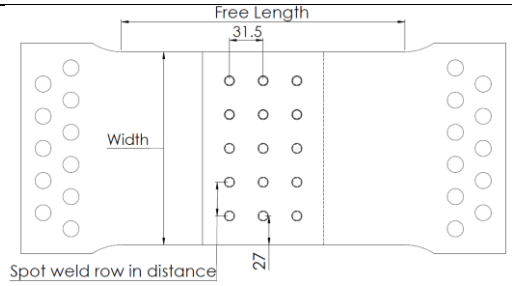	**Sample Geometry**	
	Spot weld row spacing, p	
	$S = 2 - 6d_{SW}$ increment of $0.5d_{SW}$	$Se = 3d_{SW}$ $e = 25\ mm$ $p = 3.5d_{SW}\ (54\ mm)$ $B = 2\ mm$

A strategy that is similar to the strategy applied to optimise the spot weld row distance was deployed in this case, as detailed in Appendix D. From the embedded numerical model, all geometries have demonstrated similar structural behaviours, where the optimised distance varies from $3.5 - 4d_{SW}$. This distance represents 90% of the maximum load for each geometry. Note that an increase in the distance S decreases the static strength of the panel joint. Vlieger [108] demonstrated via an experimental study that the rivet spacing in row has an optimum distance, where small and larger distances have demonstrated low fatigue strength. Afterwards, few geometries were chosen to perform the quasi-static lap shear test and the simulation using the cohesive numerical model: small distance ($S = 2d_{SW}$), optimum ($S = 3.5d_{SW}$) and large distance ($S = 5d_{SW}$). The static tests confirmed the results of the numerical simulation, where the pitch distance of $3.5d_{SW}$ represents 90% of the maximum load, as shown in Fig. 4.39A. Two main conclusions can be drawn: (i) an increase in the distance S the joint experiences an increase in the maximum load and (ii) further increases of this distance do not cause a significant increase in panel strength. Fig. 4.39B presents the stress analysis for Panel 3 x 5 [$3.5d_{SW}$] and the stress distribution through the width close to first spot weld. It can be seen that the outer spot welds carries a significantly greater load than the loads of the inner spot welds. This behaviour is well-known and is primarily attributed to the relative displacement of the spot welds. The outer spot welds are displaced from the anti-symmetry plane due to their large distance from the plane compared with the distance of the inner spot welds, which is reflected in the distribution of load between two spot welds.

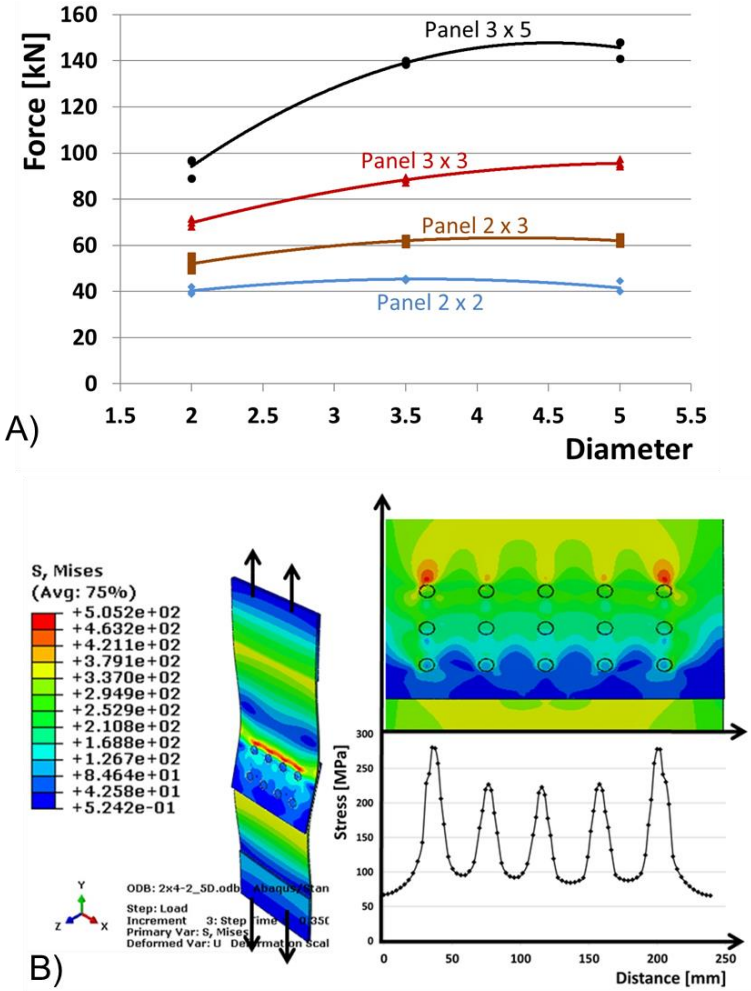

Figure 4.39. A) Quasi-static lap shear tests; B) Stress distribution in the width of the panel.

The DIC analysis confirms the hypothesis above described, Fig. 4.40A displays the lap shear strength curve for Panels 3 x 5 [$p = 2d_{SW}$] and [$p = 3.5d_{SW}$], and Fig. 4.40B and C displays the respective DIC. The outer spot welds experiences a higher load than the loads of the inner spot welds. For this reason, as the applied load increases, the outer spot welds start yielding and failure may start in this location. It may also be observed that in smaller distances the spot welds interact with each other, the strain is significantly high and sudden failure of the joint occurs rather than the progressive failure of the joint. These results conclude that the optimum distance where the spot welds rows do not affect each other is $3.5d_{SW}$ in all cases.

4.5.5. Joint structural efficiency or integrity of the joint

A perfect joint can be designed with substantial weight and production costs. Thus, a compromise among the joint integrity, weight and cost must be achieved to produce an efficient joint, which is referred to as overall joint structural efficiency. According to Niu [51], it is considered good practice to balance the design limitations on sheet width and length (manufacturing consideration) with safety consideration.

From the lap shear test in multiple-spot welds, the experimental observations reveal four typical failure modes, as shown in Fig. 4.41. Tension failure (Fig. 4.41A) occurs where a crack originates close to a spot weld nugget and propagates through the width. Shear failure (Fig. 4.41B) occurs due to poor weld quality. In Plug Pull-Out failure mode (Lower or Upper plate

failure, Fig. 4.41C and D, respectively); as already described, the crack is originated close to the spot weld and propagates circumferentially to the nugget and through the thickness.

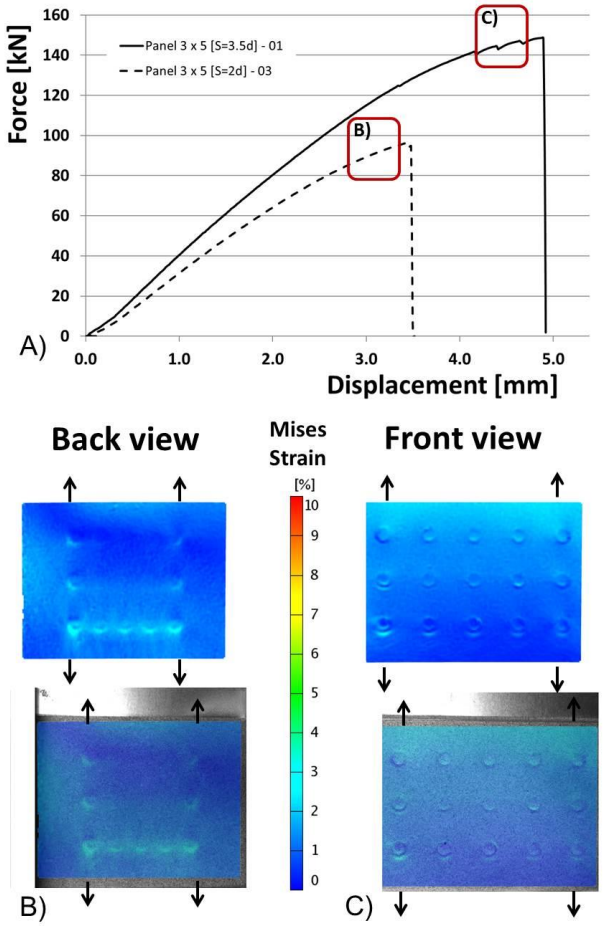

Figure 4.40. A) Lap shear test for Panel 3 x 5 B) DIC evaluation of the Panel 3 x 5 [$p=2d_{SW}$]; C) DIC evaluation of the Panel 3 x 5 [$p=3.5d_{SW}$].

The experimental investigation has confirmed that the highest mechanical strength is associated with the tension failure mode, whereas. The lowest mechanical strengths were observed in plug pull-out failure mode. Likewise, in rivets, the integrity of a joint is connected to the failure modes, where two typical failure modes can be correlated to the refill FSSW: tension failure and bearing failure; pull through [51]. The tension failure mode presents similarities to refill FSSW, where the fracture occurs through the width of the plate and produces higher mechanical loads. The second failure mode, in a manner similar to PPO, the lower or upper plate is pulled without the failure of the rivet or spot weld.

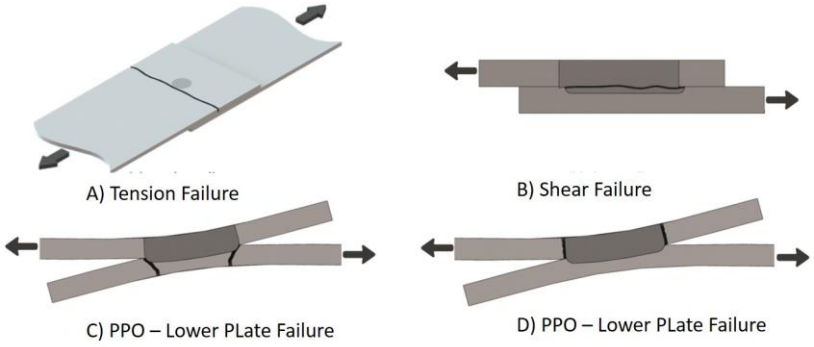

Figure 4.41. Typical failure modes of a splice refill FSSW Joint.

The joint structural efficiency diagram provides information regarding the mechanical strength of the joint in terms of diameter and width—the d/W ratio—and relates to the joint integrity (failure modes) [109]. For low d/W ratios, the PPO/Pull through failure mode is expected, and tension failure is expected for high ratios. In a similar manner, the concept of structural efficiency is proposed for refill FSSW considering the experimental results from the quasi-static tests. The diagram is constructed in terms of the spot weld diameter and width of the plate for multiple-spot weld rows only. The structural efficiency of the lap joint E_{fSpot} represents the mechanical strength of the base material

$$E_{fSpot} = \frac{F_{max}}{\sigma_{uts}.W.B} \qquad \text{Equation (4.7)}$$

where F_{max} is the maximum load force of the lap shear test, W is the width, B is the thickness and σ_{uts} is the ultimate strength of the base material. From the lap shear test, F_{max} and the failure mode are obtained. The σ_{uts} is obtained from the tensile test and has a value of $450\ MPa$. The mechanical strength of the plate, in terms of the tension failure, is considered as a plate with a hole, where the efficiency E_{fhole} is defined as

$$E_{fhole} = \frac{\sigma_{max}}{\sigma_{uts}}\left(1 - \frac{d_{hole}}{W}\right) \qquad \text{Equation (4.8)}$$

The representative failure tension is calculated by Eq. 4.7. When $d_{hole}/W = 0$, no hole exists, and when $d_{hole}/W = 1$, no material is present to carry any load. The tension failure for refill FSSW is considered to be a plate without any defect, as defined in Eq. 4.8. Fig. 4.42 presents the joint structural efficiency of a lap joint with a thickness of 2 mm in AA2024-T3 produced by refill FSSW. This diagram indicates the mechanical strength in terms of the d_{SW}/W ratios and the probable failure mode; the triple-spot weld rows—PPO—and double-spot weld rows—PPO lines. The most likely failure mode is Plug Pull-out. In the case of tension failure, the joint efficiency ranges between $60 - 70\%$ of the base material. For the PPO failure mode, the efficiency is approximately 50%.

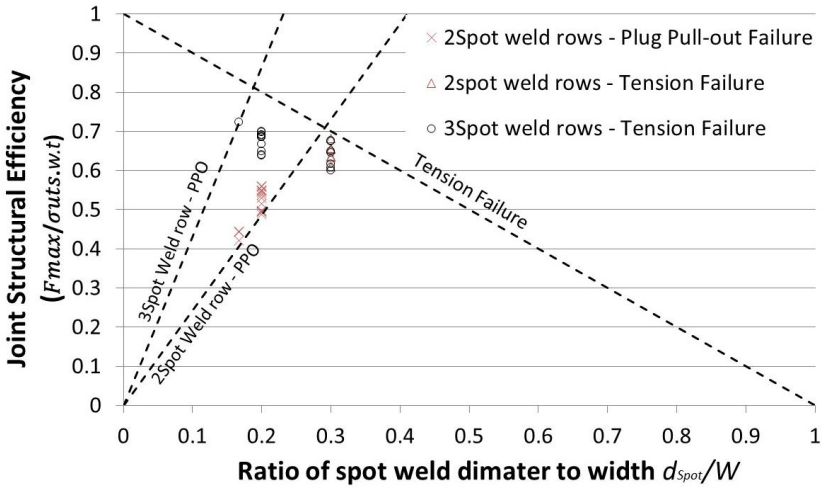

Figure 4.42. Structural efficiency of the lap joint refill FSSW Joint.

4.5.6. Friction forces

In rivets, it has been recognized that friction at the faying surface accounts for some of the transfer load through the joint. The load transfer by friction has a dual effect on the fatigue life: it has the favourable effect of decreases the bearing force but has the unfavourable effect

of causing fretting damage corrosion; this damaging process is known to generate microcracks in a surface under fatigue loading [97]. To determine the amount of the load transferred by friction (T_{fr}), several authors have proposed different techniques to directly or indirectly measure T_{fr} from the quasi-static lap shear test, i.e., instrumented fasteners are equipped with rosette strain gauges to record the shear stress. In addition, several investigations of the influence of the squeeze force on the friction between two mating sheets for riveted lap joints have been published [110]. Although the efforts in this direction have produced interesting results, the T_{fr}-values have exhibited significant scatter.

The detailed FE model that was developed in this section is capable of predicting the individual influence of the fastener in complex geometries. The spot weld diameter, position, pattern, bonding ligament near a spot weld and friction surface of the upper and lower plates were considered. Establishing a concrete relationship between T_{fr} and the total load P would be audacious. Therefore, it is of interest to investigate the general information or general trends of T_{fr} for this purpose, a cohesive model with a double-spot weld row and a friction coefficient (μ_{fr}) that varies between 0.2, 0.4 and 0.6 was considered.

Fig. 4.43 presents the contact pressure along the path at the faying surface under a remote tensile pressure of $100MPa$. The maximum contact pressure on the faying surface occurs at the stir zone boundary and rapidly increases and decreases. Although the shape of the contact pressure does not change with the friction coefficient, its peak values increases when the friction coefficient increases.

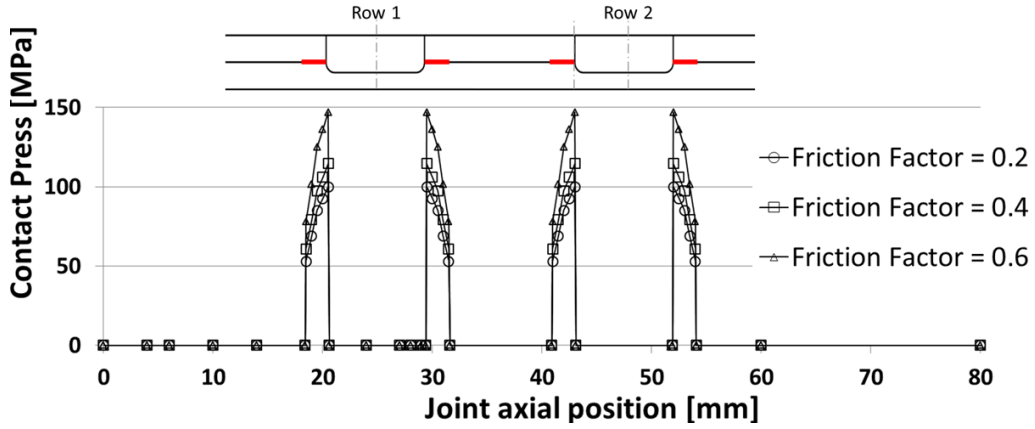

Figure 4.43. Effect of friction coefficients on contact stress distribution on the faying surface.

Local changes in the contact areas may cause relative motion. As shown in Fig. 4.44 and indicated by the numerical analysis, a smaller region of contact exists between two mating sheets at the faying surface beneath the spot weld nugget. The load transferred by friction is concentrated in this region, which is reflected in the slight slip motion and exemplified by the shear stress at the faying surface where the maximum shear stress occurs near the nugget. This region is significantly smaller than the radius of the spot weld nugget. Although the SEM analysis and fractography do not reveal any evidence of the fretting damage initiation in this region, it is the most likely location for fretting damage initiation, and therefore, where microcracks should form.

An attempt to obtain the friction load was proposed considering that the external tensile load is transferred between two plates through the spot weld and a number of contact surfaces,

each of which contributes to fulfil the force equilibrium. As defined by Eq. 4.9, the load transmitted by friction (T_{fr}) and the load transmitted by the spot weld (T_{Str}) must be equal to the external load. Then, the load transmitted by each spot weld was obtained from the reaction force of the node. Afterwards, this force was used to obtain the friction force to establish the force equilibrium.

$$\sum T_{fr} + T_{Str} + P = 0 \qquad \text{Equation (4.9)}$$

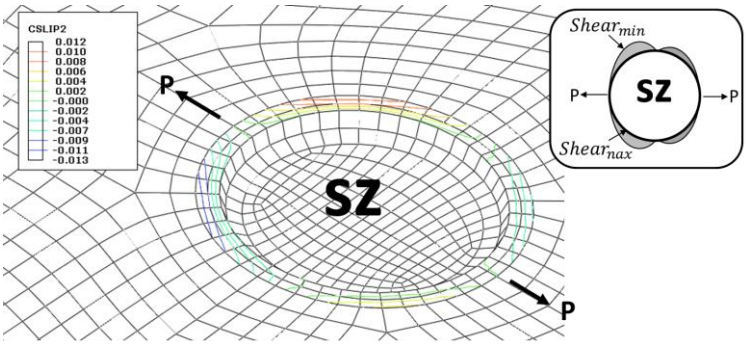

Figure 4.44. Slip motion at the faying surface beneath the spot weld nugget, and detail of the shear stress.

As shown in Fig 4.45A, T_{fr} is presented as a percentage considering the external applied load. All friction coefficients presented similar behaviours. When the level of the applied load is low, the friction is primarily localised in the spot weld vicinity, and the transferred load (T_{tr}) is dominated by friction ($60 - 50\%$) due to the bonding mechanism Stage A. No relative motion occurs between the contact surfaces in this stage, which defines the stick condition of the contact. At one point when the load overcomes the maximum force and the bonding mechanism is extinguished, the surfaces present a relative motion, the plates begin to slide relative to each other (Stage B) and the secondary bending start to act. Obtaining the friction force is difficult at this time. Once sliding has initiated, the load transferred by friction between the plates remains constant despite additional increases in the applied load ($35 - 17\%$). Fig. 4.45B presents the same simulation after a couple of cycles. In this case, the bonding mechanism does not acts in the vicinity of the spot weld. When the load applied to the joint is low, the friction force may be relevant ($40 - 27\%$). At some point, when the load is increased, the friction is fully developed and the plates start to slide relative to each other. Once sliding has started, the load transferred by friction between two plates remains constant during further increase of the applied load ($30 - 17\%$).

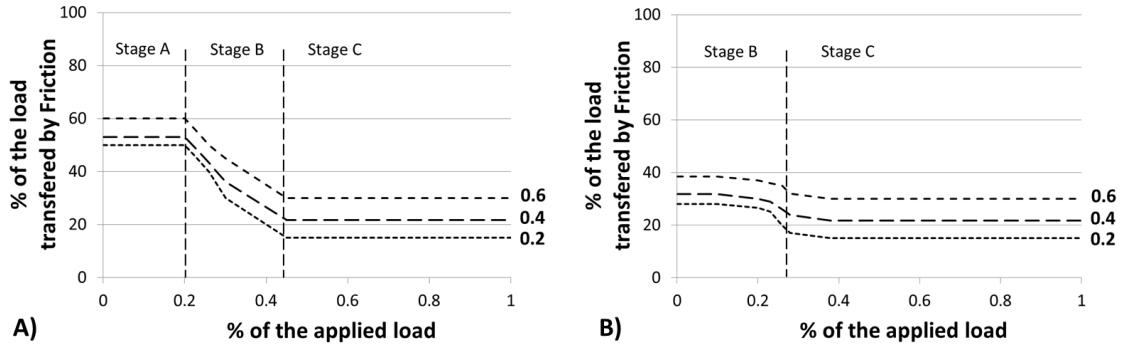

Figure 4.45. Percentage of the load transferred by friction. A) First cycle; B) After a couple of cycles.

4.6. Concluding remarks

Although single-spot weld rows present poor fatigue strength and should be avoided, uniaxial tests on small specimens are useful to derive the key design curves in terms of load vs. displacement. One typical flaw observed in the characterisation of the spot weld was the lack of refill; it is present at the interface between the SZ and the TMAZ, at which the outer surface of the sleeve penetrates the plates; with appropriate weld parameters, this flaw is not present anymore in the spot weld. In addition, the hook profile influences the failure load properties in high-mechanical-strength welds; the main geometrical feature is the hook tip curvature. Of all the fracture modes, the crack initiated at the hook tip.

Altogether, the structural integrity of the spot weld lap joint evidence a complex local stress state under tensile loading. The structural integrity is attributed to the transfer load from the upper plate to the lower plate, secondary bending, stress concentration, bonding ligament and friction between two plates. An external longitudinal tension load was transferred between two plates through a number of contact surfaces, each of which contributed to fulfil the force equilibrium.

The distance from the sheet edge has a sensible effect on the fatigue life; where a minimum distance has to be observed, increasing the sheet edge distance does not produce better fatigue properties. Multiple-spot weld rows improve the fatigue strength of the joint. In general, large distances between rows imply high fatigue properties of the lap joints, which are primarily associated with a reduction of the secondary bending promoted by the eccentricity of the load path.

The distance of the spot weld in a row is based on the static strength. In this case, an optimum distance was developed, if the distance decreases, the structural integrity of the joint also decreases; when this distance increases, the integrity decreases. Table 4.10 summarises the minimum or optimum distances that were developed for a spot weld lap joint; in addition, typical minimum or optimum distances for rivets are also listed. It can be observed that the distances of spot weld and rivets are similar in all cases: sheet edge, row spacing and row distance.

Table 4.10. Comparison between refill FSSW and riveting of the minimum/optimised distances.

Fastener Diameter	Fastener d_{rivet}=6.35mm	Spot-Weld
Sheet Edge, Se	$2d_{rivet}$ $(12.7mm)$	$3d_{SW}$ $(31.5mm)$
Row spacing, p	$4d_{rivet}$ $(25.4mm)$	$3.5d_{SW}$ $(31.5mm)$
Row distance, S	$4d_{rivet}$ $(25.4mm)$	$3.5d_{SW}$ $(31.5mm)$

Concluding, a good design of the lap joint configuration may significantly improve the fatigue life, and it is the most important single factor that directly affects the structural integrity of a joint. The trade-off between increasing fatigue life and increasing cost depends on how critical an area is for fatigue. This section may help structural engineers in their critical evaluations of the best joint configuration in lap joints produced by spot welds.

Chapter 5.

Stress Intensity Factor

The main objective of this chapter is to obtain accurate Stress Intensity Factors (*K-factors*) for fatigue cracks in lap shear specimens that are loaded under remote stress, which produces a combination of tension and bending stresses. The combination of a tension case and a bending case is interesting considering the typical joint configuration in a pressurised aircraft fuselage. As observed in sections 2.2 and 2.3, the *K-factors* are essential to Damage Tolerance Philosophy to predict the crack growth and estimate the residual strength. If the stress intensity factors are not available in the literature, FE calculations should be considered.

In the literature, several *K-factors* solutions are presented for many crack geometries and load conditions, e.g., [111-113]. However, these solutions cannot be applied to integral joints produced by refill FSSW due to their complex geometry and boundary conditions. Thus, this section provides the *K-factors* solution to the skin for several joint configurations (different number of rows). The generation of the solutions is based on the finite element method via the eXtended FEM (XFEM).

In riveted structures, fatigue cracks are initiated at the edge of a hole as a part-through thickness crack, which subsequently becomes a through-thickness crack, which is also known as a through crack [49, 57]. However, in the case of refill FSSW under cyclic loads, a crack is initiated at the hook tip in front of the weld, where the peak stress was observed and circumferentially grows to this initial point and becomes a through crack. Consequently, the geometries of fatigue cracks and their propagation comprise a phenomenon that is analysed in this study.

In section 5.1, an experimental investigation of the fatigue crack initiation and propagation is performed followed by a discussion of the results. The crack geometries and crack propagation shapes are provided. The calculations of the *K-factors* with XFEM are discussed in section 5.2, where the numerical model is proposed and developed. In section 5.3, the results of the *K-factors* are presented, and the crack growth predictions are compared with the test results in section 5.4. The main findings of the chapter are summarised in section 5.5.

5.1. Experimental investigation

A systematic experimental investigation has been conducted to realise and document the crack initiation, crack growth and behaviour of a crack under the dominant load conditions of a pressurised large aircraft [53, 114, 115]. As previously mentioned, the eccentricity of the load path of a joint promotes the secondary bending, which is correlated to the out-of-plane displacement. Consequently, the remote stress is decomposed into a tension stress and a bending stress. These two load conditions dominate the crack initiation and growth. The reconstruction of the crack history is typically performed by a scanning electron microscopic and optical microscopic [93]. In this section, the different fracture modes observed during the lap shear fatigue experiments performed in Chapter 4 are investigated. Then, the crack initiation and propagation are explored, and the mechanism is identified under different load conditions via fracture surface analysis. Once the fracture modes observed in single-, double-

and triple-spot weld rows are identical, the fracture mechanism observed in a single-spot weld row is presented. Identical crack shapes and boundary conditions are applied in all geometries.

5.1.1. Crack initiation - Failure mode and fracture surface under high-cycle fatigue

Two different fracture modes were identified at loads of 40% of the ultimate lap shear strength or loads of lower strength: through the sheet – upper plate (TS-UP) and through the sheet – lower plate (TS-LP). Both fracture modes were observed at similar stress amplitudes and exhibited a similar fatigue life, as shown in Table B.1 and Table B.2. For the failure analysis, samples tested under the stress amplitude of $13.375\ MPa$ or 30% of the ultimate lap shear strength were employed.

For the TS-UP fracture mode, the crack propagated through the width of the upper plate perpendicular to the load direction, as demonstrated in Fig. 5.1A. After the fatigue test, the sample was aligned in a cross-sectioned manner to the load direction (Fig. 5.1B). The fractography revealed that the specimen failed along the dominant crack, which propagated from the hook at the interface of the upper and lower plates towards the top surface through the thickness. In a higher-magnification view of the hook, as presented in Fig. 5.1C, the crack appears to nucleate at the hook tip or near the hook tip. In addition to the dominant crack, a secondary crack is located on the opposite side (Fig. 5.1D); this crack occurs when the dominant crack is sufficiently large along the upper plate width. Consequently, the secondary bending increases and intensifies the stresses, which generates another crack. However, the crack growth rate of the secondary crack is lower than the crack growth rate of the dominant crack and has not contributed to the final failure [36].

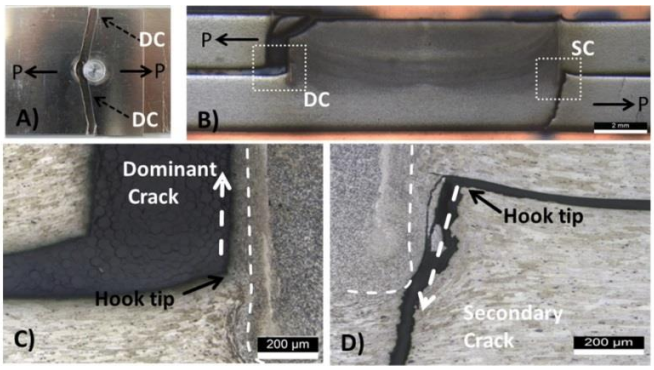

Figure 5.1. Crack propagation for TS-UP, specimen loaded at 13.375 MPa or 30% of the ULSS: A) Overview of the fracture; B) Cross-section of the spot weld shows the location of the dominant crack (DC) and secondary crack (SC); C) Magnified view of the hook interface and DC; and D) Magnified view of the hook interface and secondary crack.

Fig. 5.2 presents the fracture surface of the TS-UP fracture mode; the analysis was performed in the separated upper plate on the dominant crack side. Higher magnifications are highlighted in regions C-H. Region C is located at the interface between the upper plate and the lower plate, which is also referred to as the hook. This region is characterised by a smooth free surface. This characteristic illustrates the weak or non-bonding area of the hook interface [13]. Region D shows very pronounced fatigue striations that spread towards the upper surface near the hook interface. The perpendicular fatigue striation direction indicates that the origin of the fatigue crack is most likely located between region C and region D at the hook tip, which is consistent with the findings of a previous study [92]. Region E is located near the upper

surface. The fatigue striations are spread upwards, which indicates that the crack linearly propagated from Regions C and D to Region E. Signs of fatigue secondary cracks in Regions D and E are also observed. Regions F and G present a slightly altered direction of the crack propagation. The fatigue striations are spread upwards but are not perpendicular to the upper surface; instead, the striations indicate the circumferential progression from the crack origin, which characterises local stress changes and a complex internal structure of the joint [92]. Outside the spot weld (Region H), the fatigue striations are entirely longitudinal, which indicates that the crack propagated in the width direction. Next, the crack uniformly grew along the upper plate width.

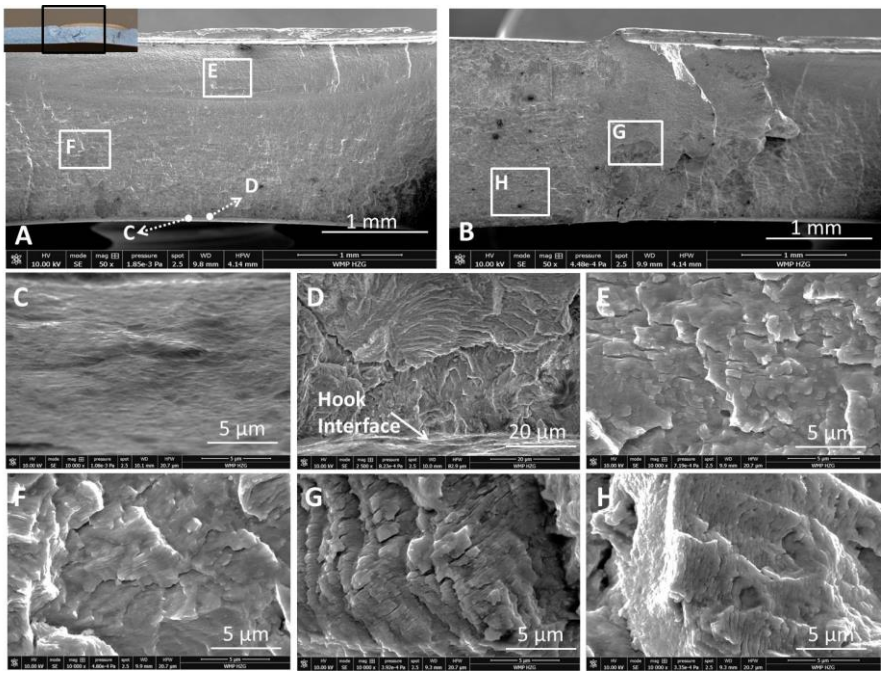

Figure 5.2. SEM of the TS-UP fracture mode and magnified regions C-H.

For the TS-LP fracture mode, the crack propagates along the lower plate width perpendicular to the load direction, as shown in Fig. 5.3A. Similar to the TS-UP fracture mode, the specimen was cross-sectioned in the load direction after the fatigue test. The specimen failed due to a dominant crack that propagates from the hook interface towards the lower free surface through the thickness (Fig. 5.3B). The magnified view of the hook tip (Fig. 5.3C) demonstrates that the dominant crack nucleates at the hook tip and follows its angle. On the opposite side, secondary cracks were observed (Fig. 5.3D). In this case, two fracture paths were identified: the first path is oriented parallel to the load direction in plane-shear, and the second path is oriented towards the upper plate. A similar behaviour was identified by Rao et al. [36] for FSSW; the authors suggested that secondary cracks do not contribute to the final failure as the crack growth rate is significantly low. Lanciotti and Polese [116] observed dominant and secondary crack phenomena in resistance spot welds via numerical analysis. The authors suggested that cracks in these regions may occur due to an increase in stress near the nugget on both sides.

Fig. 5.4 displays the fracture surface analysis of the TS-LP fracture mode. The study was performed in the separated lower plate on the dominant crack side. Highly magnified views are highlighted in Regions C-H. Region C shows a free and smooth surface, which is typical of the hook region. However, the first indications of fatigue striations are observed, as indicated

by the arrow. Regions D and E present very pronounced fatigue striations towards the lower free surface, which indicates that the fatigue crack origin is near the interface between the lower plate and the upper plate, which is similar to the TS-UP fracture mode. Near the lower surface—Region F—the fatigue striations are spread in many directions due to a change in the local stress state. However, the progression marks are primarily oriented towards the lower free surface, which indicates that the crack origin is linear to Regions C, D and F. Region G shows fatigue striations spread in many directions, predominantly downwards with a slightly circumferential slope to the crack origin. Region H is located outside the spot weld. The fatigue striations are oriented towards the width of the lower plate.

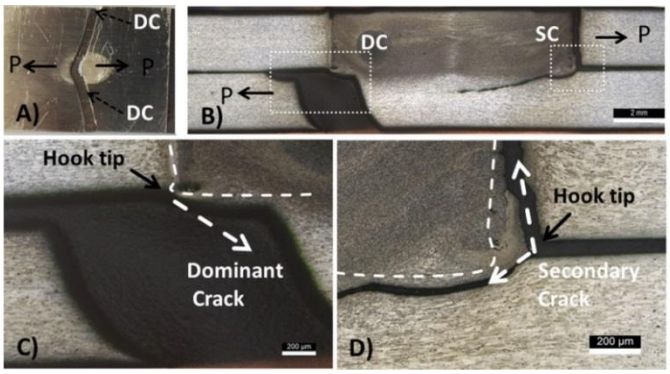

Figure 5.3. Crack propagation for TS-LP, specimen loaded at 13.375 MPa or 30% of the ULSS: A) Overview of the fracture; B) Cross-section of the spot weld shows the location of the dominant crack (DC) and secondary crack (SC); C) Magnified view of the hook interface and DC; D) Magnified view of the hook interface and secondary crack.

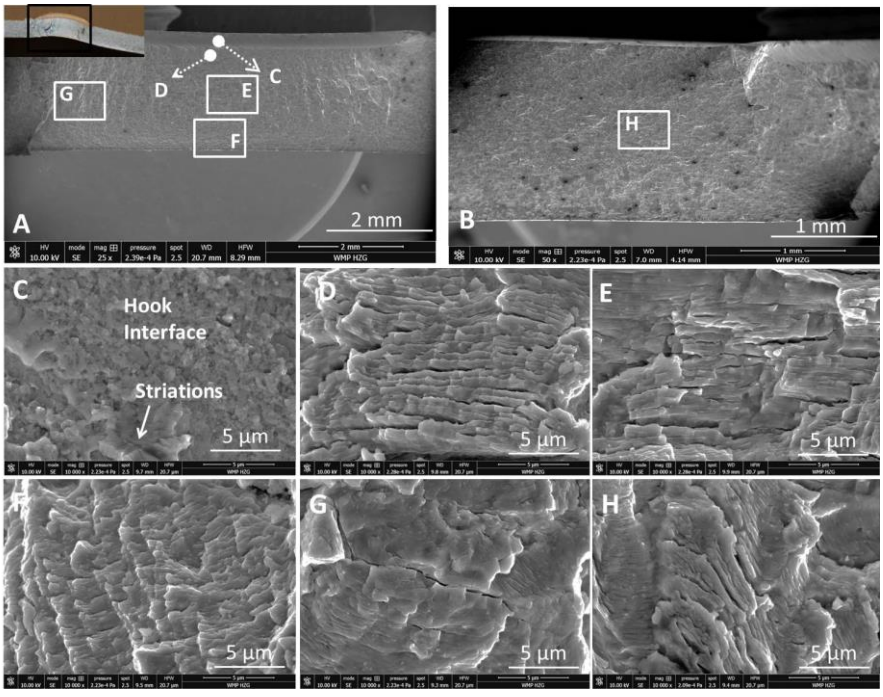

Figure 5.4. SEM of the TS-LP fracture mode and magnified regions C-H.

Additionally, an analysis of the fracture surface close to the left edge was performed. Both fracture modes present similar behaviours. Fig. 5.5 shows the TS-LP fracture mode. Fig. 5.5A presents a mixture of ductile dimples and fatigue striations longitudinal to the left edge of the material thickness, which signifies the transition region between fatigue failure and ductile

fracture. Closer to the edge, as shown in Fig. 5.5B, only ductile dimples are observed, which suggests a catastrophic failure due to sample overload.

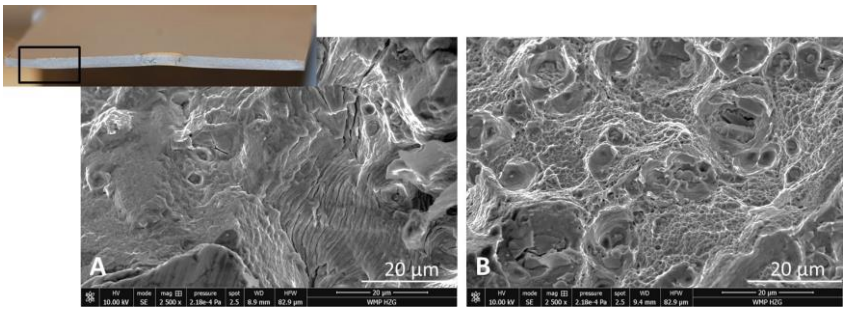

Figure 5.5. Fracture surface of the TS-Lower plate fracture mode close of the left edge A) Mixture of ductile dimples and fatigue striations; B) Closer to the edge only ductile dimples are observed.

The crack propagation was tracked from its origin until complete failure. In both cases—TS-UP (Fig. 5.6A) and TS-LP (Fig. 5.7B)—the dominant crack initiated at the hook tip. As observed in Chapter 4, the maximum stress concentration occurs in front of the weld aligned to the load plane, which promotes a triaxial state of stress at the hook tip. The crack propagates through the thickness, as indicated by the arrows and confirmed by the fracture surface analysis, where the fatigue striations near the hook region are oriented towards the faying surface. In addition, signs of fatigue striations were identified close to the hook tip. No ratchet marks were observed. A non-presence of multiple crack origins was identified. Subsequently, the crack slowly grew across the fatigue zone and circumferentially propagated to the crack origin as a result of the complex state of stress and complex internal grain structure [36]. In the case of a resistance spot weld [117] and friction stir spot weld [36, 118], the hook tip has been analysed as a stress intensity factor and acts at the crack origin, which affects the driving force of the crack initiation and crack propagation. Additionally, the shear loading promotes the secondary bending in the spot weld region, and the stress distribution amplifies the hook effect [36, 117, 118].

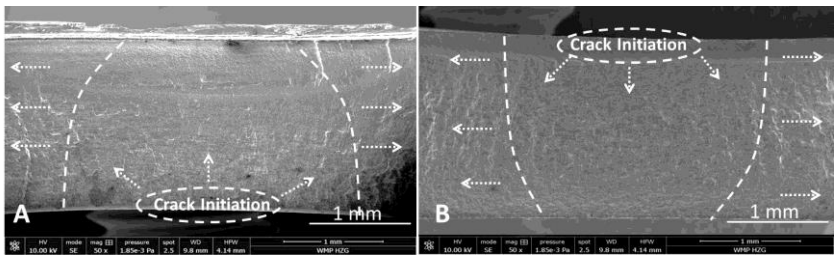

Figure 5.6. Crack initiation and propagation: A) TS-Upper plate and B) TS-lower plate.

5.1.2. Crack initiation - Failure mode and fracture surface under low-cycle fatigue

The fracture mode identified for low-cycle fatigue life was PPO, which was observed only in samples tested under a stress amplitude of $22.2\,MPa$ or 50% of the ultimate lap shear strength, as shown in Table B1 and B2. Fig. 5.7A presents the PPO fracture mode, where a crack is visible along the lower plate width, similar to the TS-LP fracture mode. However, the spot-weld was completely removed from the upper plate. After the fatigue test, the sample was cross-sectioned along the longitudinal plane, as shown in Fig. 5.7B. The fractography revealed that the spot weld failed as the dominating fatigue crack propagated from the hook tip through the sheet thickness towards the lower surface (Fig. 5.7D). Next, the crack

propagated along the lower plate width. Due to overstress and secondary bending, the crack propagated along the spot-weld circumference in a ductile failure mechanism and failed by PPO halfway across the lower plate (Fig. 5.7C).

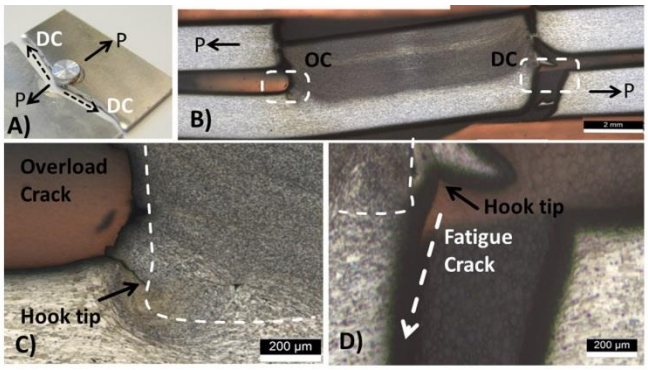

Figure 5.7. Crack propagation for PPO, specimen loaded at 22.22 MPa or 50% of the ULSS: A) overview of the fracture; B) Cross-section of the spot weld shows the location of the dominant crack (DC) and overload crack (OC); C) Magnified view of the hook interface and DC; D) Magnified view of the hook interface and OC.

Fig. 5.8A presents the PPO fracture mode and the highlighted Regions C-H. Fig. 5.8B schematically presents the crack initiation and propagation, which will be discussed during the text. The fracture surface and crack propagation of the PPO fracture mode exhibited some similarities compared with high-cycle fracture modes. Region C is located at the hook region and presents a free and smooth surface, which is characteristic of the interfacial hook region [13]. Close to the hook formation in the lower plate, progressive marks are very pronounced towards the lower free surface in Region D. As previously mentioned, such a characteristic of the fatigue striation indicates that the crack origin is near this region. Region E presents fatigue striations that are spread downwards in many directions, which indicates that the crack circumferentially propagates to the origin. Region F, which is located outside the spot weld region, shows longitudinal fatigue striations along the width direction of the lower plate. Regions G and H are located in the spot weld in the upper plate, and ductile dimples are observed in these regions. When the dominant crack length increases, the shear stress in the remaining spot-weld area increases until the crack length attains a critical size, where the remaining cross-section cannot sustain the shear overstress and the joint catastrophically fails around the spot weld.

5.1.3. Crack propagation mechanism

From the point of view of aircraft structures and damage tolerance philosophy, the knowledge of crack propagation is essential for understanding the joint integrity. Based on the results, the crack initiation and propagation can be described. As previously mentioned, three different fracture modes exist: TS-UP, TS-LP for high-cycle fatigue life and PPO for low-cycle fatigue life.

In all observed fracture modes, a crack initiates in front of the joint at the hook tip or at the interface between the upper sheet and the lower sheet. As mentioned in Chapter 4, the crack likely nucleates in front of the spot weld at the location in the joint that is subjected to high stresses and strains.

For refill FSSW, after nucleation, the crack grows and adjusts its shape to a circumferential crack. Fig. 5.9A schematically represents the crack growing history from an initial point to a

through the thickness crack, as demonstrated by dashed lines 1 to 4. Determining the crack shape parameter h/b for lap-shear specimens can be difficult when the cracks do not have a perfect elliptical crack shape. The crack shape is attributed to the effect of the plane stress at the crack tip, which causes local plasticity, and the crack closure effect is presented. In addition, the bending stresses distribution through the thickness creates a higher stress at the faying surface. As a result, the crack front will lag behind the lower surface [57].

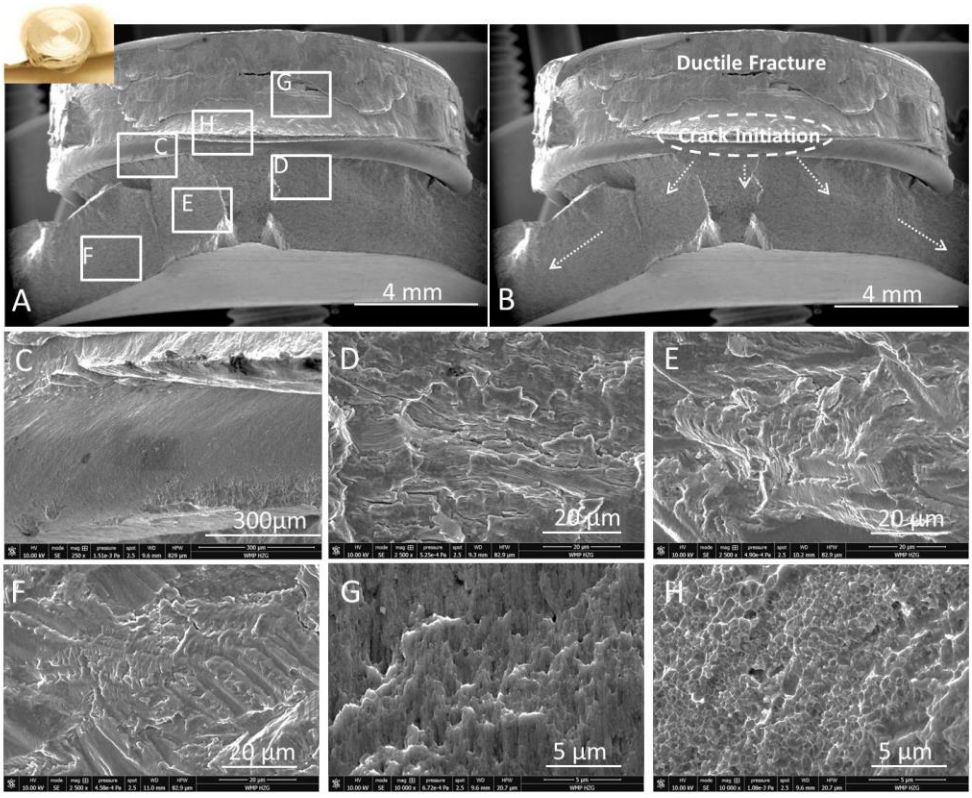

Figure 5.8. SEM of the PPO fracture mode and magnified regions C-H.

At this point, the bending factor defined in Eq. 4.6 becomes even more important. When k_b is considerably larger than one, the bending stress at the faying surface amplifies the effect of the crack at the faying surface; consequently, the crack growth along this surface becomes problematic. This finding explains the poor fatigue strength in a single-spot weld. The bending factor of refill FSSW in lap-splice joints is slightly higher than one, and it may be expected that the crack becomes detectable by visual inspection at the outer surfaces of the joint [6, 53, 57].

Via an extensive fractography study, de Rijck [57] demonstrated that the elliptical crack shape is $h/b \approx 1$ and remains fairly constant during its propagation when the crack becomes visually detectable at the outer surface. Aided by a travelling optical microscopic and a ruler coupled to the microscope, the *in situ* observation during the fatigue test revealed that the crack became through the thickness when a crack length of $2a = 4mm$ $(a = 2mm)$ is attained, as observed in Fig. 5.9A and B.

For high-cycle fatigue life, the crack circumferentially grows along the TMAZ in both directions for 1/8 of the weld circumference or until approximately $45°$ degrees from the loading direction, as illustrated in Fig. 5.10. Then, the crack propagates towards the base materials at a relatively low rate. Eventually, the crack becomes unstable and asymmetrical, and final failure is imminent. For low-cycle fatigue life, the crack symmetrically grows on both sides around the

spot joint. At approximately 45° degrees, as indicated in the image, the angle between the crack and the loading direction becomes perpendicular, and the crack propagates along the material width. When the remaining area of the plate is too small and promotes out-of-plane displacement, the ductile fracture occurs around the SZ due to shear overload. In all cases, the fracture propagates in the TMAZ as this region presents a coarse grain structure and low hardness value.

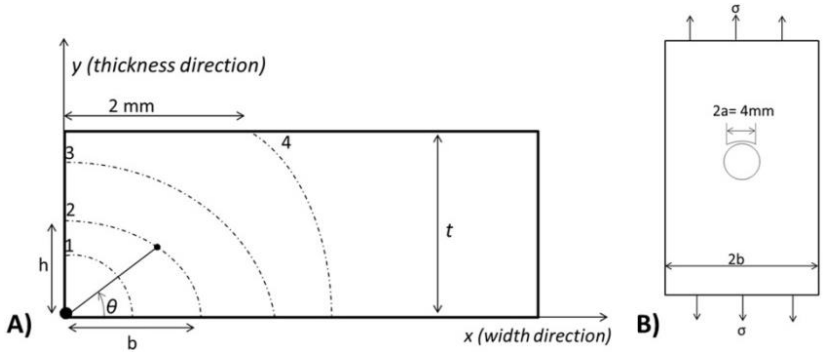

Figure 5.9. Schematic of crack initiation: A) Crack initiation and propagation form the ignition point; B) Through thickness crack.

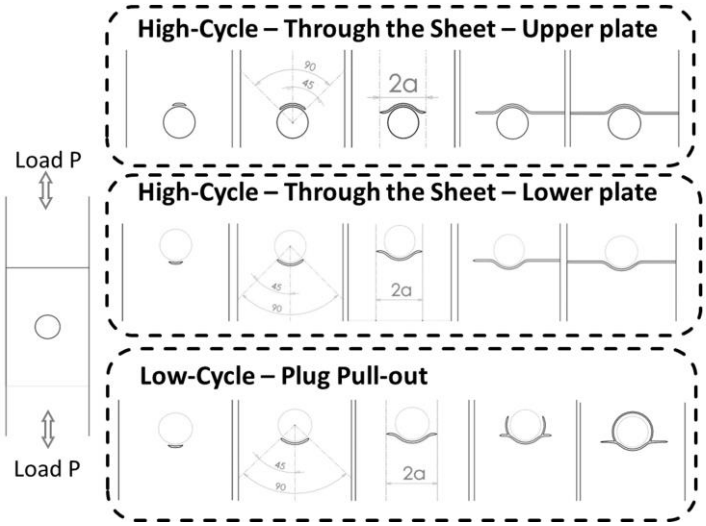

Figure 5.10. Schematic crack propagation: TS – upper plate and TS – lower plate. Schematic crack propagation: PPO.

5.2. Analytical investigation

The experimental investigation enables an understanding of the crack growth characteristics, behaviours and crack shapes. The aggressive performance and weight optimisation are driving the aerospace industry towards the use of advanced numerical simulation tools; consequently, a reduced number of structural tests for design certification and durability are needed. In this section, the analytical investigation was performed using the solver ABAQUS® [72] by applying the numerical technique eXtended Finite Element Method (XFEM) in three dimensional geometries.

5.2.1. eXtended Finite Element Method for stationary crack

Currently, several numerical methods are available to calculate the stress intensity factors for three-dimensional cracked geometries. Despite the success using finite elements in a computational fracture, the mesh generation by the conventional double-node approach

requires that the mesh contours the geometric discontinuities. As a result, considerable mesh refinement is needed in the neighbourhood of the crack tip to adequately capture the singular asymptotic fields.

Developed by Belytschko et al. [65], Moës et al. [69] and Sukumar et al. [61], the eXtend finite element method (XFEM) eliminates the mesh dependency that is associated with modelling cracked surfaces. This numerical method facilitates simulation of discrete cracks along an arbitrary volume and a solution-dependent path without re-meshing, and directly provides stress intensity factors as part of the solution [119].

The XFEM enriches the original geometrical domain (the crack is not included) with local enrichment functions in conjunction with additional degrees of freedom to represent the discontinuity of the cracked element, which is also referred to as phantom nodes [65, 66, 72]. In the following paragraphs, the enrichment of the finite element approximation is described. The crack is typically described by asymptotic enrichment functions to capture the singularities of the crack tip and the discontinuous displacement jump functions across the crack surfaces. The displacement vector function $\boldsymbol{u}$ with the partition of unity enrichment is

$$\mathbf{u} = \sum_{I=1}^{n} N_I(x) \left[\mathbf{u}_I + H(x)\mathbf{a}_I + \sum_{\alpha=1}^{4} F_\alpha(x)\mathbf{b}_I^\alpha \right] \qquad \text{Equation (5.1)}$$

where n is the number of nodes in the mesh, $N_I(x)$ represents the nodal shape functions, $\mathbf{u}_I$ is the classical nodal displacement vector, and $\mathbf{a}_I$ and $\mathbf{b}_I^\alpha$ are the nodal displacement vectors linked to the Heaviside jump function $H(x)$ across the crack surfaces and crack-tip functions $F_\alpha(x)$ [65, 66, 72].

The Heaviside jump function assumes a positive value above the crack and a negative value below the crack, as described in Eq. 5.2.

$$(x) = \begin{cases} 1 \text{ if } (\mathbf{x} - \mathbf{x}^*).\mathbf{n} \geq 0 \\ -1 \text{ otherwise} \end{cases} \qquad \text{Equation (5.2)}$$

where $\mathbf{x}$ is a sample (Gauss) point, $\mathbf{x}^*$ is the point on the crack near $\mathbf{x}$, and $\mathbf{n}$ is the unit outwards normal to the crack at $\mathbf{x}^*$.

The crack tip enrichment consists of the isotropic elastic functions $F_\alpha(x)$, which incorporates the radial and angular behaviours in the two-dimensional asymptotic displacements, as expressed by Eq. 5.3, and exhibits improved accuracy

$$F_\alpha(x) = \left[\sqrt{r}\sin\frac{\theta}{2}, \sqrt{r}\cos\frac{\theta}{2}, \sqrt{r}\sin\theta\sin\frac{\theta}{2}, \sqrt{r}\sin\theta\cos\frac{\theta}{2} \right] \qquad \text{Equation (5.3)}$$

where r and θ are polar coordinates in the $\hat{x}_1 - \hat{x}_2$ plane with its origin at the crack tip and $\theta = 0$ is tangent to the crack at the tip. These functions span the asymptotic crack-tip function of elasto-statics, and $\sqrt{r}\sin\frac{\theta}{2}$ considers the discontinuity across the crack face [61, 65, 69, 120].

Figure 5.12 schematically represent a conventional cracked XFEM domain. The elements cut through by a crack are split into two elements: the tip or near-tip of the crack and its asymptotic functions. The nodes with Heaviside enrichment present two additional degrees of freedom, one degree for each coordinate. At the crack tip, the nodes are enriched with eight additional degrees of freedom by the isotropic elastic functions $F_\alpha(x)$ [72, 120-122].

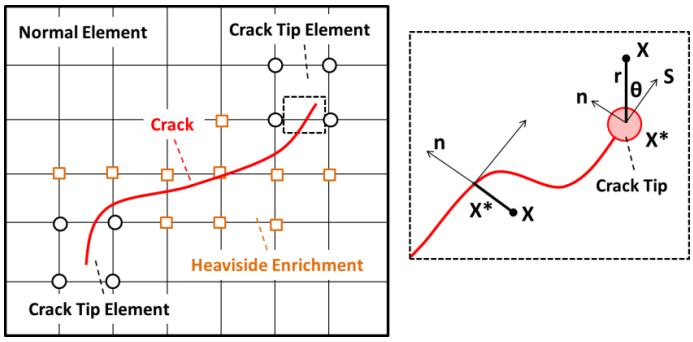

Figure 5.11. Illustration of normal and tangential coordinates for a smooth crack, B) The discontinuous jump function across the crack surfaces.

In ABAQUS®, the *K-factors* are directly obtained as output from every contour at every node along the crack front. The *K-factors* are evaluated by the convergence with respect to the number of contours. A mean value for the converged contours is calculated and applied as the *K-factors* in the respective crack geometry.

$$K_{I,Converged} = \frac{1}{C_{tot} - C_{excl}} \sum_{i=C_{excl}+1}^{C_{tot}} K_{I,i} \qquad \text{Equation (5.4)}$$

where C_{tot} is the total number of contours in the contour domain evaluation, and C_{excl} is the excluded number of contours.

5.2.2. Generation of the three dimensional finite element model

Including a large variety of load conditions, widths, thicknesses, distances between spot-welds, and stir zone sizes in this investigation would be overenthusiastic. Thus, the loading conditions and geometries were limited to those relevant to the experiments. The crack lengths were chosen according to the experimental investigation. The validation of the *K-factors* was performed to compare the crack growth data with the crack growth prediction.

Radaj and Zhang [123] decomposed the loads that exist in a spot weld into several symmetric and anti-symmetric types of loads based on the superposition of the linear elastic theory. A 3D numerical model is capable of substituting the decompositions of the loads for global *K-factors* and a *J-Integral* considering all the structural stresses present in the specimens; namely, tension, bending and shear stress.

To analyse the stationary crack, the similar 3D numerical model developed in Chapter 4 was considered, and few considerations were added to apply the initial crack. First, the model was built to represent the hoop stress in the fuselage of an aircraft, as depicted in the boundary conditions in Fig. 5.12. The displacements in the u_1, u_2 *and* u_3 directions were restrained on the extremities. In addition, vertical movement of the external portions of both plates was not allowed. The external load P was specified. The tensile load is an applied uniform load, and the bending stress is assumed to be linearly distributed through the thickness near the spot-weld. This model was generated to simulate multiple crack sizes or shapes in the same model by changing the crack shell or modifying its geometry in the boundary condition.

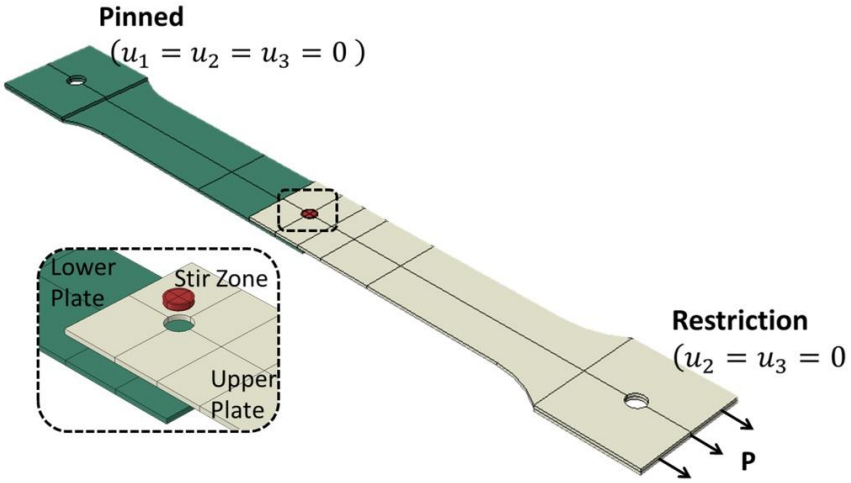

Figure 5.12. Lap-shear geometry and boundary condition.

Although the XFEM technique alleviates the mesh dependency of the numerical model and eliminates the requirement of the mesh to contour the geometric discontinuities in fracture mechanics analysis. The selection of the mesh and mesh size has the important role in the model of providing sufficient accuracy in the stress concentration singularity and accurately predicting the crack growth, as discussed in Chapter 6.

After an initial testing phase, only (locally) uniformly sized structured meshes were employed. Free meshes were applied in a few test cases; however, these meshes poorly performed. In the case of plane stress, full-integration elements exhibited high accuracy. In studies of fracture mechanics using numerical techniques, the parameter selected for the range of mesh density is given by the plastic zone size r_p

$$r_p = \frac{1}{2\pi}\left(\frac{K_{max}}{\sigma_{ys}}\right)^2 \qquad \text{Equation (5.5)}$$

Dougherty and co-workers [124, 125] conducted a mesh refinement study to determine the element length (L_e) along the crack plane. For element sizes that are coarser than $L_e = 0.15r_p$, in the wake of the crack, the stress and strains were discontinuous with a periodic pattern. For element sizes that are finer than $L_e = 0.15r_p$ the wake stress and strain contour of the cracks were continuous and parallel to the crack plane. Therefore, element sizes less than $L_e = 0.1r_p$ are required to adequately capture the crack wake plasticity effects. These findings are consistent with the findings of other studies [5, 126]. In this study, the most accurate results were obtained using squared full-integration elements with a global mesh size of $L_e = 0.1r_p$ in the region of the crack. In situations, in which the bending stresses dominate, a very fine mesh is required due to interactions of the local stress concentration with the crack tip stress field [72, 103, 104].

The contact between the lower plates and upper plates was defined as tangential, and a friction coefficient that permitted some relative motion of the surfaces was set. When the surfaces were sticking, the magnitude of sliding was limited to the elastic slip or shear stress. In addition, a normal behaviour was considered. The interaction between the SZ surfaces in contact with the upper and lower plates was considered to be a surface-based tie constraint. This interaction constrained the translational motion and rotational motion, as well as all other degrees of freedom for the surface pairs [72].

A very important aspect of this fracture mechanics model is the “crack contact”: for an element cracked or intersected by a stationary crack, the strength of the element is assumed to be zero. However, the compressive behaviour of the crack must be considered. The pressure-overclosure relationship governs the behaviour only when the crack is “closed” and the contact normal stress only when the crack is “open”. Any tangential slip is assumed to be purely elastic and is resisted by the elastic strength of the element, which produces shear forces. The contact properties that are utilised in this study are listed in Table 5.1.

Table 5.1. Contact properties of the numerical model.

Type	Discretisation Method	Property	Friction Coefficient	Shear Limit	Stiffness Scale Factor	Contact at zero pressure
Tie	surface-to-surface	constrained	-	-	-	-
Interaction	surface-to-surface	tangential	0.2-0.4	1-100 MPa	-	-
		normal	-	-	-	-
Crack	-	normal (argumented Lagrangian)	-	-	1	0

To implement the XFEM stationary crack approach, ABAQUS® considers full element enrichment. The domain of the elements that are affected by the enriched formulation is defined by the following Abaqus keywords:

Input File: *ENRICHMENT,INTERACTION=*interaction_property_name*
*SURFACE INTERACTION, NAME=interaction_property_name
*SURFACE BEHAVIOR

The enrichment definition must be associated with a region of the model. Only degrees of freedom in elements within these regions are potentially enriched with special functions

Input File: *ENRICHMENT,ELSET=*Geometry,* NAME=*Fat-crack,* TYPE=STATIONARY CRACK,

The crack position is defined as an Initial Condition:

Input File: *INITIAL CONDITIONS, TYPE= ENRICHMENT

The K-values and J-Integral evaluations are based on contour integration around the crack tip. This analysis is requested using the following keywords:

Input File: *CONTOUR INTEGRAL, CRACK NAME=*Fat-Crack*, CONTOURS=*5(Number of Contour)*, TYPE=K FACTORS(or J FACTOR), XFEM

The output requested for the analysis:

PHILSM Signed distance to describe the crack surface.
PSILM Signed distance to describe the initial crack front.
STATUSXFEM Status of the enriched element. (One if the element is completely cracked, and zero if the element contains no crack. If the element is partially cracked, the value lies between one and zero).
ENRRTXFEM All components of the strain energy release rate when LEFM with XFEM is employed.

5.2.3. Hook Geometries and crack shapes for finite element analysis

The hook and crack profiles that are applied to the finite element model are based on experimental investigation; refer to Chapter 4 for the hook profile and the experimental investigation in this chapter for the crack profile. Considering the number of hook geometries,

the crack profile and load cases that are analysed in this section, a large number of numerical models has to be generated. Discretisation errors are possible during manual construction of each model. Thus, an automated procedure was developed to eliminate discretisation errors and directly obtain the results from the model with minimum manual input.

To analyse the structural influence of the hook curvature and assess the *K-factors* around the spot weld in lap joints, the hook was considered to be an initial crack. Fig. 5.13A shows the schematic hook profile measurement that is considered in this analysis. To implement a crack in the 3D main domain using the XFEM numerical technique, an arbitrary shell must be embedded in the 3D geometry. Fig. 5.13B shows a downwards hook placed in the hook location as a crack. First, the *K-factors* for a "flat" hook ($\theta = 180°$) were analysed to determine the critical locations of the circumferential hook. Afterwards, the hook angle θ was changed from $\theta = 0°$ to $\theta = 360°$ for every $10°$ considering the geometry presented in Fig. 5.15B, and the *J-integral* of the critical location was extracted. As described in Chapter 4, the bonded width (BW) and hook height (Hh) have not presented significant influence in the ultimate lap shear strength; and they were not analysed and remained constant for all analysed geometries.

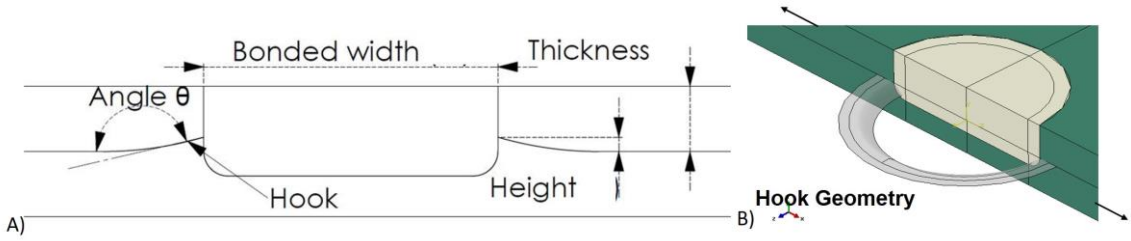

Figure 5.13. A) Schematic hook profile measurement: bonded width; B) A downwards hook placed in the hook location as a crack.

The fatigue crack geometry is an approximation of the real crack that occurs during the fatigue loading of the specimen. As described, the crack profile may be elliptical at its initial point. In this study, a through-thickness crack without any elliptic shape was considered. The crack profile obtained by fractography reconstruction reveals that a crack with a length of 4 mm became a through crack, which was confirmed by SEM analysis, where the fatigue striations are longitudinal in the direction of the width. Thus, it was selected as the initial crack. Afterwards, the crack was systematically increased in both directions with a ratio of $2a/2W = 0.1$. The analysis focused on single-, double- and triple-spot weld row geometries. When the crack is placed as close as possible to the stir zone, a minimal distance must be considered to avoid the numerical inconsistency due to zero-thickness elements. As observed in the experimental investigation, similar cracks were witnessed in the upper and lower plates. Consequently, a numerical analysis was performed in geometries with a crack in the upper and lower plates. To validate the calculated *K-factors'* with the experimental calculation, they were analysed for nominal stresses of 30, 50, 85 and 100 MPa.

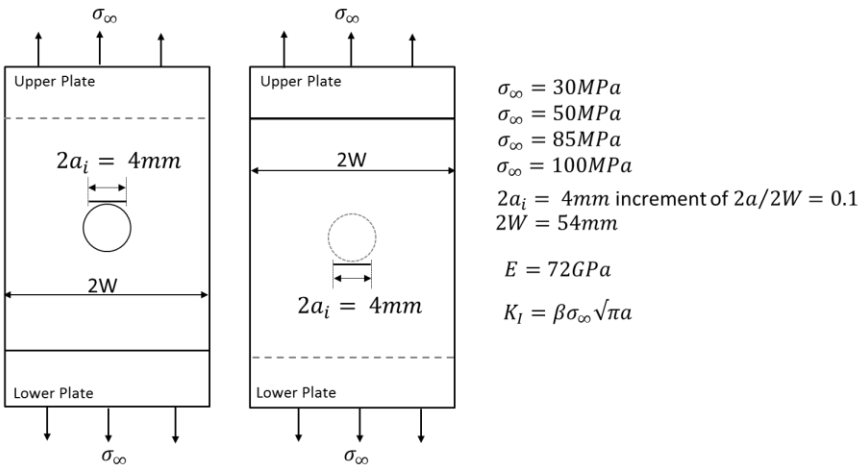

Figure 5.14. Lap-shear geometry and boundary condition for calculation of K-factors.

5.2.4. Verification of methodology

As the XFEM is a novel numerical technique for directly obtaining the values of the *K-factors*, the accuracy of the numerical model must be verified and mesh convergence must be performed, which is usually achieved using a specimen with a known analytical solution for calibration. For this purpose, the XFEM numerical model applied a centre crack tension (CCT) plate benchmark. The K_I*-factors* are compared with the analytical solution:

$$K_I(a) = \sigma\sqrt{\pi a}\beta\left(\frac{a}{W}\right) \qquad \text{Equation (5.6)}$$

where σ is the remote applied stress, a the crack length, and W is the width. The finite width correction function is [111]

$$\beta\left(\frac{a}{W}\right) = \sqrt{\sec\frac{\pi a}{2W}} \qquad \text{Equation (5.7)}$$

A CCT plate with a width of $2W = 250\,mm$, length of $300\,mm$ and thickness of $2\,mm$ thickness was analysed. The numerical model was performed with two different element types: (i) linear hexahedral eight-node element with fully integrated incompatible mode (ABAQUS: C3D8I); and (ii) quadratic element (ABAQUS: C3D20R). The analysis of Fig. 5.15 indicates that both element types are sufficiently accurate compared with the analytical calculations. In addition, the difference between the *K-factor* solutions obtained from linear elements and the *K-factor* solutions obtained from quadratic elements is minimal. These results and the small gain that can be achieved by considering a quadratic linear element, the linear element will be applied onwards to conserve computational time. For small crack ratios $(a/W < 0.25)$, the error is inferior to 2%, for larger crack ratios $(a/W > 0.25)$ the error is inferior to 5% considering both elements analysed.

The study demonstrates the accuracy of the extended finite element method for three-dimensional *K-factors* computations. The method provides a robust and versatile numerical tool for solving crack problems in complex structural components without the need to explicitly align the mesh with the crack. By eliminating the need to include crack surfaces in the model, mesh generation is substantially simplified. This method facilitates the modelling of crack growth for fatigue studies, as a single mesh suffices.

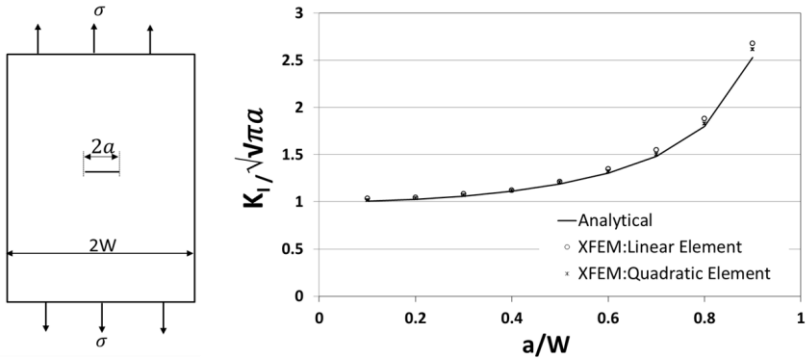

Figure 5.15. XFEM applied to Centre Crack Tension (CCT) Plate Benchmark.

5.3. Results and discussion

The fatigue failure in the spot welds produced by refill FSSW can be divided into three stages. In Stage I - Crack Nucleation, the crack nucleates from the hook geometry along the spot-weld circumference. In Stage II - Through-thickness Crack Propagation, the crack grows and propagates through the sheet thickness. In Stage III – Width Crack Propagation relates to the crack propagation along the width direction of the specimen. Accurate *K-factors* for all fatigue failure stages are needed to estimate the fatigue life based on the linear elastic mechanics.

In this section, the influence of the hook geometry will be analysed in terms of fracture mechanics; it corresponds to Stage I. As the crack grows from the faying surface through the thickness of the specimen, the crack is not detectable by visual inspections. As demonstrated by Fawaz et al. [127] and de Rijck et al. [128], the crack shape or the ellipticity of the crack influences the *K-factors;* as a result, Stage II will not be explored. The *K*-values of Stage III of fatigue failure are obtained in terms of mode I.

5.3.1. Stage I - Crack Nucleation and Hook Influence

The hook profile acts as a natural crack along the spot weld circumference; consequently, the fatigue crack emanates from the pre-existing crack tip. Pook [129] developed analytical solutions for a lap shear specimen and considered two infinite thin plates that are joined over part of their common plane under symmetric loading conditions, in which *K-factors* at the crack tip depend on the bending moment that acts on the plate in the vicinity of the crack tip. However, spot welds are more complex, and the *K-factors* vary along the circumference. This step is important and necessary to develop life prediction and design tools for product development.

Many researchers have developed numerical models to obtain *K-factors* solutions for similar and dissimilar joints in lap shear loading conditions. For example, Zhang and co-workers [130, 131] developed useful formulas to obtain the *K-factors* for dissimilar joints produced by resistance spot welds. However, these solutions were obtained from closed-form stress solutions that consider a rigid inclusion in a finite plate. The authors considered that a kinked crack arises from a main flat crack. This approach cannot be applied in refill FSSW as the experimental investigation did not indicate a flat hook, and the fatigue crack follow the angle of the main fatigue crack.

As *K-factors* vary point by point along the hook circumference, the first step is to identify the distributions and the critical location at which the maximum *K-factors* occur. Fig. 5.16A shows

a typical lap-shear specimen and a cylindrical coordinate system that is located at the spot weld centre. The orientation θ is measured counterclockwise from Point A. Point A ($\theta = 0°$) is aligned in the force direction, and Point B ($\theta = 180°$) is located on the opposite side of Point A. Point C and D are located at $\theta = 90°$ and $\theta = 270°$ degrees of the force direction, respectively. Fig 5.16B presents the normalised K_I, K_{II} and K_{III} as a function of the $Angle\ \theta$ along the hook circumference, which is based on the three-dimensional finite element model that is developed for a lap-shear specimen with a flat $Hook\ angle = 0°$. Note that the *K-factors* are normalised by the K_{II} solution at the critical Point A ($\theta = 0°$). As shown in Fig. 5.16B the maxima of the K_I solutions are located at Point A ($\theta = 0°$) and Point B ($\theta = 180°$). The maximum and minimum of K_{II} are located at Point A ($\theta = 0°$) and Point B ($\theta = 180°$), respectively, whereas the maximum and minimum of K_{III} are located at Point C ($\theta = 90°$) and Point D ($\theta = 270°$), respectively. Note that K_{II} at Point B is negative. In this case, the distributions of the *K-factors* along the hook circumference are similar to the distributions of the *K-factors* in the resistance spot weld [123, 130, 132, 133].

Fig. 5.16C shows the *K-factor*s solutions for the case of the downwards hook. The maxima of K_I is located at Point B ($\theta = 180°$). Unlike the flat hook, K_I at Point A ($\theta = 0°$) presents differently than K_I at Point B. The critical locations and distribution of K_{II} are identical to the critical locations and distribution of the flat hook at Point A ($\theta = 0°$) and Point B ($\theta = 180°$), respectively. The maximum and minimum of K_{III} are located at Point C ($\theta = 90°$) and Point D ($\theta = 270°$). Fig. 5.16D shows the stress intensity factors for the upwards hook. The results present a similar behaviour for the case of the downwards hook; however, the maxima K_I is located at Point A ($\theta = 0°$) instead of Point B.

The results indicate that critical locations in shear loading conditions are located at Point A ($\theta = 0°$) and Point B ($\theta = 180°$) for mixed modes I and II, where K_{II} is the dominant stress intensity factor. The critical location with a minimum mode III are denoted as Point C ($\theta = 90°$) and Point D ($\theta = 270°$). Note that K_{II} in all cases present a similar value. The computational results have confirmed the experimental investigation in which the geometric function of the hook significantly modifies the structural response under shear loads. Consequently, understanding how the geometry affects the *K-factors* is important.

The experimental investigation reveals that the hook angle is the geometric function that has a major influence on the lap shear strength. Therefore, only the hook angle will be addressed in this section. As Points A and B have yielded the highest values for mode I and mode II, the *K-factors* for these points will be analysed for all hook angles. The hook angle varies between $0°$ and $360°$, where $0° < Hook\ Upwards < 180°$, $180° < Hook\ Downwards < 360°$ and $Hook\ Flat = 0° = 180° = 360°$ and varies for each $10°$.

As the *K-factors* at the crack comprise both K_I and K_{II}, this study is performed in terms of the *J-integral*. The *J*-integral is a path-independent integral that is applicable in linear and nonlinear materials, where it is defined along the path Γ that extends from an arbitrary point on the lower crack surface to the upper surface. Considering a homogeneous body that is subjected to a biaxial deformation field, the *J-integral* can be related to the *K-factors*:

$$J = \frac{1}{8\pi}\mathbf{K}^T \boldsymbol{B}\boldsymbol{K} \qquad \text{Equation (5.8)}$$

where $\mathbf{K} = [K_I\ K_{II}\ K_{III}]$ and $\boldsymbol{B}$ are a diagonal matrix, which is referred to as a pre-logarithmic energy factor matrix, for homogeneous, isotropic materials. Equation 5.8 can be written as

$$J = \frac{1}{E}\left({K_I}^2 + {K_{II}}^2\right) + \frac{1}{2G}{K_{III}}^2 \qquad \text{Equation (5.9)}$$

where G is the shear modulus. Fig. 5.17A and B present a schematic plot of the main interface at the tip of the hook with the hook angle θ. At the tip of the crack, K_I and K_{II} represent the global mode I stress intensity factor and the global mode II stress intensity factor, respectively. Note that the arrows in the figure represent positive global and local *K-factors*. For a flat hook, the results at Point A have demonstrated that a low value of the *J-integral* is attained when the angle is upwards with the angle $\theta \approx 40° - 50°$. Subsequently, this value increases until the maximum $\theta \approx 100° - 110°$, and the *J-integral* decreases until a low value at $\theta \approx 250° - 260°$ is achieved and then increases. Conversely, the *J*-integral at Point B decreases when the angle increases until $\theta \approx 100° - 110°$. Subsequently, the *J*-integral increases until the highest value $\theta \approx 250° - 260°$ is attained and quickly decreases until $\theta \approx 310° - 320°$.

From this analysis, the angle that shows the highest value at Point A is $\theta \approx 100° - 110°$ when the hook is oriented upwards. Point B attains its highest values when the hook is oriented downwards $\theta \approx 250° - 260°$. Note that the highest value of J-integral is oriented upwards, which confirms the results of the fatigue experimental investigation. The material near the hook tip at Point B is compressed by the adjacent material. According to Pook [129], the energy release rate or the *K-factors* at a crack tip depends on the bending moment that acts on the volume in the vicinity of the crack tip.

The *K-factors* along the hook circumference under shear loading present a significant influence of the stress near the spot weld. The K_I*-factor* at Point A, which is aligned in the load direction, is dependent on the bending conditions. The K_{II}*-factor* at the critical locations is a function of the bending stress and tension. The K_{III}*-factor* is a function of the shear stress.

5.3.2. Stage III – Width crack propagation

The *K-factors* were calculated using the finite element model developed in this section and the previously described boundary conditions. In this study, two different crack locations for single-, double-, and triple-spot weld rows were considered: (i) in front of the first spot weld row of the upper plate; and (ii) after the last spot weld row in the lower plate. The variation of the $\frac{a}{W}$ ratio for different specimen widths must be conducted to ensure the geometry and size independence and transferability of the *K-factors* solutions to a real structure.

As a consequence of low levels of the out-of-plane nodal displacement over the load range in this analysis, fracture mode III (tearing) demonstrated low values and was eliminated. Due to the perfect symmetry of the crack length, fracture mode II (shearing type) have presented lower-order values compared with fracture mode I. Consequently, its consideration only minimally affects the crack propagation prediction in the width direction. Therefore, pure fracture mode I (opening type) was considered.

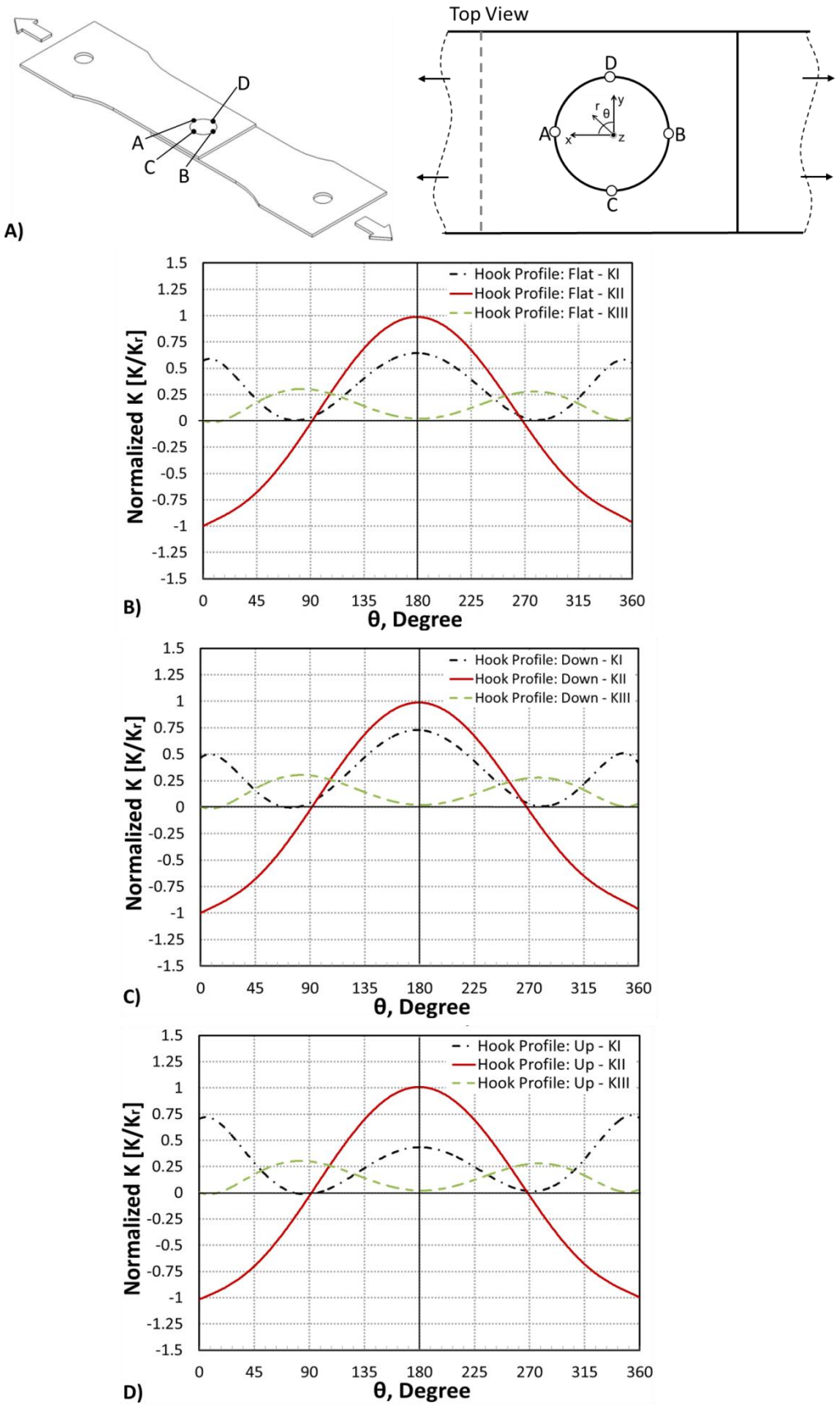

Figure 5.16. A) Lap shear specimen and a cylindrical coordinate system centred at the spot weld centre; B) Normalised *K-factors* for flat hook flat Hook; C) *K-factors* for downwards hook profile; C) *K-factors* for upwards hook profile.

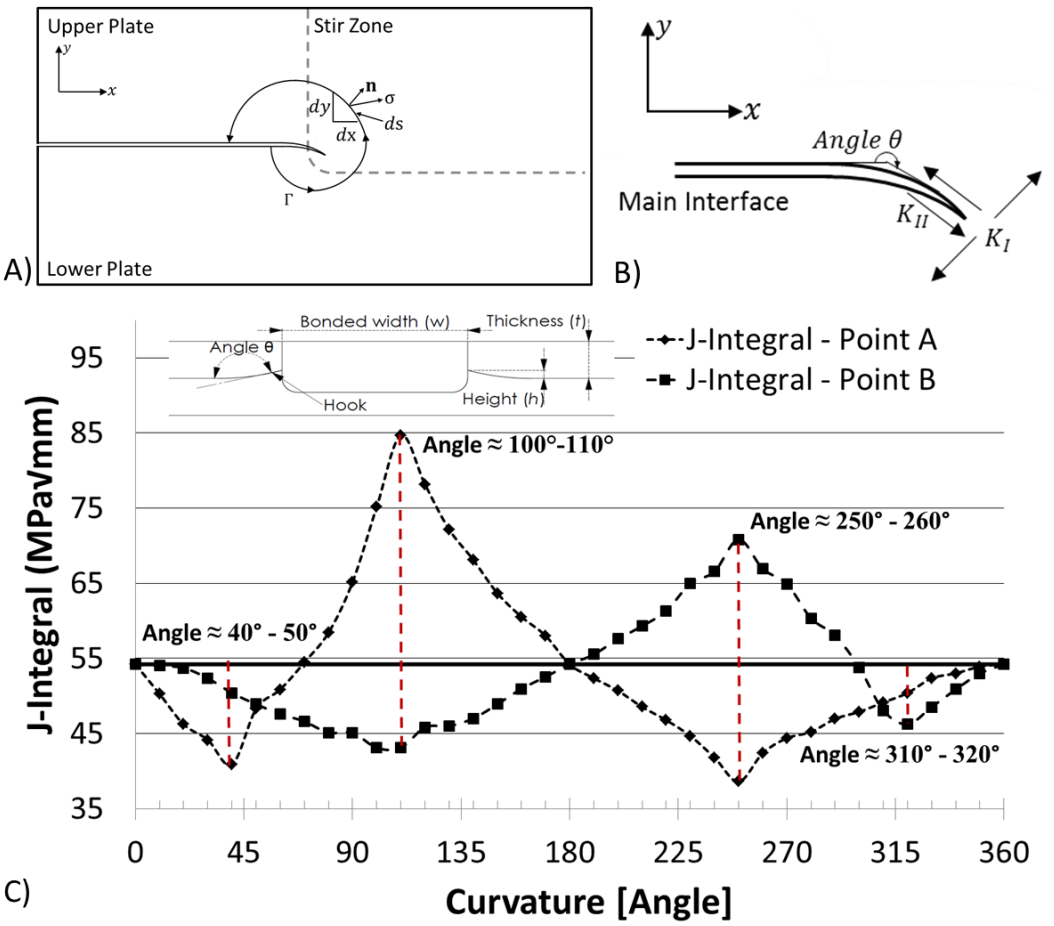

Figure 5.17. A) Arbitrary *J-integral* path at hook tip; B) Schematic plot of the main interface and at the tip of the hook, with the hook angle; C) Influence of the hook tip on the structure behaviour.

The same FE mesh density approach that was developed for the crack region and applied in the previous sections was employed in all cases in this study. The large number of elements in the crack region provides a more accurate stress field near the crack tip and obeys a simple logic, where increasing the number of elements (number of degrees of freedom) around the crack enables the finite element model to simulate the stress singularity at the crack tip with high accuracy. The numerical model must accurately predict the crack constraints in the plane stress state and the crack intersection with the free surfaces. The load was applied in the surfaces of the clamp region to replicate the test.

The stress intensity factor of a cracked skin panel is usually defined as

$$K_I = \sigma\sqrt{\pi a}\beta\left(\frac{a}{W}\right) \qquad \text{Equation (5.10)}$$

where $\beta\left(\frac{a}{W}\right)$ is the boundary correction factor that considers the effect of the finite width and crack length as a function of the remote stress, which is defined as

$$\sigma = \frac{F_{xx}}{2WB} \qquad \text{Equation (5.11)}$$

where F_{xx} is the applied force perpendicular to the crack, the width is $2W$, and the thickness is $B\ (=2)$. The K_I*-factors* K_I^{FE} are obtained from the numerical model. Afterwards, the boundary correction factor $\beta\left(\frac{a}{W}\right)$ for each crack length is defined as

$$\beta\left(\frac{a}{W}\right) = \frac{K_I^{FE}}{\sigma\sqrt{\pi a}} \qquad \text{Equation (5.12)}$$

The results have shown that the K_I*-factors* at the faying surface have a slightly higher magnitude than the K_I*-factors* at the outside free surface. This behaviour is primarily related to the bending stress, where its higher value at the faying surface tends to open the crack more than its value at the outside free surface. The major difference of the K_I*-factors* between the faying surface and outside free surface was lower than 10%; this condition was not considered in the analysis. Thus, to obtain an accurate K_I^{FE}, the K_I*-factor* of each node in the crack tip was considered and divided by the number of nodes

$$K_I^{FE} = \frac{\sum K_I^{FE}}{nodes} \qquad \text{Equation (5.13)}$$

To ensure the load independency of the boundary correction factor, their values were analysed for each remote stress. This step of the study is important for minimising or eliminating any numerical inconsistencies. The $\beta\left(\frac{a}{W}\right)$ for $\sigma = 100\ MPa$ was applied in subsequent analyses.

The calculated boundary correction factors are shown in Fig. 5.18A, B and C as a function of the crack ratio $\frac{a}{W}$ for single-spot weld row, double-spot weld rows and triple-spot weld rows, respectively. In all cases, the boundary correction factor $\beta\left(\frac{a}{W}\right)$ shows a progressive increase when the crack length increases. In addition, the crack in the upper plate presents similar behaviours and values. The global trend reveals that an increase in the number of rows causes the $\beta\left(\frac{a}{W}\right)$ to become more stable for longer cracks. The *K-factors* of the model increase with an increase in the load concentration. In addition, the decrease in $\beta\left(\frac{a}{W}\right)$ for a higher number of spot weld rows is attributed to a decrease in the bending factor. Consequently, the bending stress through the thickness also decreases.

For multiple-spot weld rows, in the presence of the symmetric crack, the middle-spot weld row transfers a higher percentage of the total load that is applied to the joint, whereas the spot weld where the crack is located transfer a lower percentage of the applied load. In the last spot weld, the load transfer remains almost constant.

5.3.3. Effective Stress Intensity Factor

Elber [54] suggested that the effects of crack closure and opening effects (crack plasticity) at the crack tip modifies the *K-factors* range, which is an important aspect of fatigue crack growth. The significantly higher stress at the crack tip induces a local plastic strain and in-plane deformation. Elber realised that the local plastic strain that is created during tensile loading does not completely recover. This finding implies that a plastic wake during unloading is formed at the crack tip, and the remote material from this region remains elastic, which constrains the plastic wake during unloading and forces the crack to close. Consequently, the crack surfaces must be in contact while the specimen remains in tension [2, 5]. The crack

closure effect removes the stress singularity at the crack tip, which only opens during reloading when the positive stress level σ_{op} is attained. This effect changes the stress range, where the crack is fully opened when

$$\Delta\sigma_{eff} = \sigma_{max} - \sigma_{op} \qquad \text{Equation (5.14)}$$

at the determined crack length a.

During cyclic loading, crack closure occurs if the local stress $\sigma_{min} < \sigma_{op}$. The crack is partly (or fully) closed at σ_{min}. The crack tip during loading is fully open when $\sigma = \sigma_{op}$ and remains open until σ_{max}. During unloading, the crack remains open until crack closure starts at the crack tip. The corresponding closure stress level σ_{cl} is usually assumed to be approximately equal to σ_{op}. An important aspect to be recognised is that the *K-factor* at the tip of the crack is present as long as the crack tip is open. As soon as the tip is closed, the stress singularity disappears. The concept of ΔK_{eff} is generally accepted and applied in prediction models; this concept includes the assumptions that the fatigue crack extension Δa is fully controlled by $\Delta\sigma_{eff}$. As a result, the Elber concept established the fatigue crack growth rate as

$$\frac{da}{dN} = C(U\Delta K)^m$$
$$\Delta K_{eff} = U\Delta K \qquad \text{Equation (5.15)}$$

where U is defined as the stress intensity ratio. The studies developed by Elber of the stress ratio $-0.1 \leq R \leq 0.7$ for 2024-T3 aluminium alloy revealed that U depends on the *R*-ratio as follows:

$$U = 0.5 + 0.4R \qquad \text{Equation (5.16)}$$

Schijve [1] proposed an improved stress intensity ratio, which represents a more realistic behaviour and accounts for the crack closure opening effects for $-1 \leq R \leq 1$,

$$U = 0.55 + 0.33R + 0.12R^2 \qquad \text{Equation (5.17)}$$

Another way of obtaining K_{max}, K_{open} and σ_{open} is to perform an elastoplastic FE analysis of a crack under cyclic loads by calculating the crack opening stress levels. In this study, σ_{open} is assumed to be function of the *R*-ratio; in addition, a structural analysis is performed to check the influence of the number of spot weld rows. As a result, the fatigue crack growth is defined as

$$\Delta K_{eff} = K_{max} - K_{open} \qquad \text{Equation (5.18)}$$

where

$$K_{max} = \beta\left(\frac{a}{W}\right)\sigma_{max}\sqrt{\pi a}$$
$$K_{open} = \beta\left(\frac{a}{W}\right)\sigma_{open}\sqrt{\pi a} \qquad \text{Equation (5.19)}$$

For a given structure, when β and σ_{open} are obtained, the fatigue life for a given load can be predicted. As previously stated, the equation $da/dN = f(\Delta K_{eff})$ implies that da/dN only depends on ΔK_{eff}.

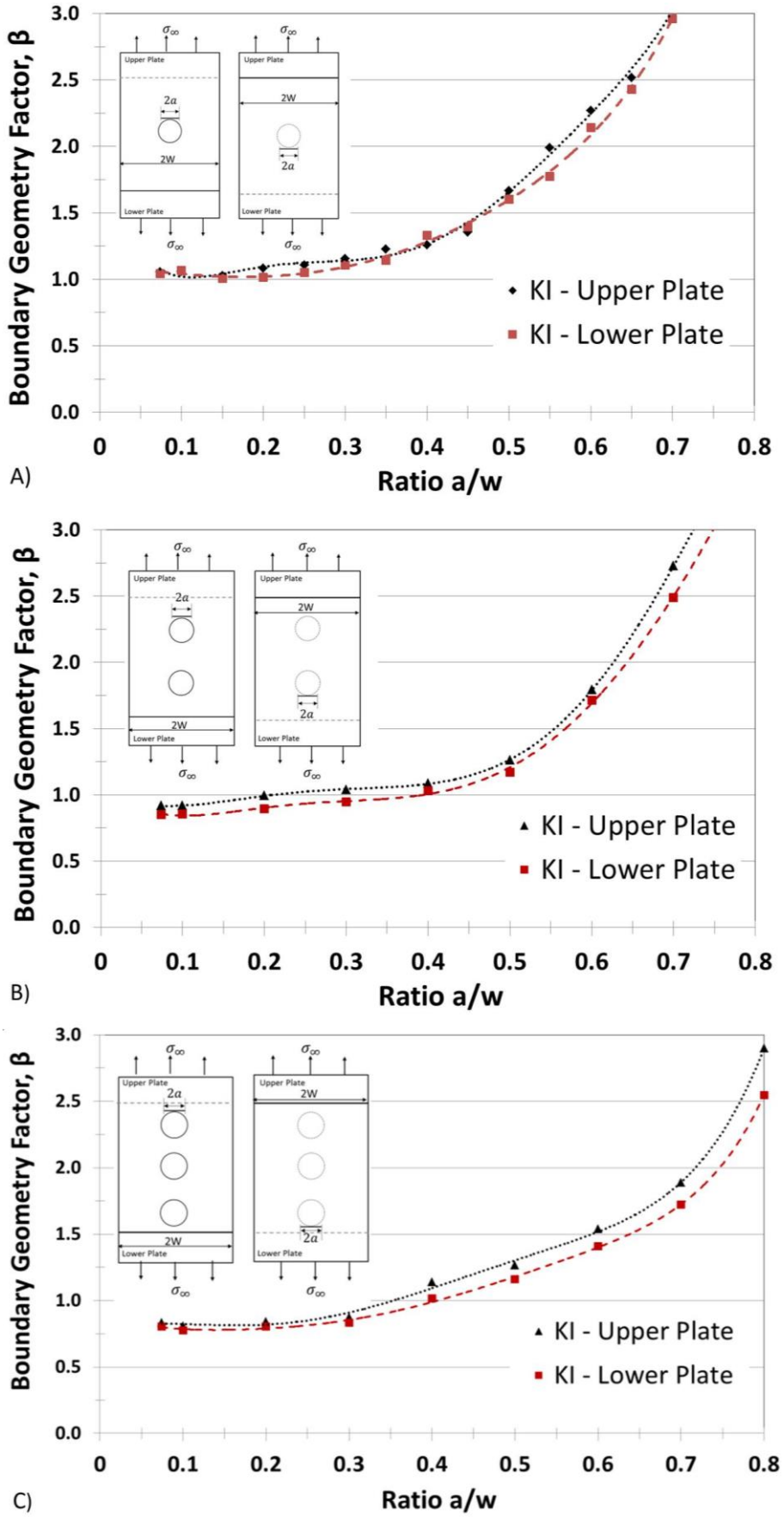

Figure 5.18. Calculated boundary correction factors: A) Single-spot weld row; B) Double-spot weld row; and C) Triple-spot weld row.

The plastic limit load is the maximum load that can be sustained by a given structure that is composed of a perfectly plastic material. In this condition, the deformation increases while the load is held constant [134]. The plastic limit analysis solution defines a plastic collapse load for a material with no strain hardening and indicates an initial plastic load for hardened materials [3, 135]. This approach can generate suitable approximations for the plastic load by real structures [3, 136]. Therefore, a study of the strain hardening effect on the crack behaviour of the stress opening level for different hardening conditions is performed. Fig. 5.19 shows a common stress-strain curve, where the material presents strain hardening; an elastic-perfectly material without strain hardening is also presented as a perfectly plastic material. The simplified defect assessment of the plastic limit is commonly employed as an approximation, in which only the yield strength is necessary as an input in the FE model. In the case of strain hardening materials, the stress-strain curve must be described as a table of values that considers the stresses and strain obtained from experimental data.

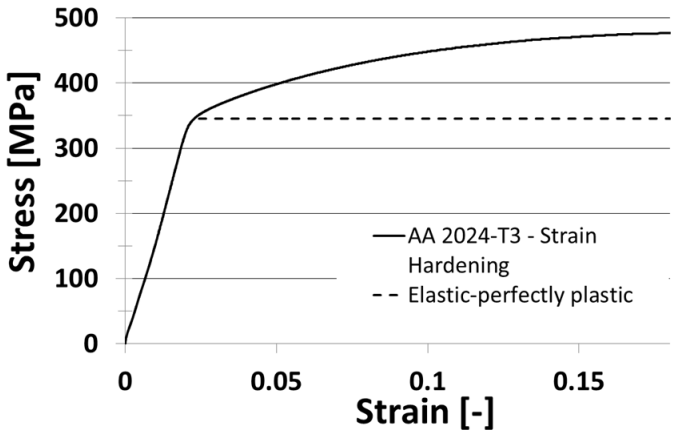

Figure 5.19. Stress strain behaviours in two plasticity models.

Once the crack opening stress σ_{op}, and consequently, K_{op} can change its levels with heat treatment (plastic zone size at the crack tip), geometry of the crack, specimen thickness and initial crack length, a proper measurement and technique is necessary. In the literature, two different approaches for obtaining σ_{op} are described:

Approach 1: Stress that corresponds to the separation of the fracture surfaces at the first ligament (node) behind the crack tip.

Approach 2: During loading, the compressive stress perpendicular to the crack tip changes to a tensile stress; the crack is considered to be fully open and the corresponding applied stress is referred to as the crack opening stress σ_{op}.

For correct crack propagation analysis and residual strength of thin sheets with stable crack growth lead to a need to obtain the σ_{op} in function of the crack length. Different crack length were analysed using the same mesh and boundary condition as in the calculation of the *K-factors*. Cyclic steps were added to these numerical models. Approach 2 was chosen for the σ_{op} calculation, which is an effective driving force for the crack propagation study [4, 5].

The level of crack opening stress versus the normalised crack length was obtained from the FE model of a sample with single-spot weld rows under constant amplitude stress $\sigma_{max} = 100\ \mathrm{MPa}$ and the stress ratio $R = 0.1$. The investigation was conducted using a perfectly plastic material and a strain-hardening material. The level of crack opening stress ratio versus

crack length for the plastic limit analysis and strain-hardening is presented in Fig. 5.20. Strain hardening produces a low level of σ_{op}, which is a similar behaviour identified by Pommier [137]. The author suggested that strain hardening is caused by low plastic strain and plastic wake at the crack tip produced by the strain hardening material and less compressive residual stress due to the plasticity. The crack opens earlier than a crack in the case of an elastic-perfectly plastic material. Consequently, the crack propagation rate is expected to be faster in the case of strain hardening. This finding is consistent with the findings of Pommier et al. [138] and Athanasios [5].

The analysed crack lengths were equivalent to the crack lengths of the *K-factors* until the crack became unstable. These crack lengths are useful for the study of the relationship with ΔK_{eff}, especially in cases with small crack lengths. In addition, the empirical level of stress proposed by Elber U_{Elb} and Schijve U_{Sch} is also presented. The results are in an expected region in terms of the stress intensity ratio. The stress intensity ratio proposed by Schijve is consistent with high-accuracy cases with elastic-perfectly plastic materials. The U_{Elb} has a better fit for strain hardening materials.

$$U_{Elb} = 0.5 + 0.4R = 0.54$$
$$U_{Sch} = 0.55 + 0.33R + 0.12R^2 = 0.5842$$

Equation (5.20)

The main finding based on the results of the crack closure effect in refill FSSW is that the crack closure is independent of the initial crack. A difference is observed in the initial crack length between the empirical and the result obtained via numerical model; however, this difference is only 15% of the maximum stress intensity ratio. The empirical Elber and Schijve stress intensity ratios provide a good approximation and support the findings, which confirm that the crack opening stress is primarily affected by the *R*-ratio of cyclic stress and is relatively independent of the maximum applied stress and initial crack length [5, 137, 138].

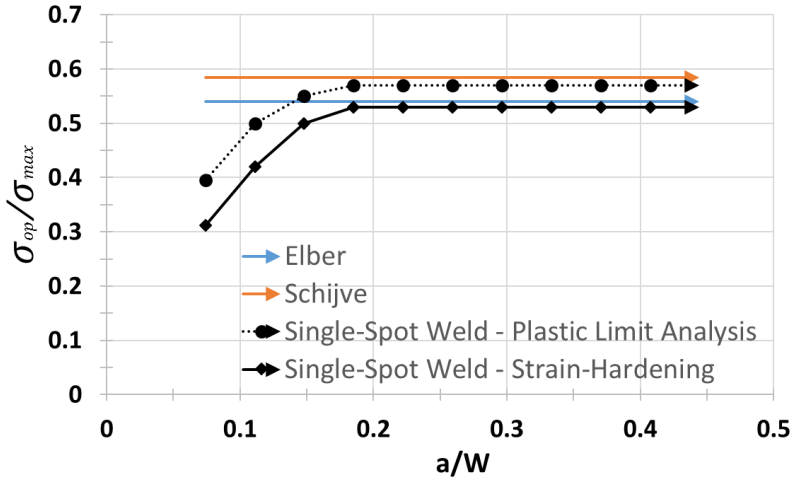

Figure 5.20. Level of crack opening stress ratio versus crack length for plastic limit analysis and strain-hardening.

5.3.4. Crack growth prediction

One method of verifying the *K-factors* developed during this section and evaluating the consideration is to predict the crack growth. In this section, the crack growth prediction was performed with the developed *K-factors*. The crack growth solution comprises the boundary

correction factor $\beta\left(\frac{a}{w}\right)$ for a specified crack length and the Elber´s stress intensity ratio, as well as the load case.

The results of the crack growth prediction were compared with the *in situ* crack propagation measurements. A travelling microscope was set up in front of the specimen to measure the crack length. The results have been investigated for a triple-spot weld row specimen under remote tension stress. The measurement started when the first well-defined crack front shape was visible on the outside free surface. The fatigue crack initiation occurred at the third weld row in the lower plate. Afterwards, the crack longitudinally grew along the lower plate width. The geometry and loading conditions are described in Fig. 5.21. The linear-elastic approach was employed in this section due to its straightforwardness; the boundary correction factor $\beta\left(\frac{a}{w}\right)$ calculated by ABAQUS® as established as an input.

Fatigue crack growth is a cycle-by-cycle process, where the crack grows in every cycle. For each crack extension Δa, the number of cycles can be obtained from the calibrated curve da/dN. This value can also be obtained using the Paris relation between da/dN and ΔK

$$\frac{da}{dN} = C\Delta K^n \qquad \text{Equation (5.21)}$$

Replacing the *K-factors,* the following equation is obtained:

$$\frac{da}{dN} = C\left(\beta\left(\frac{a}{w}\right)\Delta\sigma\sqrt{\pi a}\right)^m \qquad \text{Equation (5.22)}$$

Inappropriate *K-factors* are unsafe as the crack growth life can be over predicted. In this study, the ΔK range is modified by the effects of cyclic plasticity (crack closure) via the argument of the effective stress intensity factor ΔK_{eff}. The ΔK in the Paris relation is replaced by ΔK_{eff}, and Equation 5.15 is expressed as

$$\frac{da}{dN} = C\Delta {K_{eff}}^n = C\left(\beta\left(\frac{a}{w}\right)\Delta\sigma_{eff}\sqrt{\pi a}\right)^m \qquad \text{Equation (5.23)}$$

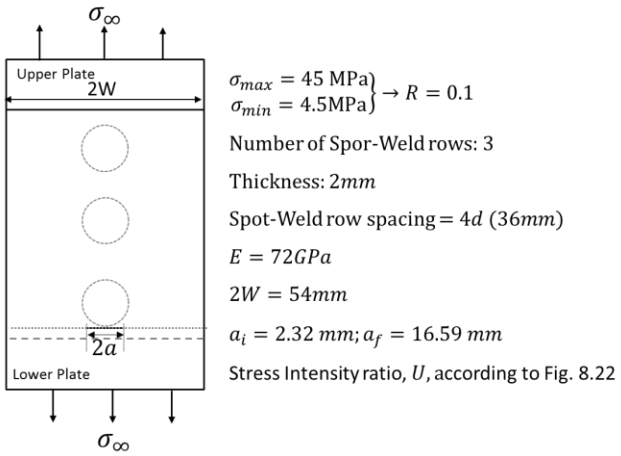

Figure 5.21. Geometry and loading conditions for the crack growth prediction.

The crack growth prediction for a triple-spot weld row specimen under remote tensile stress is shown in Fig. 5.22. The first well-defined crack front shape observed in the experiment was established as the initial crack a_i in the crack growth prediction model. The growth was calculated until the last crack front was observed prior to complete failure of the specimen.

The predictions do not precisely follow the experimental values but are considered to be consistent with the crack propagation curve. The results of the prediction are representative of other geometries. The calculated *K-factors* provide sufficient accuracy for crack growth life prediction of fatigue for through-thickness cracks that grow under remote tensile stress.

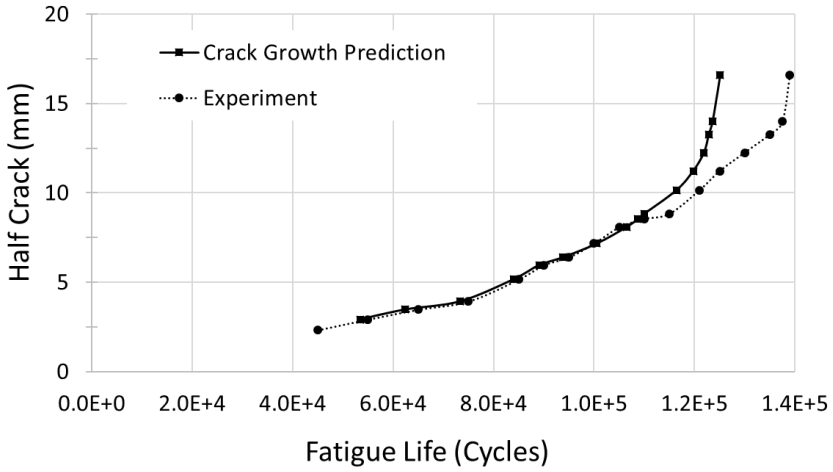

Figure 5.22. Comparison between experiment and prediction for three-spot weld row.

5.4. Concluding remarks

A detailed elastic-plastic and elastic-perfectly plastic FE model has been developed to obtain *K-factors* and understand the crack growth mechanism in refill FSSW for single-, double- and triple-spot weld rows. A 3D XFEM numerical technique has been applied to achieve the *K-factors* solutions.

The complete 3D numerical models were simulated under a remote tension stress, which produced a combined tension and bending stress. The influence of the secondary bending can be easily analysed and determined with this numerical model. The model provided a simple and powerful means to understand the crack profile and crack growth behaviour under combined tension and bending loading.

Prior to the investigation of *K-factors* solutions, an experimental understanding of the crack initiation and propagation until final failure was necessary. The fractured surface analysis using the SEM enables a fracture reconstruction of the larger part of the fatigue crack. Failure of the samples with a high-cyclic fatigue life occurred along the material width. The crack initiated at hook formation and circumferentially propagated through the thickness to the crack origin. Then, the crack propagated around the spot weld until the critical angle of 45° degrees was aligned in the load direction. Then, the crack propagated along the material width.

For a low-cyclic fatigue life, the fracture mode was identified as Plug Pull-Out. The primary crack was initiated at the hook tip and propagated through the lower plate thickness. Subsequently, the crack propagated along the width, which was similar to the propagation for a high-cycle fatigue life. When the resistance area was excessively small, the joint could not sustain the overstress, and the spot-weld catastrophically failed.

In all cases, the fatigue crack initiation started at the hook tip. Therefore, the hook curvature was considered to be a stress intensity factor. Fracture mode I (opening) and mode II (shearing) occurred at the critical locations (points A and B, Fig. 5.16), and Fracture mode III

(tearing) occurred at the critical location points C and D. The welding parameters can change the hook geometry, and consequently, the *K-factors* solutions also change.

Based on the cyclic simulations, the crack opening stress is influenced by the *R*-ratio and is relatively independent of the initial crack length. This finding is advantageous for a structural analysis using various amplitudes.

Once the crack growth is influenced by the *K-factors*, accurate *K-factors* must be obtained. Using the developed *K-factors* and the Linear Elastic Fracture Mechanism for prediction of crack growth, the results have demonstrated sufficient accuracy for the experimental data obtained from a fatigue through crack until final failure in remote tension loading conditions.

The Paris relation is useful for estimating the effect of the design stress level on the crack growth life. Plasticity-induced crack closure is an important phenomenon for understanding the macrocrack growth behaviour. The crack closure concept has prompted the ΔK_{eff} concept, which is helpful in accounting for the stress ratio R.

Chapter 6.

Fatigue Crack Growth and Residual Strength

The basic concept of the damage tolerance philosophy is to ensure the safety of a structure throughout its service life. As previously mentioned, the damage tolerance approach assumes that the designed structure presents initial cracks caused by manufacture defects or maintenance handling and assumes that the fatigue life of the structure is consumed with slow crack growth to the critical crack length, at which failure will occur. A damage tolerance analysis provides information about the effect of cracks on the strength of a component or structure. This information is presented in crack growth diagrams and residual strength diagrams.

Once macrocracks in aircraft structures are acceptable, an understanding of how fast the crack grows and the crack path/behaviour is mandatory. Although numerous experimental investigations of the behaviours of crack initiation and crack growth have been performed, a numerical model of the fatigue crack growth is important to maximize the information about the test, predict the crack behaviours in different boundary conditions and reduce the number of experiments. An interesting question may be raised here. Is a realistic simulation of a fatigue test for crack growth more simple and more time-consuming than the fatigue test of a component?

Static failure in an aircraft structure occurs when the structure cannot carry an applied load. To prevent catastrophic static failure throughout the expected service life, the load capacity must be evaluated in the potentially cracked structure. The residual strength is the capacity of load carrying of a cracked structure and is a function of material toughness, crack size, crack geometry and structural configuration. The determination of residual strength in terms of the *K-factors* on an arbitrary structure generally requires the support of detailed numerical analyses.

The first part of this chapter—Section 6.1—addresses the fatigue crack growth of the refill FSSW, where the experimental investigation is presented. Since crack propagation in refill FSSW structures is performed for the first time typical defects and the failure scenarios should be defined. Section 6.2 presents the background of residual strength in riveted structures. The numerical model for fatigue crack growth is developed in section 6.3. The results of the experimental and numerical investigations are presented, and the theoretical methodology is discussed in Section 6.4. The chapter's conclusions are provided in section 6.5.

6.1. Fatigue crack growth

6.1.1. Experimental investigation

For the analysis of the fatigue crack growth in refill FSSW, panels were designed for fatigue testing. The widths of the panels and the number of spot welds were restricted by the capacity of the fatigue test machine and the clamping system; only specimens with triple-spot weld rows and five spot welds in a row—Panels 3 x 5—were possible. After the weld, no post-

processing was applied to the specimens. The clamping system must ensure a homogeneous load distribution at the specimen ends. The analysis of this study focuses on the tension panel for which damage tolerance is most critical to aircraft design. In addition, the generic form of wider panels enables the study of different scenarios of crack growth.

The service loads of aircraft structures are predominantly random. Irregularities in fatigue loading produces a transient effect on the fatigue crack growth rates and may significantly affect the fatigue life. Thus, the prediction of fatigue crack growth is a very difficult task due to the complexity of the involved fatigue damage process. The majority of fatigue analysis is dependent on test data [139]. Depending on the cruise altitude and aircraft type, the hoop stress can vary between 80 and $120MPa$ [51]. The tested specimens were loaded in tension to provide a remote stress of $S_{max} = 77.5\ MPa$ at a frequency of $5\ Hz$. The crack growth is recorded by periodic observations of the locations of the two crack tips using a travelling optical microscope with a magnification factor of 40.

The generic geometries of the multiple-spot weld panels were designed according to the minimum distances obtained in Chapter 4. An intrinsic objective of the experimental investigation is to obtain sufficient data for validation of the numerical model and the theoretical methodology. For this reason, different geometries were tested. Table 6.1 presents an overview of the specimens in this investigation. The two aluminium 2024-T3 lap splice joints had a similar sheet thickness (B), width (W), distance of the spot-weld from the sheet edge (S_e), edge distance (e) and spot-weld pitch row distance (S). Three different samples with altered spot-weld row spacing (p) were tested: $2d$, $3.5d$ and $5d$. The geometries of the specimens were chosen to validate the numerical models.

Table 6.1. Specimen properties for test programme.

Panel 3 x 5	**Sample Geometry**			**Loading Condition**
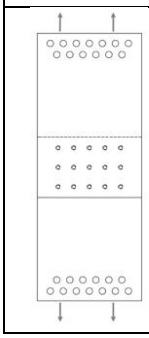	$\boldsymbol{p = 2d}$	$\boldsymbol{p = 3.5d}$	$\boldsymbol{p = 5d}$	
	$S_e = 3d$ $p = 2d$ $S = 3.5d$ $e = 25\ mm$ $W = 240\ mm$ $B = 2\ mm$	$S_e = 3d$ $p = 3.5d$ $S = 3.5d$ $e = 25\ mm$ $W = 240\ mm$ $B = 2\ mm$	$S_e = 3d$ $p = 5d$ $S = 3.5d$ $e = 25\ mm$ $W = 240\ mm$ $B = 2\ mm$	$S_{max} = 77.5MPa$ $S_a = 34.5MPa$ $R = 0.1$ $f_r = 5Hz$

6.1.2. Failure scenarios

In the following section, the failure scenarios that were observed during the experimental observations are proposed and described for the damage tolerance analysis, the current failure scenarios remain under study analysis. For this study, three failure scenarios have been proposed, and an additional scenario in panels without defects is considered as a reference for analysis purposes.

When a panel with finite width is uniaxially loaded, the edge effect occurs. The two outer spot weld columns transfer greater load than the inner spot weld, which is a consequence of the difference in the lateral contraction in the width direction of the sample. As result, the crack tends to initiate at the outer spot welds, which is undesirable [2, 55]. As observed in Chapter 4, the failure of multiple-spot weld rows under fatigue loading has demonstrated that the crack

have a tendency to start at outer spot weld rows. Fatigue crack initiation occurs in regions of high stress concentration located at or near the spot welds. The analysis revealed that approximately 75% of the load is transferred by the outer spot weld rows. Thus, the critical planes in fatigue and damage tolerance must be considered for the two outer rows [140, 141].

The following locations of crack initiation were assumed (Fig. 6.1A):

1. Defect in the upper plate: $\mathbf{SpotWeld_{1x3}}$
2. Defect in the lower plate: $\mathbf{SpotWeld_{3x3}}$

The first failure scenario is crack propagation from a flaw at the weld joint, as described in Fig. 6.1B, where a lack of refill of the spot weld can occur. The hypothesis that is considered with this crack initiation is that under cyclic loads and after crack nucleation, the crack will propagate faster and longitudinal to a plate under the influence of the TMAZ and HAZ that surrounds the spot weld. The crack starter notch consists of a drilled hole around the spot weld; in the extreme case, no load is transferred by the defected spot weld. This defect must be located on the upper plate in $\mathrm{SpotWeld_{1x3}}$.

The second failure scenario is crack propagation considering a fatigue crack. This crack initiates at the faying surface at the hook tip; as this damage may not be immediately detected, continued cyclic loading will create a through the thickness crack in front of the weld and a skin crack, as described in section 5.1. The crack starter notch consists of a longitudinal cut, as shown in Fig. 6.1C, and the tip contains two sharp corners. During the fatigue crack propagation trial tests, the travelling microscope detects an initial through the thickness crack of $2a = 4mm$. However, the crack simultaneously started in the outer spot weld columns (multiple site damage). To ensure that the crack would start at the "fatigue crack" tip and avoid the multiple site damage, a larger initial crack was chosen: $2a = 20mm$. In addition, the trial tests revealed that the crack propagated in the lower plate in front of the third row. Therefore, the location of the fatigue crack is the lower plate in front of $\mathrm{SpotWeld_{3x3}}$. The third failure scenario was proposed to simulate an initial crack of riveted structures with a cut in the middle of the spot weld, as shown in Fig. 6.1C. The starter notch is identical to the second failure scenario (through the thickness $2a = 20mm$). The location of the crack is the lower plate $\mathrm{SpotWeld_{3x3}}$.

In all failure scenarios, the crack front is perpendicular to the plane of the specimen, which implies that the central crack has only one dimension—the crack length. The lengths of the cracks are measured from the centre line of the specimen to the tip of the crack. In general, the growth of the two cracks is symmetrical. Thus, the total tip-to-tip crack length can be indicated by the single value $2a$. Table 6.2 summarises the test programme of the fatigue crack propagation analysis and indicates the failure scenario for the defect/crack location of the sample.

Table 6.2. Sample failure scenario for the fatigue crack propagation test programme.

Sample	Failure Scenario	Defect Location	Obs.
Panel 3 x 5 [p=3.5d] – 01	Free Defect	-	Trial Test
Panel 3 x 5 [p=3.5d] – 02		-	Trial Test
Panel 3 x 5 [p=3.5d] – 03		-	Trial Test
Panel 3 x 5 [p=2d] – 01	Fatigue Crack	$\mathrm{SpotWeld_{3x3}}$ [LP]	Crack Propagation
Panel 3 x 5 [p=2d] – 02		$\mathrm{SpotWeld_{3x3}}$ [LP]	Crack Propagation
Panel 3 x 5 [p=2d] – 03		$\mathrm{SpotWeld_{3x3}}$ [LP]	Crack Propagation

Panel 3 x 5 [p=5d] – 01	Free Defect	-	Crack Propagation/Reference
Panel 3 x 5 [p=5d] – 02		-	Crack Propagation/Reference
Panel 3 x 5 [p=5d] – 03		-	Crack Propagation/Reference
Panel 3 x 5 [p=5d] – 04	Lack of Refill	$\mathrm{SpotWeld}_{1x3}$ [UP]	Crack Propagation
Panel 3 x 5 [p=5d] – 05		$\mathrm{SpotWeld}_{1x3}$ [UP]	Crack Propagation
Panel 3 x 5 [p=5d] – 06		$\mathrm{SpotWeld}_{1x3}$ [UP]	Crack Propagation
Panel 3 x 5 [p=5d] – 07	Fatigue Crack	$\mathrm{SpotWeld}_{3x3}$ [LP]	Crack Propagation
Panel 3 x 5 [p=5d] – 08		$\mathrm{SpotWeld}_{3x3}$ [LP]	Crack Propagation
Panel 3 x 5 [p=5d] – 09		$\mathrm{SpotWeld}_{3x3}$ [LP]	Crack Propagation
Panel 3 x 5 [p=5d] – 10	Rivet	$\mathrm{SpotWeld}_{3x3}$ [LP]	Crack Propagation
Panel 3 x 5 [p=5d] – 11		$\mathrm{SpotWeld}_{3x3}$ [LP]	Crack Propagation
Panel 3 x 5 [p=5d] – 12		$\mathrm{SpotWeld}_{3x3}$ [LP]	Crack Propagation

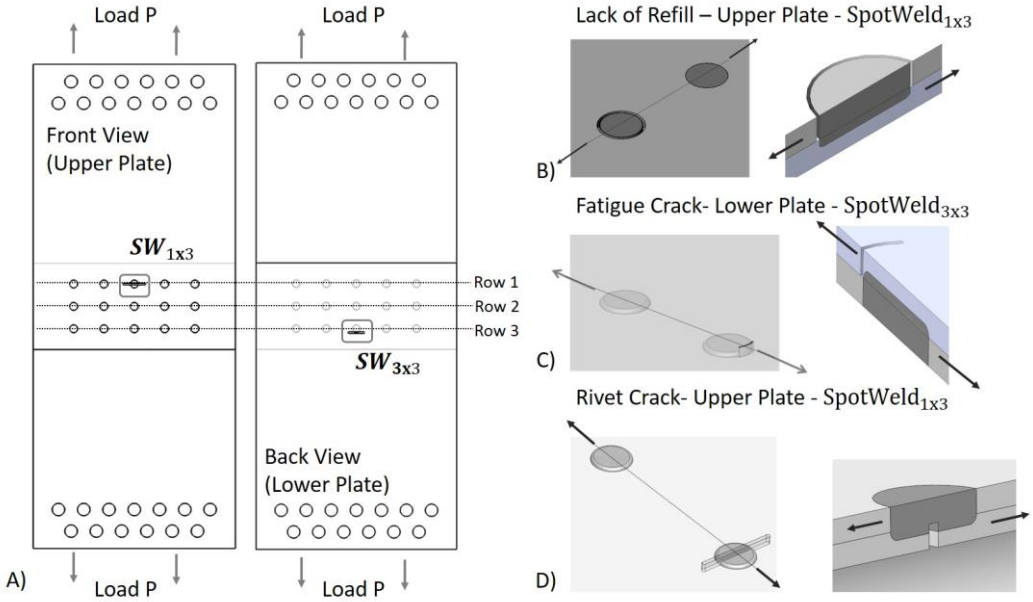

Figure 6.1. A) The locations of crack initiation; B) Lack of Refill; B) Fatigue Crack; C) Rivet Crack.

6.1.3. Fatigue crack growth in panels and the similarity concept

The following section provides a short review of the fatigue crack growth in refill FSSW and the application of the similarity concept, which is based on the stress intensity factor, as described by Schijve [1].

In riveted structures, the peak stress usually occurs at the two outer rows, where the highest bending stress defines the critical location. Similar to the refill FSSW lap joints, the secondary bending induces higher stresses levels at the faying surface; therefore, the fastener stress concentration combined with the higher bending at the faying surfaces defines the most likely location for the peak stress and crack initiation. Empirical calculation methods, such as the calculation method adopted by Fokker Aerostructures, can be employed to calculate the peak stress [142]. This calculation method assumes that joints with similar stress and stress ratios have identical fatigue crack initiation lives and can be predicted using SN curves from the literature or reference. In addition, the Miner rule for accumulation damage can be applied in variable amplitude load cases [57, 107].

After crack initiation, a period of slow crack growth rate is described by the literature. The crack coalesces at the highest stress concentration location to form a part-through thickness

crack. Due to secondary bending, the crack elliptically grows through the width direction towards the outer surface. When the crack reaches the outer surfaces, it becomes a through-the-thickness crack. Although the crack fronts tend to remain slanted to a certain extent, the fatigue initiation life is based on the minimum detectable crack size; this initial crack size must be considered in the crack growth analysis [2, 55, 143].

To estimate the crack growth in riveted lap joints, two different method that are based on stress intensity factors are well-accepted in the literature. The first method considers the extreme cases of through-the-thickness and surface cracks, where the through-thickness cracks present the highest crack growth rate and the surface cracks present the lowest crack growth rate. The crack growth rate of the sample is assumed to be an average between these two crack configurations. The second methodology for the riveted lap joint with glare is based on the stress intensity factors at the crack tip at the faying surface. This crack growth calculation method assumes that the crack driving force is led by the local stress field near the crack tip at the faying surface, which unquestionably modifies the crack opening stress. This methodology includes the effect of secondary bending and proposes a conservative crack growth rate.

As discussed in Chapter 5, the *K-factors* indicate the severity of the stress around the crack tip. Considering that the cyclic stress ($\Delta S = S_{max} - S_{min}$) corresponds to the stress intensity factor range ($\Delta K = K_{max} - K_{min}$), the stress ratio *R* is constant for the cyclic stress and *K-factors* [1].

$$R = \frac{S_{min}}{S_{min}} = \frac{K_{min}}{K_{min}} \qquad \text{Equation (6.1)}$$

The similarity principle states that specimens with different crack lengths and cyclic stress but similar ΔK cycles should have the same crack extension Δa per cycle. As a result, the crack growth rate da/dN has to be equivalent and be a function of K_{min} and K_{max}.

$$\frac{da}{dN} = f(K_{max}, K_{min}) \qquad \text{Equation (6.2)}$$

The crack growth function in Eq. 6.2 can be rewritten as a function of ΔK and the stress ratio R $(= K_{min}/K_{max})$ and replaced by

$$\frac{da}{dN} = f_R(\Delta K, R) \qquad \text{Equation (6.3)}$$

Note that the similarity principle reveals the relationship between Δa and similar ΔK cycles. Therefore, the fatigue crack mechanism and the da/dN curve must be obtained from an experimental investigation.

In addition, the crack closure phenomenon modifies the range of *K-factors* (cyclic plasticity), as described in Chapter 5. Thus, the ΔK_{eff} is defined as

$$\Delta K_{eff} = K_{max} - K_{open} \qquad \text{Equation (6.4)}$$

where

$$K_{max} = \beta \sigma_{max} \sqrt{\pi a}, \qquad K_{open} = \beta \sigma_{open} \sqrt{\pi a} \qquad \text{Equation (6.5)}$$

The parameters K_{max}, K_{open} and σ_{open} are determined by the developed numerical model. Then, the $\beta\left(\frac{a}{W}\right)$ considers the structural geometry and σ_{open}, and the cyclic plasticity and the fatigue crack growth can be predicted for a given load spectrum. This method is applied in a constant amplitude loading analysis. Usually, the final failure is assumed when the K_{max} attains the critical value of K_C for plane stress conditions. In aircraft applications, namely, the damage tolerance design philosophy, the final failure of cracked structures is addressed by the residual strength as a function of crack length [4, 123].

6.2. Residual strength methodology

The residual strength indicates the load level at which unstable crack growth occurs. In most cases, the residual strength is related to fatigued and cracked joints and the capability to carry the load through the reduced section [55]. The current approach in riveted joints is based on linear elastic fracture mechanics, in which the *K-factors* are the crack tip parameter. The development of the residual strength capability usually involves three major steps:

(a) development of the relationship among the applied stress σ, the crack length a, and the applied stress intensity factor for the given structural configuration;
(b) selection of an appropriate failure criterion based on material behaviour at the crack tip (plane strain or plane stress);
(c) fracture strength σ_f and critical crack size a_c are obtained by utilising the results of the first two steps, and the residual strength diagram for the given structural configuration is plotted.

The stress intensity factor for the structural configuration has to be obtained. The *K-factors* correlate the local stress with the applied load, structural configuration and crack length. In the literature, some criteria for residual strength have been proposed according to the behaviour at the crack tip. For the plane strain, the fracture toughness K_{IC} is a material constant. However, the fracture toughness K_C of the material in this study (plane stress) depends on the width and thickness of the plate. The failure criterion that considers the *R*-curve yields the best accuracy to define the residual strength for the thickness. Due to the lack of *R*-curve data for this spot-welded panel, the residual strength will be calculated using a static failure criterion. Fracture toughness data can be obtained from the Damage Tolerant Design Data [86, 87]. The critical value is $K_{max} = 74\ M\mathrm{Pa}\sqrt{\mathrm{m}}$ for a plate with the same material and similar thickness.

The static failure criterion, or Irwin's Criterion, considers an unstable fracture when the *K-factors* attain or exceed the fracture toughness. Thus, the applied stress that exceeds the K_C for a given crack length is referred to as the fracture strength.

The critical fracture strength σ_f for the critical length a_c is calculated using the following relation:

$$K_C = \sigma_f \beta \sqrt{\pi a_c} \qquad \text{Equation (6.6)}$$

where K_C is the fracture toughness. Therefore, the diagram σ_f vs. a_c provides the residual strength that is required in the design analysis of airframe structures. This approach has been applied by several researchers and has been demonstrated to be useful in airframe design.

6.3. Analytical investigation

The experimental investigation has been employed for the evaluation and calibration of the numerical models, where the crack shapes and crack growth characteristics were obtained. For the analytical investigation, two numerical models have been developed by applying the numerical technique eXtended Finite Element Method. The stationary crack model is used to obtain the *K-factors* in the panels; this model is identical to the models described in Chapter 5, with similar mesh density, mesh element, contact and constraints.

The XFEM crack growth model in three-dimensional geometries is similar to the stationary crack; however, to implement the damage evolution (crack growth), few tools must be implemented in the original code. As the technology is relatively new, e.g., this model cannot be built in ABAQUS CAE® [72], an explanation of the numerical tools is provided. The three-dimensional model for the refill FSSW lap joint is subsequently described.

6.3.1. eXtended Finite Element Method for crack growth model

To obtain accurate contour integral results for a cracked three-dimensional surface, a detailed mesh density, which can be cumbersome in crack growth models where the mesh contours the geometrical crack, is required. In general, these models require an efficient remeshing code or technique. The XFEM provides an efficient method for simulating the arbitrary crack growth without remeshing [72]. The discontinuities and the singularities of the crack tip are ensured by the enrichment functions in conjunction with additional degrees of freedom, as described in section 5.2.

The XFEM crack growth model is based on the principles of the Linear Elastic Fracture Mechanism. The onset and growth of the crack are based on the Paris law and characterised by the relative fracture energy release rate at the crack tip. Note that this model considers the fatigue accumulation as a small time-scale crack increment phenomenon. The crack grows at any time increment, which enables the *R*-ratio effect on the plastic zone at the crack tip to be included in the crack closure hypothesis.

By definition, the LEFM approach requires the presence of an initial crack, which extends when the fracture criterion f attains the critical value 1.0

$$1.0 \leq f \leq 1 + f_{tol} \qquad \text{Equation (6.7)}$$

within a given tolerance f_{tol}. If $f > 1 \ + f_{tol}$, the crack extension criterion is satisfied.

Input File: *SURFACE BEHAVIOR
*FRACTURE CRITERION, TOLERANCE=f_{tol}

The Paris law relates the relative fracture energy rate to the crack growth rate. Below the threshold G_{thresh}, no crack growth occurs; above the upper limit G_{pl}, the crack growth is unstable. The fatigue crack growth initiation criterion is defined as

$$f = \frac{N}{c_1 \Delta G^{c_2}} \geq 1.0 \qquad \text{Equation (6.8)}$$

where c_1 and c_2 are material constants and N is the cycle number. Thus, the elements ahead of the crack tip will be fractured when the component or structure is loaded at the upper G_{thresh} limit. If this criterion is satisfied, the crack growth rate da/dN is calculated based on

the energy release rate ΔG. The rate of the crack growth per cycle is given by the Paris law if $G_{thresh} < G_{max} < G_{pl}$. G_{max} corresponds to the maximum energy release rate when the structure is cyclically loaded. If $G_{max} > G_{pl}$, the cycle number count dN increases by one.

$$\frac{da}{dN} = c_3 \Delta G^{c_4} \qquad \text{Equation (6.9)}$$

c_3 and c_4 are the material constants.

Input File: *SURFACE BEHAVIOR
*FRACTURE CRITERION, TOLERANCE=f_{tol}, TYPE=FATIGUE

The prerequisites of three-dimensional crack growth models comprise a three-mode-mix formulae to calculate the equivalent fracture energy release rate G_{equiC}. The solver ABAQUS has three law models: BK law [144], power law [145], and Reeder law [146]. The selection of an appropriate model is usually empirically achieved. In this study, the power law model was selected; it is described in Wu and Reuter [145]

$$\frac{G_{equi}}{G_{equiC}} = \left(\frac{G_I}{G_{IC}}\right)^{a_m} + \left(\frac{G_{II}}{G_{IIC}}\right)^{a_n} + \left(\frac{G_{III}}{G_{IIIC}}\right)^{a_0} \qquad \text{Equation (6.10)}$$

where G_I, $G_{II}, and\ G_{III}$ are internal variables. G_{IC}, G_{IIC}, and G_{IIIC} are calculated based on the critical equivalent strain energy release rate and the fracture strength of the material. For isotropic materials, the constants a_m, a_n, and a_0 are set to 1.0. The G_{thresh} and G_{pl} can be specified in terms of the G_C by default: $G_{thresh} = 0.01G_C$ and $G_{pl} = 0.85G_C$.

Input File: *SURFACE BEHAVIOR
*FRACTURE CRITERION, TOLERANCE=f_{tol}, TYPE=FATIGUE, MIXED MODE BEHAVIOR=*POWER*

To extrapolate the damage from one cycle to the number of cycles over which the crack propagates, ABAQUS® uses a Direct Cyclic adaptive algorithm. The crack length a grows at the number of cycle ΔN by fracturing at least one enriched element ahead the crack tip. Some important characteristics of the model code that are many times neglected by modellers and direct influence on the accuracy of the results, and the crack growth direction vector: (i) the Fourier number; (ii) the number of interactions (stabilised solution number), and (iii) the number of increment steps between the maximum loading and minimum loading. These characteristics are empirically defined.

Input File: *DIRECT CYCLIC, FATIGUE

The linear extension length Δa is calculated based on the maximum value of ΔK_{Ieq}; then, a constant value of the maximum crack extension can be applied for this crack tip, and the crack increment is obtained as

$$\Delta a = \Delta a_{max} \left(\frac{\Delta K_{Ieq}}{\Delta K_{Ieq,max}}\right)^m \qquad \text{Equation (6.11)}$$

The arbitrary crack extends at a direction perpendicular to the maximum principal stress. The crack growth direction θ_c, at crack tip, when the local shear stress is zero, is defined as

$$K_I \sin\theta_c + K_{II}(3\cos\theta_c - 1) = 0 \qquad \text{Equation (6.12)}$$

The solution of this equation is expressed as

$$\theta_c = 2\tan^{-1}\left(\frac{K_I - \sqrt{{K_I}^2 + {K_{II}}^2}}{4K_{II}}\right) \qquad \text{Equation (6.13)}$$

where the equivalent mode I is defined as

$$K_{Ieq} = K_I\cos^3\left(\frac{\theta_c}{2}\right) - 3K_{II}\cos^2\left(\frac{\theta_c}{2}\right)\sin\left(\frac{\theta_c}{2}\right) \qquad \text{Equation (6.14)}$$

After fracture of the element at the end of the stabilised cycle, the stiffness is zero, the load is redistributed to the neighbours' elements, the new relative fracture energy release rate is calculated for the elements ahead of the crack tip, and the next cycle is calculated.

The output of the analysis:

PHILSM Signed distance to describe the crack surface.

PSILM Signed distance to describe the initial crack front.

STATUSXFEM Status of the enriched element (one if the element is completely cracked, and zero if the element contains no cracks. If the element is partially cracked, the value lies between one and zero.

ENRRTXFEM All components of the strain energy release rate when LEFM with XFEM is employed.

CYCLEINIXFEM Number of cycles to initialise the crack at the enriched element.

6.3.2. Generation of the three-dimensional model

Following the samples with one column, the analysis is expanded to larger panels. A description of the Panel 3 x 5 used in the analysis is provided. A stationary crack model is applied to evaluate the *K-factors*; they are subsequently compared with the small samples, and the residual strength is analysed. As previously mentioned, the stationary crack model and the fatigue crack growth model are identical; the main difference is the code developed for the fatigue model. However, few considerations are necessary to achieve reliable results.

The displacements $u_1, u_2\ and\ u_3$ and the vertical movement of the panel were restrained in one of the extremities, and the external load P was specified to restrain the vertical movement on the opposite extremity of the panel, as described in Fig. 6.2, where the initial crack is detailed. The tensile load P is uniformly applied on the clamping surface area, and the bending stress is assumed to be linearly distributed through the thickness near to the spot welds. The geometry function $\beta\left(\frac{a}{W}\right)$ is defined for the panel and the stress is defined as

$$\sigma = \frac{P}{2WB} \qquad \text{Equation (6.15)}$$

where P is the applied load, $2W$ is the panel width, and $B(= 2.0\ mm)$ is the skin thickness.

In the case of fatigue crack growth models, when direct cyclic analysis is iteratively employed to obtain a stabilised solution; geometric nonlinearities can be included only in a general step prior to the direct cyclic step. Contact between the upper plate and lower plate cannot be included during the crack propagation; it is a source of error once a percentage of the load is

transferred by friction between the plates. However, the constrains between the spot weld and the plates and the surface contact of the crack have not changed.

Considering the mesh density for fatigue crack growth, a compromise regarding the mesh density and the time computational is necessary. If the crack length increment is too small, a very fine mesh ahead of the crack tip is required, which may require a very small time increment in the simulation and costly computational time. If the crack extension is too long, the crack path cannot consistently represent a real crack. Generally, finer mesh in the interesting simulation region should be connected to a coarser mesh density in the other regions using the multipoint constrain. This consideration requires a smooth transition between two regions.

Therefore, a finer mesh density in the crack region and ahead of the crack tip is applied considering the convenient approach employed in the stationary crack analysis $L_e = 0.1r_p$. Outside of the crack region, a coarser mesh density is applied [124, 125].

The fatigue crack growth model is applied to analyse the influence of the joint configuration in the number of cycles to failure. In addition, different initial crack sizes are evaluated under cyclic loading, which is a better determination that the crack growth will provide the real number of cycles until failure.

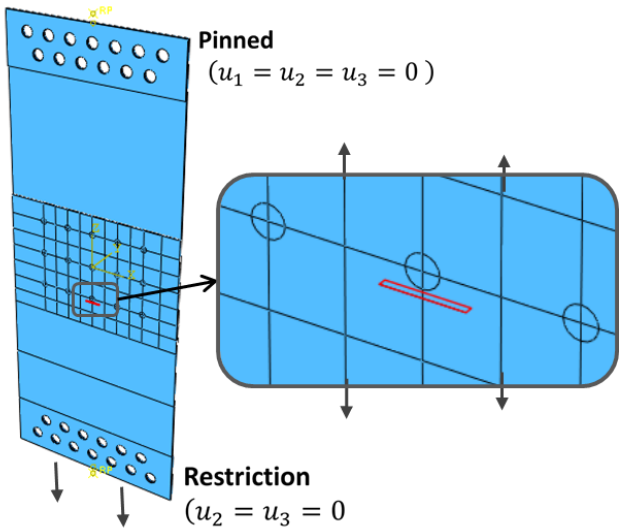

Figure 6.2. Boundary condition of the fatigue crack growth model, and details of the initial crack.

The constants for the numerical model are described in Table 6.3.

Table 6.3. Fatigue constants for fatigue crack growth model [59, 88].

Properties	Values
G_I, G_{II}, G_{III}	2400
c_1	1.1088E-7
c_2	2.9436
$c_3 = c_1/2$	0.55044E-7
$c_4 = c_2/2$	1.47
a_m, a_n, a_0	1

6.4. Results and discussion

6.4.1. Crack growth propagation for different failure scenarios

As previously mentioned, the analysis of the crack propagation focuses on the through-thickness crack; the length of this type of crack enables it to be observed on the panel surface. Table 6.4 summarises the results obtained for the failure scenarios that are previously described in Panels 3 x 5 [p=5d].

Table 6.4. Sample failure scenario for the fatigue crack propagation test programme.

Sample	Failure Scenario	Fracture mode	Number of cycles
Panel 3 x 5 [p=5d] – 01	Free Defect	Tension – 3rd row LP	146028
Panel 3 x 5 [p=5d] – 02		Tension – 3rd row LP	148985
Panel 3 x 5 [p=5d] – 03		Tension – 3rd row LP	151088
Panel 3 x 5 [p=5d] – 04	Lack of Refill	Tension – 3rd row LP	141521
Panel 3 x 5 [p=5d] – 05		Tension – 3rd row LP	136892
Panel 3 x 5 [p=5d] – 06		Tension – 3rd row LP	138785
Panel 3 x 5 [p=5d] – 07	Fatigue Crack	Tension – 3rd row LP	112957
Panel 3 x 5 [p=5d] – 08		Tension – 3rd row LP	109556
Panel 3 x 5 [p=5d] – 09		Tension – 3rd row LP	107390
Panel 3 x 5 [p=5d] – 10	Rivet	Tension – 3rd row LP	114044
Panel 3 x 5 [p=5d] – 11		Tension – 3rd row LP	117175
Panel 3 x 5 [p=5d] – 12		Tension – 3rd row LP	118848

Before the comparisons of the failure scenarios in terms of crack length vs. life cycles are achieved, the results from the experiments are shown in Fig. 6.3 and the crack configuration/propagation is described in Fig. 6.4. For a defect-free (crack free) failure scenario, the average number of cycles is $150\ kCycles$. The cracks have initiated on the third row in the lower plate at the outer spot welds (SW_{3x1} and SW_{3x5}) in the lower half of the spot weld row with approximately the same number of cycles $2a_i \rightarrow 55000$. Subsequently, the cracks slowly and symmetrically grew to the spot welds ($2a_1 \rightarrow 115000$). Then, they longitudinally propagated towards the centre of the sample, where the crack growth rate increased until the final failure. As observed in section 4.5, the stress analysis of the plate indicated that higher stresses are located at the outer spot welds. A similar behaviour is observed in the rivets of the crack propagation test; however, this phenomenon can be diminished by applying a higher squeeze force in the outer rivet rows.

In case of the lack of refill failure scenario, the crack propagation is similar to the free defect. However, the final failure of the sample has an average of 138 kCycles, which is slightly lower than the free defects failure scenario. The crack propagation exhibited similar behaviour, and the crack initiated in the same location (SW_{3x1} and SW_{3x5}, Lower Plate) at $2a_i \rightarrow 45000$. Then, the cracks slowly, symmetrically and longitudinally propagated to the spot weld ($2a_1 \rightarrow 102500$) towards the centre of the panel. The intact spot welds near the Lack of Refill defect carries a greater load than the free defect scenarios; this defect overstressed the adjacent spot welds and the crack does not initiate at the refill defect.

Numerous small cracks can simultaneously initiate along rows of rivets/spot welds, which are also referred to as multiple sites damage (MSD). The presence of more than one crack and their interactions are problems in the engineering fields. Due to the intact panel, the outer spot welds carry more loads from the inner spot welds; consequently, the cracks tend to initiate at these locations in fatigue crack propagation tests. The integrity of the panel

decreases with an increase in the number of cracks; in general, the life of the panel considerably decreases in a specimen when the largest cracks grow towards each other and suddenly links and forms a large crack, which causes rupture of the structure. MSD analyses have presented challenges in their evaluation via numerical analysis. Although the evaluation of the MSD is beyond the scope of this study, the development of a numerical model enables the implementation of numerous cracks in the model. The model has proven to be efficient and capable of including the interactions among neighbouring cracks to determine the stress intensity factor solutions.

In the case of a fatigue failure scenario due to a large initial crack with a sharp end on both sides, the crack propagates from the initial crack and symmetrically and slowly grows ($2a_1 \rightarrow 105000$) towards the edge of the panel. Then, multiple cracks develop at the outer spot welds ($2a_2 \rightarrow 107500$). An effective crack was established for the analyses ($2a = 115mm$). These cracks grew towards each other until final failure ($2a_2 \rightarrow 114044$). A similar behaviour and fatigue life was observed in the case of a riveting failure scenario. In the beginning, the crack propagated towards the sheet edge with a small inclination towards the typical line of failure. The crack symmetrically and slowly grew until the effective crack formed. Then, multiple cracks are developed at the outer spot welds, and the cracks grew towards each other until final failure.

In the FE simulations of the panels, the variation in the crack size forces the equilibrium of the forces between the intact spot welds. For example, for an initial crack of $2a = 40mm$ under the applied stress of $80MPa$, the maximum stress in the outer spot weld is $50MPa$. When the crack grows to $2a = 80mm$, the stress is $80MPa$. When the crack grows to $2a = 115mm$, the stress at the outer spot weld is $100MPa$. Fig. 6.5 shows the stress for different crack lengths and reveals that the stresses in the inner spot weld inversely decrease with an increase in crack length.

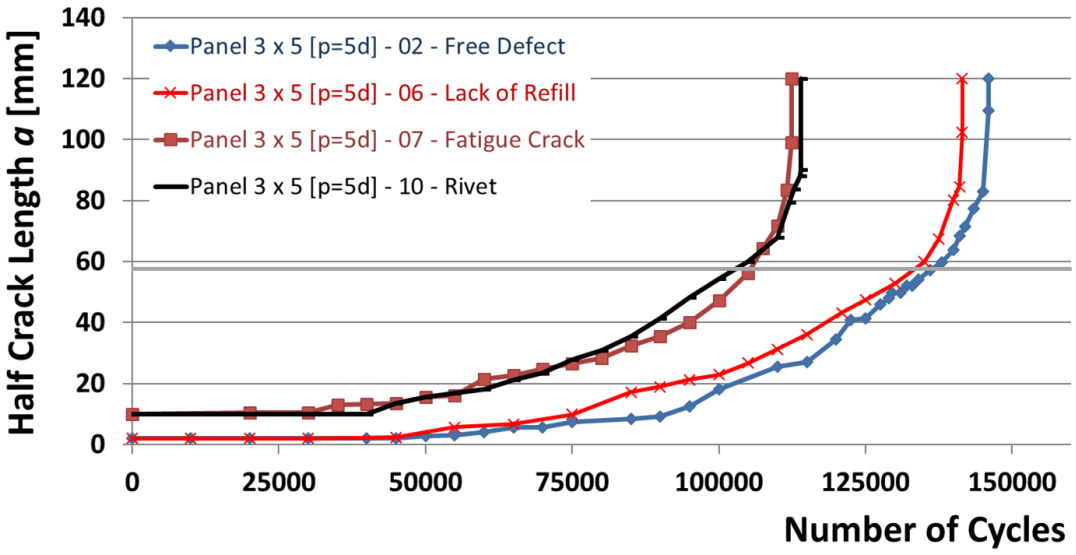

Figure 6.3. Fatigue crack growth for different failure scenarios.

Crack Configuration					
Number of Cycles	**Failure Scenario: Defect Free**				
	SW_{3x1}	SW_{3x2}	SW_{3x3}	SW_{3x4}	SW_{3x5}
0 (initial Crack)					
$2a_i$ →55000 $2a_1$ →115000					
$2a_1$ →125000					
Number of Cycles	**Failure Scenario: Lack of Refill**				
	SW_{3x1}	SW_{3x2}	SW_{3x3}	SW_{3x4}	SW_{3x5}
Initial Crack					
$2a_i$ →45000 $2a_1$ →102500					
$2a_1$ →120000					
Number of Cycles	**Failure Scenario: Fatigue**				
	SW_{3x1}	SW_{3x2}	SW_{3x3}	SW_{3x4}	SW_{3x5}
0 (initial Crack)	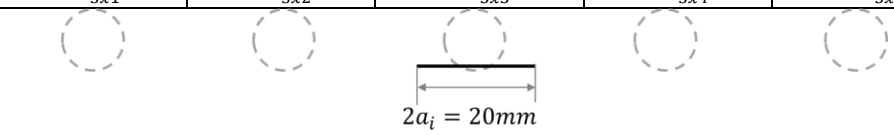				
$2a_1$ →105000	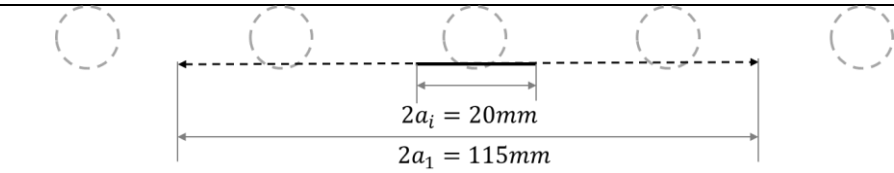				
$2a_2$ →107500 $2a_2$ →114044	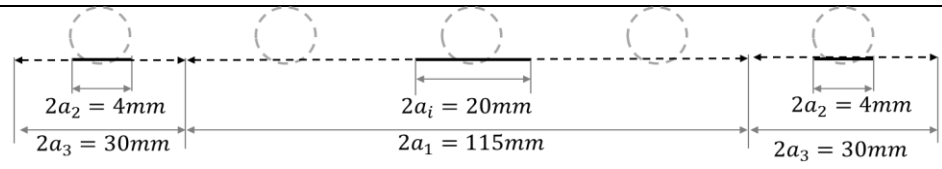				

Figure 6.4. Crack configuration/propagation for the different failure scenarios.

Number of Cycles	Failure Scenario: Riveting				
	SW_{3x1}	SW_{3x2}	SW_{3x3}	SW_{3x4}	SW_{3x5}
0 (initial Crack)			$2a_i = 20mm$		
$2a_1$ →105000			$2a_i = 20mm$ $2a_1 = 40mm$ $2a_3 = 115mm$		
$2a_2$ →107500 $2a_2$ →114044	$2a_4 = 4mm$ $2a_5 = 30mm$		$2a_i = 20mm$ $2a_1 = 40mm$ $2a_3 = 115mm$		$2a_4 = 4mm$ $2a_5 = 30mm$

Figure 6.4. Crack configuration/propagation for the different failure scenarios.

The crack growth data generated may be useful in assessing the critical defected in service life of refill FSSW panels. Although, this work is generic in nature, the results can be appropriate to compare to the current technology of assembly with different joint processes. In the following sections, the fatigue crack failure scenario is considered to be an initial crack, once the crack nucleated at the sharp corner of the defect and stably propagated towards the edge of the panel. The crack in the Lack of Refill and Free-Defect failure scenarios have initiated at the outer spot welds in a multiple site damage condition; consequently, fatigue crack growth analyses became untrustworthy.

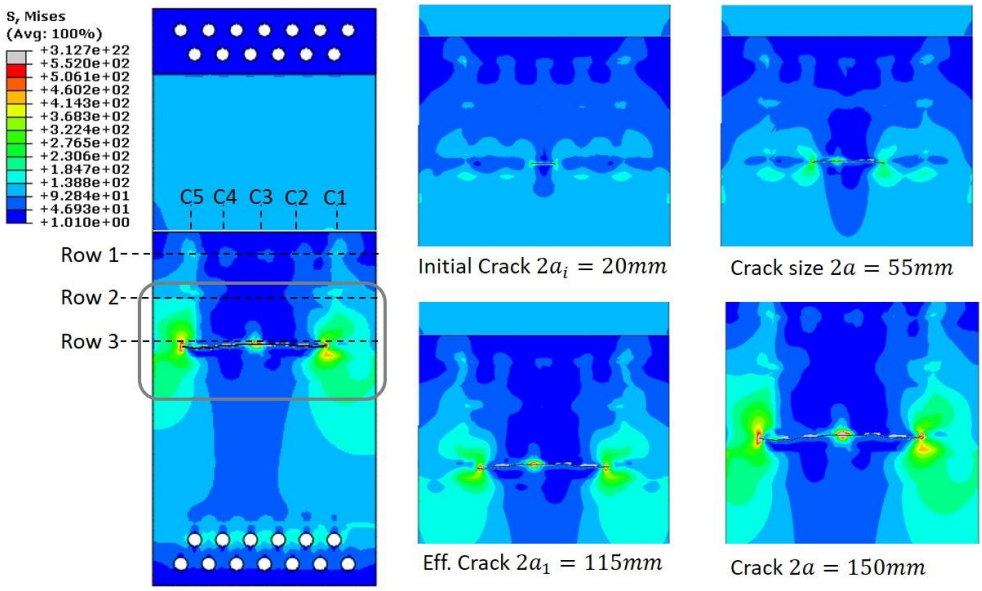

Figure 6.5. Stress distribution at crack tip for different crack lengths.

6.4.2. Influence of the spot weld row distance in crack propagation

This study is extended for the analyses of different joint configurations, namely, spot weld row distances in larger panels. The initial crack is assumed to start in front of the spot weld SW_{3x3} in the lower plate with a length of $2a_0 = 20mm$, which simulates the fatigue crack propagation failure scenario, where the crack symmetrically propagates in both directions

perpendicular to the load direction. The effort of this section is to investigate the behaviour of the joint configuration in cracked panels under constant amplitude loads and evaluate the fatigue crack propagation model; reliable numerical models for fatigue damage prediction can provide the required background for a comprehensive understanding of fatigue phenomena [147].

Before analysing the influence of the spot weld row distance in crack propagation panels in terms of crack length vs. number of cycles is achieved, as shown in Fig. 6.6, the comparison between the experimental results and numerical results must be performed (solid lines represent the experimental results, and the dashed lines represent the results of the numerical models). For this purpose, two geometries were experimentally and numerically analysed: Panel 3 x 5 [p=2d] and Panel 3 x 5 [p=5d]. Table 6.5 lists the results in terms of the number of cycles until failure. Reasonable accuracy between the numerical models and the experimental results is achieved; however, some instabilities occur for large cracks. Consequently, the crack growth rate is high, and the number of cycles to failure is low. The numerical model is capable of simulating fatigue crack propagation, and the model can be extended to different boundary conditions.

The effect of the spot weld row distance is investigated using an FE analysis for the welded panels. For a small pitch distance, the predicted life of the panel is low. An increase in the pitch distance causes a constant increase in the life of the panel until the pitch distances $p = 5d$ and $p = 8d$ are attained. Although an increase in the fatigue life occurs, this increase is not sensible. The increase in the fatigue life for longer pitch distances is a consequence of the lower bending stress in the panel; when the pitch distance decreases, the overlap decreases and the bending factor increases, as described in Chapter 4.

Table 6.5. Fatigue crack propagation test programme for numerical and experimental analyses.

Sample	Fracture mode	Number of cycles
Panel 3 x 5 [p=2d] – 13	Tension – 3rd row LP	93509
Panel 3 x 5 [p=2d] – 14	Tension – 3rd row LP	90689
Panel 3 x 5 [p=2d] – 15	Tension – 3rd row LP	94608
Panel 3 x 5 [p=5d] – 07	Tension – 3rd row LP	112957
Panel 3 x 5 [p=5d] – 08	Tension – 3rd row LP	109556
Panel 3 x 5 [p=5d] – 09	Tension – 3rd row LP	107390
Num. Panel 3 x 5 [p=2d]	Tension – 3rd row LP	88957
Num. Panel 3 x 5 [p=3.5d]	Tension – 3rd row LP	103001
Num. Panel 3 x 5 [p=5d]	Tension – 3rd row LP	109207
Num. Panel 3 x 5 [p=8d]	Tension – 3rd row LP	114740

Fig. 6.7 illustrates the stress intensity factor solutions vs. the normalised crack length for an unstiffened panel. As expected, the β-*solutions* increase as the crack increases. At the initial crack propagation stage, the β-*solutions* lightly decreases when the pitch distance increases. As the length of the crack changes from its initial length, the difference in β increases. As the structure does not reveal any stiffener, the β-*solutions* rapidly increase at the point that the crack length is sufficiently large for the *K-factors* to fracture the sample. Therefore, the β-*solutions* and the crack growth behaviour resemble the crack growth of the panel joined by refill FSSW.

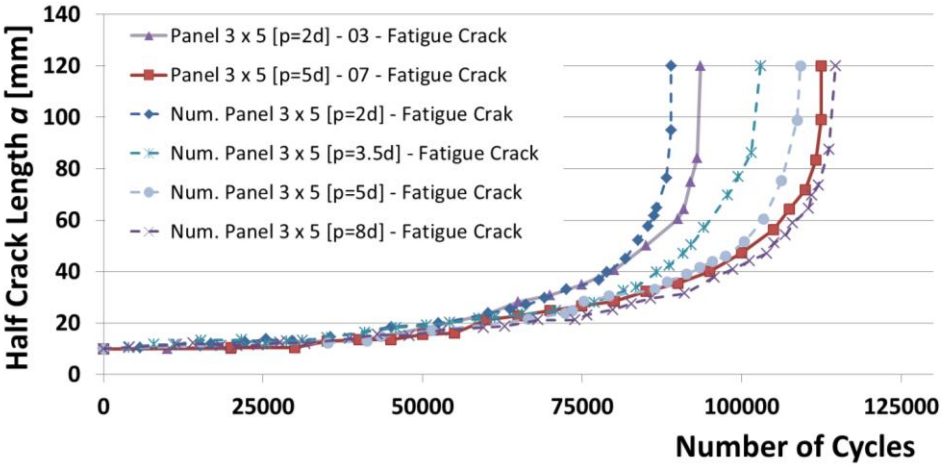

Figure 6.6. Fatigue crack growth for the different joint configuration – spot weld row distance.

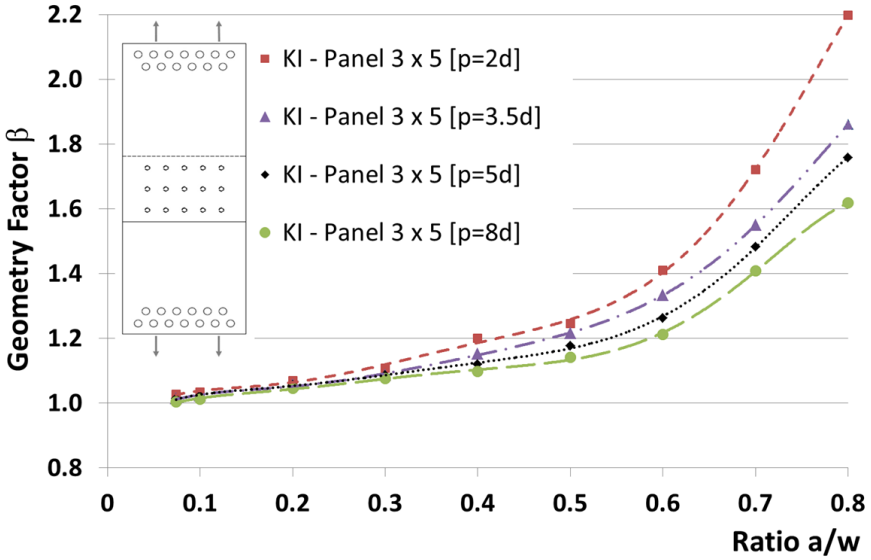

Figure 6.7. Stress intensity factor for different joint configurations – spot weld row distance.

6.4.3. Results of initial crack size

The objective of this section is to check the potential of the fatigue crack growth model and understand the fatigue failure of refill FSSW using a numerical model. Additional experimental curves for similar conditions were not available. Thus, the comparisons among the numerical predictions do not present a range of experimental scatter. The influence of initial crack size is investigated with Panel 3 x 5 [p=5d]. One of the main advantages of XFEM models is that they require few changes in the code to perform the simulations with several boundary conditions.

An essential aspect of fatigue crack growth analysis is the selection of initial crack size (a_i). A large number of cycles in fatigue crack growth occur when the crack is smaller than a few millimetres. The correct choice of the initial crack size is dependent on the size of the initial defect. However, the visualisation and measurement of these defects are very difficult even with sophisticated inspection equipment. In addition, cracks initiate at hidden locations at the faying surface of the sheets. Thus, a larger a_i is more conservative; as discussed by several authors, the SIF for a small crack is limited and compromises the application of the similarity principle. Application of the concept of a stress intensity factor to an aircraft structure when the size of a crack is on the order of 1 to 3 mm is recommended numerical practice [1].

In this calculation, the most conservative scenario is to assume that a_i is a through the thickness crack with a length of $2a_i = 4\,mm$ that grows in both directions. This initial crack was observed during the experimental fatigue crack growth study. The numerical simulations are based on the following data and loading conditions:

- Initial crack: $1.96mm$ in experiment;
- Initial crack: $2mm$, $5mm$, $7.5mm$ and $10mm$ (numerical models);
- Constant amplitude load: $S_{max} = 88MPa, R = 0.1$

In Fig. 6.8A, the fatigue crack growth for all simulated initial cracks are illustrated. For refill FSSW, the crack growth rate in the last part of the fatigue crack growth period is relatively high; the critical crack size has a minimal effect on this crack growth period and the final number of cycles. The entire range of the simulation in each case yields interesting results in terms of crack growth for a valid initial crack length. For the same crack length, the number of cycles considerably increases for a smaller initial crack. For example, for a critical crack length of $a_c = 60mm$, the number of cycles significantly decreases to 211500, 161582, $139207, and\ 109587$ for $a_i = 2mm$, $5mm$, $7.5mm$ and $10mm$, respectively. The crack growth from $50mm$ to $100mm$ increases the fatigue life by 10%, as the crack growth rate in this region is higher than the crack growth rate in other regions. If the initial crack increases from $2mm$ to $10mm$, the crack growth increases approximately four times due its very low crack growth rate. These results have a practical interest. In addition, the fatigue crack model considers that a substantial part of the crack growth life is consumed by the crack growth of small cracks. As described in Fig. 6.8B.

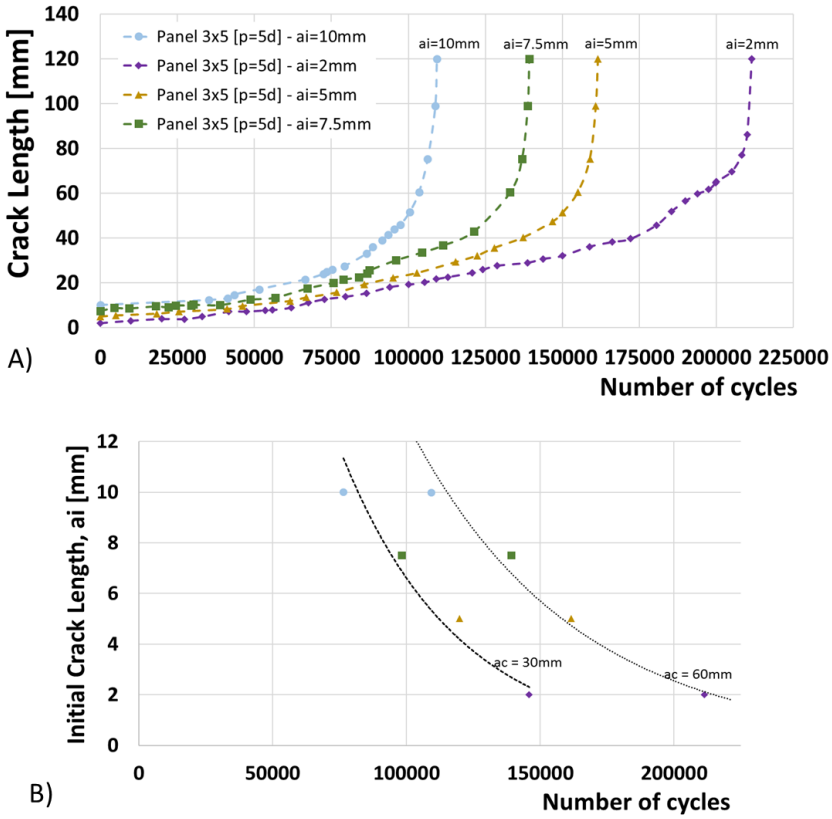

Figure 6.8. A) Study of the initial crack influence on the fatigue crack growth; B) Influence of the initial crack size for different crack critical lengths.

6.4.4. Residual strength of refill FSSW

Defining several critical crack lengths for a given fracture toughness K_C is a typical method for evaluating the relationship between crack length and fracture strength. The *R*-curve approach is the more accurate methodology for describing the residual strength in riveted joints. Due to the lack of data, the residual strength in refill FSSW is calculated considering the abrupt failure criterion, where the fracture occurs when the stress intensity factor at the crack tip attains or exceeds the fracture toughness of the material ($K \geq K_C$). This approach is based on classical methodology for riveting in monolithic aluminium sheets; it was modified to employ the particularities of refill FSSW, namely, to describe the stress state at the spot weld nugget.

In this study, the development of the residual strength considers the fatigue crack growth numerical model, in which the *K-factors* connect the local stress state of the panel with the crack geometry, joint configuration and the nominal stress. Note that the influence of the secondary bending and the transferability of the *K-factors* to the residual strength is solved per se, as the *K-factors* were developed with the same joint configuration. As previously described, the residual strength can be estimated by Eq. 6.6.

In general, the material toughness depends on the thickness. When the thickness is such that the crack tip plastic zone size is on the order of the plate thickness, the toughness attains a maximum value $K_{C(\max)}$, the critical value of the fracture toughness in this study is $K_C = 75MPa, \text{and } \sqrt{m}$ was obtained for an unstiffened riveted panel with similar thickness and width [147]. The stress level corresponded to the design limit load considered for AA2024-T3 is $240MPa$ [4]. The joint geometries that are analysed in this section were identical to the joint geometries of the panels investigated in section 6.4.2: Panel 3 x 5 [p=2d], Panel 3 x 5 [p=3.5d], Panel 3 x 5 [p=5d] and Panel 3 x 5 [p=5d].

The calculated residual strength curves for all joint configurations are shown in Fig. 6.9. The principal indication from these curves is to maintain a minimum fracture strength to avoid catastrophic failure of the structure. In all joint configurations, the residual strength exceeds the limit load. The fracture strength abruptly decreases when the crack extends, and the crack propagation may become unstable in a fast uncontrollable manner, which causes complete fracture of the component. Due to the lack of an inherent feature in this single load path, the stress intensity factor decreases, as consequence, it increases the fatigue life. In addition, a substantial difference exists between the residual strength curves at any crack length; this difference is also related to the fracture toughness of the material. Thus, an increase in K_C causes an increase in σ_f.

The discussion of the results must consider the gain in residual strength with a higher distance between two spot weld rows; it represents a larger overlap area but higher manufacturing costs and weight are expected. The secondary bending is lower with a higher distance of the spot weld rows; the results emphasise the influence of the secondary bending, where a change in the design represents a significantly higher integrity strength of the joint. As the bending stresses act in the joint, Panel 3 x 5 [p=8d] offers a higher residual strength than the panels with lower distances in the spot weld rows. The crack length-life data are cross-correlated with the residual strength-crack length data.

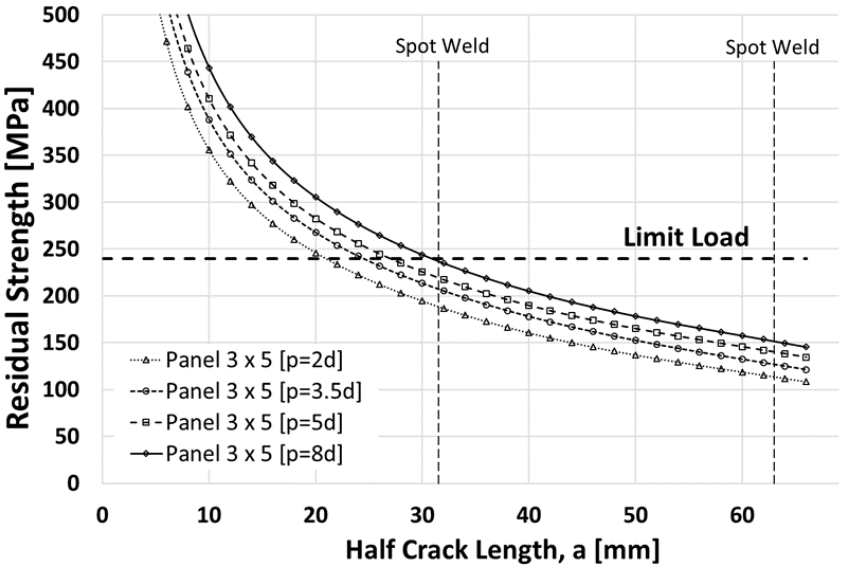

Figure 6.9. Residual strength of Panel 3 x 5 produces by refill FSSW.

6.5. Concluding remarks

The crack growth data that are generated in this chapter may be useful in assessing the critical crack length in–service and establishing inspection intervals. Although this study was generic, the results should be directly applicable to current operation structures.

The failure scenario investigation demonstrated that the crack nucleated from the hook profile at the faying surface may be considered as the critical defect in refill FSSW. The implementation of its defect produces joints with a significant lower fatigue life. In integrally welded structures, crack initiation may be attributed to the weld defects and the edges and macrostructure features at hidden locations or the faying surface of the sheets due to local stress concentration. These situations are undesirable but cannot be avoided. Regarding the damage tolerance philosophy, they must be considered to provide reliable fatigue predictions.

The joint configuration and the mutual interference of the crack length and spot welds comprises a very complex scenario due to the deep and intricate influence of these parameters on the residual strength. Consequently, addressing this scenario requires significant expertise of FE modelling. The fatigue crack growth has provided accurate results in terms of fatigue crack propagation; it can be extended to several joint configurations and can minimise the number of experimental tests. The variation in the *K-factors* for different joint configurations proves the influence of the secondary bending, where high bending factors yield a high crack growth rate and low fatigue life.

The damage tolerance of a structure is based on the progress of degradation/damage accumulation until a finite crack occurs, and the crack propagates until the failure process culminates in a complete failure of the structure. As secondary bending has a significant influence on the residual strength; in addition, an increases the pitch distance in a row, the bending factor decreases. The ultimate tensile strength decreases with an increase in bending. The residual calculations suggested the need for a compromise between the manufacturing and weight costs and the strength of the joint [141].

Chapter 7.
Conclusions

7.1. Summary

In terms of the design optimisation and safety of airframe structures, fatigue is the primary damage mechanism in an aeronautical structure, and a typical fatigue failure unexpectedly occurs. The airframe design is closely correlated with interactions between cracks and fastened components. The extensive use of integral structural welded joints represents an important challenge of the damage tolerance design, where a complete comprehension of crack initiation and crack growth is mandatory for applying these solid-state processes in the aerospace industry.

Damage tolerance behaviour is considered to be the main issue for the application of these structures and further development of lightweight and cost-effective airplanes. Therefore, the main objectives of this study were to improve the knowledge of the mechanical behaviour and to propose a verified approach to predict the residual strength behaviour of the joints produced by refill FSSW (refer to section 1.2). In this context, this study is ground-breaking work that provides an engineering approach to predicting the design optimisation and methods for obtaining the stress intensity factors and residual strength of refill FSSW panels. A series of sensitive analysis were conducted.

As described in Chapter 4, the structural integrity of the spot weld lap joint evidences a complex local stress state under tensile loading. The structural integrity is a result of the transfer load from the upper plate to the lower plate, secondary bending, stress concentration, bonding ligament and friction between the plates. A suitable design of the lap joint configuration may significantly improve the service life. The design is the most important factor that directly affects the structural integrity of the joint and the fatigue life. Although a single-spot weld row presents very poor fatigue strength and should be avoided in structures, uniaxial tests on small specimens are useful for deriving the key design curves in terms of load vs. displacement (refer to section 4.2). Multiple-spot weld rows improve the fatigue strength of the joint. In general, larger distances between rows imply higher fatigue properties of the lap joints, are primarily associated with a reduction of the secondary bending promoted by the eccentricity of the load path and amplifies the stress concentration of the spot weld (refer to section 4.5). Table 4.10 summarises the minimum or optimum distances developed for a spot weld lap joint; in addition, the usual distances for rivets are also informed.

In Chapter 5, a detailed elastic-plastic and elastic-perfectly plastic FE model was developed to obtain *K-factors* and understand the crack growth mechanism in refill FSSW for single-, double- and triple-spot weld rows. A 3D XFEM numerical technique was applied to achieve the *K-factors* solutions (refer to section 5.2). Complete 3D numerical models were simulated for a remote tension stress, which produced a combined tension and bending stress. The influence of secondary bending can be easily analysed and determined with this numerical model, which has provided a simple and powerful means to understand the crack profile and crack growth behaviour under combined tension and bending loading. The crack closure concept has led to

the ΔK_{eff} concept, which is helpful in accounting for the stress ratio R. The $\Delta K_{eff}(R)$ equations are based on empirical evidence. Prior to the investigation of *K-factors* solutions, experimentally understanding the crack initiation and propagation until final failure was necessary. The fractured surface analysis using the SEM enables the fracture reconstruction for the larger part of the fatigue crack (refer to section 5.1). In all cases, the fatigue crack initiation started at the hook tip. Therefore, the hook curvature was considered to be a stress intensity factor.

The crack growth data that was generated in Chapter 6 may be useful in assessing the critical crack length in–service and establishing the inspection intervals. Although this study was generic, the results should be directly applicable to current operation structures. The failure scenario investigation demonstrated that the crack nucleated from the hook profile at the faying surface may be considered as the critical fracture mode in refill FSSW. In integrally welded structures, crack initiation from weld defects and the edges and macrostructure features at hidden locations or at the faying surface of the sheets is possible due to local stress concentration. These situations are undesirable but cannot be avoided. Regarding damage tolerance philosophy, they must be considered to provide reliable fatigue prediction (refer to sections 6.1 and 6.4). The fatigue crack growth has provided accurate results in terms of fatigue crack propagation; it can be extended to several joint configurations and can minimise the number of experimental tests. The damage tolerance of a structure is based on the progress of degradation/damage accumulation until a finite crack occurs, and the crack propagates until the failure process culminates in complete failure of the structure. Secondary bending has a significant influence on the residual strength, and an increase the pitch distance in a row causes a decrease in the bending factor. The ultimate tensile strength decreases with an increase in bending (refer to section 6.4). The residual strength calculations suggested that a compromise between the manufacturing and weight costs and the strength of the joint is necessary.

In Chapter 6, a fatigue crack growth numerical model was developed. Agreement with the experimental data in terms of fatigue crack growth life has been achieved (refer to sections 6.3 and 6.4). Considering this model, the amount of preliminary experiments can be reduced, which conserves time and cost. This model can be run for a short time throughout the formation of the joint. This step is an important step towards various design optimisations in unknown design condition. In addition, a comprehensive understanding of the structural behaviour and interaction with the crack growth, which enable significant improvement of the integrity and quality of the joint, can be achieved.

7.2. Conclusions

From the experimental and numerical analysis that was performed during this study, the following conclusions are formed:

- Refill FSSW showed high reproducibility, with relatively low standard deviations within the investigated range of parameters. Once the stability of the process was proven, further investigation of the weld parameter optimisation was performed. More important than obtaining the optimised weld parameters is establishing a correlation between the weld process and the macrostructure features and joint integrity. In this context, the typical flaw observed in the characterisation of the spot weld was a lack of refill; it is present at the

interface between the SZ and the TMAZ, at which the outer surface of the sleeve penetrates into the plates. In addition, the hook profile influences the failure load properties in high-mechanical-strength welds; the main geometrical feature is the hook tip curvature. In all fracture modes, the crack initiated at the hook tip;

- The design optimisation can be effectively supported by numerical modelling. A parametric study can be easily performed to determine the performance limits of a given structural design;
- The distance from the sheet edge has a sensible effect on the fatigue life; where the minimum distance has to be observed, and increasing the sheet edge distance from the minimum distance does not represent better fatigue properties. Multiple-spot weld rows improve the fatigue strength of the joint. In general, larger distances between rows imply higher fatigue properties of the lap joints, which is primarily associated with a reduction in the secondary bending promoted by the eccentricity of the load path and amplifies the stress concentration of the spot weld. The distance of the spot weld in row is based on static strength, in this case, an optimum distance was developed. If the distance decreases, the structural integrity of the joint also decreases; when this distance increases, the integrity decreases;
- In the coupon-level analysis of crack growth, the first part was dedicated to the stress intensity factor. Once the fatigue crack initiation started at the hook tip, it was considered to be a stress intensity factor. Note fracture mode I (opening) and fracture mode II (shearing) at the critical locations (points A and B, Fig. 5.16) and fracture mode III (tearing) at the critical location points C and D of Fig. 5.16. The welding parameters can change the hook geometry and the *K-factors* solutions;
- The combined tension and bending stress promoted by the eccentricity of the load path under a remote tension stress can be easily assessed by the 3D-XFEM numerical model in this study. It has provided an easy and powerful investigation tool to understand the crack shape and crack growth behaviour under the influence of the secondary bending in terms of the stress intensity factors. An increase in the bending factor by the reduction of the number of the spot weld rows and/or distances between spot weld rows causes an increase in the local tensile, which causes a decrease in the fatigue life of the joint;
- The study of the mechanical behaviour was extended to panels produced by refill FSSW. The design for damage tolerance is necessary from a safety point of view. Thus, significant attention should be paid to failure scenarios and proving that a structure can tolerate the crack growth;
- The fatigue crack growth numerical model is consistent with the experimental data for larger panels. An analysis of different joint configurations and the initial crack was possible. An increase in the distance between the spot weld rows caused an increase in the fatigue life. This model can assist engineers in developing structural concepts that will assure slow crack growth, less frequent inspection and limited repairs.

References

[1] J. Schijve, Fatigue of Structures and Materials, 2 ed., Springer Netherlands, 2009.

[2] J. Schijve, Fatigue damage in aircraft structures, not wanted, but tolerated?, International Journal of Fatigue, 31 (2009) 998-1011.

[3] E. Seib, Residual strength analysis of laser beam and friction stir welded aluminium panels for aerospace applications, in: Institute for Materials Research, Technischen Universität Hamburg-Harburg, Hamburg-Harburg, 2006, pp. 2012.

[4] X. Zhang, Y. Li, Damage Tolerance and Fail Safety of Welded Aircraft Wing Panels, AIAA Journal, 43 (2005) 1613-1623.

[5] A. Theos, Design and analysis of welded aircraft wing panels, in: School of Engineering, Cranfield Univesity, Cranfield, 2005.

[6] R. De Rijck, S. Fawaz, A Simplified Approach for Stress Analysis of Mechanically Fastened Joints, in: Fourth Joint Dod/FAA/NASA Conference on Aging Aircraft, 2000.

[7] G. Meo, Design Stress Analysis and Cost Studies of Welded Aircraft Structures, in: School of Applied Science, Cranfiled University, Cranfield, UK, 2000.

[8] G. Bussu, Damage tolerance of welded aluminium aircraft structures, in: School of Applied Sciences, Cranfield University, Cranfield, 2000.

[9] C. Vidal, V. Infante, P. Vilaça, Assessment of improvement techniques effect on fatigue behaviour of friction stir welded aerospace aluminium alloys, Procedia Engineering, 2 (2010) 1605-1616.

[10] L.C. Campanelli, U.F.H. Suhuddin, A.Í.S. Antonialli, J.F. dos Santos, N.G. de Alcântara, C. Bolfarini, Metallurgy and mechanical performance of AZ31 magnesium alloy friction spot welds, Journal of Materials Processing Technology, 213 (2013) 515-521.

[11] G. Pieta, J. dos Santos, T.R. Strohaecker, T. Clarke, Optimization of friction spot welding process parameters for AA2198-T8 sheets, Materials and Manufacturing Processes, 29 (2014) 934-940.

[12] A.H. Plaine, A.R. Gonzalez, U.F.H. Suhuddin, J.F. dos Santos, N.G. Alcântara, The optimization of friction spot welding process parameters in AA6181-T4 and Ti6Al4V dissimilar joints, Materials & Design, 83 (2015) 36-41.

[13] M.D. Tier, T.S. Rosendo, J.F. dos Santos, N. Huber, J.A. Mazzaferro, C.P. Mazzaferro, T.R. Strohaecker, The influence of refill FSSW parameters on the microstructure and shear strength of 5042 aluminium welds, Journal of Materials Processing Technology, 213 (2013) 997-1005.

[14] W. Huang, T.J. Wang, Y. Garbatov, C.G. Soares, Fatigue reliability assesment of riveted lap joint of aircraft structures, in: Iternational Journal of Fatigue, 43 (2012) 54-61.

[15] R.S. Mishra, Z.Y. Ma, Friction stir welding and processing, Materials Science and Engineering: R: Reports, 50 (2005) 1-78.

[16] R. Nandan, T. DebRoy, H.K.D.H. Bhadeshia, Recent advances in friction-stir welding – Process, weldment structure and properties, Progress in Materials Science, 53 (2008) 980-1023.

[17] G. Çam, Friction stir welded structural materials: beyond Al-alloys, International Materials Reviews, 56 (2011) 1-48.

[18] T. DebRoy, H.K.D.H. Bhadeshia, Friction stir welding of dissimilar alloys – a perspective, Science and Technology of Welding and Joining, 15 (2010) 266-270.

[19] K.P. Mehta, V.J. Badheka, A Review on Dissimilar Friction Stir Welding of Copper to Aluminum: Process, Properties, and Variants, Materials and Manufacturing Processes, 31 (2016) 233-254.

[20] T.-Y. Pan, Friction Stir Spot Welding (FSSW) - A Literature Review, 2007.

[21] P.A. Colegrove, H.R. Shercliff, 3-Dimensional CFD modelling of flow round a threaded friction stir welding tool profile, Journal of Materials Processing Technology, 169 (2005) 320-327.

[22] R. Crawford, G.E. Cook, A.M. Strauss, D.A. Hartman, M.A. Stremler, Experimental defect analysis and force prediction simulation of high weld pitch friction stir welding, Science and Technology of Welding and Joining, 11 (2006) 657-665.

[23] P. Avinash, M. Manikandan, N. Arivazhagan, K.D. Ramkumar, S. Narayanan, Friction Stir Welded Butt Joints of AA2024 T3 and AA7075 T6 Aluminum Alloys, Procedia Engineering, 75 (2014) 98-102.

[24] U. Suhuddin, L. Campanelli, M. Bissolatti, H. Wang, R. Verastegui, J.F. dos Santos, A review on microstructural and mechanical properties of friction spot welds in Al-based similar and dissimilar joints, in: Proceedings of the 1st International Joint Symposium on Joining and Welding, Woodhead Publishing, 2013, pp. 15-21.

[25] S.T. Amancio-Filho, A.P.C. Camillo, L. Bergmann, J.F. dos Santos, S.E. Kuri, N.G. Alcântara, Preliminary investigation of the microstructure and mechanical behaviour of 2024 aluminium alloy friction spot welds, Mater Trans, 52 (2011) 184-190.

[26] U.F.H. Suhuddin, V. Fischer, J.F. dos Santos, The thermal cycle during the dissimilar friction spot welding of aluminum and magnesium alloy, Scripta Materialia, 68 (2013) 87-90.

[27] G.E.T.t.D.S. MacKenzie, Handbook of Aluminum - Volume 2 Alloy Production and Materials Manufacturing, Marcel Dekker, Inc., 270 Madison Avenue, New York, NY 10016, 2003.

[28] B.S. Parra, V.T.; Alcântara, N.G.; Rosendo, T.; dos Santos, J.F., An Invesigation on Friction Spot Welding in AA6181-T4 Alloy, Tecnol. Metal. Mater. Miner., (2011) 6.

[29] A.A.M. da Silva, J.F. dos Santos, T.R. Rosendo, F.D. Ramos, C.C.P. Mazzaferro, M.A.D. Tier, L. Bergmann, J.A.E. Mazzaferro, T.R. Strohaecker, Performance Evaluation of 2-mm Thick Alclad AA2024 T3 Aluminium Alloy Friction Spot Welding, in: AeroTech Congress & Exhibition, SAE Los Angeles, California, USA, 2007.

[30] A. Ali, M.W. Brown, C.A. Rodopoulos, S. Gardiner, Characterization of 2024-T351 friction stir welding joints, J Fail. Anal. and Preven., 6 (2006) 83-96.

[31] U. Suhuddin, V. Fischer, F. Kroeff, J.F. dos Santos, Microstructure and mechanical properties of friction spot welds of dissimilar AA5754 Al and AZ31 Mg alloys, Materials Science and Engineering, 590 (2014) 384-389.

[32] Y.H. Yin, A. Ikuta, T.H. North, Microstructural features and mechanical properties of AM60 and AZ31 friction stir spot welds, Materials & Design, 31 (2010) 4764-4776.

[33] T.S. Rosendo, Estudo do Desempenho Mecânico de Solda(s) Ponto por fricção (FSpW) da Liga AA6181-T4, in: Programa de Pós-Graduação em Engenharia de Minas, Metalúrgica e de Materiais, Universidade Federal do Rio Grande do Sul, Porto Alegre, 2009, pp. 132.

[34] Z. Shen, X. Yang, Z. Zhang, L. Cui, T. Li, Microstructure and failure mechanisms of refill friction stir spot welded 7075-T6 aluminum alloy joints, Mater Design, 44 (2013) 476-486.

[35] T. Rosendo, B. Parra, M.A.D. Tier, A.A.M. da Silva, J.F. dos Santo, T.R. Strohaecker, N.G. Alcântara, Mechanical and microstructural investigation of friction spot welded AA6181-T4 aluminium alloy, Materials and Design, 32 (2011) 16.

[36] H.M. Rao, J.B. Jordon, M.E. Barkey, Y.B. Guo, X. Su, H. Badarinarayan, Influence of structural integrity on fatigue behavior of friction stir spot welded AZ31 Mg alloy, Materials Science and Engineering: A, 564 (2013) 369-380.

[37] J.Y. Cao, M. Wang, L. Kong, L.J. Guo, Hook formation and mechanical properties of friction spot welding in alloy 6061-T6, J Mater Process Technol, 230 (2016) 254-262.

[38] D. Broek, Elementary engineering fracture mechanics, Springer Netherlands, Netherlands, 1986.

[39] T.L. Anderson, Fracture Mechanics: Fundamentals and Applications, 2005.

[40] G.R. Irwin, Analysis of Stress and Strain Near the End of a Crack Traversing a Plate, Journal of Applied Mechanics, 24 (1957) 5.

[41] A.A. Griffith, The Phenomena of Rupture and Flow in Solids, Philosophical Transactions of the Royal Society of London A: Mathematical, Physical and Engineering Sciences, 221 (1921) 163-198.

[42] G.R. Irwin, The crack extension force for a crack at a free surface boundary, in: N.R.L.R. 5120 (Ed.), 1958.

[43] G.P. Cherepanov, Crack propagation in continuous media: PMM vol. 31, no. 3, 1967, pp. 476–488, Journal of Applied Mathematics and Mechanics, 31 (1967) 503-512.

[44] J.R. Rice, A Path Independent Integral and the Approximate Analysis of Strain Concentration by Notches and Cracks, Journal of Applied Mechanics, 35 (1968) 379-386.

[45] J.W. Hutchinson, Singular behavior at the end of a tensile crack in a hardening material, Journal of the Mechanics and Physics of Solids, 16 (1968) 13-31.

[46] J. Rice, G.F. Rosengren, Plane Strain Deformation Near a Crack Tip in a Power-Law Hardening Material, Journal of the Mechanics and Physics of Solids, 16 (1968) 1-12.

[47] F.A. McClintock, A Criterion for Ductile Fracture by the Growth of Holes, Journal of Applied Mechanics, 35 (1968) 363-372.

[48] P.C.P. J.W. Hutchinson, Elastic-Plastic Fracture, in: ASTM-STP-668 American Society for Testing and Materials, Philadelphia, 1979.

[49] A. Skorupa, M. Skorupa, T. Machniewicz, A. Korbel, Fatigue crack location and fatigue life for riveted lap joints in aircraft fuselage, International Journal of Fatigue, 58 (2014) 209-217.

[50] P. Paris, F. Erdogan, A Critical Analysis of Crack Propagation Laws, Journal of Basic Engineering, 85 (1963) 528-533.

[51] M.C.Y. Niu, Airframe Structural Design: Practical Design Information and Data, 07/01 ed., Cambridge University Press, 2016.

[52] X.-K. Zhu, J.A. Joyce, Review of fracture toughness (G, K, J, CTOD, CTOA) testing and standardization, Engineering Fracture Mechanics, 85 (2012) 1-46.

[53] T.M. M. Skorupa, J. Schijve, A. Skorupa, A. Korbel, Measurements of Rivet Flexibility and Load Trasfer in a Lap Joint, Solid Mechanics and Its Applications, 189 (2012) 63-69.

[54] W. Elber, The Significance of Fatigue Crack Closure, Engineering Fracture Mechanics, 2 (1970) 37-45.

[55] L.F.M. Silva, J.P.M. Gonçalves, F.M.F. Oliveira, P.M.S.T. de Castro, Multiple-site damage in riveted lap-joints: experimental simulation and finite element prediction, Internation Journal of Fatigue, 22 (2000) 319-338.

[56] P.M.G.P. Moreira, P.F.P. de Matos, P.P. Camanho, S.D. Pastrama, P.M.S.T. de Castro, Stress intensity factor and load transfer analysis of a cracked riveted lap joint, Materials & Design, 28 (2007) 1263-1270.

[57] R. De Rijck, Stress Analysis of Fatigue Cracks in Mechanically Fastened Joints: An analytical and experimental investigation, in: DUP Science, Technische Universiteit Delft, The Netherlands, 2005, pp. 316.

[58] H. Vlieger, The residual strength characteristics of stiffened panels containing fatigue cracks, Engineering Fracture Mechanics, 5 (1973) 447-477.

[59] J.P. Gallagher, F.J. Giessler, A.P. Berens, USAF for Damage Tolerant Design Handbook: Guidelines for the Analysis and Design of Damage Toleant Aircraft Structures, National Technical Reports, USA, 2002.

[60] A. International, ASTM E561-15a, in: Standard Test Method for KR Curve Determination, ASTM, West Conshohocken, PA, 2015.

[61] N. Sukumar, N. Moës, B. Moran, T. Belytschko, Extended finite element method for three-dimensional crack modelling, International Journal for Numerical Methods in Engineering, 48 (2000) 1549-1570.

[62] R.S. Barsoum, Triangular quarter-point elements as elastic and perfectly-plastic crack tip elements, International Journal for Numerical Methods in Engineering, 11 (1977) 85-98.

[63] J.E. Akin, The generation of elements with singularities, International Journal for Numerical Methods in Engineering, 10 (1976) 1249-1259.

[64] A. Carpinteri, M. Paggi, N. Pugno, Numerical evaluation of generalized stress-intensity factors in multi-layered composites, International Journal of Solids and Structures, 43 (2006) 627-641.

[65] T. Belytschko, T. Black, Elastic crack growth in finite elements with minimal remeshing, International Journal for Numerical Methods in Engineering, 45 (1999) 601-620.

[66] J.M. Melenk, I. Babuška, The partition of unity finite element method: Basic theory and applications, Computer Methods in Applied Mechanics and Engineering, 139 (1996) 289-314.

[67] T. Strouboulis, I. Babuška, K. Copps, The design and analysis of the Generalized Finite Element Method, Computer Methods in Applied Mechanics and Engineering, 181 (2000) 43-69.

[68] T. Strouboulis, K. Copps, I. Babuška, The generalized finite element method: an example of its implementation and illustration of its performance, International Journal for Numerical Methods in Engineering, 47 (2000) 1401-1417.

[69] N. Moës, J. Dolbow, T. Belytschko, A finite element method for crack growth without remeshing, International Journal for Numerical Methods in Engineering, 46 (1999) 131-150.

[70] D.J. Cartwright, D.P. Rooke, Approximate stress intensity factors compounded from known solutions, Engineering Fracture Mechanics, 6 (1974) 563-571.

[71] Rybicki E.F., K. M.F., A Finite Element Calculation of Stress Intensity Factors by a Modified Crack Closure Integral., Eng Fract Mech, (1977) 9.

[72] ABAQUS, Abaqus Documentation, Dassault Systèmes, Providence, RI, USA (2018).

[73] NASGRO, Fracture mechanics and fatigue crack growth analysis software reference manual manual, NASA Johnson Space Center and Soutwest Research institute, USA (2018)

[74] AFGROW, Component Object manual, Wright-Patterson air force base, USA(2002).

[75] ESACRACK, Structures user manual, European Space Agency (EASA), Netherlands (2000).

[76] R. Branco, F.V. Antunes, J.D. Costa, A review on 3D-FE adaptive remeshing techniques for crack growth modelling, Engineering Fracture Mechanics, 141 (2015) 170-195.

[77] W.H. Gerstle, L.F. Martha, A.R. Ingraffea, Finite and boundary element modeling of crack propagation in two and three dimensions, Engineering with Computers, 2 (1987) 167-183.

[78] W.H. Gerstle, A.R. Ingraffea, R. Perucchio, Three-dimensional fatigue crack propagation analysis using the boundary element method, International Journal of Fatigue, 10 (1988) 187-192.

[79] L.F. Martha, P.A. Wawrzynek, A.R. Ingraffea, Arbitrary crack representation using solid modeling, Engineering with Computers, 9 (1993) 63-82.

[80] Z. Lu, Y. Xiang, Y. Liu, Crack growth-based fatigue-life prediction using an equivalent initial flaw model. Part II: Multiaxial loading, International Journal of Fatigue, 32 (2010) 376-381.

[81] S. Geniaut, E. Galenne, A simple method for crack growth in mixed mode with X-FEM, International Journal of Solids and Structures, 49 (2012) 2094-2106.

[82] N. Sukumar, D.L. Chopp, E. Béchet, N. Moës, Three-dimensional non-planar crack growth by a coupled extended finite element and fast marching method, International Journal for Numerical Methods in Engineering, 76 (2008) 727-748.

[83] R. Zettler, Section 3 - Material Deformation and joint formation in friction stir welding, in: D. Lohwasser, Z. Chen (Eds.) Friction stir welding: from basics to applications, The welding Institute (TWI), Woodhead Publishing, Cambridge, UK, 2010, pp. 42-72.

[84] S.L. Ferreira, R.E. Bruns, H.S. Ferreira, G.D. Matos, J.M. David, G.C. Brandao, E.G. da Silva, L.A. Portugal, P.S. dos Reis, A.S. Souza, W.N. dos Santos, Box-Behnken design: an alternative for the optimization of analytical methods, Anal Chim Acta, 597 (2007) 179-186.

[85] E.M.M.I. John R. Wagner Jr., Harold F. Giles Jr., Extrusion: The Definitive Processing Guide and Handbook, William Andrew, England, 2012.

[86] Federal Aviation Administration, Battelle Memorial Institute, Metallic materials properties development and standardization (MMPDS-04), Federal Aviation Administration, 2008/2009.

[87] ASM Metals HandBook Volume 2: Properties and Selection: Nonferrous Alloys and Special-Purpose Materials, ASM International, USA, 1992.

[88] ASM Metals HandBook Volume 4: Heating Treating, ASM International, USA, 1992.

[89] ISO 6892, Metallic materials - Tensile testing Part1: Method of a test at room temperature, (2009).

[90] ISO 14324, Resistance spot welding — Destructive tests of welds — Method for the fatigue testing of spot welded joints (2003).

[91] R. Sakin, İ. Ay, Statistical analysis of bending fatigue life data using Weibull distribution in glass-fiber reinforced polyester composites, Materials & Design, 29 (2008) 1170-1181.

[92] P.S. Effertz, V. Infante, L. Quintino, U. Suhuddin, S. Hanke, J.F. dos Santos, Fatigue life assessment of friction spot welded 7050-T76 aluminium alloy using Weibull distribution, International Journal of Fatigue, 87 (2016) 381-390.

[93] A.H. Plaine, U.F.H. Suhuddin, N.G. Alcântara, J.F. dos Santos, Fatigue behavior of friction spot welds in lap shear specimens of AA5754 and Ti6Al4V alloys, International Journal of Fatigue, 91, Part 1 (2016) 149-157.

[94] A. Skorupa, M. Skorupa, Riveted Lap Joints in Aircraft Fuselage: Design, Analysis and Properties (Solid Mechanics and Its Applications), Springer, Netherlands, 2012.

[95] J. Ekh, J. Schön, Load transfer in multirow, single shear, composite-to-aluminium lap joints, Composites Science and Technology, 66 (2006) 875-885.

[96] R.P.G. Müller, An experimental and analytical investigation on the fatigue behaviour of fuselage riveted lap joints: the significance of the rivet squeeze force and a comparison of 2024-T3 and Glare 3, in, Delft University of Technology, Delft, The Netherlands, 1995.

[97] A.M. Brown, P.V. Straznicky, Simulating fretting contact in single lap splices, Int. J. Fatigue, 31 (2009) 375-384.

[98] N. Aslan, Y. Cebeci, Application of Box–Behnken design and response surface methodology for modeling of some Turkish coals, Fuel, 86 (2007) 90-97.

[99] G. Pieta, Aplicação do processo de soldagem a ponto por fricção em estruturas Aeronáuticas: Otimização de Parâmetros de Processo e Avaliação da Integridade das Soldas para a Liga de Alumínio 2198-T8, in: Programa de Pós Graduação em Engenharia de Minas, Metalúrgica e de Materiais, UFRGS, Porto Alegre, 2013, pp. 157.

[100] S.H. Chowdhury, D.L. Chen, S.D. Bhole, X. Cao, P. Wanjara, Lap shear strength and fatigue life of friction stir spot welded AZ31 magnesium and 5754 aluminum alloys, Mater Sci Eng: A, 556 (2012) 500-509.

[101] T. Rosendo, M. Tier, J. Mazzaferro, C. Mazzaferro, T.R. Strohaecker, J.F. Dos Santos, Mechanical performance of AA6181 refill friction spot welds under Lap shear tensile loading, Fatigue & Fracture of Engineering Materials & Structures, (2015) 178-189.

[102] ISO 14273:2000, Specimen dimensions and procedure for shear testing resistance spot, seam and embossed projection welds, (2000).

[103] S.S. Rao, Analysis of three-dimensional problems, in: The Finite Element Method in Engineering, Butterworth-Heinemann, Burlington, 2005, pp. 399-420.

[104] O.C. Zienkiewicz, R.L. Taylor, J.Z. Zhu, The Finite Element Method: its Basis and Fundamentals, seventh ed., Butterworth-Heinemann, Oxford, 2013.

[105] H. Ghiasi, D. Pasini, L. Lessard, Optimum stacking sequence design of composite materials Part I: Constant stiffness design, Composite Structures, 90 (2009) 1-11.

[106] S. Tabatabaei, E. Bedogni, D. Ivanov, S. V. Lomov, MESO-scale damage modelling of textile composite using the embedded element technique and contact algorithm, 2014.

[107] J.H. Schijve, A., The effect of secondary bending on the fatigue strength of 2024-T3 Alclad riveted joints., National Aerospace Laboratory NLR., Netherlands (1969).

[108] H. Vlieger, Results of uniaxial and biaxial tests on riveted fuselage lap joint specimens, in: Proceedings of FAA/NASA International Symposium of Advanced Structural Integrity Methods for Airframe Durability and Damage Tolerance, NASA CP 3274,, Hampton, , 1994, pp. 911–930.

[109] H.-S. L.J., An Engineer´s Viewpoint on Design and Analysis of Aircraft Structural Joints, in: International Conference on Aircraft Damage Assessment and Repair, Melbourne, Autralia, 1991.

[110] R.P.G. Müller, An experimental and analytical investigation on the fatigue behaviour of fuselage riveted lap joints: the significance of the rivet squeeze force and a comparison of 2024-T3 and Glare 3, in: Delft University of Technology, Delft, Delft, The Netherlands, 1995.

[111] H. Tada, P.C. Paris, G.R. Irwin, The Stress Analysis of Cracks Handbook, Third ed., Paris Productions Inc., St. Louis, USA, 2000.

[112] D.P. Rooke, Compendium of stress intensity factors, H.M.S.O., London, England (1970).

[113] Y. Murakami, Stress Intensity Factors Handbook, Pergamon Press, Amsterdam, Netherlands, 1987.

[114] J. Ha, H. Huh, J.H. Song, J.H. Lim, Prediction of failure characteristics of spot welds of DP and trip steels with an equivalent strength failure model, Int.J Automot. Technol., 14 (2013) 67-78.

[115] D.V.T.G. Pavan Kumar, S. Sathiya Naarayan, S. Kalyana Sundaram, S. Chandra, Further numerical and experimental failure studies on single and multi-row riveted lap joints, Engineering Failure Analysis, 20 (2012) 9-24.

[116] A. Lanciotti, C. Polese, Fatigue crack propagation in tensile shear stainless steel spot welded specimens, Fatigue & Fracture of Engineering Materials & Structures, 31 (2008) 76-84.

[117] S. Hassanifard, M.A.M. Bonab, G. Jabbari, Investigation of fatigue crack propagation in spot-welded joints based on fracture mechanics approach, Journal of Materials Engineering and Performance, 22 (2012) 245-250.

[118] D.A. Wang, C.H. Chen, Fatigue lives of friction stir spot welds in aluminum 6061-T6 sheets, Journal of Materials Processing Technology, 209 (2009) 367-375.

[119] L. Nash Gifford, P.D. Hilton, Stress intensity factors by enriched finite elements, Engineering Fracture Mechanics, 10 (1978) 485-496.

[120] Y. Murakami, S. Nemat-Nasser, Interacting dissimilar semi-elliptical surface flaws under tension and bending, Engineering Fracture Mechanics, 16 (1982) 373-386.

[121] R. Pourmodheji, M. Mashayekhi, Improvement of the extended finite element method for ductile crack growth, Materials Science and Engineering: A, 551 (2012) 255-271.

[122] J. Shi, D. Chopp, J. Lua, N. Sukumar, T. Belytschko, Abaqus implementation of extended finite element method using a level set representation for three-dimensional fatigue crack growth and life predictions, Engineering Fracture Mechanics, 77 (2010) 2840-2863.

[123] D. Radaj, S. Zhang, Stress intensity factors for spot welds between plates of unequal thickness, Engineering Fracture Mechanics, 39 (1991) 391-413.

[124] J.D. Dougherty, Combined Experimental and Finite Element Study of Fatigue Crack Closure in 1070M Steel, in, The University of Akron, 1994.

[125] J.D. Dougherty, J. Padovan, T.S. Srivatsan, Fatigue crack propagation and closure behavior of modified 1070 steel: Finite element study, Engineering Fracture Mechanics, 56 (1997) 189-212.

[126] D. Camas, P. Lopez-Crespo, A. Gonzalez-Herrera, A.S. Cruces, B. Moreno, Study of Fatigue Cracks with Numerical and Experimental Methods, Procedia Engineering, 160 (2016) 13-20.

[127] S.A. Fawaz, D. Hill, Validation of stress intensity factors of diametrically opposed corner cracks in a hole, International Journal of Fatigue, 31 (2009) 712-718.

[128] J.J.M. de Rijck, S.A. Fawaz, Stress intensity factors and crack interaction in adjacent holes, Engineering Fracture Mechanics, 68 (2001) 963-969.

[129] L.P. Pook, Approximate stress intensity factors obtained from simple plate bending theory, Engineering Fracture Mechanics, 12 (1979) 505-522.

[130] S. Zhang, Approximate stress intensity factors and notch stresses for common spot-welded specimens Welding Journal, 78 (1999) 7.

[131] S. Zhang, Fracture mechanics solutions to spot welds, International Journal of Fracture, 112 (2001) 247-274.

[132] D. Radaj, Stress singularity, notch stress and structural stress at spot-welded joints, Engineering Fracture Mechanics, 34 (1989) 495-506.

[133] D.A. Wang, P.C. Lin, J. Pan, Geometric functions of stress intensity factor solutions for spot welds in lap-shear specimens, International Journal of Solids and Structures, 42 (2005) 6299-6318.

[134] D.L. Smith, Plastic Limit Analysis, in: D.L. Smith (Ed.) Mathematical Programming Methods in Structural Plasticity, Springer Vienna, Vienna, 1990, pp. 61-82.

[135] T.-K. Song, Y.-J. Kim, J.-S. Kim, T.-E. Jin, Mismatch limit loads and approximate J estimates for tensile plates with constant-depth surface cracks in the center of welds, International Journal of Fracture, 148 (2007) 343-360.

[136] P.G. Hodge Jr, Plastic Analysis of Structures, McGraw-Hill, New York, 1959.

[137] S. Pommier, Plane strain crack closure and cyclic hardening, Engineering Fracture Mechanics, 69 (2002) 25-44.

[138] Pommier, Bompard, Bauschinger effect of alloys and plasticity-induced crack closure: a finite element analysis, Fatigue & Fracture of Engineering Materials & Structures, 23 (2000) 129-139.

[139] A.T. Kermanidis, S.G. Pantelakis, Fatigue crack growth analysis of 2024 T3 aluminium specimens under aircraft service spectra, Fatigue & Fracture of Engineering Materials & Structures, 24 (2001) 699-710.

[140] R. Jones, L. Molent, S. Pitt, Study of multi-site damage of fuselage lap joints, Theoretical and Applied Fracture Mechanics, 32 (1999) 81-100.

[141] R. S. Piascik, S. A. Willard, M. Miller, The characterization of widespread fatigue damage in fuselage, 1994.

[142] J.J. Homan, A.A. Jongebreur, Calculation Method for Predicting the Fatigue Life of Riveted Joints, in: 17th Symposium, Durability and structural integrity of airframes (ICAF), Stockholm, 1993, pp. 16.

[143] S.J. Moreira, S.M.O. Tavares, P.M.S.T. de Castro, Morphing structures and fatigue: The case of an unmanned aerial vehicle wing leading edge, Fatigue & Fracture of Engineering Materials & Structures 40, (2017) 1601-1611.

[144] M.L. Benzeggagh, M. Kenane, Measurement of mixed-mode delamination fracture toughness of unidirectional glass/epoxy composites with mixed-mode bending apparatus, Composites Science and Technology, 56 (1996) 439-449.

[145] E.M. Wu, R.C. Reuter, Crack Extension in Fiberglass Reinforced Plastics, T and M Report, University of Illinois, vol. 275, 1965.

[146] J. Reeder, K. Song, P. Chunchu, D. Ambur, Postbuckling and Growth of Delaminations in Composite Plates Subjected to Axial Compression, in: 43rd AIAA/ASME/ASCE/AHS/ASC Structures, Structural Dynamics, and Materials Conference, American Institute of Aeronautics and Astronautics, 2002.

[147] R. Galatolo, R. Lazzeri, Experiments and model predictions for fatigue crack propagation in riveted lap-joints with multiple site damage, Fatigue & Fracture of Engineering Materials & Structures, 39 (2016) 307-319.

Lists

List of Figures

List of Tables

Appendix

A – Fatigue results

Single-spot weld

Tables B.1 and B.2 summarise the fatigue test for conditions C16 and C15, respectively. The tables list the different load percentages, stresses, cycles to failure and failure mode. The stopping criterion for the tests was fracture or durability after 10^7 cycles.

Table A.1. Fatigue Test for C16.

Load(%)	$S_{max}(MPa)$	$S_{min}(MPa)$	$S_a(MPa)$	Cycles	Failure Mode*
10	9.9	0.99	4.5	>10,000,000	-
				>10,000,000	-
				>10,000,000	-
15	14.9	1.486	6.688	1780860	TS-UP
				1585253	TS-UP
				1480982	TS-UP
20	19.8	1.98	8.917	369756	TS-UP
				340024	TS-LP (SC)
				324270	TS-UP (SC)
25	24.8	2.5	11.146	145596	TS-UP
				134416	TS-UP (SC)
				132888	TS-UP (SC)
30	29.72	2.972	13.375	145870	TS-LP (SC)
				133875	TS-UP (SC)
				105875	TS-LP (SC)
40	39.63	3.96	17.833	20599	TS-UP (SC)
				17322	TS-LP (SC)
				15100	TS-UP (SC)
50	49.53	4.95	22.292	5373	PPO
				4924	PPO
				4700	PPO

*TS-U – Through the Sheet Upper Plate
TS-L – Through the Sheet Lower Plate
SC – Evident presence of secondary crack
PPO – Plug-Pull Out

TableA.2. Fatigue Test for C15.

Load(%)	$S_{max}(MPa)$	$S_{min}(MPa)$	$S_a(MPa)$	Cycles	Failure Mode*
10	8.98	0.89	4.04	>10,000,000	-
				>10,000,000	-
				>10,000,000	-
15	13.47	1.34	6.625	1458117	TS-UP
				1361402	TS-LP
				1229826	TS-UP
20	17.96	1.796	8.085	591121	TS-UP(SC)
				449138	TS-LP
				609954	TS-LP
25	22.45	2.24	10.10	139152	TS-LP
				179704	TS-UP (SC)
				186753	TS-LP (SC)
30	26.94	2.69	12.225	93141	TS-UP (SC)
				109385	TS-LP (SC)
				99192	TS-UP (SC)

40	35.92	3.59	15.16	19625	TS-LP (SC)
				42696	TS-UP (SC)
				15400	TS-UP (SC)
50	44.90	4.49	22.20	4407	PPO
				3831	PPO
				9782	PPO

*TS-U – Through the Sheet Upper Plate
TS-L – Through the Sheet Lower Plate
SC – Evident presence of secondary crack
PPO – Plug-Pull Out

The empirical estimator $\ln(\ln(1/1-MR))$ versus the corresponding fatigue life $\ln(cycle)$, which is also known as the Weibull plot, establishes the linear tendency for each load level considered in the analysis. From this linear trend, the Weibull slope (β) and characteristic life (α) can be derived via linear regression, considering $b = \beta \ln(\alpha)$. Fig. B.1 presents the Weibull plots for the tested stress amplitudes. When the samples tested with 10% of the lap shear strength do not fail, the results of these samples cannot be employed in the Weibull distribution analysis. Table B.3 summarises the β and α values for each stress amplitude and Weibull mean life.

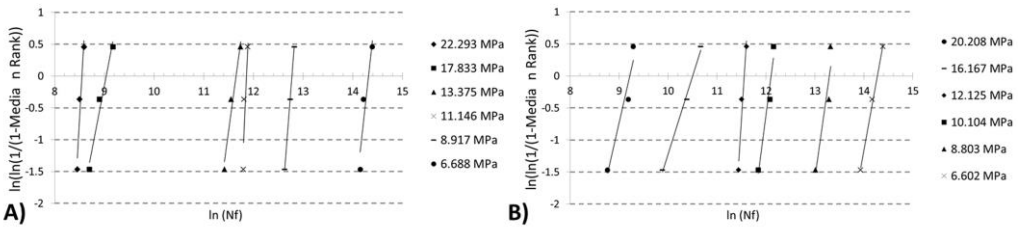

Figure A.1. Weibull plots for each stress amplitude: A) C16; B)C15.

Table A.3. Weibull parameters and mean life for stress amplitudes C15 and C16.

Weld Parameter	S_a (MPa)	Characteristic life (α) (Cycles)	Shape parameter (β)	Weibull mean Life (Cycles)
C16	6.688	1648504	13.752	1565874
C16	8.917	352956	5.7848	340100
C16	11.146	141197	17.116	138205
C16	13.375	125744	9.8778	107613
C16	17.833	7404	16.186	7676
C16	22.292	5160	7.1273	5024
C15	6.625	1828913	5.2292	1768181
C15	8.085	593455	5.3933	580962
C15	10.104	180878	5.8022	177336
C15	12.225	104353	11.668	103332
C15	15.1667	36389	2.4262	34708
C15	22.208	10077	3.3554	9775

B – Temperature measurements

The thermal cycle during refill FSSW was performed to understand the temperature development during the process. Three K-type thermocouples (TC) were employed, as illustrated in Fig. C.1. TC01 is located outside of the stir zone, below the clamping ring at the interface between the upper plates and lower plate. TC02 and TC03 are located 3 mm from the upper surface below the sleeve and probe within the limits of the stir zone. The temperature values were recorded at a frequency of 50 Hz

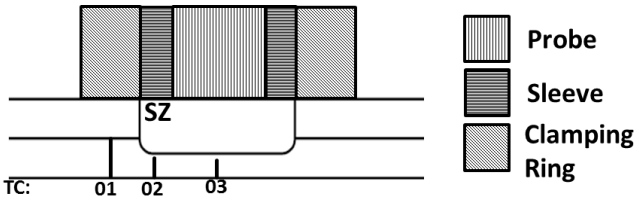

Figure B.1. Distribution of the thermocouples for temperature measurement.

Fig. C.2A presents the thermal cycle of the weld for C16; during sleeve plunging, the temperature under the probe rapidly increased to 370 °C and slightly decreased to 360 °C. It represents 75% of the melting temperature in AA2024-T3 (500 °C). Then, the temperature stabilised and slightly increased to the peak temperature (375 °C) during the dwell time and sleeve retraction. The temperature decreases during the surface dwell stage. Fig. C.2B shows the thermal cycle for condition C5; this sample presents a considerable amount of voids and flaws. Similar behaviours of condition C16 are displayed. However, a small discrepancy in the peak temperature, which is correlated to the exactly height position of the thermocouples, is observed. Note that the temperature abruptly decreased to a minimum of 290 °C at the end of the sleeve retraction stage and increased again during surface dwell.

The temperature decrease during the plunging stage occurs due to a reduction of the material viscosity. Consequently, no friction heating is generated; this phenomenon is well-known as stick-slip transition. In free-defect joints, the material viscosity increases the friction heating, and the stick-slip transition phenomenon is stabilised. Consequently, the temperature progressively increases to the peak temperature. In flawed welds, a sharp temperature decrease during the retraction stage is observed. Thus, the stick-slip transition phenomenon is believed to directly affect the quality of the joints. A non-appropriate heat input leads to a reduction of the plasticised material viscosity, and the stick-slip transition phenomenon affects the material flow and temperature. This phenomenon is generally detrimental to mechanical strength by promoting voids.

The base material is softened during the welding process and experienced dynamic recrystallisation due to the SZ refined-equiaxed grain structure; the starting temperature for recrystallisation is approximately 50% of the melting temperature. The intensive plastic deformation promoted by the tools assists in the grain refinement. The peak temperature at the clamping ring is approximately 245 °C (less than 50% of the material melting temperature), and more or less shear deformation justifies the coarse grain structure of the TMAZ, where dynamic recrystallisation does not occur.

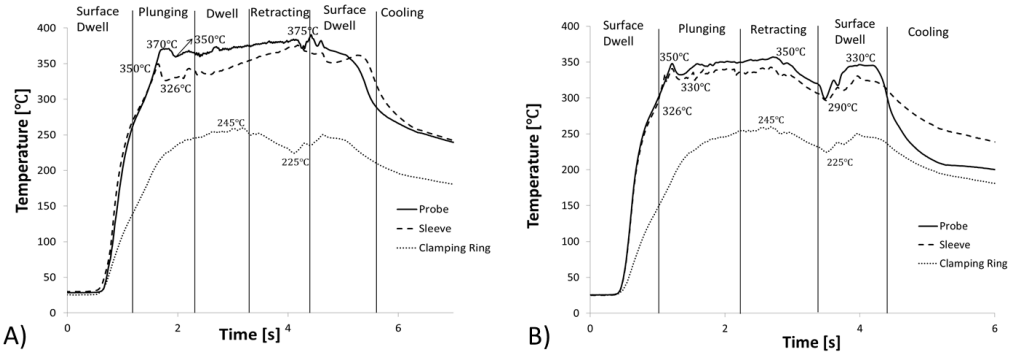

Figure B.2. Temperature measurement during refill FSSW: A) C16 and, B) C5.

C – Optimisation of panels

Fig. D.1 and Fig. D.2 show the results of the spacing optimisation of the numerical and quasi-static loading, where the *y*-axis represents the normalised lap shear force as a function of the maximum force from the geometry in the analysis. A strategy similar to the strategy applied to optimise the spot weld row distance was deployed in this case. From the embedded numerical model, all geometries have shown similar structural behaviours, where the optimised distance varies from $3.5 - 4d_{SW}$. This distance represents 90% of the maximum load for each geometry. Note that an additional increase in the distance S decreases the static strength of the panel joint

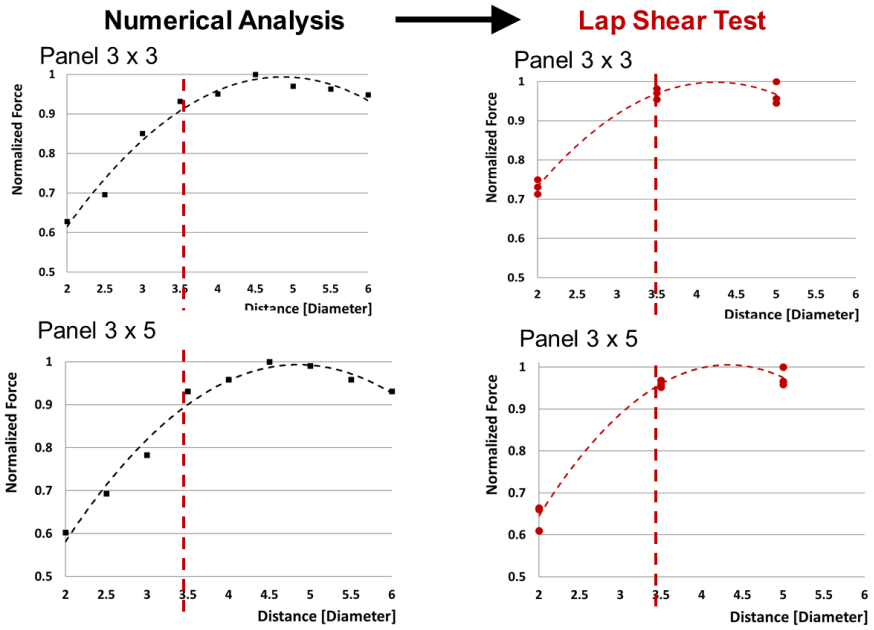

Figure C.1 Optimisation of the distance in row for Panels 3 x 3 and Panels 3 x 5.

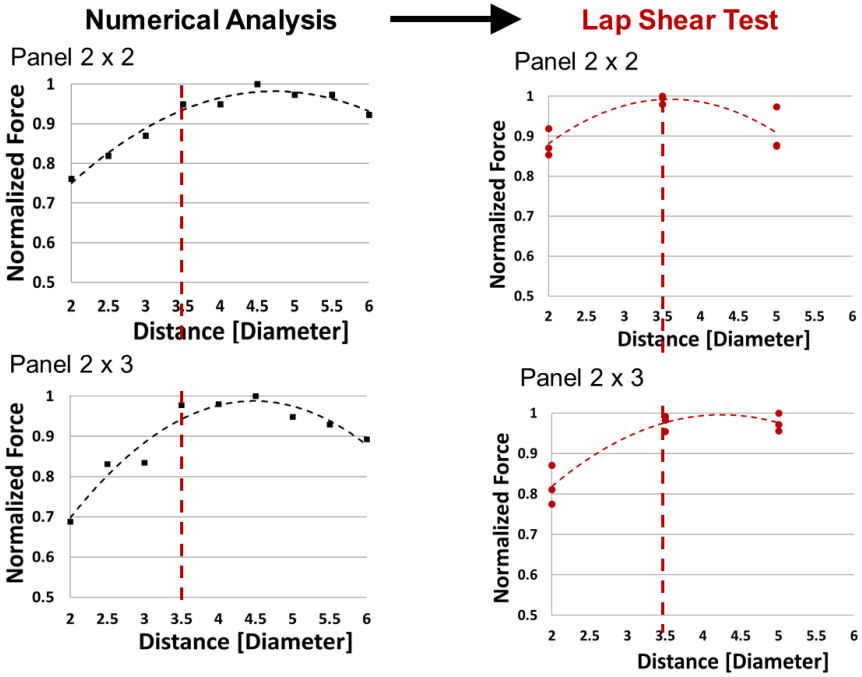

Figure C.2 Optimisation of the distance in row for Panels 2 x 2 and Panels 2